BAKU STATE UNIVERSITY

7th INTERNATIONAL CONFERENCE MTP-2021: MODERN TRENDS IN PHYSICS

DECEMBER 15 - 17, 2021

BAKU STATE UNIVERSITY
BAKU, AZERBAIJAN

PROCEEDINGS

VOLUME II

BAKU STATE UNIVERSITY
33, Academician Zahid Khalilov Street,
Baku, Azerbaijan
Phone: (+994 12) 430 32 45
Fax: (+9942 12) 598 33 76
E-mail: info@bsu.edu.az

ISBN 978-9952-546-53-8

ISSN: 2522-4352

Co-organizers:

BAKU STATE UNIVERSITY

7th INTERNATIONAL CONFERENCE MTP-2021:

MODERN TRENDS IN PHYSICS

DECEMBER 15-17, 2021

BAKU STATE UNIVERSITY, BAKU, AZERBAIJAN

PROCEEDINGS

VOLUME II

BAKU - 2021

Conference organized by
Baku State University

In collaboration with
STAR-NET Regional Network for Education and Training in Nuclear Technology
Joint Instute for Nuclear Research, Dubna
University of Szeged, Hungary
Sapienza University of Rome, Italy

Conference website: http://mtp2021.bsu.edu.az/

Proceedings of the 7th international conference MTP-2021: Modern trends in Physics. Volume II. December 15-17, 2021. Baku State University. Baku, Azerbaijan 2021. – 216 p.

ISSN: 2522-4352

ISBN: 978-9952-546-53-8

CONTENTS

CARBON NANOTUBES DECORATED WITH NICKEL NANOPARTICLES FOR AMMONIA DETECTION

SA AHMADOVA[1], NN MUSAYEVA[1] and G TREVISI[2]

[1]Institute of Physics, ANAS, H.Javid ave. 131, AZ-1143, Baku, Azerbaijan
[2]IMEM-CNR Institute, Parco Area delle Scienze, 37/A, 43124 Parma, Italy
E-mail: shahla.ahmadova05@gmail.com

The paper reports research on sensory effect of the decoration of carbon nanotubes (CNTs) with nickel nanoparticles. Decoration of functionalized multiwall CNTs (f-MWCNTs) with nickel nanoparticles was carried out by electron-beam (e-beam) evoporation. The morphology and structure of pristine, functionalized and nickel-coated MWCNTs were observed by Scanning Electron Microscope (SEM), Transmission Electron Microscope (TEM), and the effect of functionality and nickel decoration on quality of MWCNTs was analyzed by Raman spectroscopy. The sensor element was developed on dielectric substrate based on f-MWCNTs and Ni/f-MWCNTs and its sensitivity to ammonia gas was studied. It was found that the decoration of f-MWCNTs with nickel nanoparticles leads seven times increasing of its sensitivity to ammonia at room temperature. Parameters, such as selectivity, response, and self-recovery time were also characterized. Defined that, Ni/f-MWCNTs sensors show the highest sensitivity to NH_3 compared to ethanol (CH_3CH_2OH), methanol (CH_3OH), acetone (CH_3COCH_3) at room and 45,3^{0}C temperatures.

Keywords: carbon nanotubes (CNTs), nickel, decoration, SEM, TEM, Raman spectroscopy
PACS: 82.47Rs, 88,30rh, 61.46.+w

Introduction

Every year a large amount of toxic gases from factories and plants are released into the atmosphere, and pollutants are released into the environment. Such ecosystem pollutants have destroying effects on living things on land and in water, as well as on humans [1]. Ammonia gas among these gases is a very toxic. If the concentration of ammonia in the air exceeds 350 mg/m^3, all work must be stopped. Inhalation of air containing ammonia is very harmful to the respiratory tract and vision, and even in high concentrations can be fatal. Since these toxic gases pollute the environment, preventing them is always important. Fast, sensitive, durable and selective devices are essential for easy and effective detection of toxic gases/vapors during environmental monitoring.

There are different materials and technologies have been developed and applied for toxic gas detection [2, 3]. The important task is to have more sensitive and selective, energy safety, low cost technology and device for such detection.

In this work tubular carbon structure - carbon nanotubes (CNTs) are selected to developing of toxic gas sensors, because CNTs - has the highest bearing capacity, the largest area per unit mass, very high thermal (eg. diamond) and electrical conductivity (eg. copper), which are important for integrated circuits. Depending on their chirality, they can be semiconductor or conductor as metal, chemically inert, and heat-resistant. These properties can be applied to transistors, sensors, diodes, parts of modern microscopes, etc. [4].

Composite nanoparticle-nanotube structures that combine the unique properties of CNTs and nanoparticles have many applications such as nanoelectronics, catalysis, chemical sensors, fuel cells, and hydrogen storage devices [5-9]. CNTs are widely used to detect various toxic qases and vapours due to their good electrical and high adsorption properties. It has

been already developed sensors that can detect vapors of various gases and aromatic substances by functioning CNTs [10, 11].

In fact that, the pristine CNTs are relatively inert in the environment, and this makes actual to activate their outer walls in order to use them in sensor elements. There are different methods to activate of the surface of CNTs, as covalent and noncovalent functionalization, decoration by inorganic and organic (metal oxide nanoparticles [12], polymers [13], non-polymeric organic materials [14] and catalytic metal nanoparticles [15-17]) materials.

In this work the CNTs have been synthesized by Aerosol CVD method, purified and after chemical functionalization decorated with Nickel nanoparticles. The obtained materials have been characterized by SEM, TEM and Raman spectroscopy methods. The sensor elements have been developed and tested in the vapor medium of ammonia, asetone, ethanol and methanol.

Experimental

Preparation of CNTs

The synthesis process of CNTs was carried out in an aerosol Chemical Vapor Deposition (A-CVD) facility. Liquid hydrocarbon - heptane and ferrum catalysts (Ferrocene), were used as raw materials. A high-frequency (800kHz) ultrasound device was used to obtain the aerosol during the synthesis process. CNTs were grown at atmospheric pressure and temperatures T = 950^0C and synthesized in the presence of H_2+Ar gases. As a result, the obtained CNTs were mechanically removed from the quartz tube after cooling in an argon atmosphere [18]. The characteristics of the obtained CNTs are shown in Table 1.

Table 1

The properties of obtained CNTs	Value
Type	MWCNTs
Outer diameter	32-65nm
Inner diameter	3-5 nm
Purity	90%
Length	100-500μm
Special surface area	10-20 m2/g
Electrical conductivity	104-107 S/m
Color	Black

Functionalization of MWCNTs

The MWCNTs need to be purified before oxidation and decoration with metal to achieve optimal performance, because during synthesis, amorphous carbon, and other pyrolitic carbon structures are formed. MWCNTs were washed 3 times with xylene and once with cyclohexane at 80^0C. It was then washed at the same temperature for 2 hours in a 1:1 ratio of nitric acid and water. Finally, it was washed in deionized water and dried. After the purification process, the MWCNTs were functionalized. At this stage, HNO_3 and H_2SO_4 are mixed in a 3:1 ratio in a round-bottomed flask. Then 100 mg of pristine MWCNTs were added. The resulting mixture was sonicated at room temperature for 5 hours. After sonication, it was washed with

deionized water until neutralized. Finally, the black powders were washed with ethanol and dried in drying oven at 80^0C.

Decoration of f-MWCNTs with Ni nanoparticles

To decorate with nickel, the oxidized MWCNTs were first mixed with deionized water to disperse it on the dielectric surface (ceramic) and a f-MWCNTs network was created. After drying, the sample was placed in the vacuum (10^{-2} Torr) chamber of the Angstrom Engineering Equipment and using e-beam evaporation method, 5-10 nm thickness pure nickel (99.99%) was deposited.

Material characterization

To have more information about surface morphology and structure parameters, and effects of chemical processes with acids, such as purification, functionlization and metal (Ni) decoration on MWCNTs, observations by SEM and TEM microscopes were carried out. The SEM images show (Fig. 1), that purifying and functionalization did not adversely affect the morphology and not damaged (broken) the grown so long (150-200 mkm) nanotubes. This fact was confirmed by observation them in TEM microscope (Fig. 2).

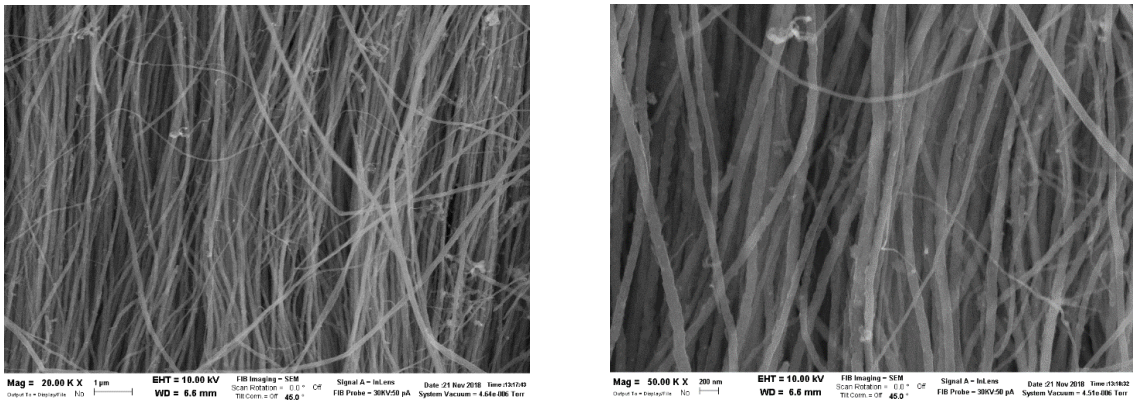

Fig. 1. SEM images of purified (left) and functionalized (high magnification) MWCNTs

The right picture is the high magnification HR-TEM image of the MWCNT in the left picture, which demostrate of their smooth walls. In the right image the straight lines are the walls of the CNT, i.e. the atomic planes of C whose interdistance is 0.342 nm. The inner channel of the MW is the stripe between the 2 sets of the lattice planes of C. The CNT is 19 nm wide and its outer borders are visible in the right image.

Figure 3 shows morphology of the f-MWCNTs after decoration with nickel. A higher resolution image (Fig. 3 right) shows the presence of densely spaced nickel nanoparticles on the surface of f-MWCNTs. Such arrangement of nanoparticles on the CNT walls increases the probabilities of bonding between carbon and nickel atoms, which means the role of nickel nanoparticles in the sensory properties of the nanocomposite Ni/f-MWCNTs.

The influence of Ni decoration to vibrational modes of the f-MWCNTs was analysed by Raman spectroscopy method (Fig. 4). There is a assuming that, the full covering of CNTs by

densely spaced Ni nanoparticles lead to decreasing the intensity of G-graphie band-sp^2 hybridized carbon atoms on the nanotube wall, and/or increasing of D-band, which connected with deffects and sp^3 hybridized carbon atoms (see table 2).

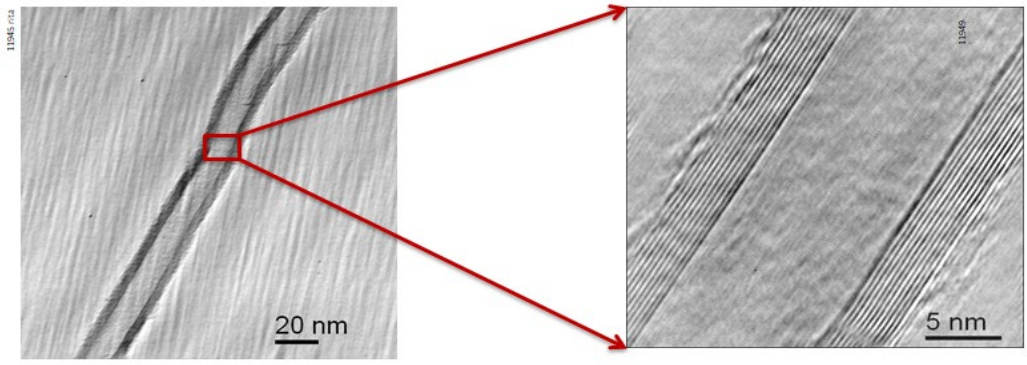

Fig. 2. TEM picture of one CNT which diameter is approx. 19 nm

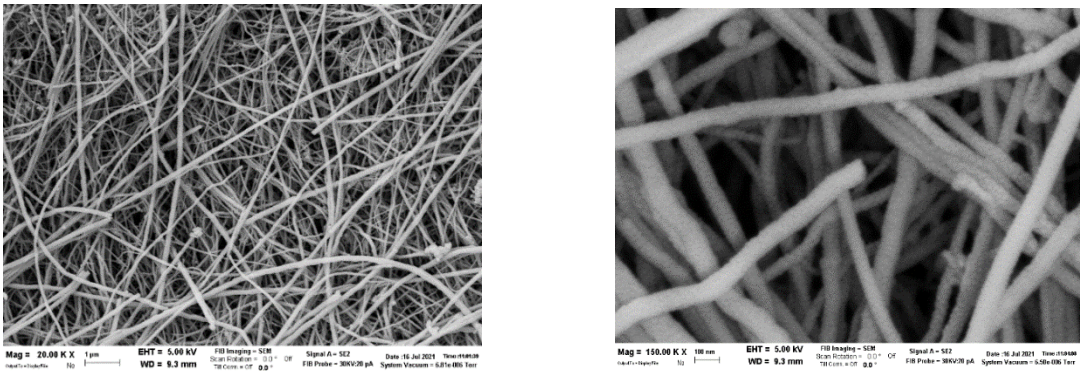

Fig. 3. SEM images of Ni decorated f-MWCNTs right image is high magnification picture of the left one

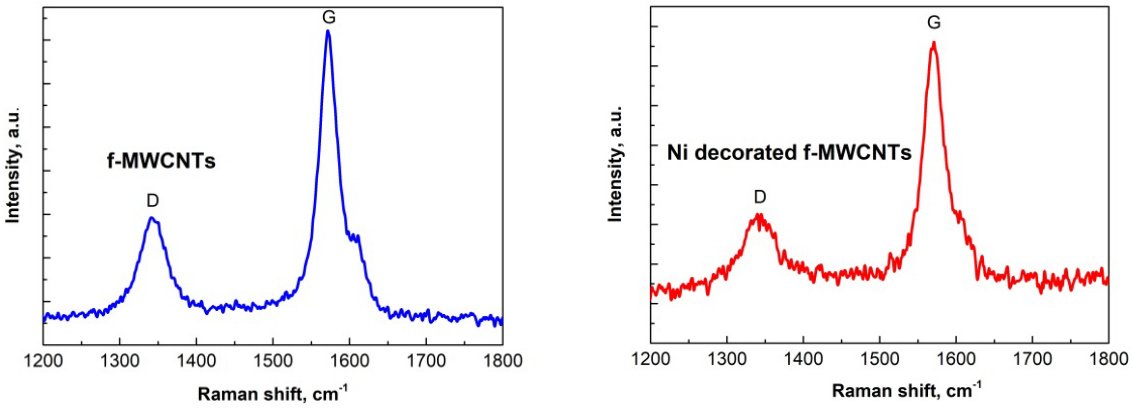

a) b)

Fig. 4. Raman spectra of f-MWCNTs (a) and Ni/f-MWCNTs(b), including corresponding (I_D/I_G) values (see table 2)

Table 2.

Sample	D-band (cm^{-1})	G-band (cm^{-1})	I_D/I_G
f-MWCNTs	1343	1573	0.39
Ni/f-MWCNTs	1339	1569	0.43

Gas sensing characterization

The silver contacts were deposited on network like f-MWCNTs and Ni/f-MWCNTs dispersed on ceramic substrates (Fig. 5). The realized sensors show a value of resistance of ranging 20-23 Ohm.

To test of the sensitivity of the sensor to gases and vapors the sensor elements were placed in hermetic closed test cell, which has input and output pipes for the testing gases (Fig. 6). The gas sensing experiments were performed by evaluating the change in resistance of the sensor material. After each testing, the sensor element kept for stabilization for 30-60 minutes depending from gases type and concentration of them.

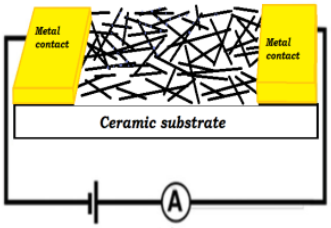

Fig. 5. MWCNTs based sensor structure

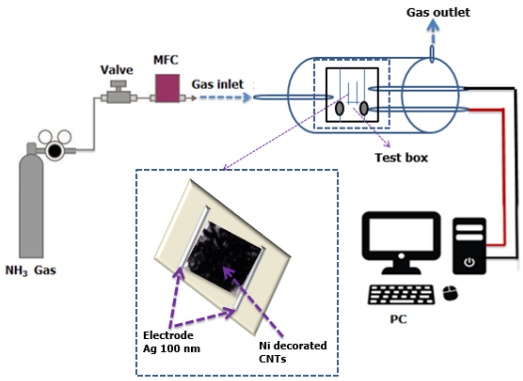

Fig. 6. Sensor testing system

The Fig. 7. shows the resistance response of the sensor elements to 40 ppm ammonia at room temperature. It is defined that after decoration with Nickel nanoparticles, the sensitivity of the material to ammonia is increasing 7 times.

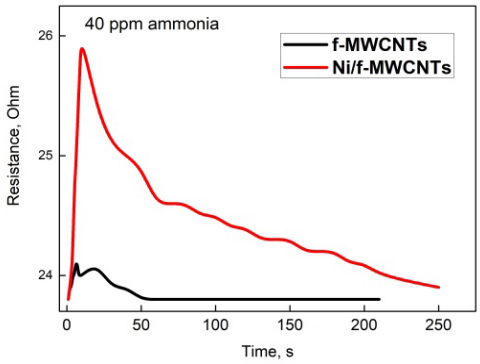

Fig. 7. Resistance response of the sensor elements to 40 ppm ammonia at room temperature

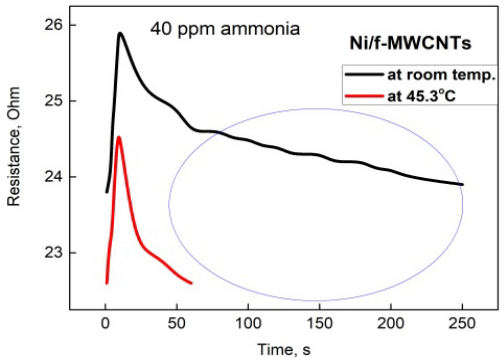

Fig. 8. Temperature influence to recovering time of the sensor element based on Ni/f-MWCNTs at 40 ppm ammonia.

In order to control sensitivity and recovering time of the sensor it was heated till 45.3^{0}C. In this case while the intensity of the sensitivity was the same, but the recovering time is decreased approximately 5 times (Fig. 8).

Selectivity testing was carried out at 45.3^{0}C temperature using one drop of each liquid phase substances. While the concentration of the other substances in the test chamber was 3-4 times higher than ammonia in ppm, the sensitivity of the sensor to ammonia was 5 times

higher than, for example, methanol (see Fig. 9.).

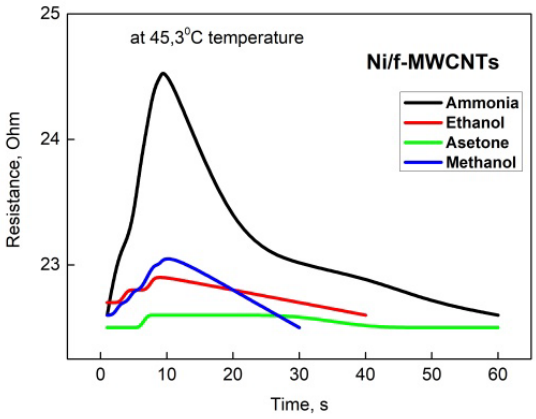

Fig. 9. Selectivity testing of the sensor element based on Ni/f-MWCNTs.

Conclusions

This work concludes that although the pristine CNTs have absorption properties in open air, they surface can be active after their functionalization by carboxyl or hydroxyl groups. This is open the door to use such CNTs for sensors to detect different specific gases. It was observed no quality change (not damaging of the CNTs structure) during chemical functionalization that is confirmation of chose optimal reaction method. The nickel nanoparticles covered f-MWCNTs surface without any contamination.

It was observed that the sensitivity to ammonia is increased ~7 times as a result of deposition of nickel nanoparticles on f-MWCNTs. Ni/f-MWCNTs sensors show the highest sensitivity to NH_3 compared to ethanol (CH_3CH_2OH), methanol (CH_3OH), acetone (CH_3COCH_3) at room and 45,3^{0}C temperatures.

Also it was observed that the recovery time of the sensor was decreased by five times at 45,3^{0}C temperature than at room temperature. It was controlled high temperatures, and concluded that 45,3^{0}C is optimal operation temperature for such sensor for detection of ammonia.

As a result, it is concluded that such Ni/f-MWCNTs material can be successfully applied as high sensitive, selective and cost effective ammonia sensor working at room and near to it temperatures. The researches in this field are continuing.

Acknowledgments

Authors would like to thank Dr.Cesare Frigeri, IMEM–CNR, Parma Italy for TEM analysis and Mr.Elnur Baghiyev, Institute of Physics, ANAS for his help in Ni deposition at Angstrom Engineering Equipment.

References

1. Khalilova H.Kh. Chemical Problems 2019, v. 4 (17), p. 500. DOI:10.32737/2221-8688-2019-4-500-517
2. Popov V.N. Materials Science and Engineering R 2004, v. 43, p. 61. DOI:10.1016/j.mser.2003.10.001
3. Musayeva N., Orujov T., Hasanov R., Sultanov Ch., Ferrari C., Frigeri C., Trevisi G., Beretta S., Bosi M.,

R.Verucchi, L.Aversa, F.Sansone, F.Rispoli, L.Baldini. Materials Today: Proceedings 2020, v. 20, p.46. doi.org/10.1016/j.matpr.2019.08.218

4. Rahman G., Najaf Z., Mehmood A., Bilal S., Shah A., Mian S., Ali G. An Overview of the Recent Progress in the Synthesis and Applications of Carbon Nanotubes 2019, v. 5 (1), p. 3. doi.org/10.3390/c5010003
5. Dresselhaus M.S., Avouris P., Introduction to carbon materials research, In Dresselhaus M.S., Dresselhaus G., Avouris P. (Eds.), Carbon nanotubes: synthesis, structure, properties, and applications Chapter-2, Sringer, 2001, p.1-9.
6. Alivisatos A.P., Science 1996, v. 271 (5251), p. 933.
7. Hu J., Ouyang M., Yang P., Lieber C.M. Nature 1999, v. 399, (6731), p. 48.
8. Luo J., Jones V.W., Maye M.M., Han L., Kariuki N.N., Zhong C.J. J. American Chemical Society 2002, v. 124 (47), p. 13988.
9. Kong J., Chapline M.G., Dai H. Advanced Materials 2001, v. 13 (18), p.1384. DOI:10.1002/1521-4095(200109)13
10. Zhang W.D., Zhang W.H. J. Sensors 2009, p. 160698. doi.org/10.1155/2009/160698
11. Goldoni A., Petaccia L., Lizzit S., Larciprete R. J. Phys. Condens. Matter 2010, v. 22, p. 013001. DOI:10.1088/0953-8984/22/1/013001
12. Bee-Yu Wei, et al. Sens. Actuators B-Chem. 2004, v. 101, p. 81.
13. Dai L.M., Soundarrajan P., Kim T. Pure App. Chem. 2002, v. 74, p. 1753. DOI:10.1351/pac200274091753
14. Yael Z. et al. ACS Nano 2011, v. 5, p. 6743. DOI: 10.1021/nn202314k
15. Leghrib R., et al. Carbon 2010, v. 48, p. 3477. DOI:10.1016/j.carbon.2010.05.045
16. Star A., Joshi V., Skarupo S., Thomas D., Gabriel J.C.P. Phys. Chem. 2006, v. 110, p. 21014. doi.org/10.1021/jp064371z
17. Baccar H., Thamri A., Clément P., Llobet E., Abdelghani A. Beilstein J Nanotech. 2015, v. 6, p. 919. doi.org/10.3762/bjnano.6.95
18. Abdullayeva S.H., Musayeva N.N., Frigeri C., Huseynov A.B., Jabbarov R.B., Abdullayev R.B., Sultanov Ch.A., Hasanov R.F. Journal of Advances in Physics 2015, v. 11 (4), p. 3229. DOI:10.24297/jap.v11i3.6943

DIELECTRIC HYSTERESIS IN SUBMICRON BARIUM TITANATE PARTICLES

AR IMAMALIYEV[1], GF GANIZADE[1] and SHA HUMBATOV[2]

[1]Instiute of Physics of ANAS, Baku, Azerbaijan
[2]Department of Chemical Physics of Nanomaterial, Faculty of Physics, Baku State University, Baku, Azerbaijan
E-mail: rahimoglu@mail.ru shirxan-humbatov@mail.ru

In this work, the dielectric properties of monodisperse 0.2 μm sized barium titanate ($BaTiO_3$) particles are investigated. To prevent strong aggregation of polarized $BaTiO_3$ particles, the surfaces of these particles were coated with oleic acid. Analysis of the capacitance-voltage characteristics of barium titanate thin film allows us to reveal some patterns. As in a bulk crystalline sample of $BaTiO_3$, the dependence of the dielectric permittivity on the electric field has a hysteresis behavior. The coercive field is higher (2.5 kV/cm) compared to bulk samples (1.5 kV/cm). From the saturation value of the dielectric constant, we estimated the spontaneous polarization of barium titanate particles: Ps=0.15μC/cm2. This is two orders of magnitude less than bulk samples of $BaTiO_3$ (26μC/cm2). An explanation of the results on the basis of the core-shell model is presented.

Keywords: barium titanate, ferroelectric ceramics, spontaneous polarization, perovskite structure
PACS: 77.84.–s, 77.90.+k, 75.60.-d

Introduction

Barium titanate ($BaTiO_3$) is a ferroelectric with high spontaneous polarization (26 μC/cm^2) and is widely used as elements in various devices: memory devices, nonlinear capacitors and super capacitors, infrared sensors, laser frequency doubler, ultrasonic generator, positive temperature coefficient thermistors etc. [1-3].The constructive combination of the features of submicron particles and nanoparticles of $BaTiO_3$ with other functional materials can lead to qualitatively new effects, which makes it possible to expand their applications. For example, composites based on polymers and $BaTiO_3$ particles are used in charge storage devices, multilayer ceramic capacitors, voltage sensors, etc. In the future, $BaTiO_3$ particles can be used in liquid crystal displays, because the addition of these particles to liquid crystals in small amounts drastically improves some of the characteristics of electro-optical effects in the liquid crystal, such as driving voltage, response time etc. [4-7].

To optimize the characteristics of barium titanate based composites and colloid systems, it is necessary to clarify how the properties of submicron $BaTiO_3$ particles change in comparison with a bulk sample of a $BaTiO_3$ crystal. In this work, the dielectric properties of mono disperse $BaTiO_3$ particles with a size of 200nm has been investigated.

Experiment

$BaTiO_3$ particles were purchased from company US Nano.Fig. 1 shows scanning electron micrograph of these particles in JOEL JSM-767F. To prevent strong aggregation of polarized $BaTiO_3$ particles, the surfaces of these particles must be coated with suitable surfactant. For this purpose, the stabilizer oleic acid was added to the barium titanate powder in a weight amount of 16% (volume fraction 57%).

Dielectric measurements of obtained slurry type mixture were carried out in a special cell consisting of two plane-parallel glass substrates, the inner surfaces of which are covered with

a transparent ITO electrode. The sample thickness is fixed with a special 50 µm Teflon spacer. A micrograph of the system of particles $BaTiO_3$ - oleic acid is shown in Fig. 2 (Karl Zeiss microscope equipped with 14 MP Am Scope camera).The capacitance-voltage characteristic of the cell was measured using an E7-20 RLC meter, which allows a bias voltage of up to 40 V to be applied.

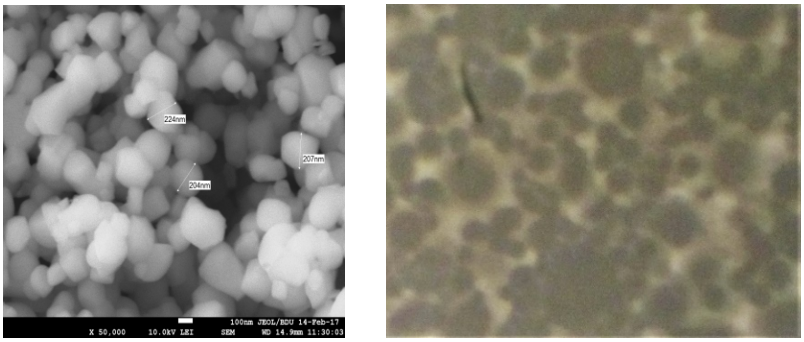

Fig. 1. Scanning electron micrograph of these particles:
(a) Pure $BaTiO_3$; (b) system of particles $BaTiO_3$ - oleic acid

Discussion and conclusions

On the basis of this characteristic, the dependence of the dielectric constant of the colloid on the electric field strength was constructed, which is shown in Fig. 2.

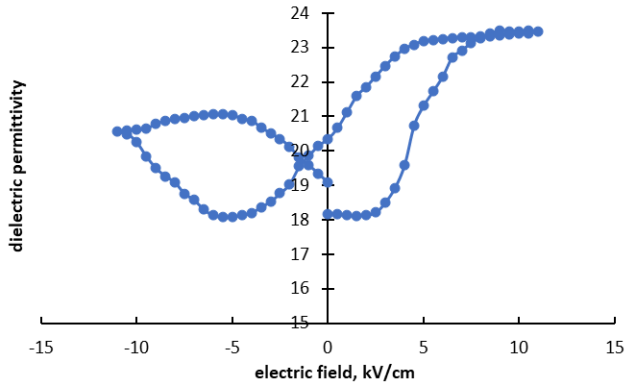

Fig. 2. The dependence of the dielectric constant of the system of particles $BaTiO_3$ - oleic acid on the electric field strength

Analysis of the graph reveals the following patterns:

1) As expected, the dependence of the dielectric constant on the electric field has a hysteresis character;

2) The change in dielectric constant begins with a field strength of 2.5 kV/cm;

3) The coercive field is 5 kV/cm;

4) The saturation of the dielectric constant occurs at a field of 10 kV/cm.

The presence of dielectric hysteresis indicates that the 200 nm barium titanate particles still retain their ferroelectric properties. The difference is that, in large $BaTiO_3$ samples, the increase in the dielectric constant with increasing field has a non-threshold character and is associated with the transition from the polydomain state to the single-domain state. But in a

medium dispersedwith small $BaTiO_3$ particles, this occurs, starting from a field strength of 2.5 kV/cm.

Using the Landau formula [8]

$$\sqrt[3]{\varepsilon_{eff}} = f\sqrt[3]{\varepsilon_m} + (1-f)\sqrt[3]{\varepsilon_p} \quad (1)$$

for the effective dielectric constant of a heterogeneous system consisting of two dielectrics, where $f = 0.57$ is the volume fraction, and $\varepsilon_m = 2.6$ is the dielectric constant of oleic acid, it is easy to find the dielectric constant of barium titanate particles corresponding to an unpolarized state (zero field) and a state with saturated polarization:

$$\varepsilon^p_{min} = 66.7 \text{ and } \varepsilon^p_{max} = 172.5$$

The value of the coercive field has a significantly increased value (10 kV/cm) in comparison with a large crystal of barium titanate (1.5 kV/cm) [9]. We estimated the spontaneous polarization of $BaTiO_3$ particles using the formula

$$P_S = \varepsilon_0(\varepsilon^p_{max} - \varepsilon^p_{min})E \quad (2)$$

and obtained approximately 0.15 μC/cm^2, which is much less than that of the bulk crystal of $BaTiO_3$ (26μC/cm^2 [10]). Based on general considerations, this can be attributed to the increased role of the surface with decreasing particle size. According to modern concepts, submicron barium titanate particles consist of a tetragonal core and a cubic shell with a thickness of about 10 nm (core-shell model [11]). In addition, the degree of tetragonality c/a, which is directly related to the value of spontaneous polarization, also decreases with decreasing particle size of barium titanate particles [12].

A for the polarization saturation field of $BaTiO_3$, it has nearly same value for particlesas a bulk sample [13].

References

1. Garbovskiy Yu., Zribi O., Glushchenko A., Emerging Applications of Ferroelectric Nanoparticles in Materials Technologies, Biology and Medicine, http://dx/doi/org/10.5772/52616
2. Burcu Ertuğ. American Journal of Engineering Research 2013, v. 2 (8), p. 1.
3. Vijatović M.M., Bobić J.D., Stojanović B.D. Science of Sintering 2008, v. 40, p. 235.
4. Reznikov Y., Ferroelectric Colloids in Liquid Crystals, Liquid Crystals beyond Displays: Chemistry, Physics, and Applications edited by Quan Li, John Wiley & Sons, Inc., Hoboken, New Jersey, 2012, 573 p.
5. Ibragimov T.D., Imamaliyev A.R., Bayramov G.M. Optk 2016, v. 127, p. 1217.
6. Ibragimov T.D., Imamaliyev A.R.,.Bayramov G.M. Ferroelectrics 2016, v. 495, p. 60.
7. Imamaliyev A.R., Humbatov Sh.A., Ramazanov M.A. Beilstein Journal of Nanotech. 2018, v. 9, p. 824.
8. Landau L.D., Lifshits E.M. Electrodynamics of continuous media, 1985, 474 p.
9. Shieha J., Yeha J.H., Shub Y.C., Yen J.H. Materials Science and Engineering B 2009, v. 161, p. 50.
10. Blakemore J., Solid state physics, Cambridge University Press 1985, 517 p.
11. Sedykh P., Michel, E.Charnaya D., Haase J., Ferroelectrics 2010, v. 400, p. 135.
12. Yu J., Chu J., Nanocrystalline Barium Titanate, Encyclopedia of Nanoscience and Nanotechnology Edited by H. S. Nalwa, v. 6, p. 389-416.
13. Cross L.E., Ferroelectric ceramics. Tutorial reviews, theory, processing, and applications. Basel etc.: Birkhäuser Verlag, 1993, p. 1– 85.

SIMULTANEOUS EFFECT OF EXTERNAL FACTORS ON THE ELECTRIC STRENGTH OF POLYETHYLENE+NANOCLAY NANOCOMPOSITES

AR SADYGOVA[1], AA HADIYEVA[1], PB ASILBEYLI[1] and KHO SADIG[2]

[1] Institute of Physics of ANAS, H.Javid Ave. 33, AZ1143, Baku, Azerbaijan
[2]Azerbaijan State Oil and Industry University, Azadlig Ave. 20, Baku, AZ1001, Azerbajan
E-mail: arzu-sadigova@mail.ru

The simultaneous effects of mechanical load and electrical discharge on the electrical durability (τ_E) and mechanical durability (τ_M) of high density polyethylene (HDPE) and nanoclay (NC) nanocomposites has been investigated. Comparing physical properties with structural changes, it has been shown that carbonyl groups are formed during the breaking of macromolecules under the simultaneous influence of external factors. In the nanocomposite, the decomposition rate under the simultaneous exposure to an electrical discharge and mechanical load is lower than that of HDPE.

Keywords: nanoclay, nanocomposite, electrical discharge, electric strength
PACS:46.w, 82.35.Np, 71.38.k

Introduction

When using products obtained from polymers in real conditions, they are exposed to the simultaneously complex effects of mechanical load, strong electrical field and discharge, temperature, radiation, etc., and in the process of practical application quickly fail (disintegrate). In order to increase the lifetime of these products and prevent their disintegration, polymers-based composites with various additives are used in industry. Composite materials are a system formed by two or more phases that differ in chemical composition and structure [1, 2, 3].

In general, polymer-based composites began to be produced in the 40s of the last century. The first polymers used as matrices were elastomers and epoxies (fiberglass). After that, thermoplastic polymers, as well as polyolefins, began to be used as matrices. At present there are various additives for polymer matrices [4, 5]. Substances used as additives fall into two main classes. The first type – solid additives (chalk, talc, aluminum hydroxide, graphite, etc.) are introduced in order to increase the strength, hardness, heat resistance and reduce gas permeability of the material. The second type of additives are introduced to conserve organic raw materials and reduce the cost of the product.

In the studies [6-9], changes in the dynamic-mechanical, electrical, deformation and optical properties of polymers based composite materials with organic and inorganic additives have been observed, and little information has been given about the mechanism of this change.

Experiments show that the decomposition rate (the number of broken bonds) in the process of decomposition, which occurs under the simultaneous influence of several external factors, depends on the changes caused by each factor [10]. Under these conditions, more wear-resistant materials are selected by determining the mechanical and electrical durability of the polymers, and the study of polymer-based composites with various additives is of scientific and practical interest.

Taking these into account, in the given study, mechanical durability (τ_M) was measured with simultaneous exposure to an electrical discharge and electrical durability (τ_E) with

simultaneous exposure to a mechanical load for pure high-density polyethylene (HDPE) and HDPE+3,0% nanoclay nanocomposite.

Experiments and methods

Reagents

Nanoclay (NC) in a form of a powder in different percentages (1,0; 2,0; 3,0; 4,0; 6,0; 8,0; 10,0 %) is mechanically mixed with polyethylene by hot pressing method (425 K, 150 MPa, 10 minutes), thin samples (70-100 μm) were obtained. Since both components are in powder form and have approximately the same density, a homogeneous mixture is obtained. The additive used as NC is montmorillonite (MMT) layered silicate and the dimensions of these layers are approximate: 200 nm in length and 1mm in width [11, 12]. In the center, there are Al, Mg and Fe atoms surrounded by a layer of silicon oxide. The disturbance of the electrostatic equilibrium within the clay with such a structure increases, and negatively charged particles are formed outside the layer. Negatively charged particles are neutralized by absorption of Na^+, Ca^+ cations. The fact that Na^+MMT particles are in such a flat shape leads to the formation of a layered structure with a polymer matrix by stacking the layers on top of each other. The uniform distribution of clay in the polymer indicates that the nanocomposite has an ideal structure.

The mechanical and electrical durability of nanocomposites obtained in different percentages of NC can be measured at different temperatures. These measurements made it possible to determine the lifetime (durability) at various mechanical loads and electric fields from the moment of loading the sample to the moment of its destruction. A device for measuring (τ_M) must meet two basic requirements: the voltage and temperature applied during each test must not change.

Equipment

To compensate for the increase in mechanical load caused by the applied load during the experiment, an automatic decrease in the force created by the constant load as the length of the sample increases is carried out using a curved lever [10]. To study the force dependence of the mechanical strength, the samples were cut with a special shovel-shaped knife with a width of 1,5 mm and a length of the working part of 10 mm. To study the structural changes, the optical density (D) of the C=O (carbonyl) group corresponding to the 1720 cm^{-1} wave frequency of nanocomposites was calculated and compared with the strength properties using infrared (IR) absorption spectroscopy in the frequency range of 400-2500 cm^{-1}.

Results and discussion

The effect of NC on the mechanical and electrical durability of HDPE has been studied in our previous research [13]. Depending on the amount of NC, the mechanical strength (σ) increases to 3,0% and then begins to decrease as the amount of additive increases. The electric strength (E) gradually decreases with an increase in the amount of additive in nanocomposites (Fig. 1).

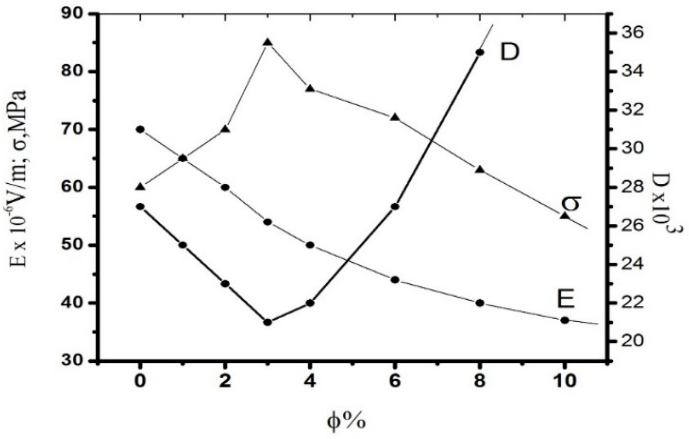

Fig. 1. Dependence of mechanical and electrical durability and optical density on the amount of NC

As (τ_M) of the exposed to electrical discharge (aged) samples has been studied before [14], this work was undertaken because of the simultaneous effect of the electrical discharge on τ_σ, which we often encounter in practice. Instead of taking measurements for all nanocomposites, we can determine the role of NC in the mechanical decomposition process by taking one (HDPE + 3,0% NC with the highest σ) and comparing it with pure samples.

Figure 2 represents the dependence of the mechanical durability logarithm ($lg\tau_M$) of the HDPE and HDPE+3,0% NC nanocomposite on σ under the simultaneous exposure to an electrical discharge. The accepted electrical discharge voltage is U=7·10^{3}V and 9·10^{3}V.

As shown in Fig. 2 (curves 1, 2, 3), the dependence of $lg\tau_M$ under mechanical load under the action of an electrical discharge in a sample without a NC consists of two linear parts. One of them ($\sigma > \sigma^*$) coincides with the $lg\tau_M$ (σ) dependence, which is not affected by the electrical discharge (curve 1), and the other ($\sigma < \sigma^*$) differs in slope from curve 1 (curves 2, 3). σ^* - is the breakdown voltage of the straight line.

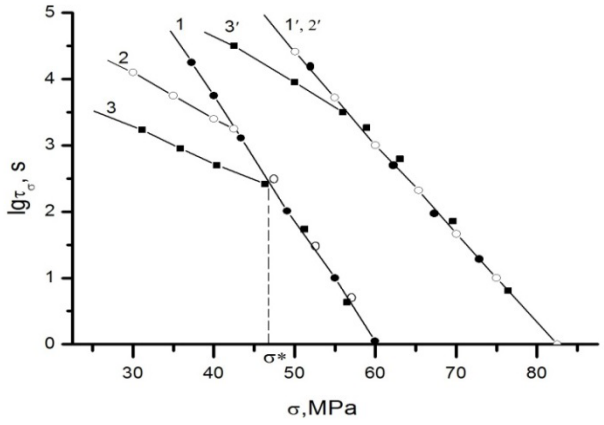

Fig. 2. Dependence of mechanical durability on mechanical load during simultaneous exposure of HDPE (1-3) and HDPE+3,0% NC (1′-3′) nanocomposite to electrical discharge.

1,1′ ~U=0; 2,2′~ $U = 7 \cdot 10^3$V; 3,3′~$U = 9 \cdot 10^3$V

At values of mechanical load $\sigma < \sigma^*$durability is reduced with respect to the durability when the discharge is not affected simultaneously (curve 3). Then the following expressions

are obtained for the durability:

$$\tau_{M,U} = A_U \exp(-\alpha_U \sigma), \text{ if } \sigma < \sigma^* \quad (1)$$

$$\tau_{M,U}=\tau_M=A \exp(-\alpha\sigma), \text{ if } \sigma > \sigma^* \quad (2)$$

The observed dependence can be explained as follows: another decomposition process arising during the discharge is added to the thermal fluctuation decomposition process under the influence of a mechanical load. If $\sigma > \sigma^*$, the durability of the sample under load is also determined mainly by the effect of thermal fluctuations, but in the load range $\sigma < \sigma^*$ it accelerates the electrical discharge, which simultaneously affects the broken bonds with thermal fluctuations. As the discharge voltage increases, the breaking point in the $lg\tau_M$ (σ) dependence shifts towards higher values of σ and smaller values of τ_M.

It is known that in the presence of oxygen in radical reactions in the macromolecule are formed end groups with different oxygen content [15 - 16]. Therefore, the effect of both σ and U makes the oxidation of polyethylene more intense.

In HDPE+3,0% NC nanocomposite NC plays an antioxidant role [14], on the one hand increases σ and τ_M (curve 1' in Figure 2), on the other hand simultaneous electrical discharge does not change τ_M ($U = 7 \cdot 10^3 V$, curve 2′) on the dependence of $lg\tau_M$ (σ), or changes it slightly ($U = 9 \cdot 10^3 V$, curve 3′).

In the manufacture of samples, they are exposed to external factors (temperature, pressure). To find out what changes in the structure are caused by NC, the optical density of the C=O group corresponding to the wave frequency of 1720 cm^{-1} of HDPE and nanocomposites was calculated by IR absorption spectroscopy in the frequency range 400÷2500 cm^{-1}. Depending on the amount of NC in Figure 1, D_{1720} decreases to 3,0% amount of NC and then increases. During the manufacturing of samples, C=O carbonyl groups are formed and oxidized under the influence of temperature and pressure. NC prevents oxidation up to a certain percentage and accordance with this, mechanical strength increases.

The $lg\tau_M$ (σ) dependence observed with the simultaneous exposure to an electrical discharge is an elementary act of breaking chemical bonds underlying the decay (both thermal fluctuation and electrical discharge) in polymer macromolecules. Due to the accumulation of broken bonds and at the expense of both effects, the rate of decomposition increases and the durability decreases.

Thus, the absence of changes in τ_M (curve 2´) and a slight change (curve 3´) after the simultaneous exposure to an electrical discharge (U=7·10^3 V) of polyethylene nanocomposite with the addition of 3,0% NC, under these conditions, shows that NC plays an antioxidant role, as in the case of wear under the influence of an electric field in advance [14], this property of NC increases the mechanical strength of polyethylene and its resistance to electrical discharge to a certain extent.

Figure 3 represents the dependence of the electrical durability logarithm of the HDPE and HDPE+3,0% NC nanocomposite on the field intensity under the simultaneous exposure to a mechanical load. As it is seen, the linear dependence of $lg\tau_E$ on E does not change under the simultaneous exposure to a constant temperature and a constant mechanical load, i.e. the

dependence $lg\tau_E = f(E)$ is written in a well-known empirical expression:

$$\tau_E = Bexp(-\beta E).$$

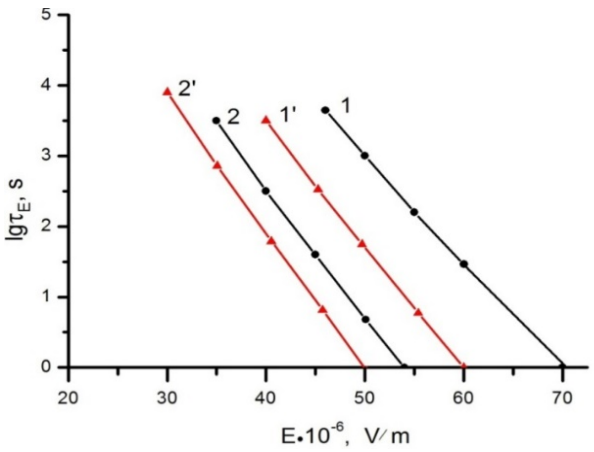

Fig. 3. Dependence of the electrical durability on E of the $HDPE(1, 1')$ and HDPE+3,0% NC (2, 2') nanocomposite under the simultaneous exposure to a mechanical load (σ=5 MPa), 1', 2'~ mechanically loaded samples

However, under equal conditions, the effect of mechanical load causes a decrease in τ_E. The rate of reduction of the electric strength of the nanocomposite obtained by the inclusion of 3,0% NC in polyethylene is lower than that of pure polyethylene. The rate of reduction of the electric strength is 15% in HDPE and 10% in nanocomposite.

The ionization process inside the polymer in an electric field causes an electrical breakdown (perforation). In individual studies [3,13], the mechanical strength of NC incorporated various polymer-based nanocomposites is maximized by a certain amount of additive. The electric strength of nanocomposites gradually decreases depending on the amount of NC. Since the conductivity of NC (χ=10^{-4} $Om^{-1}\cdot m^{-1}$) is greater than the conductivity of HDPE (χ =$10^{-12\div14}$ $Om^{-1}\cdot m^{-1}$), the conductivity of nanocomposite increases [14]. Polymer macromolecules are stretched under the simultaneous exposure to a mechanical load. Mechanical load increases the existing non-uniformity (microcracks, pores, etc.). This, in turn, leads to an uneven distribution of the electric field in the sample and shortens the lifetime. During the simultaneous exposure to a mechanical load, the electric strength of both samples is decreased, and the rate of reduction in HDPE is higher than that in nanocomposite, NC plays a more active role in destructive processes.

Conclusion

The mechanical strength of NC added nanocomposite samples based on HDPE increased in the amount of additive by 3,0% to 42% and is more resistant to the simultaneous effects of electrical discharge. During the simultaneous impact of mechanical load, electric strength in both samples decreased. The decrease was 15% for HDPE and 10% for HDPE+3,0% NC nanocomposites. When samples are obtained, carbonyl groups C=O are formed due to the breaking of chemical bonds. NC included in HDPE acts as an antioxidant, preventing the formation of carbonyl groups up to a certain percentage.

References

1. Volkova T.S., Bader E.Ya. Aviation materials and technologies: Scientific and technical collection 2010, v. 2, p. 56-57.
2. Magerramov A.M. Structural and radiation modification of electret, piezoelectric properties of polymer composites. Elm, Baku, 2001.
3. Ramazanov M.A., Abasov S.A., Rasulova A.A. et al. J. Fizika 2009, v. 15, p. 25.
4. Panova L.G., Fillers for polymer composite materials. Textbook. Saratov State Technical University, Saratov, 2010.
5. Shevchenko V.G. Fundamentals of physics of polymer composite materials. Moscow State University, Moscow, 2010.
6. Özcanlı Y.L., Boydağ F.Ş., Alekberov V.A., Hikmet I., Cantürk M. Mod Phys Lett B 2007, v. 21, p. 1415. https://doi.org/10.1142/S0217984907013663
7. Miktaev A.K., Kaladzhyan A.A., Lednev O.B., Mikitaev M.A. Electronic journal "Investigated in Russia" 2004, v. 83, p. 912.
8. Delozier D.M., Orwoll R.A., Cahoon J.F., Johnston N.J., Smith J.G., Connell J.W. Polym. 2002, v. (43), p. 813. https://doi.org/10.1016/S0032-3861(01)00640-1
9. Chang J.H., Kim S.J., Joo Y.L., Im S. Polym. 2004, v. 45, p. 919. https://doi.org/10.1016/j.polymer.2003.11.037
10. Regel V.R., Slutsker A.I., Tomashevsky E.Ye. Kinetic nature of solids strength. Nauka, Moscow, 1974.
11. Vaia R.A., Ishii H., Giannelis E.P. Adv. Mater. 1996, v. 8, p. 29.
12. Vaia R. A., Jandt K.D., Kramer E.J., Giannelis E.P. Macromolecules 1995, v. 28, p. 8080. https://doi.org/10.1021/ma00128a016.
13. Ramazanov M.A., Sadygova A.R., Abbasov I.I, Asilbeyli P.B. ANAS Transactions 2017, v. 5, p. 41.
14. Ramazanov M.A., Sadygova A.R., Safiyev A.R. Power Engineering Problems 2017, v. 1, p. 69.

ELECTRONIC AND MAGNETIC PROPERTIES OF A15 AND D8$_m$ PHASE Ti_3Sb

SO MAMMADOVA

Institute of Physics of Azerbaijan National Academy of Sciences, AZ1143, Baku, Azerbaijan
E-mail: seide.memmedova@physics.science.az

I present a study of the structural, electronic, and magnetic properties between of the cubic A15-phase and the tetragonal D8$_m$-phase in the Ti_3Sb compound by using density-functional theory (DFT) within the spin generalized gradient approximations (SGGA). The lattice constants (crystal structures) of Ti_3Sb have been calculated and compared to the available experimental values. The Ti_3Sb compound crystallizes in W_5Si_3 and Cr_3Si structure type. The total magnetic moment of the Ti_3Sb was investigated in case of vacancy and in the 2×1×1 supercell by Mn substitution for Sb and Ti atoms, separately. The calculated density of states (DOS) and Mulliken population analysis presents that A15-Ti_3Sb exhibit metallic behavior more than D8$_m$-Ti_3Sb. The metallic behavior mainly depends on the electronic interaction between Ti and Sb atom near Fermi level. Besides, to better get the difference in the electronic structure of two Ti_3Sb phases, the electronic structures of A15- Ti_3Sb and D8$_m$-Ti_3Sb are calculated.

Keywords: A15-phase, D8$_m$-phase, Ti_3Sb, electronic and magnetic properties, first-principles calculations.
PACS: 31.15.E−, 71.15.−m, 71.15.Mb, 75.50.Gg

Introduction

The topologically non-trivial band structure of A15 compounds has attracted owing to the possible realization of topological superconductivity. The standard crystal structure symmetry of A15 type superconductors, with spin-orbit coupling, creates gapped crossing near the Fermi level. The topological surface states near the Fermi surface of A15 superconductors Ta_3Sb, Ta_3Pb, and Ta_3Sn was revealed in the recent theoretical investigation, point out to host a topological superconductor candidate [1, 2]. In [3] work classifies Ti_3Ir, Ti_3Sb as a time-reversal preserved topological superconductor.

In recently titanium antimonides have been exposed to research in some areas such as electrode materials for lithium batteries, hydrogen storage materials, interface materials for skutterudite-based thermoelectric devices. Utilizing some preparation methods such as arc-melting, melting in alumina crucibles and in silica tubes Kjekshus et al. [4] detected four titanium antimonides: cubic Ti_3Sb (β-W-type, Cr_3Si-type) and tetragonal Ti_3Sb- (W_5Si_3-type [5]), two compounds with orthorhombic structures $Ti_{1.7}Sb$ (space groups Pmma, $Pmc2_1$ or Pma2) and $Ti_{1.2}Sb$ (Pbam or Pba2). As cubic Ti_3Sb was displayed to irreversibly transform into the tetragonal modification, the latter was considered to be a aluminium and silicon stabilized phase [6, 7].

Unfortunately, there are few investigations devoted on the electronic and magnetic properties of A15-Ti_3Sb and no publications about this D8$_m$-Ti_3Sb compound. The aim of this paper is to compare the electronic and magnetic properties between the D8$_m$ and A15 phases of Ti_3Sb. DOS were received and the Fermi surfaces structures were calculated by implemented the Atomistix ToolKit with the spin generalized gradient approximation for the exchange-correlation potential within the formalism of the DFT. The conceptual framework of this paper is structured as follows. In Section 2, the method and calculation details are displayed. In Section 3, the electronic and structural properties, density of state, as well as magnetic moment are calculated and discussed. Finally, conclusions are presented in Section 4.

Computational methods

The calculations were performed for the Ti_3Sb compound in two prototype from constructed by Kjekshus [4] using the DFT method implemented using the Atomistix ToolKit. The electronic and magnetic properties of Ti_3Sb with a monovacancy are studied theoretically. The calculation was performed of the relaxed crystal structure and of the magnetic moment for the 2×1×1 Ti_3Sb supercell in case of Mn substitution for Ti and Sb separately.

First-principles calculations of electronic and magnetic properties were carried out on the based on the spin-polarized density functional theory. The spin generalized gradient approximation in the Perdew–Burke–Ernzerhof (PBE) parameterization was employed for the exchange–correlation functional. The kinetic cut-off energy was 150 Ry. The primitive cell of Ti_3Sb was relaxed and optimized with force and stress tolerances of 0.01eV/Å and 0.01eV/Å^3, respectively. A 10 x 10 x 10 k point was used for geometry optimization and total energy calculations.

Discussion

In this study, the electronic band structure, magnetic moment, and density of state for the Ti_3Sb compound constructed by Kjekshus [4] according to two different symmetry groups, were investigated. Here, the physical properties were calculated using the Atomistic Simulation Software QuantumATK in accordance with the Ti_3Sb Pm-3n (no.223) cubic group symmetry based on the Cr_3Si type structure. The lattice parameter a = 5.2186 Å is described in Table 1. $D8_m$ -Ti_3Sb was selected as W_5Si_3 type structure I4/mcm (no.140) tetragonal space group symmetry and lattice parameters a = 10.465 Å, c = 5.2639 Å, c/a= 0.503 Å.

Table 1. Crystallographic structural data for Ti_3Sb.

Compound	Prototype	Space group	Strukturbericht designation	Lattice parameters [Å]			Comments
				a	b	c	
Ti3Sb	W5Si3	I4/mcm no.140	D8m	10.465	-	5.2639	[4]
Ti3Sb	Cr3Si and "β-W"	Pm-3n no.223	A15	5.2186	-	-	[4]

A15 superconducting Ti_3Sb compound based on the Cr_3Si prototype

In the Al5 structure of A_3B compounds, A sites are occupied by transition elements in groups IV, V, VI, and the B sites by both transition and non-transition elements from group III [8]. The A15 compounds have a primitive cell of 8 atoms and belong to the space group Pm-3n. The A_3B cubic unit cell has two B atoms at (0, 0, 0) and (0.5, 0.5, 0.5) sites and six A atoms at (0, 0.5, 0.75), (0.5, 0.75, 0), (0, 0.5, 0.25), (0.5, 0.25, 0), (0.25, 0, 0.5), and (0.75, 0, 0.5).

The Figure 1 shows atomic structure of the A15-Ti_3Sb and its direction of the magnetic moment. The Ti atoms in the Ti_3Sb form a system of three essentially non-interacting orthogonal linear chains parallel to the unit cell edges. The extraordinary superconducting properties of the Ti_3Sb compound are believed to be primarily associated with these linear chains of transition-element Ti atoms.

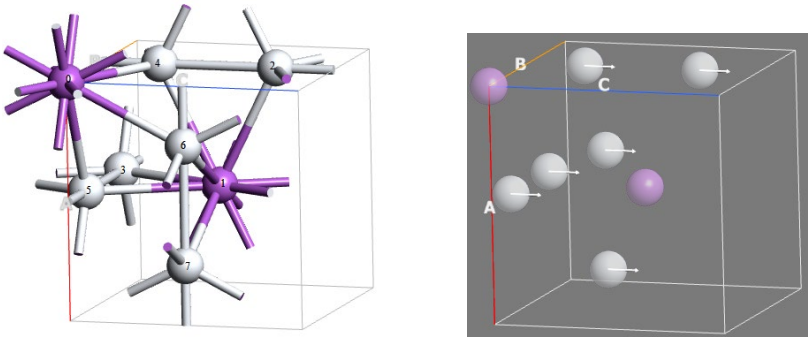

a) **b)**

Fig. 1. Atomic structure of the a) A15-Ti_3Sb, b) direction of the magnetic moment. Sb atoms are purple and Ti atoms are gray.

The Figure 2 illustrates the band structure of Ti_3Sb plotted for high symmetry points Γ-X-M-Γ-R-X at T=300K. The band structure at T=300K exhibit transitions of electrons from valence band to conduction band at M and at R high symmetry points in Ti_3Sb there is no electrons from -10.0eV to -6.0eV, which revealed that this is metallic compound because of the absence of band gap. The band structure has been calculated based on density functional theory within spin-polarized PBE-GGA approximation. The plots of the band structure and total density of states for A15-Ti_3Sb were calculated as shown on figure below:

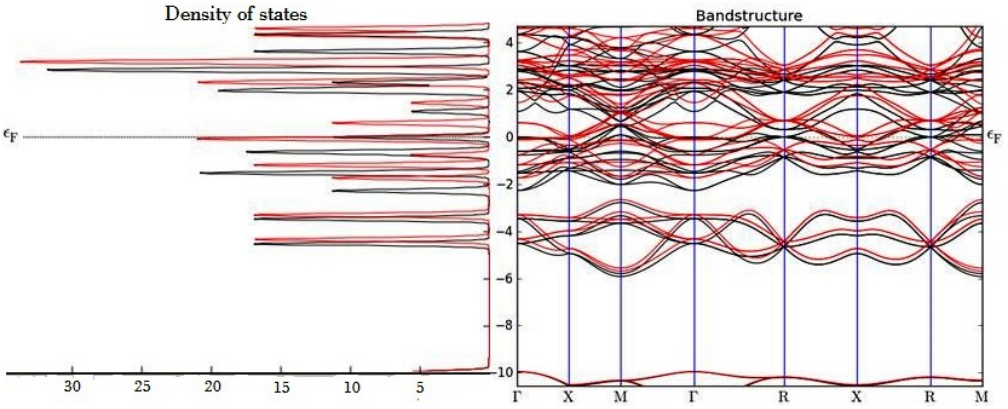

Fig. 2. Electronic band structure and total DOS of the A15-Ti_3Sb.

The Figure 3 displays the DOS which was constructed for s-, p- and d-electrons of A15-Ti_3Sb. The black curve corresponds to electrons with the direction of the spin up and the red the direction of the spin down. Ab initio calculation DOS for Ti_3Sb shows that Fermi level for the s, p, d- electrons with spin-up and spin-down exist significiant imbalance [Fig. 3 a, b, c].

The Table 3 presents the total magnetic moments for the A15-Ti_3Sb compound. The magnetic moment calculations were done by Mulliken population analysis. The total magnetic moment is 3.67μ_B for the Ti_3Sb. The value of the magnetic moment decreases as 0.162μ_B when creating vacancy by transition element Ti occupying A site. However, the vacancy existence of the semi-metal Sb in B, the value of the magnetic moment increases as 5.94 μ_B.

A15-Ti_3Sb supercell structures containing 16 atoms displayed in Figure 4 point the positions of the atomic sites occupied by the doped Mn atom in the place of Ti and Sb atoms,

separately. Substituting the Ti_3Sb with Mn atom in the each supercell structure leads to the new compounds $Ti_{2.75}SbMn_{0.25}$ and $Ti_3Sb_{0.916}Mn_{0.0834}$. The Ti_3Sb supercell was doped with Mn, in the doping concentration of 25% to replace Ti atoms and 8.34 % to replace Sb atoms.

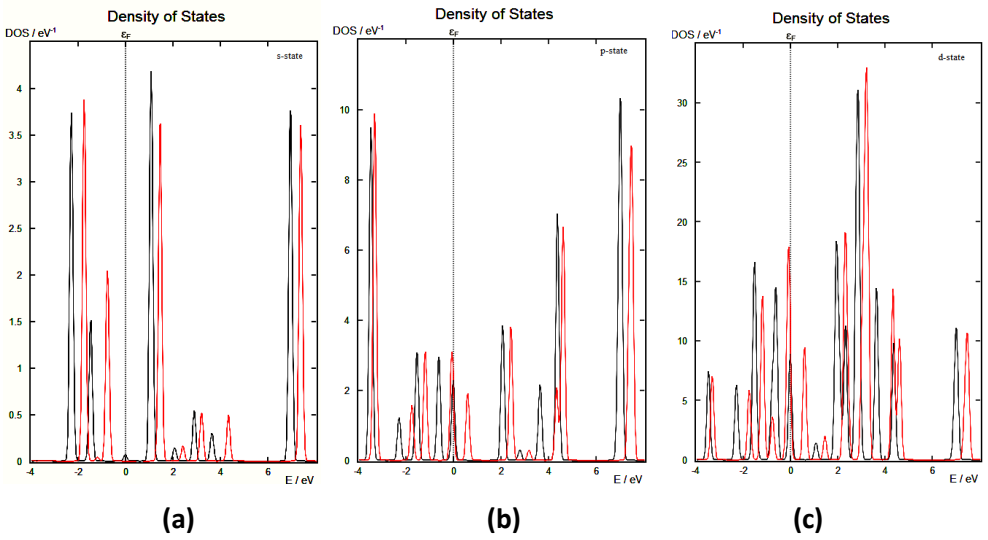

Fig. 3. The DOS for spin up and spin down s-, p-, d- electrons of the A15-Ti_3Sb compound: a) s-state, b) p-state, c) d-state.

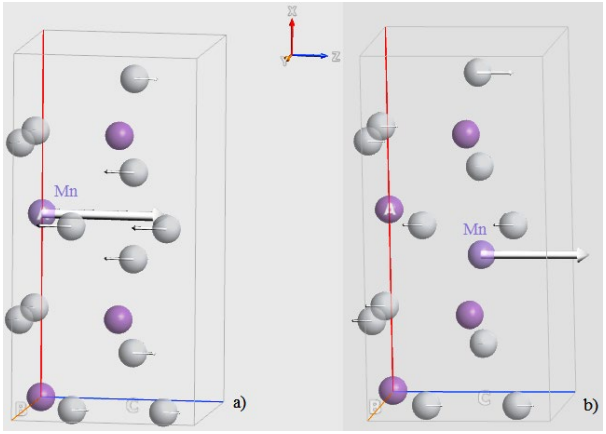

Fig. 4. Direction of the magnetic field for a) $Ti_3Sb_{0.916}$ $Mn_{0.0834}$ and b) $Ti_{2.75}SbMn_{0.25}$.

The total magnetic moment of $Ti_3Sb_{0.916}$ $Mn_{0.0834}$ and $Ti_{2.75}SbMn_{0.25}$ are acquired 0.776μ_B and 3.094μ_B (opposite direction of the magnetic field), respectively. The Figure 4-a (b) presents opposite direction and on the preferred direction of the magnetic field for Ti atoms and Mn atom in the $Ti_3Sb_{0.916}$ $Mn_{0.0834}$ ($Ti_{2.75}SbMn_{0.25}$). In the $Ti_3Sb_{0.916}Mn_{0.0834}$ compound the local magnetic moment are obtained by 3.1941μ_B and 0.6μ_B, -0.889μ_B for Mn atom and 6th(15th), 10th(14th) Ti atom, accordingly. In the $Ti_{2.75}SbMn_{0.25}$ structure are calculated the local magnetic moment of 2.754 μ_B for Mn and 0.927 μ_B for Ti (Figure 4b).

The 3d electronic states of Mn d orbital are clearly visible from the plot of spin polarized partial density of states as displayed in the Figure 5.

$D8_m$ - Ti_3Sb compound based on the W_5Si_3 structure type

The next prototype structures of Ti_3Sb compound has been taken into account: the W_5Si_3

prototype structure -D8$_m$. Wyckoff positions were selected as Ti (4b) 0, 1/2, 1/4, Ti (16k) x, y, 0, Sb (4a) 0, 0, 1/4, Sb (8h) x, x+1/2, 0. The Figure 6 displays atomic structure of the D8$_m$-Ti$_3$Sb.

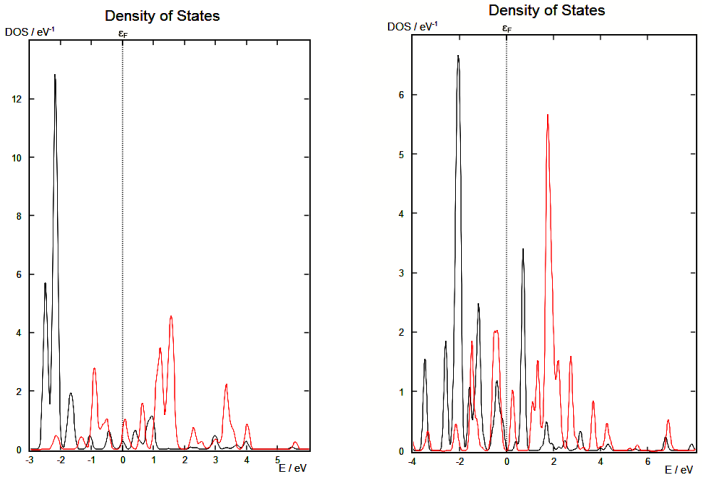

(a) **(b)**

Fig. 5. PDOS d-state for a) $Ti_3Sb_{0.916}Mn_{0.0834}$, b) $Ti_{2.75}SbMn_{0.25}$.

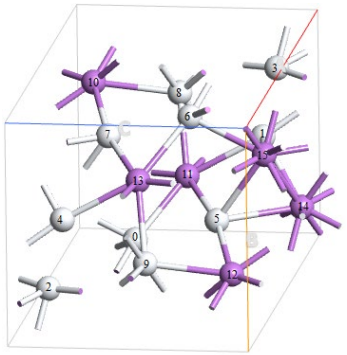

Fig. 6. Atomic structure of the D8$_m$-Ti$_3$Sb.

Band structure along symmetry directions around the Fermi level and total DOS for D8$_m$-Ti$_3$Sb are presented in Figure 7.

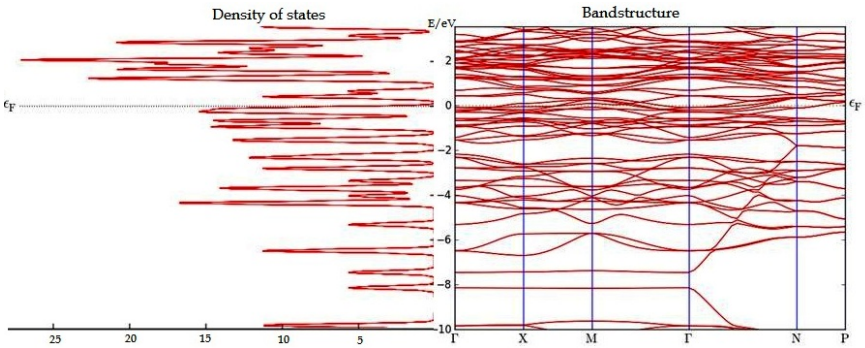

Fig. 7. Electronic band structure and total DOS of the D8$_m$ -Ti$_3$Sb.

To next investigation the effect of structure on the mechanical properties, the electronic structure of the D8$_m$-Ti$_3$Sb is studied. Besides, to better get the difference in the electronic

structure of two Ti_3Sb phases, the electronic structure of $D8_m$-Ti_3Sb is calculated. DOS for spin up and spin down s, p, d- electrons of the D8m-Ti_3Sb presents that exist slight imbalance (Figure 8). It can be seen that the DOS profiles of the $D8_m$-Ti_3Sb across the Fermi level, indicating that they exhibit metallic behavior lower than A15-Ti_3Sb. Furthermore, the density of states of the Ti_3Sb phases at the Fermi level is mainly contributed by Ti-d state and Sb-p state, indicating that the metal behavior of these structures is attributed to the localized hybridization between Ti atom and Sb atom. This is related to the surrounding of the Ti (4b) atoms by four Sb atoms at a distance of 2.8Å.

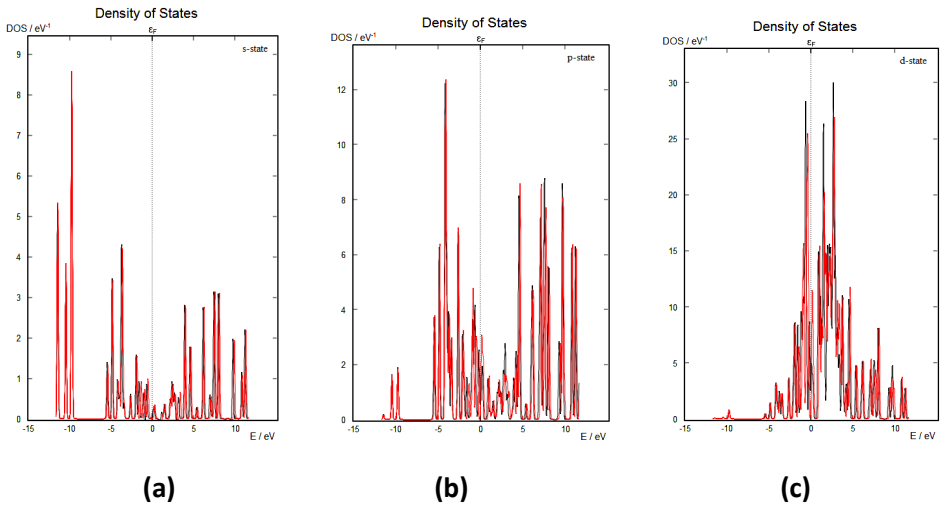

Fig. 8. The DOS for spin up and spin down s-, p-, d- electrons of the $D8_m$-Ti_3Sb compound: a) s-state, b) p-state, c) d-state

The results of magnetic moments for the $D8_m$-Ti_3Sb compounds are shown in the Table 3. The magnetic moment is 0.01 μ_B for $D8_m$-Ti_3Sb. The total magnetic moment is obtained 1.247μ_B (2.543μ_B) due to Ti (Sb) vacancy in $D8_m$-Ti_3Sb. In the $D8_m$-Ti_3Sb compound with Ti (Sb) vacancy the local magnetic moment are obtained by 0.344μ_B (0.638μ_B) and 0.456μ_B (0.451 μ_B) for 7th(8,9th), 8th(1,2th) Ti (Sb) atom, accordingly.

Mn atom is doped into the 2×1×1 $D8_m$-Ti_3Sb supercell such that structure is formed as $Ti_{2.196}SbMn_{0.834}$ and $Ti_3Sb_{0.95}Mn_{0.05}$. The $D8_m$-Ti_3Sb supercell was doped with Mn, in the doping concentration of 8.34 % to replace Ti atoms and 5% to replace Sb atoms.

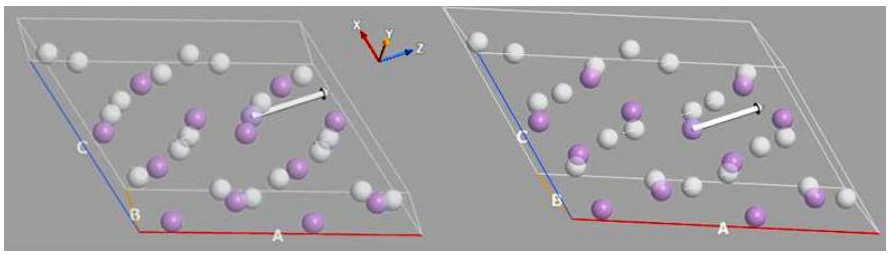

Fig. 9. Direction of the magnetic field for a) $Ti_{2.196}SbMn_{0.834}$ and b) $Ti_3Sb_{0.95}Mn_{0.05}$

The total magnetic moment of $Ti_{2.196}SbMn_{0.834}$ and $Ti_3Sb_{0.95}Mn_{0.05}$ are acquired 0.853μ_B

and -0.319μ_B (opposite direction of the magnetic field), respectively. The Figure 9-a (b) presents opposite direction and on the preferred direction of the magnetic field for Ti atoms and Mn atom in the $Ti_{2.196}SbMn_{0.834}$ ($Ti_3Sb_{0.95}Mn_{0.05}$). In the $Ti_{2.196}SbMn_{0.834}$ compound the local magnetic moment are obtained by 2.919μ_B and 0.324μ_B, -0.518 for Mn atom and 25th, 8th(24th) Ti atom, accordingly (Figure 9a). In the $Ti_3Sb_{0.95}Mn_{0.05}$ structure are calculated the local magnetic moment of 2.854 μ_B for Mn and -0.502 μ_B for Ti (Figure 9b).

The plot of spin polarized partial density of states are displayed in the Figure 10 for Mn atom doped into $D8_m$-Ti_3Sb.

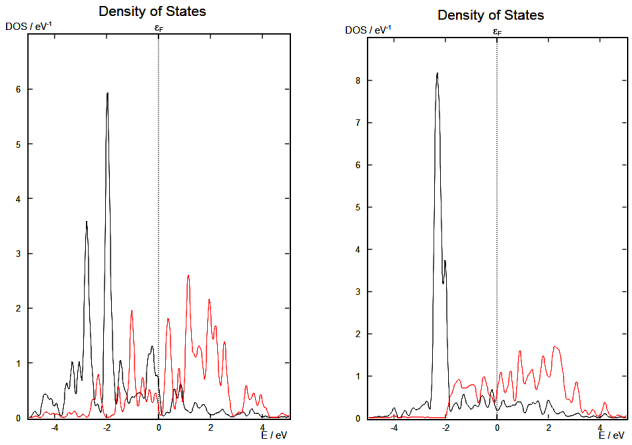

(a) **(b)**

Fig. 10. PDOS d-state for a) $Ti_{2.196}SbMn_{0.834}$ and b) $Ti_3Sb_{0.95}Mn_{0.05}$

In A15-Ti_3Sb structure the atomic radius between Ti and Sb is 2.92Å, and between Ti and Ti is 2.609Å. In another structure, in $D8_m$-Ti_3Sb, the atomic radius between Ti and Sb is 2.8Å, and between Sb and Sb is 2.63Å (Table 2).

Table 2. Atomic radii.

Method	Atomic radii, Å		
	Ti-Sb	Ti-Ti	Sb-Sb
A15-Ti_3Sb	Ti_2-Sb_1 (2.92)	Ti_2-Ti_4 (2.609)	---
$D8_m$-Ti_3Sb	Ti_0-Sb_{11} (2.8)	---	Sb_{14}-Sb_{15} (2.63)

Note that, the magnetic moment varies depending on the change in distance between transition metal Ti and semi-metal Sb, as well as Ti and Ti, Sb and Sb. Upon doping and creating vacancy these structural parameters in Ti_3Sb change. Accordingly, the formed local magnetic moments near Ti_3Sb vacancies also alter.

Table 3. The value of magnetic moment and total energy for A15 and $D8_m$ structures of Ti_3Sb.

Compound	A15 structure		$D8_m$ structure	
	Magnetic moment	Total energy	Magnetic moment	Total energy
Ti_3Sb	3.67 μ_B	-1387.84912eV	0.01 μ_B	-2716.16602eV
Ti_3Sb with Ti vacancy	0.162 μ_B	-1205.57862eV	1.247 μ_B	-2534.61354eV
Ti_3Sb with Sb vacancy	5.94 μ_B	-1232.63167eV	2.543 μ_B	- 2562.05016eV

$Ti_{2.75}SbMn_{0.25}$	3.094 μ_B	-3212.91140eV		
$Ti_3Sb_{0.916}$ $Mn_{0.0834}$	0.776μ_B	-3242.23966eV		
$Ti_{2.196}SbMn_{0.834}$			0.853 μ_B	-5869.39277eV
$Ti_3Sb_{0.95}$ $Mn_{0.05}$			-0.319 μ_B	-5898.76162eV

Conclusion

In the present paper, the band structure and magnetic moment of the Ti_3Sb according to two different tetragonal and cubic symmetry groups based on the W_5Si_3 and Cr_3Si prototypes were calculated by using the first-principles density functional theory. The cubic crystal structure A15-Ti_3Sb compound and its magnetic properties in comparison with magnetic properties of the tetragonal crystal structure $D8_m$-Ti_3Sb compound were studied (Table 3). The total magnetic moment for A15-Ti_3Sb is acquired 3.67 μB, for $D8_m$-Ti_3Sb is 0.01 μ_B. In the presence of Ti and Sb vacancies for A15 and $D8_m$ phases in the Ti_3Sb compound the magnetic moments are acquired different values as presented in Table 3. There are found slight increasing value of the magnetic moments in Mn doped $D8_m$ structure of Ti_3Sb supercell compare than in Mn doped A15 structure. The magnetic moment obtain various values depending on the distinct atomic radii in two Ti_3Sb compounds. Note that, the calculated atomic radii of the Ti-Sb (2.92 Å) bond in A15 Ti_3Sb is longer than the Ti-Sb (2.8Å) bond in $D8_m$ Ti_3Sb.

In summary, the magnetic moment of A15- and $D8_m$-Ti_3Sb was discussed. This compound can crystallize in two distinct crystal structures was shown. The calculated density of states and electron band structure present that A15-Ti_3Sb exhibit metallic behavior more than $D8_m$-Ti_3Sb.

References

1. Kim M., Wang C., Ho K. Phys. Rev. B 2019, v. 99, p.224506. DOI:https://doi.org/10.1103/PhysRevB.99.224506
2. Derunova E., Sun Y., Felser C.,. Parkin S.S.P, Yan B., Ali M.N. Sci. Adv. 2019, v. 5, p. 4. DOI: 10.1126/sciadv.aav8575
3. Manasi M., Sajilesh K. Physical Review B 2021, v. 103, p.054501. DOI:https://doi.org/10.1103/PhysRevB.103.054501
4. Kjekshus A., Grønvold F., Thorbjørnsen J. Acta Chem. Scand. 1962, v. 16, p. 1493. DOI: 10.389/acta.chem.scand.16-1493
5. Murray J.L. Phase Diagrams of Binary Titanium Alloys, Publisher: ASM International, Metals Park, Ohio, USA, 1987.
6. Kleinke H. Can. J. Chem. 2001, v. 79, p.1338. https://doi.org/10.1139/v01-121
7. Kozlov A.Y., Pavlyuk V.V. Intermetallics 2003, v. 11, p.237. https://doi.org/10.1016/S0966-9795(02)00232-7
8. Vonsovsky S.V., Izyumov Y.A.,.Kumaev. E.Z Superconductivity of transition metals, 1st ed., Springer Berlin Heidelberg, Germany, 1982.

ELECTRODEPOSITION OF In_2S_3 LAYER FOR SOLAR CELLS

S JAHANGIROVA

Baku State University, Z.Khalilov str., 23, AZ-1148, Baku, Azerbaijan
E-mail: sona_aliqizi@mail.ru

The electrochemical deposition of In_2S_3 thin films was carried out from an aqueous solution of $InCl_3$ and $Na_2S_2O_3$. The effect of the potential of deposition was studied on the cell parameters of CZS based solar cells. The obtained films depending on the deposition potential and thickness exhibited complete substrate coverage. Maximum photoelectric conversion efficiency of 12.0% was obtained, limited mainly by a low fill factor (65%). Further process optimization is expected to lead to efficiencies comparable to CdZnS buffer layers.

Keywords: Indium sulphide, CZS solar cells, electrodeposition
PACS: 81.15.Pq, 84.60.Jt, 82.45.Qr

Introduction

Solar cells based on CdZnS (CZS) chalcopyrite absorbers have reached 20.0% conversion efficiencies at the laboratory scale, using high vacuum processes [1]. However, due to the toxicity of cadmium and the possible gain in current associated with the use of a wider bandgap material, many works are carried out with the aim of developing alternative buffer layers [2]. The In_2S_3-based material is among the most relevant alternatives [3]. Several techniques, such as sputtering, atomic layer deposition (ALD), evaporation and chemical bath deposition (CBD) [2] have been used to synthesize In_2S_3 thin films on CZS. However, it seems that soft chemical based deposition techniques such as CBD which do not damage the surface of the absorbers and can provide highly conformal coating are more suitable to get high efficiency Cd-free CZS solar cells [3]. Electrodeposition is a soft technique widely used in industrial processes for large area coating, both in batch and inline systems [4]. This method, more recently applied to semiconductor synthesis, may allow to control the width of the bandgap and the doping level by monitoring solution composition, applied potential, pH and temperature [5,6]. Moreover it provides conformal growth with controlled thickness layers. All these advantages yield the method attractive for the synthesis of the absorber, the buffer layers as well as the transparent conductive oxide layer in CIGSe-based solar cells.Even if important works have been done on the electrodeposition of the CZS-based absorbers, very few attempts have been carried out so far to electrodeposit In_2S_3 buffer layers [7].

Experimental

The electrodeposition of In-S based layers was carried out using an aqueous solution containing indium chloride (5 mM), sodium thiosulfate (20 mM) as sulfur source and potassium chloride as supporting electrolyte (0.1M). A standard three-electrode setup was used. The reference electrode was a saturated mercurous sulfate electrode (MSE, E°= 0.64V/NHE) and platinum was used as the counter electrode. The deposition was carried out at 60°C.

A preliminary investigation was carried out on molybdenum-coated glass substrates to determine the optimal deposition conditions. In-S layers were then deposited on CdZnS absorbers, Al and glass substrate provided by Würth Solar.

The surface morphology of the samples was investigated by scanning electron microscopy (SEM) using a Leo Supra 35 field emission gun (FEG). The electrical properties of cells were characterized by current voltage measurements at 25°C under illumination (AM1.5 global spectrum). Absolute spectral response measurements were made with a monochromator under chopped illumination and a lock-in technique. Thermal annealing at 300°C for 10 min in air and light soaking for 60 minutes under AM 1.5 solar-type spectrum were typical post treatments.

Results and discussion

In order to define the optimal deposition potential range of the In-S thin films and the role of S, a voltammetric investigation was carried out both on Al and ITO glass substrates. Figure 1 shows cyclic voltammograms recorded at 60°C on Al and CZS substrates. As is observed on this figure, on both substrates, the deposition starts at potentials lower than –0.8V/MSE. the deposition process is more significantly inhibited on CZS absorber. On CZS a plateau is observed corresponding to a low current density between –0.8 and –1.2V, which might indicate that a different nucleation and/or deposition process occurs on this substrate compared to Al.

When sodium thiosulfate is added to the In(III) solution, a whitish colloid solution is formed. This is due to the formation of elemental sulfur which is favoured at low pH values where the $Na_2S_2O_3$ is decomposed. For solutions with the mixture of sodium thiosulfate and In(III), no oxidation peak of the In-S layer on the reverse scan is observed, whatever the substrate used, indicating the formation of a passive layer during the oxidation process. Based on these observations, when $InCl_3$ and $Na_2S_2O_3$ are mixed in acidic solutions and for potential lower than – 0.9 V/MSE, In-S compound can be formed, thanks to In_2S_3 energy formation ($\Delta G°$= -420 kJ mol^{-1}).

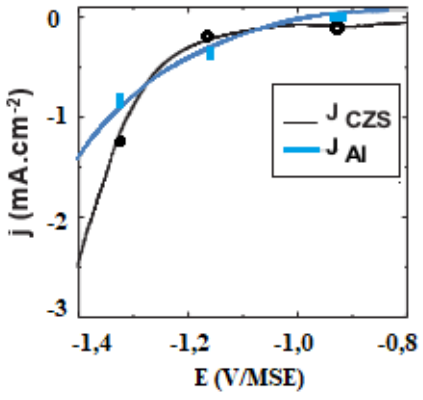

Fig. 1. Voltammetric curves recorded at 5 mVs-1, 60°C. for 0.1 M KCl, 5mM InCl3 and 20 mM Na2S2O3 solution on Al and CZS substrates.

In-S layers were deposited at various potentials on Al and CZS substrates for different electrical charges between –1.0 and –1.3 V/MSE under potentiostatic conditions. The evolution of the film morphology is presented in Figure 2. SEM observations point out that the substrate nature has a marked influence on the morphology of the buffer layer.

For films deposited on a Al substrate (Fig. 2 upper part) we can observe that, whatever the potential of deposition, films remain dense and homogenous and for the same deposition time, the electrical charge and the thickness of the buffer layer increase by decreasing the potential of deposition from –1.0V, to –1.3 V/MSE.

In parallel, In_2S_3 deposited films on CZS absorbers are dense, homogenous, and provide a conformal covering of the absorbers for films deposited at low potential <-1.1 V/MSE. However, as soon as the potential and the thickness of the layer increases, a transition in the morphology is observed and more or less disordered nanorods are growing (Fig. 2).

The global film stoichiometry can be estimated by correcting the total O % measured from a C/4 quantity corresponding to a classical ratio of O involved in the carbonaceous contaminant layer. The In/(S+O-C/4) ratios obtained are close to 0.7 for deposition at -1.3 V and -1.2 V and close to 1.0 when proceeding at -1.0 V. These values approach the one expected for an $In_2S_xO_y$ compound (with x+y = 3), which is 0.66. This means that in our case, we probably do not deposit a pure In_2S_3 layer but a mixture of oxide, hydroxide and/or oxi-sulfide compound (In(S, O, OH)). Such a mixed structure was already observed for In_2S_3 buffer layers deposited by electrodpeosition. More studies are in progress to have a better understanding of the evolution of composition of our films.

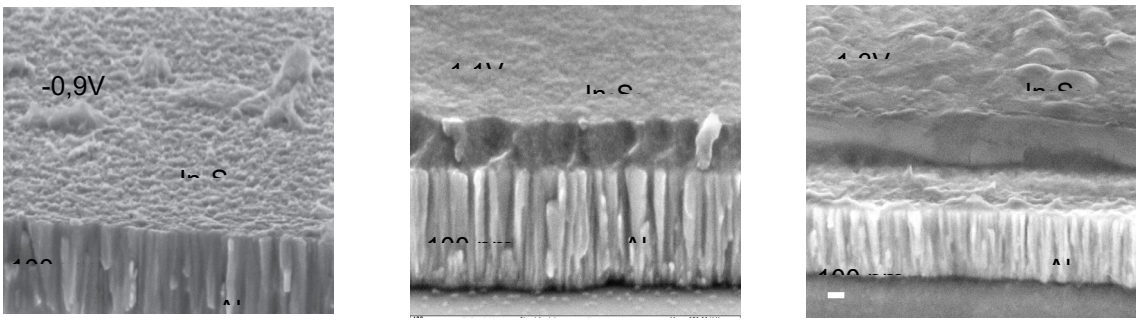

Fig. 2. Effect of the potential of deposition on film morphology deposited on Al substrate The thickness of In_2S_3 on Al as function of potential are : -0,9V : 16.5 nm, -1.1 V :124 nm and –1.3 V : 178 nm.

Cells with electrodeposited In_2S_3 layer at different deposition potentials were prepared using co-evaporated CZS absorbers. Finally, a post annealing of the completed cells in air at 200°C for 10 min and a light-soaking at room temperature for 1 h were made. Figure 3 shows the dependence of the efficiency of the CZS cells with In-S buffer layers prepared at different potential (-0.9V, -1.1V, -1.3V) and different electrical charges used for the buffer layer deposition.

As shown, for very low electrical charge values (<20 mQ/cm^2) corresponding to low thickness of In_2S_3 buffer layers, similar conversion efficiencies are obtained for layers deposited between –1.0 and –1.3 V. However, the conversion efficiency for cells deposited at –1.2V decreases markedly when the electrical charge used for the buffer layer deposition increases. On the contrary, for buffer layers deposited at–0.9 V the efficiency of solar cells increases with the increase of electrical charge. Best results are obtained for a potential of –0.9 V and an electrical charge between 10 and 20 mQ/cm^2 with a maximum efficiency of 12.0%.

Figure 4 shows the current voltage curve of one of the best cell prepared at –0.9 V compared to that with CdS (Figure 5b). An improvement of Jsc for cells with In_2S_3 buffer is observed compared to cells with CdS. For comparison the spectral responses of the cell obtained with In_2S_3 and that of a cell are shown in Figure 5b. The spectral response displays external quantum efficiencies of about 80% between 450 and 900 nm. Towards short wavelengths, for CdS buffer layers, the quantum efficiency drops from about 500 nm, while for In_2S_3 buffer layers the drop of the quantum efficiency occurs only at about 380 nm. Such a result confirms the higher value of the apparent bandgap of the In_2S_3 buffer layers. However for instance the V_{oc} and FF of the solar cells remains lower than the one with CdS buffer layers indicating the non optimized interface between CIGSe and the ED-In_2S_3.

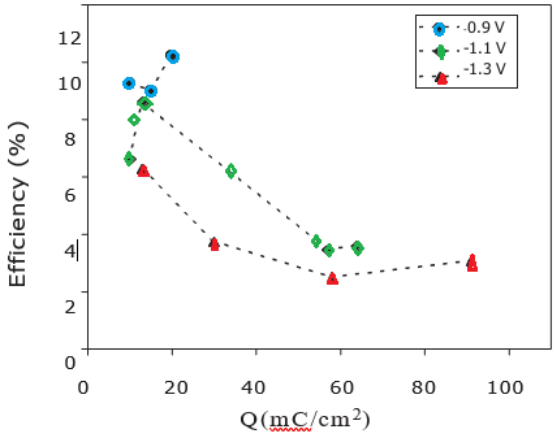

Fig. 3. Efficiency of CZS/In_2S_3 -based solar cell as a function of deposition potential and electrical quantity of deposition measured under simulated AM1.5–100 mW/cm^2 illumination.

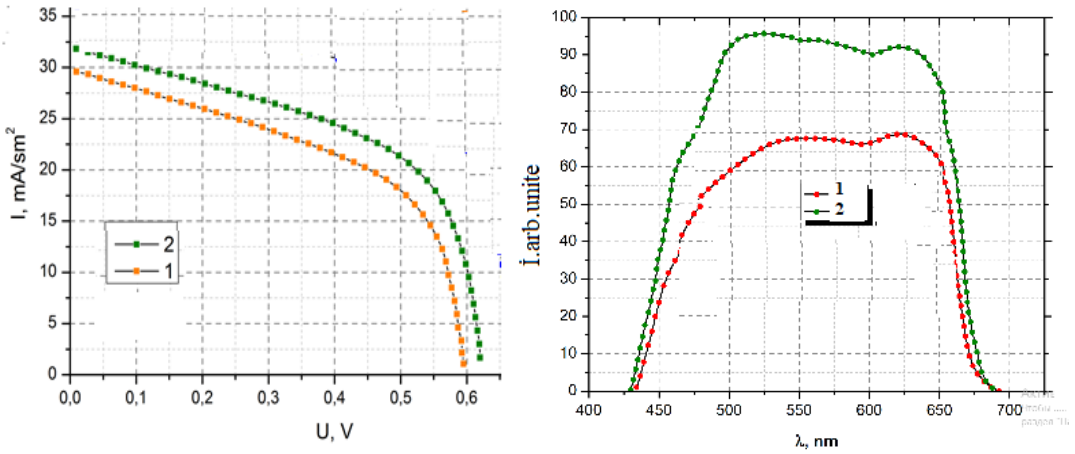

Fig. 4. (a) Current–voltage curves for best CZS cells under simulated AM1.5–100 mWcm^{-2} – Illumination with a before (1) and after (2) HT (b) Spectral responses measured under short-circuit conditions before (1) and after (2)

Conclusion

Through a systematic study of the deposition parameters of In_2S_3 layers on Al and CZS solar cells as a function of potential of deposition we have achieved a high efficiency of about 12.0%. We observed that, to obtain good efficiencies, the two key parameters are potential

of deposition and the thickness of the films. The morphology of films are highly substrate dependent and for higher deposition potential (higher than - 1.1V) and low thicknesses films exhibited good substrate coverage. Solar cells with ED-In_2S_3 layers present very good photo current densities, but cell performance was limited by the low Voc and fill factor. The low values of the open-circuit voltage and the fill factor of the best cells show that the interface quality between CZS and In_2S_3 can be more improved.

References

1. Datta. M., Landolt. D. Electrochimica Acta. 2000, v. 45 (15-16), p. 2535. DOI:10.1016/S0013-4686(00)00350-9
2. Pandey. R.K; Sahu. S.N; Chandra S. Handbook of Semiconductor Electrodeposition, New York, Basel, Hong Kong: Marcel Dekker Inc. 1996.
3. Lincot D. Thin Solid Films. 2005, v. 487 (1-2), p. 40. DOI:10.1016/j.tsf.2005.01.032
4. Hibberd CJ, Chassaing E, Liu W, Mitzi DB, Lincot D, Tiwari AN. Progress in Photovoltaics: Research and Applications. 2010, v.18 (6), p. 434.
5. Asenjo. B., Chaparro. A.M., Gutierrez. M.Ts., Heffero. J., Maffiotte. C. Thin Solid Film 2005, v. 480, p. 151. DOI: 10.1016/j.tsf.2004.11.023
6. Abdel Haleem A., Ichimura. M. Thin Solid Films. 2008, v. 516, p. 7783. DOI:10.1016/j.tsf.2008.03.009
7. Todorov. T., Carda. J., Escribano. P., Grimm. A., Klaer. J., Klenk. R. Solar Energy Mat. and Solar Cells. 2008, v. 92, p. 1274.

MONOVACANCY GRAPHENE SUPERCELLS DOPED WITH SILICON, GERMANIUM, AND LITHIUM ATOMS

SS HUSEYNOVA and SO MAMMADOVA

Institute of Physics, Azerbaijan National Academy of Sciences, AZ-1143 Baku, Azerbaijan
E-mail: s.huseynova@physics.science.az

Ab initio calculations of the vacancy formation energy and magnetic moments formed in defective graphene supercells have been carried out. In order to investigate the Si, Ge, Li -doped graphene supercells with single vacancies, we have used spin-polarized density functional theory (DFT). It was found that Si, Ge, Li -doped graphene supercells consisting of 32 (4×4), and 50 (5×5) carbon atoms with vacancies exhibit ferromagnetic spin ordering. Furthermore, the total magnetic moment in 4×4 graphene supercell with monovacancy doped by single, di, three- Si atoms are calculated. The partial density of states of Li, Ge-doped graphene supercells consisting of 32 atoms and local magnetic moments formed in the vicinity of vacancy carbon atoms are calculated. The existence of defects in graphene has an essential effect on its physical properties. The calculated energy characteristics and magnetic moments of Si, Ge, Li containing defect graphene supercells agree with the literature data.

Keywords: graphene supercell, Si, Ge, Li doped on monovacancy graphene, Atomistix ToolKit
PACS: 31.15.E-,71.15.Mb, 71.15.Nc, 75.50.Gg

Introduction

Electronic, thermal and mechanical properties of graphene make it attractive for numerous applications [1]. Graphene is like a two-dimensional (2D) crystalline material and has an electronic structure with an almost zero band gap. The physical properties of graphene can be controlled by doping or adsorption, which are the processes of adding impurities to the intrinsic atoms of the graphene lattice. For instance, silicon atoms doped graphene, called siligraphene, exhibits high optical properties and high thermal stability [2,3].

It turned out that the introduction of various defects into the graphene structure increases the stability of the graphene sheet, which is confirmed by calculations of the properties and energy of formation. It is shown that the replacement of single, di, and three carbon atoms on the surface of a 2D graphene sheet with gold strongly affects the electronic properties of graphene. The tendency of a decrease in the energy of formation of a graphene lattice with an increase in the number of defects leads to an increase in the stability of graphene. [4].

There are published data on the study of the adsorption of various adatoms on pure graphene [5,6]. In [7], the electronic properties were determined and vacancies in graphite were studied from first principles calculations. The structure of the ground state of graphite is associated with formation energy of 7.4 eV and arises as a result of a combination of symmetric relaxation and distortion of degenerate structures associated with symmetry. The formation, behavior, and healing of defects are usually determined by the energy characteristics of atomic-scale structural changes. Review article [8] is devoted to atomic-scale reactions during thermally activated and radiation-induced processes in graphene. The energies of formation of vacancies, adatoms, and topological defects in graphene are discussed. For the energy of formation, in particular, of vacancies, values are given from 7.35 to 8.58 eV.

In [9] work the adsorption of Li atoms on different types of substitution graphene mono-

layers with B-, N-, S- and Si- atoms, has been theoretically studied by first-principles calculations, based on the density functional theory. In [10] paper is published information on the investigation of the doping of Ge, Si atoms in graphene.

The silicon-based microelectronics are developed different methods for determining the characteristics and behavior control of doping and defects. These methods, taking into account modern computational methods, for example, density functional theory (DFT) calculations also make it possible to modify the properties of graphene [11,12]. Effective methods of material surface treatment in microelectronics include implantation, millisecond annealing, photostimulation, and surface engineering. However, such methods for processing and controlling defects for micro- and nanoelectronics applications that are not based on other materials, in particular on graphene, have not been developed.

In particular, surface treatment technology can be extended to graphene, opening up new possibilities for doping and defect control. To investigate these effects, we had chosen as doping element Si, Ge, Li controlling the surface of graphene. Computational studies of the behavior of vacancies in graphene make it possible to determine their effect on surface electronic states. In this study, we present ab initio DFT calculations of the electronic distortions of 2D graphene when creating a carbon vacancy. The results of calculations of the properties of graphene also doped by Ge, Li, Si atoms are considered; the results of calculations of the energy of formation are also presented. The graphene properties were calculated using the DFT method based on the first principle calculations implemented using the Atomistix ToolKit.

Computational methods

The electronic and magnetic properties of Si, Ge, Li doped graphene supercells with a monovacancy are studied theoretically. These investigations are performed by DFT using local spin density approximation (LSDA) method by employing the ATK program package. In addition, the band structure and density of states are investigated for the graphene supercell model. The energies of formation of various graphene supercells containing 32 and 50 carbon atoms have been calculated.

First-principles calculations of graphene properties were carried out on the based on the spin-polarized density functional theory. The local spin density approximation in the Perdew–Zunger (PZ) parameterization was employed for the exchange–correlation functional. The kinetic cut-off energy was 150 Ry. The primitive cell of Graphene was relaxed and optimized with force and stress tolerances of 0.01eV/Å and 0.01eV/Å^3, respectively. A 2 x 2 x 2 k point was used for geometry optimization and total energy calculations.

Discussion

The total magnetic moments were investigated for Si, Ge and Li doped different graphene supercells with a carbon vacancy (table 1). The values of the magnetic moment was derived from Mulliken population analysis [12] for graphene consisting of 32, 50 carbon atoms.

The different values of magnetic moment doped graphene depend on the graphene struc-

ture with vacancy. Graphene has a two-dimensional hexagonal crystal lattice with two identical atoms (denoted by the letters A and B) in the unit cell. Then the atomic structure of graphene can be represented as composed of two equivalents triangular sublattices of atoms A and B. The distance between the nearest graphene atoms is 0.14 nm, the lattice constant is d ≈ 0.25 nm (Figure 1).

Upon doping, these structural parameters in graphene with a vacancy change. Accordingly, the formed local magnetic moments near graphene vacancies also change.

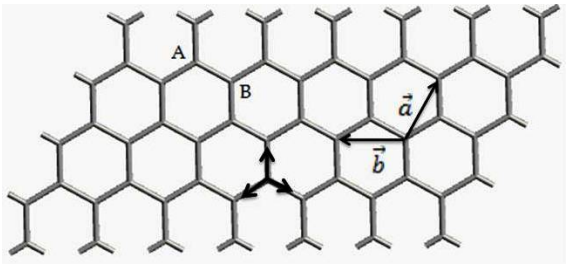

Fig. 1. The lattice of graphene.

Table 1. The value of magnetic moment for in Si, Ge, Li atom doped graphene supercells with vacancy

Graphene with monovacancy	total magnetic moments	magnetic moments around monovacancy
Si doped 4×4 graphene	0.932 μB	0.343 μB (C11) və 0.343 μB (C20)
Si doped 5×5 graphene	1.011μB	0.489 μB (C22)və 0.489 μB (C33)
Ge doped 4×4 graphene	1.002 μB	0.838 μB (C5, C13)
Ge doped 5×5 graphene	1.011 μB	0.84 μB (C17)
Li doped 4×4 graphene	1 μB	0.817 μB (C14)

Comparison of the results of our calculations of M (μB) silicon containing graphene supercells (Table 1) with a monovacancy, and published data [12] showed that the values of the total magnetic moments are in good agreement with each other. It was found that Li, Ge, Si-doped graphene supercells with vacancies exhibit ferromagnetic spin ordering. In figure 2 shows schematic of the atomic structure for Li, Ge doping graphene structure with a single carbon vacancy. Furthermore, Figure 2 illustrates the PDOS for spin up and spin down s-,p-,d-electrons of the dopant Li, Ge in the 32 atoms supercell with vacancy. The results of calculations of the PDOS of Li, Ge doped graphene with a vacancy and local magnetic moments formed in the vicinity of vacancy carbon atoms agree with the literature data, in particular, with data [11, 13].

The formation energy for graphene structure containing vacancy is defined as [12]:

$$E_f = E_{graphene+vacancy} - \left(1 - \frac{n}{N}\right) E_{graphene}$$

whereas for doping structure with vacancy, the formation energy was calculated as:

$$E_f = E_{graphene+vacancy} - \left(1 - \frac{n}{N}\right) E_{graphene} - \mu(M) \cdot$$

where $E_{graphene+vacancy}$ is the total energy of a graphene with vacancy, $E_{graphene}$ is the total energy of pure graphene, $\mu(M) = \mu(Li;Ge;Si)$ is the chemical potential, N is total number of atoms in

graphene supercell and *n* is number of vacant carbon atoms.

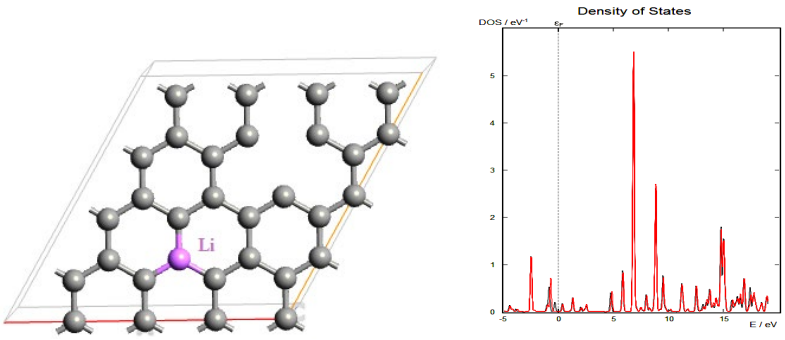

a)

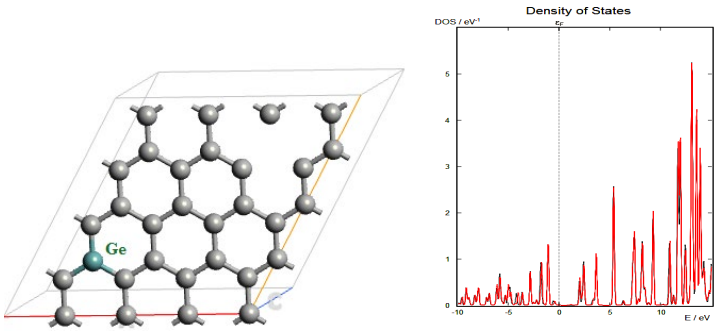

b)

Fig. 2. Atomic structure and Partial DOS of a) Li, b) Ge doped 32–atoms graphene cell with vacancy

Table 2. Formation energies for different graphene supercells

Graphene supercells	Formation energy	
	Our work	Literary data
4×4 graphene with monovacancy	8.52eV	7.30eV [12] 7.83eV [14]
Li doped 4×4 graphene monovacancy	7.19eV	7.2-8eV [13]
Ge doped 4×4 graphene monovacancy	5.04eV	
Si doped 4×4 graphene monovacancy	4.26eV	

We performed our calculations of the vacancy formation energy for 32 atom graphene supercells, as well as taking into account the effects of doping and vacancies. The vacancy formation energy for graphene supercells is given in table 2. Inspection of the results introduced in Table 2 reveals that for Si, Li, Ge doped on graphene with vacancy acquires less formation energy than the monovacancy in graphene. In other words, in silicon-doped defect graphene, the vacancy formation energy is almost two times less than in undoped graphene with a vacancy.

According to the obtained results Si, Ge and Li doped graphene supercell consisting of 32, 50 carbon atoms with vacancies differ from each other.

– The total magnetic moment are acquired about similar values as 0.932μB, 1 μB, 1.003

μB in 4×4 monovacancy graphene supercell doped by single, di, three- Si atom, respectively. The total magnetic moment Si doped 5×5 graphene with vacancy is 1.011 μ_B.

- The total magnetic moment Ge doped graphene with vacancy: 4×4 graphene 1.002μ_B, 5×5 graphene 1.011μ_B
- The total magnetic moment Li doped 4×4 graphene with vacancy: 1 μ_B.

Conclusions

The use of spin-polarized DFT calculations of the properties of 32, 50 atomic graphene supercells with vacancy shows that the properties change due to edge states in the graphene structure. In particular, the formation energy and magnetic moments for different graphene supercells differ from each other. Vacancy formation energy calculation displays that decreases from 8.52eV to 4.26eV in both of monovacancy and Si doped 32 atom monovacancy graphene. First principle calculation of total spin polarization show that Si, Ge, Li doped graphene consisting of 32 carbon atoms with vacancy magnetic moment raises with increasing number of carbon atoms. The magnetic moments in graphene supercells created near a vacancy due to Si doping (0.343-0.515μ_B) and Ge doping (0.838 μ_B) differ from each other.

References

1. Novoselov S., Geim A.K., Morozov S.V., and et al. Science 2004, v. 306, p. 666. DOI: 10.1126/science.1102896.
2. Li P, Zhou R, Zeng XC. Nanoscale 2014,v. 6, p. 11685. DOI.org/10.1039/C4NR03247K.
3. Dong H, Zhou L, Frauenheim T, Hou T, Lee S-T, Li Y. Nanoscale 2016, v. 8 (13), p. 6994. DOI.org/10.1039/C6NR00046K.
4. Fayyaz H., Muhammad I. et al. Surface Review and Letters 2019, v. 26, p. 1850142. DOI: 10.1142/S0218625X18501421.
5. Nakada K., Ishii A. Solid State Commun. 2011, v. 151, p.13. DOI10.1016/j.ssc.2010.10.036.
6. Widjaja H., Altarawneh M., Jiang Z.-T. Can. J. Phys., 2016, v. 94, p. 437. http://dx.doi.org/10.1139/cjp-2015-0671.
7. El-Barbary A.A., Telling R.H., Ewels C.P., Heggie M.I., Briddon P.R. Phys. Rev. B 2003, v. 68, p.144107. DOI.org/10.1103/PhysRevB.68.144107.
8. Skowron S.T., Lebedeva I.V., Popov A.M., Bichoutskaia E. Chem. Soc. Rev. 2015, v. 44, p. 3143. DOI: 10.1039/c4cs00499j.
9. Cheng Chang, Sha Yin, Jun Xu. RSC Advanced 2020, v. 23, p.13662. DOI: 10.1039/d0ra01086c.
10. Asadov M.M., Guseinova S.S., Lukichev V.F. Russian Microelectronics. 2020. v. 49. (5), p. 314. https://doi.org/10.1134/S1063739720050030
11. Asadov M.M., Mustafaeva S.N., Guseinov S.S., Lukichev V.F. Physics of the Solid State. 2020. v. 62 (11). p. 2224. https://doi.org/10.1134/S1063783420110037.
12. Asadov M.M., Mustafaeva S.N., Guseinov S.S., Lukichev V.F., Tagiev D. B. Physics of the Solid State 2021, v. 63 (5), p. 797. https://doi.org/10.1134/S1063783421050036.
13. Yildirim H., Kinaci A., Zhi-Jian Zhao, Maria K. Y. Chan, and Jeffrey Greeley. ACS Applied Materials & Interfaces, 2014, v. 6, p. 21141. https://doi.org/10.1021/am506008w.
14. Pablo A. Denis, Faccio R.,.Iribarne F. Computational and Theoretical Chemistry 2012, v. 995, p.1. https://doi.org/10.1016/j.comptc.2012.06.014

VISCOMETRIC AND DENSITOMETRIC STUDY OF AQUEOUS SOLUTIONS LiCl, NaCl and KCl

EA MASIMOV, BG PASHAYEV and AE SURKHAYLI

Baku State University, Z.Khalilov str., 23, Az1148, Baku, Azerbaijan
E-mail: efsanesurxayli95@gmail.com

The dynamic viscosity and density of aqueous solutions of LiCl, NaCl, and KCl salts in the range of 10-60 0C temperature and 0.01-0.07 molar fraction concentration of salts were measured, the structural features of the considered systems were studied based on the analysis of viscous flow and volume properties. For this purpose, the dependence of the activation of the viscous flow of the solution on the Gibbs energy, the enthalpy of activation of the viscous flow, the entropy of the activation of the viscous flow, and the partial molar volumes of salts in solution was analyzed. It has been found that all three salts have a destructive effect on the existing structure with increasing concentration. Thus, the KCl salt has a more destructive effect on the existing structure than the NaCl salt, and the NaCl salt has a more destructive effect on the existing structure.

Keywords: LiCl; NaCl; KCl; activation parameters of viscous flow; partial molar volumes.
PACS: 83.50.Ax, 87.58.Xs, 02.60.Cb

Introduction

It is known that several ions (Li +, Na +, K +, Mg2 +, Fe3 +, Cl-, I-, etc.) play an important role in all biological processes in a living organism. For example, Li + ion directly affects the ionic balance of the cell, Na + ion maintains acid-base balance in the body, regulates blood pressure, nerve and muscle activity, protein synthesis, K + ion regulates the amount of water in tissues, improves heart function, nervous system Na + and K + ions also play an important role in the cell membrane as a sodium-potassium pump, Cl- ion is one of the key elements of water-salt metabolism in all living organisms, I-ion to enhance immunity and synthesize thyroxine, a thyroid hormone need, etc. Note that the main activity of individual ions in biological systems occurs in the aquatic environment. No environment can be compared to water in which these ions perform as important a function as water. Therefore, the study of structural features in biological systems and the study of the effects of various substances on this structure is of great importance in modern molecular physics, physical chemistry, biophysics, molecular biology. Each water-soluble substance changes the structure of water in its way. The influence of positive and negative ions of electrolytes and neutral molecules of non-electrolytes on the structure of water differs significantly from each other.

In non-electrolyte solutions, the initial structure of water is stabilized under the influence of neutral molecules, in many cases, neutral molecules strengthen the initial structure of water [1 - 4]. In electrolyte solutions, completely different processes take place under the influence of ions. Thus, the existing structure of water is destroyed and a new structure of the solution is formed. Ions cause two opposite changes in the structure of water. On the one hand, the electric field of ions disrupts the order of the molecules inherent in pure water, and this effect leads to an increase in the entropy of the system.

On the other hand, the electric field of ions directs water molecules and leads to their regular arrangement around the ion, which leads to a decrease in entropy [5, 6].
In the end, depending on which of these two effects prevails, the change in the entropy of

the system is either positive (ions have a destructive effect on the structure of water) or negative (ions have a structural effect on the structure of water) [7].

Given the presence of Li +, Na +, K +, and Cl^- ions in living organisms, and the fact that these ions play an important role in biological processes here, the structural properties of their aqueous solutions of their salts (LiCl, NaCl, KCl) are considered. LiCl, NaCl and KCl salts are very soluble in water. As these salts are formed from strong bases and acids, they dissociate in water and break down into ions. The dynamic viscosity and density of aqueous solutions of LiCl, NaCl, and KCl salts in the range of 10-60 0C temperature and 0.01-0.07 molar fraction concentration of salts were measured, structural features of the considered system based on the analysis of viscous flow and volume properties were investigated. For this purpose, the concentration dependence of the Gibbs energy ($\Delta G_\eta^\neq$), the enthalpy of activation of the viscous stream ($\Delta H_\eta^\neq$), the entropy of the activation of the viscous flow ($\Delta S_\eta^\neq$),and the partial molar volumes of salts in the solution ($\tilde{V}$) were analyzed.

Experiment

The object of study and methods. An aqueous solution of LiCl, NaCl, and KCl of different concentrations was taken as the object of research. The LiCl, NaCl, and KCl used are chemically pure substances. Measurements were made at normal atmospheric pressure. The solutions were prepared by the gravimetric method. Bidistilled water is used in the preparation of solutions. During the preparation of the samples, an analytical scale manufactured by KERN 770 was used and the measurements were taken with an accuracy of 0.0001 g. In the study, the viscosity was measured with a 0.34 mm diameter SMV-2 capillary viscometer.

The flow time of the liquid was determined with an accuracy of ± 0.01 s on the viscometer. All measurements were made three times and their average values were taken as a result of the experiment.

The density of liquids was determined by changing the volume with a thin long-necked (throat-graded) glass pycnometer with a volume of 15 cm3. The values of both viscosity and density were determined relative to the reference fluid. Bidistilled water was used as the reference liquid, and the values of water viscosity and density were taken from [8, 9]. A viscometer and a pycnometer were placed in the thermostat to determine the viscosity and density of the solutions at different temperatures (283.15, 288.15, 293.15, 298.15, 303.15, 308.15, 313.15, 318.15, 323.15, 328.15, 333.15 K).

The temperature was measured with an accuracy of ± 0.05 K. The maximum relative error of the experiment was 0.30% when determining the density and 1.0% when determining the viscosity.

Activation of viscous flow Gibbs energy according to Frenkel and Eyring's theory [8]

$$\Delta G_\eta^\neq = RT \ln \frac{\eta}{\eta_0} \tag{1}$$

has been defined as [10, 11].

Eyring's theory is defined by the expression $\eta_0 = N_A h\rho/M$ [8]. Here, the quantities η and ρ

are the dynamic viscosity and density of the solution at absolute temperature T, R - universal gas constant, NA - Avogadro's number, h - Planck's constant, and is the molar mass of the solution.

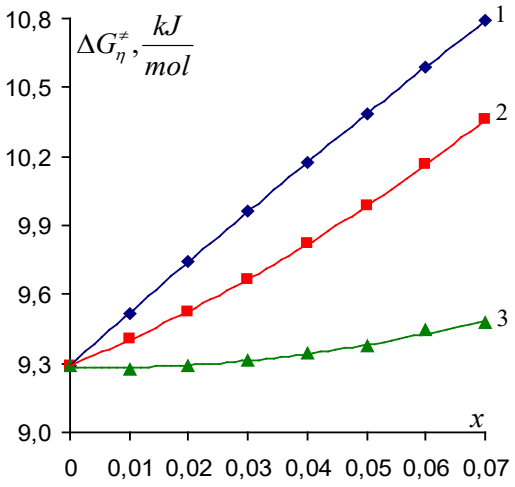

Fig. 2. Aqueous salts of LiCl, NaCl and KCl activation of the viscous flow of solutions enthalpyconcentration dependence (t=20C).

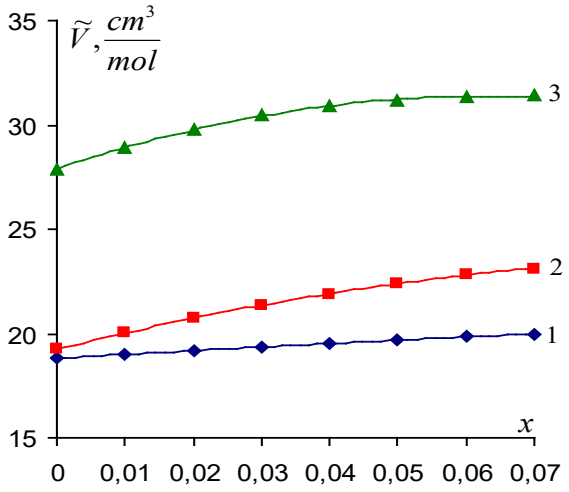

Fig.1. Aqueous salts of LiCl, NaCl and KCl Activtion of viscous of solutions Gibbs energy concentration dependence (t = 20C).

Viscous flow activation enthalpy ($\Delta H_\eta^{\neq}$)

$$\Delta H_\eta^{\neq} = R\frac{\partial \ln(\eta/\eta_0)}{\partial(1/T)} \tag{2}$$

is defined with the formula given above [9, 11]. Viscous flow activation entropy ($\Delta S_\eta^{\neq}$)

$$\Delta G_\eta^{\neq} = \Delta H_\eta^{\neq} - T\Delta S_\eta^{\neq} \tag{3}$$

has been defined as given above [8].

Partial molar volume of salts in solution (Ṽ)

$$\tilde{V} = V_m + (1-x)\left(\frac{\partial V_m}{\partial x}\right)_{p,T} \tag{4}$$

is determined by the formula [8, 12].

Here $V_m = M/\rho$ is the molar volume of the solution [8].

Results and discussion

Viscous flow activation parameters allow determining the energy and structural changes in the liquid as a result of any external influences (temperature, pressure, concentration, etc.), to obtain information about the formation and dissolution of hydrogen bonds in aqueous solutions. The dependence of the activation parameters of the viscous flow of aqueous solutions of LiCl, NaCl and KCl salts ($\Delta G_\eta^{\neq}$, $\Delta H_\eta^{\neq}$, $\Delta S_\eta^{\neq}$) on the concentration (x) at 20^0C is shown in Figures 1-3, and the dependence of the partial molar volumes of salts in the solution (Ṽ) on the

concentration (x) is shown in Figure 4.

As a result of our research, it was determined that the dependence of the concentration of all four parameters on the other temperatures studied varies with the same regularity (temperature analogous to 20^0C) at a temperature of 20^0C.

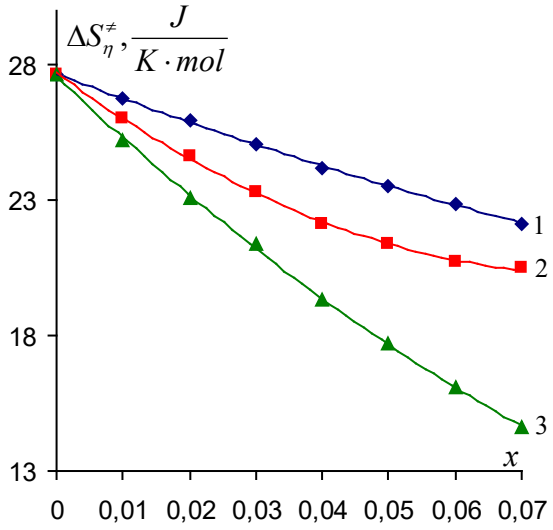

Fig. 3. Aqueous salts of LiCl, NaCl and KCl activation of the viscous flow of solutions entropy concentration dependence (t=20^0 C).

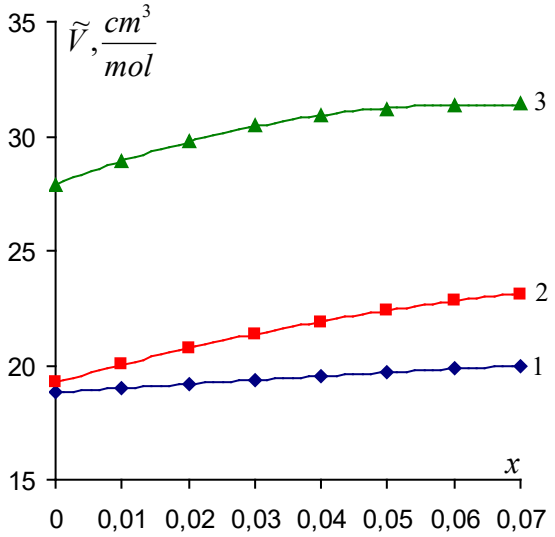

Fig. 4. Aqueous salts of LiCl, NaCl and KCl partial molar volume of salts in the viscous flow of solutions concentration dependence (t=20C).

As can be seen from Figure 1, the temperature and concentration in the considered range increase with increasing concentration for an aqueous solution of all three salts (LiCl, NaCl, KCl), as well as for a given temperature and concentration (LiCl)> (NaCl)> (KCl). According to Frenkel's and Eyring's theories [8], 1 mole is the energy expended to cross the potential wall of a molecule. It is clear that in the solutions we studied, along with water molecules, hydrated Li +, Na + and K + ions will also become active. Naturally, more energy must be expended on the activation of hydrated ions than on water molecules. The increase in concentration at a given temperature can be explained by a gradual increase in the number of activated hydrates $\Delta G_\eta^{\neq}$ compared to water molecules. The hydration energies of Li +, Na + and K + ions are ΔE (Li +)> ΔE (Na +)> ΔE (K +), the effective radii are ref (Li +)> ref (Na +)> ref (K +), and the hydration numbers are Nh (Li +)> Nh (It is like Na +)> Nh (K +).

Together with the hydrate layer, we can determine the mass of ions by mh = (Mi + NhMsu) / NA. Based on this expression, we can determine that for hydrated Li +, Na + and K + ions, mh (Li +)> mh (Na +)> mh (K +). As can be seen, for aqueous solutions of salts, the decreasing order is the same as the decreasing sequence of ΔE, ref, Nh and mh. We assume that for these reasons the value of decreases in accordance with LiCl, NaCl, KCl.

The value of the parameter $\Delta H_\eta^{\neq}$ in the considered temperature and concentration range does not change with increasing concentration for aqueous solution of LiCl salt, decreases to x ≈ 0.04 for aqueous solution of NaCl, and then almost does not change, and decreases for

aqueous solution of KCl (Figure 2).

It is also $\Delta H_{\eta}^{\neq}$ (LiCl)> $\Delta H_{\eta}^{\neq}$ (NaCl)> $\Delta H_{\eta}^{\neq}$ (KCl) for a given temperature and concentration.

Note that the changes in the solution are characterized $\Delta H_{\eta}^{\neq}$ in terms of energy. As the concentration increases, the increase indicates that the system under consideration has become relatively more structurally structured, and vice versa [10, 13].

Note that Li^+ and Na^+ ions have positive hydration, K^+ and Cl- ions have negative hydration, and the intensity of the movement of water molecules around the positively hydrated ions decreases, while the intensity of the movement of water molecules around the negatively hydrated ions increases [8, 13].

Because ions are hydrated in aqueous solutions of electrolytes, the structure of such solutions differs significantly from the structure of water [1, 3, 4].

Structural changes in the solution are characterized by the parameter $\Delta S_{\eta}^{\neq}$ [8].

Thus, as the concentration increases, the increase indicates that the system becomes more structured, and the decrease becomes relatively structured [8, 9, 10]. In the considered temperature and concentration range, the concentration decreases for an aqueous solution of all three salts (LiCl, NaCl, KCl), and also (LiCl)> (NaCl)> (KCl) for a given temperature and concentration (Figure 3). For an aqueous solution of all three salts, decreasing with increasing concentration indicates that these salts destroy the structure of the water. As can be seen, the effects of salts on the structure of water are different. Thus, NaCl is more destructive than LiCl salt, and KCl is more destructive than NaCl salt. We assume that this is due to the corresponding sequential decrease in the hydration energies of Li +, Na + and K + ions. Many studies [5, 14, 15] show that ions affect the structure of water in a sequence corresponding to the lithropic sequence of Hofmeister.

The study of volumetric properties (density, coefficient of thermal expansion, molar volume, partial molar volume, etc.) in multi-component systems is very important for the description of various processes.

These properties also play an important role in providing different models to determine the molecular structure and macroscopic properties of solutions.

The study of the volumetric properties of solutions, especially the partial molar volumes of components, allows us to clarify the nature of molecular interactions between molecules in solution. The study of this property of solutions is also very important in the description of the structural characteristics of solutions [8, 10, 11, 12].

As can be seen from Figure 4, $\tilde{V}$ increases with increasing concentration for an aqueous solution of all three salts (LiCl, NaCl, KCl) in the temperature and concentration range under consideration, as well as $\tilde{V}$ (LiCl) <$\tilde{V}$ (NaCl) <$\tilde{V}$ (KCl) for a given temperature and concentration happens. The increase in the partial molar volumes of salts in the solution as the concentration increases can be explained by the fact that the relative structure of the solution becomes disintegrated. An electric field is created around each ion in the water, and the intensity of this electric field decreases sharply as the distance increases.

In this heterogeneous electric field, water molecules are subjected to a certain orientation

around ions. As a result, the volume of water molecules collected around the ions is smaller than the volume of water in the water phase.

This compression is called the electrostriction effect [8, 12].

Note that all ions create an electrostatic effect in water [8]. The electrostatic effect depends on the surface charge density of the ion. Thus, the electrostatic effect created by small ions with a large surface load density will be stronger than the electrostrictive effect created by large ions with a small surface load density.

As the surface load densities of Li +, Na +, and K + ions decrease in a corresponding sequence, the intensity of the electric field generated near these ions and the electrostrictive effects they create in solution also decrease in a corresponding sequence. As the sizes of Li +, Na +, and K + ions increase in the corresponding sequence, the partial molar volume of the LiCl salt in solution is smaller than that of NaCl, and the partial molar volume of the NaCl salt is smaller than that of KCl, despite the decrease in the electrostrictive effects they create.

Conclusion

Analysis of the viscous flow and volume properties of water-LiCl, water-NaCl, and water-KCl systems in the range of 10-600C temperature and 0.01-0.07 molar fraction shows that as the concentration of LiCl, NaCl and KCl salts in solution increases, the structure of water disintegrates. Also, NaCl has a more destructive effect on the structure of water than LiCl salt, and KCl has a stronger destructive effect than NaCl salt. That is, the destructive effect of salts on the structure of water is enhanced in the order of LiCl, NaCl, KCl.

References

1. Leontidis E. Current Opinion in Colloid & Interface Science 2016, v. 23, p. 100.
2. Shimizu S., Matubayasi, N. Journal Physical Chemistry Chemical Physics 2017, v. 19, p. 26734.
3. Masimov E.A., Pashaev B.G., Gasanov G.Sh. Journal of Physical Chemistry 2017, v. 91 (4), p. 644.
4. Massimov E.A., Pashaev B.G., Radzhabov M.R. Journal of Physical Chemistr, 2020, v. 94 (12), p. 1909.
5. Jakubowska A., Kozik T. Journal of Chemometrics 2019, v. 33, p. 1.
6. Kondoh, M., Ohshima, Y., Tsubouchi, M. Chemical Physics Letters 2014, v. 591, p. 317.
7. Zangi, R., Berne, B.J. Journal of Physical Chemistry B 2006, v. 110, p. 22736.
8. Masimov E.A., Hasanov H.Sh., Pashayev B.G. liquid viscosity. Baku, Laman, 2016, 285 p.
9. Massimov E.A., Pashaev B.G., Gasanov G.Sh., Gasanov N.G. Uspekhi sovremennoi estestvoznanie 2015, v. 10, p. 32.
10. Massimov E.A., Gasanov G.Sh., Pashaev B.G. Journal of Physical Chemistry, 2013, v. 87 (6), p. 969.
11. Massimov E.A., Pashaev B.G., Gasanov G.Sh., Gasanov N.G. Journal of Physical Chemistry, 2015, v. 89 (7), p. 1133.
12. Atkins P., De Paula J. Physical chemistry. Oxford University Press. 2006, 1067 p.
13. Masimov E.A., Pashayev B.G., Hasanov H.Sh. Journal of Low Dimensional Systems 2018, v. 2 (1), p. 32.
14. Duignan, T.T., Parsons, D.F., Ninham, B.W. Journal Chemical Physics Letters 2014, v. 608, p. 55.
15. Flores S.C., Kherb J., Konelick N. Chen X., Cremer P.S. Journal Physical Chemistry C 2012, v. 116, p. 5730.

SPIN DYNAMICS (S = 1/2 AND S = 1) IN HEXAGONAL NANOTUBE SYSTEMS

VA TANRIVERDIYEV, VS TAQIYEV, NB MUSTAFAYEV and IN IBRAHIMOV

Institute of Physics, Azerbaijan National Academy of Sciences, Baku, Azerbaijan
E-mail: vahid_tanriverdi@yahoo.com

The stochastic Glauber dynamics is used to study dynamic behaviors in a superlattice nanotube. The time variations of the average magnetizations are investigated to obtain the phases in the systems, which are modeled as having a hexagonal cross section. The stationary solutions of the dynamic effective field coupled equations have been investigated, and the results are illustrated numerically for a particular choice of parameters.

Keywords: nanotube, Ising model, mixed spin system, mean-field approach, Glauber dynamic
PACS: 75.70. AK, 61.46.+w, 67.57.Lm

Introduction

The purpose of nanotechnology is to produce new materials at the nanometer scale. With the help of nanotechnology, researches on nanostructures are increasing day by day [1-4]. The magnetic, optical, mechanical, chemical, electrical and thermal properties of a material change dramatically when dimensions are reduced to the nanometer scale, the physical properties of the material are subject to the control of quantum mechanics [5-7].

On the other hand, nanotubes combine the properties of many different materials on their own. Experimental, analytical and computer simulation studies of magnetic nanostructures have been and continue to be done in order to better understand its properties [8-12]. Nanotube systems are the most studied nanostructures both experimentally and theoretically, and the physical properties of these systems can be described very easily and precisely using the Ising model with equilibrium statistical physics methods.

In recent years active studies have been started on the dynamic properties of these nanostructure systems. Dynamics phase transitions of Ising nanostructures under time-dependent oscillating external magnetic field were investigated using the effective field theory based on the stochastic Glauber dynamics [13-15].

In this paper, the dynamic behavior of the mixed spin (½; 1) Ising nanotubes formed by two different ferromagnetic materials will be examined using the mean dynamics and the stochastic Glauber dynamics. In order to find the phases present in the system, time-dependent behaviors of the average order parameters will be examined.

Description of the method and the model

The most optimal lattice used to describe the cylindrical nanotube system within the Ising model is the hexagonal lattice that will be used in this paper and define the nanotube system. Its schematic pattern is given in Figure 1.

The model of interest can be considered as two intertwined sublattice of the Ising model such as “*a*” and “*b*”. These spin particles are arranged in the lattice points in such a way that they form hexagonal lattices with successive layers.

The Hamiltonian expression of the cylindrical mixed spin Ising nanotube system including the crystal field or single-ion anisotropy term, and the time-dependent external magnetic field term:

$$H = -J_a \sum_{<i,j>} S_i^a S_j^a - J_b \sum_{<n,m>} S_n^b S_m^b - J \sum_{<i,n>} S_i^a S_n^b - D\left(\sum_{<i>} \left(S_i^a\right)^2 + \sum_{<n>} \left(S_n^b\right)^2 \right) - h(t)\left(\sum_{<i>} S_i^a + \sum_{<n>} S_n^b \right) \quad (1)$$

The spin of <*i*,*j*>, <*n*,*m*> and <*i*,*n*> means that the adjacent spin belonging different materials (*a*,*b*). Exchange of neighboring spins are described by the terms *J*. *D* denotes the crystal-field of single-ion anisotropy interactions term, and $h(t) = h_0\cos(\omega t)$ is the time-dependent oscillating external magnetic field.

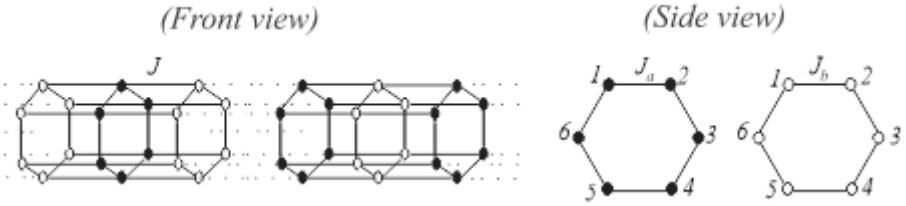

Fig. 1. A schematic pattern of the cylindrical hexagonal nanotube system that defines two different type Ising spins. The black and white spheres represent the spin magnetic atoms of different ferromagnetic materials ("*a*" and "*b*", respectively).

In this paper, the stochastic Glauber dynamics is user to study the mixed spin Ising model on successive layered hexagonal lattices under a time-depended oscillating external magnetic field. When the spins in the material "*b*" remain constant, at time "*t*", the probability function when the system has the spin configuration $S_1^a; S_2^a; ...; S_N^a$ is defined by $P^a\left(S_1^a, S_2^a, \cdots S_N^a, t\right)$ $P^A\left(\sigma_1, \sigma_2, \ldots, \sigma_j, .., \sigma_N, t\right)$. Finally, when the spins in the material "*a*" remain constant, the probability function at time "*t*" of the system is defined by $P^b\left(S_1^b, S_2^b, \cdots S_N^b, t\right)$.

Considering that the spins in the material $\alpha(\alpha = a, b)$ are fixed for a moment, the master equation is writen as

$$\frac{d}{dt} P^\alpha(S_1^\alpha, S_2^\alpha, \cdots S_l^\alpha, \cdots S_N^\alpha, t) = -\sum_l \sum_{S_l^\alpha \neq (S_l^\alpha)'} \left(w_l^\alpha(S_l^\alpha \to (S_l^\alpha)') \right) P^\alpha(S_1^\alpha, S_2^\alpha, \cdots S_l^\alpha, \cdots S_N^\alpha, t) +$$

$$+ \sum_l \sum_{S_l^\alpha \neq (S_l^\alpha)'} w_l^\alpha((S_l^\alpha)' \to S_l^\alpha)\, P^\alpha(S_1^\alpha, S_2^\alpha, \cdots (S_l^\alpha)', \cdots S_N^\alpha, t), \quad \alpha = a, b. \quad (2)$$

While the system is in equilibrium, with the help of the master equation and general definition of the canonical distribution, the probability of each spin to pass from S_l^α to $\left(S_l^\alpha\right)'$ per unit time:

$$w_l^\alpha(S_l^\alpha \to (S_l^\alpha)') = \frac{exp[-\beta \Delta E^\alpha(S_l^\alpha \to (S_l^\alpha)')]}{\tau \sum_{(S_l^\alpha)'} exp[-\beta \Delta E^\alpha(S_l^\alpha \to (S_l^\alpha)')]}, \quad \alpha = a, b \quad (3)$$

Here, $\beta=1/(k_BT)$, T is the absolute temperature and k_B is the Boltzmann constant.

The calculations carried out according to (3) make it possible to write the basic dynamic equations for the considered system in the following cases:

1) $S^a = \pm\frac{1}{2}; \quad S^b = \pm\frac{1}{2}$

The change of energy in equation (3) in this case

$$\Delta E^{\alpha}(S_l^{\alpha} \to (S_l^{\alpha})') = 2S_l^{\alpha}x^{\alpha},\ x^{\alpha} = 2J_aS^a + 2JS^b + h(t)$$

If these energy change expressions are substituted in the equation (3), $w_l^{\alpha}(S_l^{\alpha} \to (S_l^{\alpha})')$ probability densities

$$w_l^{\alpha}\left(\frac{1}{2} \to -\frac{1}{2}\right) = \frac{exp\left[-\frac{\beta x^{\alpha}}{2}\right]}{2\tau\, cosh\left[\frac{\beta x^{\alpha}}{2}\right]}, \quad w_l^{\alpha}\left(-\frac{1}{2} \to \frac{1}{2}\right) = \frac{exp\left[\frac{\beta x^{\alpha}}{2}\right]}{2\tau\, cosh\left[\frac{\beta x^{\alpha}}{2}\right]}, \quad \alpha = a, b \qquad (4)$$

If we make substitutions $m_a =< S^a >, \quad m_b =< S^b >, \quad \Omega = \tau\omega, \quad \xi = \omega t$, then using the master equation we can write the general average-area dynamic equation for the systems under consideration:

$$\begin{cases} \Omega\frac{d}{d\xi}m_a = -m_a + \frac{1}{2}tanh\left[\frac{\beta\left(2J_am_a + 2Jm_b + h(\xi)\right)}{2}\right] \\ \Omega\frac{d}{d\xi}m_b = -m_b + \frac{1}{2}tanh\left[\frac{\beta\left(2J_bm_b + 2Jm_a + h(\xi)\right)}{2}\right] \end{cases} \qquad (5)$$

2) $S^a = \pm 1/2; \quad S^b = 0, \pm 1$

The mean-area dynamic equation for this case is

$$\begin{cases} \Omega\frac{d}{d\xi}m_a = -m_a + \frac{1}{2}tanh\left[\frac{\beta\left(2J_am_a + 2Jm_b + h(\xi)\right)}{2}\right] \\ \Omega\frac{d}{d\xi}m_b = -m_b + \frac{2\,sin\,h\left[\beta\left(2J_bm_b + 2Jm_a + h(\xi)\right)\right]}{exp[-\beta D] + 2\,cos\,h\left[\beta\left(2J_bm_b + 2Jm_a + h(\xi)\right)\right]} \end{cases} \qquad (6)$$

3) $S^a = 0, \pm 1; \quad S^b = 0, \pm 1$

Similar to the equation (6), the following equation can be obtained for this case:

$$\begin{cases} \Omega\frac{d}{d\xi}m_a = -m_a + \frac{2\,sin\,h\left[\beta\left(2J_am_a + 2Jm_b + h(\xi)\right)\right]}{exp[-\beta D] + 2\,cos\,h\left[\beta\left(2J_am_a + 2Jm_b + h(\xi)\right)\right]} \\ \Omega\frac{d}{d\xi}m_b = -m_b + \frac{2\,sin\,h\left[\beta\left(2J_bm_b + 2Jm_a + h(\xi)\right)\right]}{exp[-\beta D] + 2\,cos\,h\left[\beta\left(2J_bm_b + 2Jm_a + h(\xi)\right)\right]} \end{cases} \qquad (7)$$

Numerical results and discussion

We have investigated the behavior of time variations of average magnetizations to find phases existing in the system. For this purpose, the stationary solutions of the dynamic mean-field coupled equations given by equations (5), (6) and (7) have been examined. The results are

presented in Figures 2-4. We can solve dynamic equations for a given parameters and initial values. There are two types of solutions in the system under consideration. The first type solution is a symmetric solution, and it corresponds to a paramagnetic (p) phase. In the symmetric solution, the average sublattice magnetizations m_a and m_b delayed with respect to the external magnetic field. They are equal to each other and oscillate around the zero value, conforming to the external magnetic field. The second type of solution is called a non-symmetric solution that corresponds to a ferromagnetic (or ferrimagnetic) solution. In this case, average sublattice magnetizations m_a and m_b have different values. They are not equal and they oscillate around non - zero values, i.e. $m_{a(b)} = \pm 1/2$ and $m_{a(b)} = \pm 1$, and do not conform to the external magnetic field. Some solutions corresponding to these phases are shown in Figures 2-4.

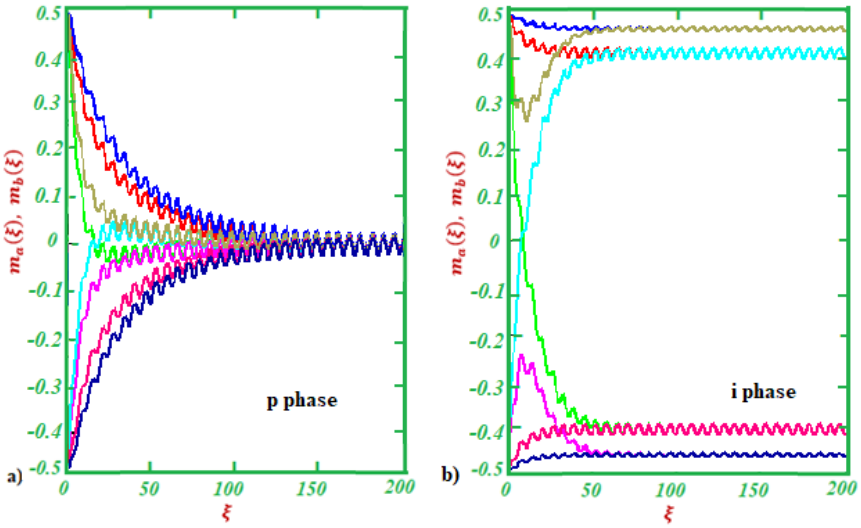

Fig. 2. Time variation of magnetization in a superlattice nanotube for $S^a = \pm 1/2$, $S^b = \pm 1/2$:
a) paramagnetic phase (k_BT/J_a=1.8, h_0/J=0.8, J_b/J_a=2, J/J_a=1.5, D/J_a= -0.5);
b) ferromagnetic phase (k_BT/J_a=0.9, h_0/J=0.8, J_b/J_a=2, J/J_a=1.5, D/J_a= -0.5).

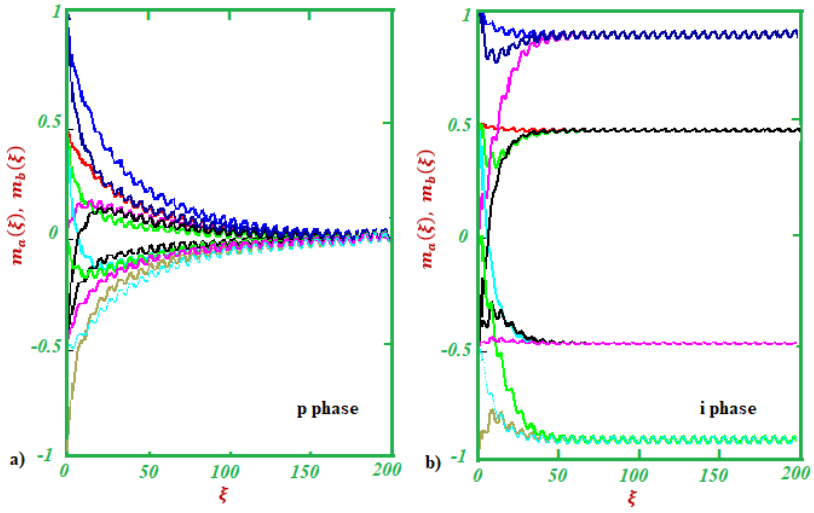

Fig. 3. Time variation of magnetization in a superlattice nanotube for $S^a = \pm 1/2$, $S^b = 0, \pm 1$:
a) paramagnetic phase (k_BT/J_a=2, h_0/J=0.8, J_b/J_a=2, J/J_a=1.5, D/J_a= -0.5);
b) ferrimagnetic phase (k_BT/J_a=0.8, h_0/J=1.8, J_b/J_a=2, J/J_a=1.5, D/J_a= -0.5).

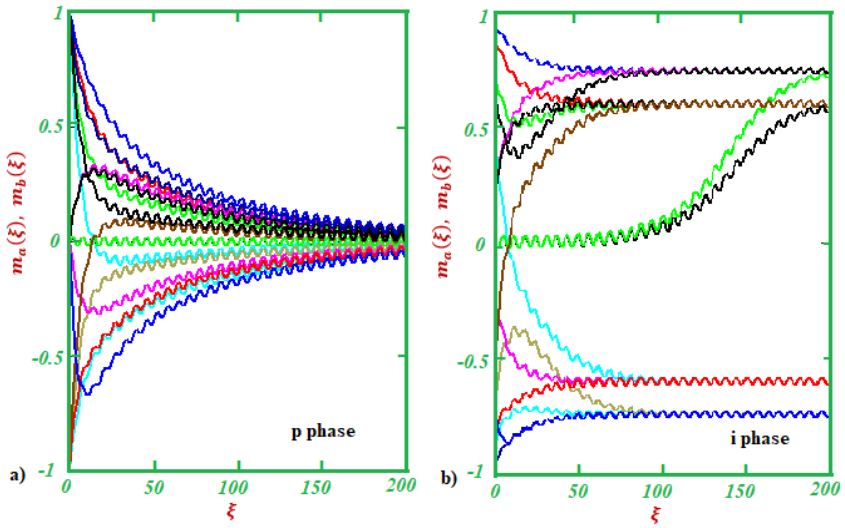

Fig. 4. Time variation of magnetization in a superlattice nanotube for $S^a = 0, \pm 1$, $S^b = 0, \pm 1$:
a) paramagnetic phase (k_BT/J_a=2.2, h_0/J=0.8, J_b/J_a=2, J/J_a=1.5, D/J_a= -0.5);
b)ferromagnetic phase (k_BT/J_a=1.4, h_0/J=1.8, J_b/J_a=2, J/J_a=1.5, D/J_a= -0.5).

References

1. Wu K., Su D. Q., Liu J. M., Saha R., Wang J. P. Nanotechnology 2019, v. 30, p. 502003.
2. Gloag L., Mehdipour M., Chen D. F., Tilley R.D., Gooding J. J. Adv. Mater. 2019, v. 31, p. 1904385.
3. Gonzalez A. L., Landeros P., Nunes A. S. J of Magnetism and Magnetic Materials 2010, v. 322, p. 530.
4. Kaneyoshi T. Phys. Status Solidi B 2011, v. 248 (1), p. 250.
5. Kantar E., Kocakaplan Y. Solid State Communications 2014, v. 177, p. 1.
6. Salazar-Enriques C. D., Restrepo-Parra E., Restrepo J. Physica E 2013, v. 52, p. 86.
7. Bin-Zhou Mi, Huai-Yu Wang, Yun-Song Zhou. J of Mag. and Magnetic Materials, 2010, v. 322, p. 952.
8. Shen W. Z., Cetinel S., Montemagno C. J. Nanoparticle Res. 2018, v. 20, p. 130.
9. Haghighi A. H., Faghih Z., Khorasani M. T., Farjadian F. J. Magn. Magn. Mater. 2019, v. 490, p. 165479.
10. Ivanov Y. P., Chuvilin A., Lopatin S., Kosel J, ACS Nano 2016, v. 10, p. 5326.
11. Grutter A. J., Krycka K. L., Tartakovskaya E. V., Borchers J. A., Reddy K. S. M., Ortega E., Ponce A., Stadler B. J. H., ACS Nano 2017, v. 11, p. 8311.
12. Canko O., Erdinç A., Taskin F., Yildirim A. F. J. Magn. Magn. Mater. 2012, v. 324, p. 508.
13. Keskin M., Ertas M., Canko O. Phys. Scr. 2009, v. 79, p. 025501.
14. Deviren B., Keskin M., Canko O. J. Magn. Magn. Mater. 2009, v. 321, p. 458.
15. Deviren B., Keskin M. J. Stat. Phys. 2010, v. 140, p. 934.

PROTECTIVE EFFECT OF HYDROGEN PEROXIDE IN THE HEMOLYSIS OF ERYTHROCYTES MEDIATED BY SILVER NANOPARTICLE

V VOINAROVSKI, A VCHERASHNIAYA and G MARTINOVICH

Belarusian State University, Minsk, Republic of Belarus
E-mail: voynarovskiy@bsu.by

In this work the regulation of the structural stability of erythrocytes by hydrogen peroxide during hemolysis by silver nanoparticles were investigated. An increase in the structural stability of the erythrocyte membrane was found during hemolysis caused by silver nanoparticles and silver nitrate upon preliminary incubation with hydrogen peroxide for 10 minutes at a concentration of 100–800 μM. The range of effect was established using a multivariate mathematical model of hydrogen peroxide metabolism in erythrocytes.

Keywords: erythrocytes; silver nanoparticles; structural stability; hydrogen peroxide
PACS: 43.80.Nd, 65.80.+n, 05.70.-a

Introduction

An important phenomenon in cellular respiration is the formation of reactive oxygen species (ROS), which have a wide spectrum of physiological and pathophysiological effects. A moderate increase in the concentration of oxidants activates defense mechanisms, due to which the balance of the formation and utilization of ROS is maintained, and an imbalance leads to cell damage and the development of diseases [1]. An important direction in the development of methods for regulating redox balance is the use of a special class of nanomaterials capable of catalyzing redox processes and thereby regulating the activity of cellular redox mechanisms. In this work, silver nanoparticles are considered as promising participants in the processes of utilization of hydrogen peroxide. Hydrogen peroxide is the main molecule of the ROS group involved in regulatory processes [2]. A moderate increase in its concentration activates the mechanisms associated with protection and adaptation, and a further increase leads to the accumulation of damage. High concentrations of hydrogen peroxide can be utilized using silver nanoparticles. Oxidation of nanoparticles with hydrogen peroxide is accompanied by the release of silver ions, which cause cell destruction. Ions are capable of disrupting the structure of proteins, lipids, nucleic acids, etc [3].

One of the most important mechanisms for increasing the structural stability of membranes is their interaction with the main protein of erythrocytes - hemoglobin. Binding takes place with membrane proteins due to covalent and non-covalent interactions or with membrane lipids as a result of hydrophobic interactions. The rate constants for the formation and decay of the hemoglobin-membrane complex depend on the oxidative state of hemoglobin. The highest binding constant is characterized by the process of interaction of methemoglobin formed during the oxidation of oxyhemoglobin. The study of the molecular mechanisms of this effect showed that with a slight and reversible oxidation, a stabilizing effect of hemoglobin on membranes is observed, while the formation of ferrylhemoglobins under the action of oxidative stress disrupts the interaction of the membrane with the cytoskeleton [4, 5].

In the general case, signal transmission, taking into account the catalytic properties of nanoparticles, is a complex chain of interrelated events, the theoretical description of which

is carried out only using multivariate models. Earlier, we showed that preliminary incubation of erythrocytes with hydrogen peroxide in micromolar concentrations induces cell adaptation to destruction by hypochlorous acid [6]. In this work the mechanisms of action of exogenous hydrogen peroxide on the structural stability of erythrocytes during hemolysis induced by silver nanoparticles were studied in *in vitro* and *in silico* experiments.

Experiment

The experiment used the blood of healthy donors, obtained in the State Institution "Republican Scientific and Practical Center for Transfusiology and Medical Biotechnology." Erythrocytes were isolated by centrifugation at 1500 rpm in phosphate-buffered saline containing 10 mM Na_2HPO_4 / KH_2PO_4, 137 mM NaCl, 2.7 mM KCl, 5 mM D-glucose (pH 7.4). Silver nanoparticles were obtained from silver nitrate using green chemistry methods. A solution of silver nitrate at a concentration of 1 mM was mixed with an aqueous extract of plants in a ratio of 9: 1 at pH 8.0 and left for 1 hour at room temperature. The end of the synthesis was established by the appearance of a localized surface plasmon resonance peak at 400 nm. The kinetics of erythrocyte hemolysis was measured using a Solar CM-2203 spectrofluorimeter (SOLAR, Belarus) by recording the optical density of the cell suspension (3×10^7 cells / ml) at a wavelength of 680nm. The concentration of erythrocytes was chosen so that the initial optical density was 0.5. 1 ml of a suspension of washed erythrocytes was added to the measuring cuvette and thermostated for 3-4 minutes at 37°C with constant stirring. Hemolysis was initiated by adding silver nitrate at a concentration of 100 μM or silver nanoparticles obtained from silver nitrate at a concentration of 250 μM to a suspension of erythrocytes with preliminary incubation with hydrogen peroxide for 10 minutes at a concentration of 100 – 800 μM. Evaluation of effect (I) was defined as the relative difference in optical density after 25 minutes of incubation with silver nanoparticles or silver nitrate in the presence of hydrogen peroxide and optical density after 25 minutes of incubation with silver nanoparticles or silver nitrate without hydrogen peroxide.

Results and discussions

As a result of the research, a mathematical model that links the transport and metabolism of hydrogen peroxide, the state of the antioxidant system of erythrocytes, the metabolic activity of cells, the redox state of hemoglobin and the structural stability of membranes has been developed. The model takes into account the processes of diffusion of hydrogen peroxide into the cell, utilization by the enzymes catalase and glutathione peroxidase, as well as interaction with hemoglobin and methemoglobin. At low concentrations of hydrogen peroxide, all processes are reversible. The reduction of methemoglobin and ferrylhemoglobin occurs with the participation of enzymes and non-enzymatic reducing agents with the consumption of energy generated in the processes of glycolysis and the pentose phosphate pathway. The interaction of proteins with the membrane is modeled by the kinetics of ligand-receptor interaction. The general scheme of the processes is shown in Figure 1.

The constructed mathematical model was nonlinear and contained 41 differential

equations. All constants and initial conditions were taken from literature sources. An analysis of the stability of the system was performed. The numerical solution of the system was performed with the Wolfram Mathematica software.

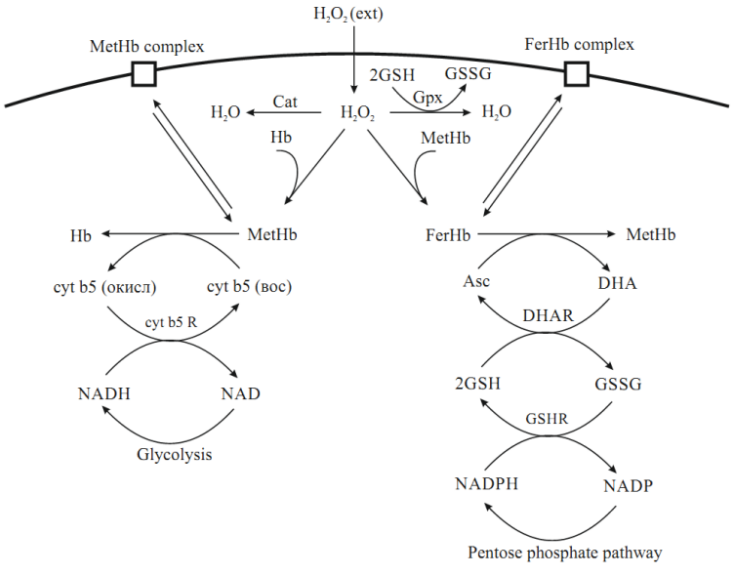

Fig. 1. Metabolic processes of erythrocytes with the participation of hydrogen peroxide, considered in the model. Hb hemoglobin; MetHb methemoglobin; FerHb ferrylhemoglobin; H_2O_2 hydrogen peroxide; H_2O_2 (ext) extracellular hydrogen peroxide; Cat catalase; Gpx glutathione peroxidase; GSH glutathione; GSSG glutathione disulfide; cyt b5 (ox) oxidized form of cytochrome b5; cyt b5 (red) reduced form of cytochrome b5; cyt b5 R cytochrome b5 reductase; NAD^+ / NADH oxidized and reduced form of nicotinamide adenine dinucleotide; Asc ascorbic acid; DHA dehydroascorbate; DHAR dehydroascorbate reductase; GSHR glutathione reductase; $NADP^+$/ NADPH oxidized and reduced form of nicotinamide adenine dinucleotide phosphate; MetHb complex membrane complex with methemoglobin; FerHb complex membrane complex with ferrylhemoglobin.

Fig. 2 shows the theoretically calculated value of the amount of formed membrane complexes of methemoglobin and ferrylhemoglobin versus the amount of extracellular hydrogen peroxide, with a cell number of 30 million and a pre-incubation time of 10 minutes. On the basis of numerical modeling of the processes of interaction of hemoglobin forms, the range of concentrations of extracellular hydrogen peroxide has been established, with the possible activation of adaptation processes, which is an experimental verification.

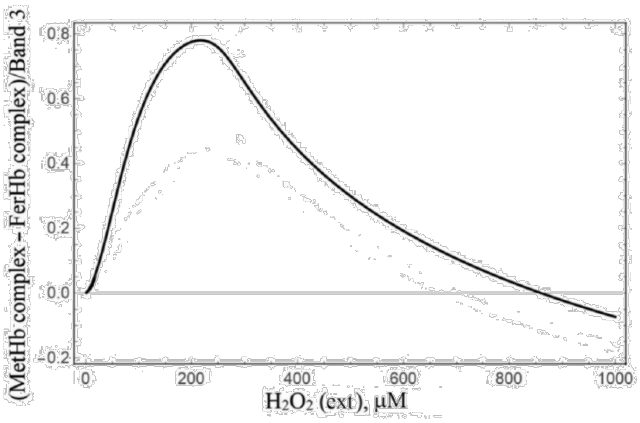

Fig. 2. Theoretically calculated difference in the number of membrane complexes of methemoglobin and ferrylhemoglobin

During the experiment, it was shown that pre-incubation of erythrocytes with hydrogen peroxide leads to a decrease in hemolyzed cells under conditions of exposure to silver nanoparticles and silver nitrate. There is a difference in the magnitude of the effect and the position of the maximum for silver nanoparticles and silver nitrate. The maximum protective effect upon destruction by nitrate at an extracellular concentration of hydrogen peroxide of 700 µM, while there is a complete absence of hemolyzed cells in comparison with the control. In turn, when the effect is destroyed by nanoparticles, it reaches a maximum at 500 µM of extracellular hydrogen peroxide, leaving one third of the initial number of cells (Fig. 3a, 3b). The protective mechanism established in the work may be associated with the formation of hemoglobin complexes on the cell membrane. The ratio of membrane complexes of various oxidized forms of hemoglobin determines the hormesis dependence of the response of erythrocytes to the action of silver ions and silver nanoparticles. The regulatory effect of hydrogen peroxide is observed at low concentrations, when the complexes formed by methemoglobin dominate on the membrane. With an increase in concentration, the proportion of destroyed erythrocytes increases, which is probably due to an increase in the amount of ferrylhemoglobin – membrane complexes. An increase in the number of ferrylhemoglobin complexes can cause lipid peroxidation processes and disrupt the interaction of the cytoskeleton with the membrane, which leads to a decrease in the effect of increasing structural stability at a high level of H_2O_2.

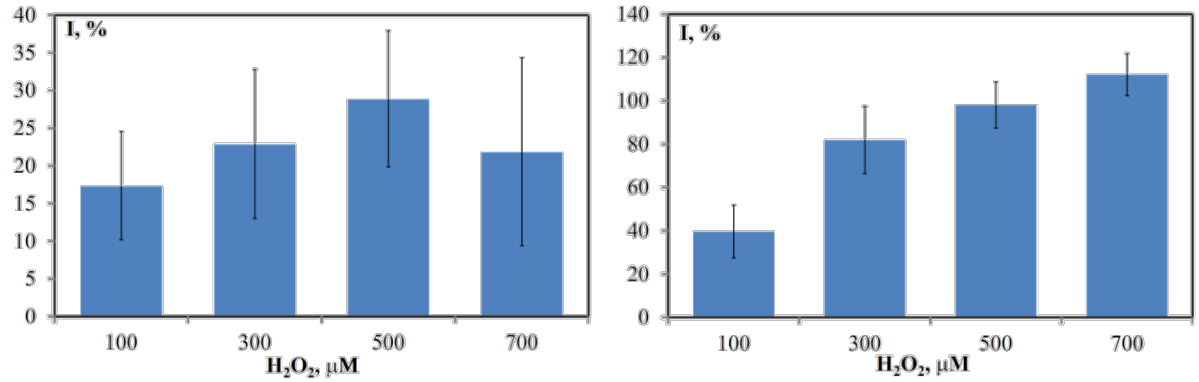

Fig. 3. The proportion of non-hemolyzed erythrocytes depending on the concentration of extracellular hydrogen peroxide (a - hemolysis with silver nanoparticles, b - hemolysis with silver nitrate)

The toxicity of silver nanoparticles is due to the release of ions that interact with the main components of the cell, which leads to the accumulation of irreversible damage. The weaker protective effect of hydrogen peroxide upon destruction by silver nanoparticles may be associated with the property of the direct interaction of the nanoparticle and hemoglobin, accompanied by the formation of an electron transfer complex. This binding is irreversible and therefore cannot lead to adaptation.

Conclusions

As a result of theoretical and experimental studies, it was shown that hydrogen peroxide

at concentrations of 100 - 700 μM activates the adaptive mechanism of erythrocytes, due to an increase in the number of membrane-bound methemoglobin, which increases the structural stability of the membrane and reduces the number of cells destroyed by silver nanoparticles and silver nitrate.

References

1. Sies H., Jones D.P. Nat. Rev. Mol. Cell Biol. 2020, v. 21 (3), p. 1. DOI: 10.1038/s41580-020-0230-3
2. Johnson R.M., Goyette G.Jr. Free Radic. Biol. Med. 2005, v. 39, p.1407. DOI: 10.1016/j.freeradbiomed.2005.07.002
3. He D., Jones A., Garg S., Pham N., Waite D. J. Phys. Chem. 2011, v. 115, p. 5461.
4. Arashiki N.; Kimata N.; Manno S.; Mohandas N.; Takakuwa Y. Biochemistry. 2013, v. 52, p. 5760. DOI: 10.1021/bi400405p
5. Kosmachevskaya. O. V.; Nasybullina. E. I.; Blindar. V. N.; Topunov. A. F. Applied Biochemistry and Microbiology, 2019, v. 55 (2), p. 83. DOI: 10.1134/S000368381902009
6. Voinarovski V.V., Martinovich G.G. Biochemistry (Moscow) Supplement Series A: Membrane and Cell Biology. 2022. v. 16 (1).

MAGNETIC PROPERTIES IN BIOLOGICAL SYSTEMS

RI KHALILOV and AN NASIBOVA

Baku State University, Department of Biophysics and biochemistry
Institute of Radiation Problems, ANAS, Baku, Azerbaijan
E-mail: hrovshan@hotmail.com

The effect of various stressors on biological systems has been studied. When studying the effects of ionizing gamma radiation, radioactive contamination, temperature on various plant and animal organisms by electronic paramagnetic resonance (EPR) it has been found that any stress factor causes the formation of signals in living systems that characterize the iron nanoparticles of iron oxide. Studies have shown that this depends on the dose of stress factors. The obtained results were confirmed by various spectroscopic methods.

Keywords: EPR signals, biological systems, magnetic nanoparticle, grape snails
PACS: 07.89.+b; 23.90.+w; 75.75.−c; 76.30.−v

Introduction

Magnetic nanoparticles - magnetite (Fe3O4) and maghemite (γ-Fe2O3) play an important role in the functioning of living systems. These nanoparticles cause magnetic properties in natural systems and the formation of a broad EPR signal, which was first detected by us [1-4].

Biological magnetic nanoparticles, first discovered in magnetotactic bacteria, have the property of "determining the geographical direction" [5].

Later, biological magnetic nanoparticles were also found in organisms such as prokaryotes, eukaryotes and archaea. Biological magnetic nanoparticles have also been found in algae, mollusks, ants, butterflies, fish, sea turtles, birds, whales and humans [6-9].

Studies have shown that the concentration of magnetic nanoparticles is relatively higher in inflamed areas of the body. In modern times, much attention is paid to the study of magnetic nanocomposites. These materials also play the role of "magnetite target" in the delivery of drugs to specific organs. However, there are still a number of obstacles to their practical application.

In general, methods for determining magnetic nanoparticles in human organs and tissues, studying their properties, their location in cells, and the interaction of magnetic nanoparticles and magnetic carriers are very important areas.

In various literatures, the presence of magnetic nanoparticles in living organisms has been studied by microscopic methods [10-12]. In our research, the phenomenon of the formation of magnetic nanoparticles in living systems was studied by the method of Electronic Paramagnetic Resonance, and the mechanism of this phenomenon is given [1, 2, 13, 14]. The objects of our research were different types of plants and some animal organisms [3, 4, 13, 15, 16].

In the presented work, by EPR method were studied some parameters during the impact of radioactive and environmental pollution on some plant species. At the same time, the effect of different doses of ionizing gamma radiation on the shell and body parts of pelvic snails (*Helix pomatia*) was determined.

Materials and methods

The studied plants (leaves and seeds) were dried in natural conditions at room temperature (25-26C).

The grape snails were irradiated with ionizing gamma radiation in different doses (150 Gy, 250 Gy, 400 Gy, 600 Gy, 800 Gy) on the RHUND-20000 device.

The body and pelvic parts of grape snails irradiated in different doses were separated and dried at room temperature.

The spectra of the samples were recorded at room temperature by Electron Paramagnetic Resonance Spectroscopy (Bruker-EMX, Germany). The recording was performed over a wide range of magnetic fields (500-5500 G). Microwave frequency: 9,870 GHz, power: 2,189 mV.

Discussion and conclusions

EPR method studies in areas with different radiation backgrounds have shown that the effects of radioactive contamination on plants produce a broad EPR signal (g = 2.32; ΔH = 320 G) characterizing nanophase iron oxide particles in both leaves and seeds.

It was found that the intensity of this signal is higher in the leaves than in the seeds.

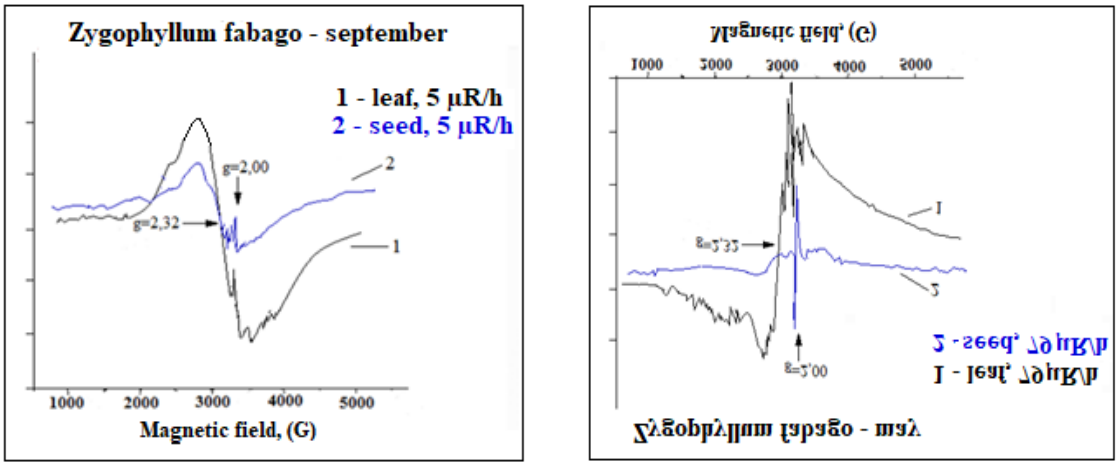

Fig. 1. EPR spectra of leaves and seeds of *Zygophyllum fabago* plant growing in controlled and radioactively contaminated areas

The experiments were repeated in different seasons (spring, summer and autumn) to determine whether any external factors, such as radiation, temperature, drought, UV rays and other stressors, played a role in the results. μ

It was found that an increase in the radiation background in all seasons of the year leads to an increase in the intensity of the broad EPR signal, which characterizes the magnetic nanoparticles in plants (Fig. 1).

The results suggest that the main role in stimulating the formation of magnetic nanoparticles in plant leaves is due to the increased radiation background with high radionuclide content (primarily this isotope 226Ra and 238U). Such radionuclides accumulate in large quantities in the leaves [4, 5]. We can assume that the generation of magnetic nanoparticles that

generate a wide EPR signal in the EPR spectrum is due to the work of a photosynthetic apparatus in the leaves of plants. Indeed, the intensities of the broad EPR signals we observed in plant seeds were much lower than in the leaves. It can be assumed that the phenomenon of stimulation of the formation of magnetic nanoparticles in plants growing in radioactively contaminated areas is associated with a partial violation of the integrity of chloroplasts due to high gamma radiation. In this case, the proximity of exogenous sources of nanoparticle formation (eg, iron ions) to the electron transport chain (ETC) of chloroplasts will increase, which will stimulate the formation of nanoparticles.

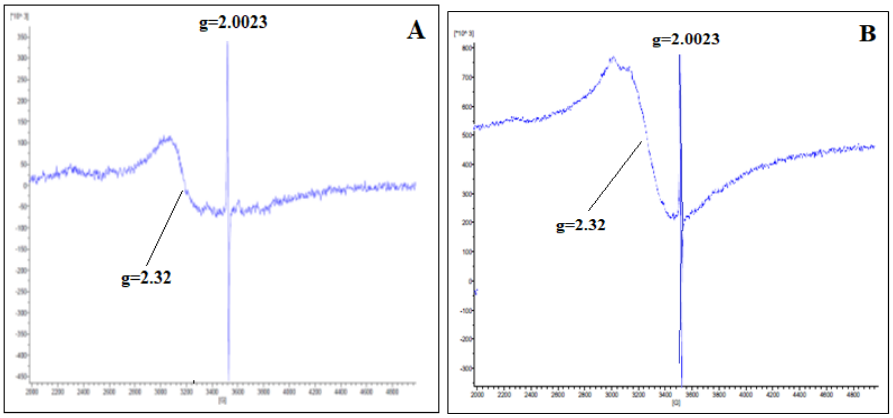

Fig. 2. EPR spectra of leaves of *Ligustrum L* collected from control (A) and contaminated area (B)

In addition, it is known that in the context of increasing anthropogenic impacts on the environment, living systems are exposed to physical and chemical factors, and the quality of the living environment is declining. Living systems, atmospheric air, soil and water, heavy metals, radionuclides, various industrial wastes, herbicides and other stressors are affected.

In this regard, paramagnetic centers in the leaves of plants *Ligustrum japonicum L.* (privet) collected from different areas according to the degree of environmental pollution were studied by EPR. It has been established that environmental pollution factors cause the generation of iron oxide magnetic nanoparticles in this plant. Experiments have shown that the parameters of broad EPR signals recorded in the leaves of plants during environmental pollution are identical to the parameters of EPR signals of magnetic nanoparticles.

Ligustrum japonicum L. was collected from two different areas of Baku (park area (control)) and the airport road with heavy traffic), which differ in the degree of pollution.

Paramagnetic centers were studied in these plants by the EPR method and a broad EPR signal (g = 2.32; ΔH = 500 G) and a free radical signal (g = 2.0023; ΔH = 10 G) characterizing iron oxide magnetic nanoparticles were recorded in them (Fig. 2).

Based on the change in the intensity of EPR signals received from the Ligustrum plant collected from areas with different levels of environmental pollution, it was found that the pollution has a significant effect on the formation of magnetic nanoparticles in this plant. As the degree of pollution increases, the generation of nanophase iron oxide magnetic nanoparticles in the leaves of the plant intensifies.

Subsequent experiments were performed with animal organisms (shell snails (Helix

pomatia)). Controlled (non-irradiated) and irradiated in different doses (150 Gy, 250 Gy, 400 Gy, 600 Gy, 800 Gy) snails after 60 days of storage in the laboratory (24-25˚C temperature, 16 hours light, 8 hours dark) -separated and their EPR spectra were recorded.

Interpretation of the EPR spectra of the pelvic parts of the control and irradiated snails showed that they contained free radical signals and signals of copper ions. The gradual increase in the radiation dose from 150 Gy to 600 Gy led to the formation of a signal characterizing the magnetic nanoparticles of iron oxide in these spectra, and the intensity of this signal increased with increasing radiation dose. When the radiation dose reached 800 Gy, a decrease in the signal intensity of nanophase crystalline nanoparticles was observed. EPR spectra of control and irradiated body parts of snails were also recorded. In addition to the free radical signal during irradiation at doses of 150 Gy and 250 Gy in these spectra, very high-intensity signals characterizing iron oxide magnetic nanoparticles were observed as a result of biomineralization.

Radiation at doses of 400 Gy, 600 Gy, 800 Gy led to a gradual decrease in the intensity of these signals and an increase in the intensity of free radical signals.

An increase in free iron ions in the body under the influence of stress factors (150 Gy and 250 Gy) leads to the formation of magnetic nanoparticles of iron oxide as a result of biomineralization due to the reducing medium. The decrease in the intensity of this signal with increasing radiation dose can be explained by the lack of a reducing medium. The fact that the dynamics of changes in the signals received in the pelvis are identical to the signals received in the body may be due to the fact that the pelvis is fed directly the body.

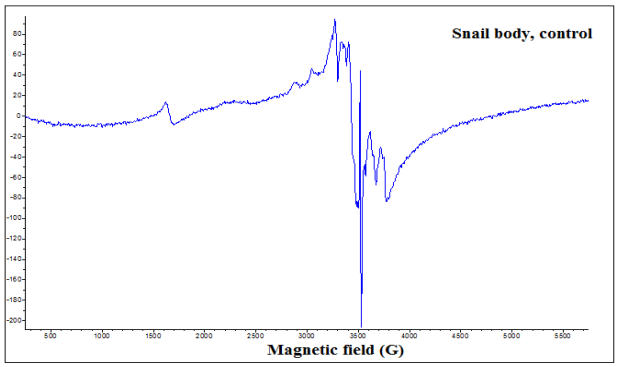

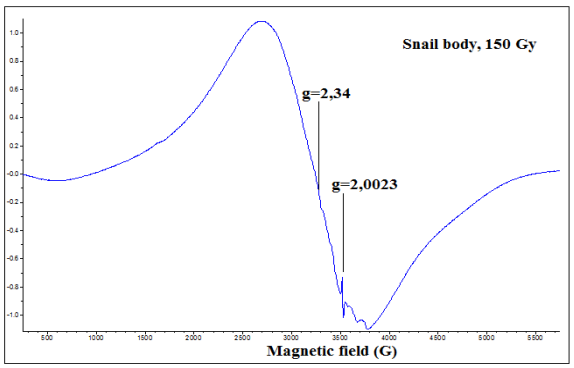

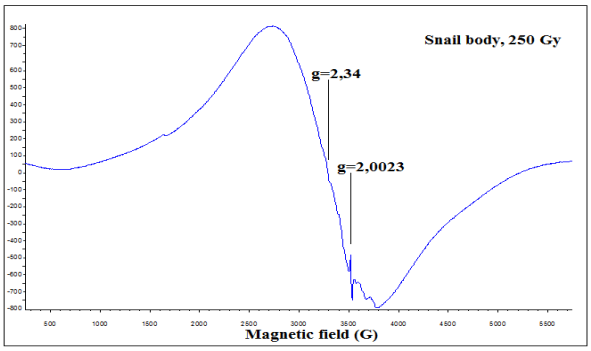

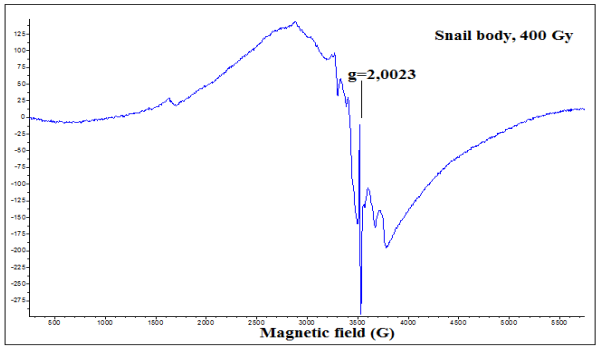

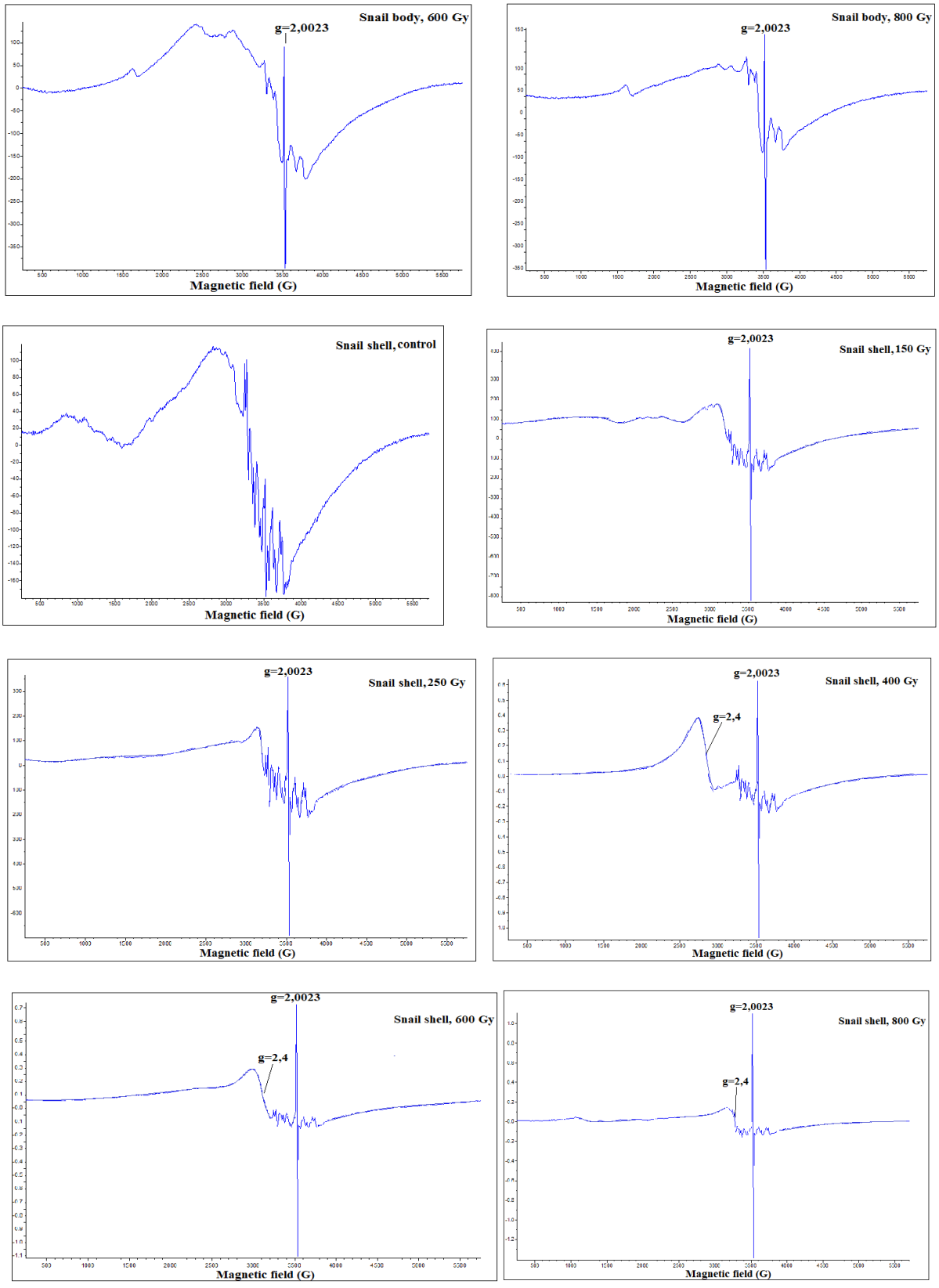

Fig. 3. EPR spectra of body and shell parts of grape snails irradiated at different doses of gamma irradiation

References

1. Khalilov R.I., Nasibova A.N.., Serezhenkov, Ramazanov M.A., Kerimov M.K., Garibov A.A., Vanin A.F. J. Biophysics 2011, v. 56 (2), p.316.

2. Nasibova A.N., Trubitsin B.V., İsmayılova S.M., Fridunbayov İ.Y., Qasımov U.M., Khalilov R.İ. ANAS Reports 2015, v. 2, p. 35.
3. Nasibova A., Khalilov R., Qasumov U., Trubitsin B., Tikhonov A. European Journal of Biotechnology and Bioscience 2016, v. 4 (2), p. 43.
4. Nasibova A.N., Khalilov R.I. Journal of Development Research 2016, v. 6 (3), p. 7071.
5. Kai Chen J.X., Chen X. Nano Research. 2009, v. 2 (4), p. 261.
6. Nasibova A. Advances in Biology & Earth Sciences 2019, v. 4 (3), p.196.
7. Nasibova A.N., Kazimli L.T., Gurbanova M.F., Khalilov R.I. Determination of environmental quality using EPR spectra of grape snails mathematics. Computing. Education - XXVII international conference - Moscow 2020.
8. Gorobets O., Gorobets S., Koralewski M. Journal Nanomedicine 2017, v.12, p. 4371.
9. Khomutov G.B, Potapenkov K.V., Koksharov Y.A., Trubitsin B.V., Tikhonov A.N., Mamedov M.D., Nasibova A.N., Ismailova S.M., Khalilov R.I. Magnetic nanoparticles in biomimetic and biological systems: generation of iron oxide magnetic nanoparticles in DNA complexes, isolated chloroplasts and high plants.XII International Conference on Nanostructured Materials (Nano-2014). 2014, Moscow, Russia.
10. Gorobets S., Gorobets O., Sharay I., Yevzhyk L. Functional Materials 2021, v. 28 (2), p. 315.
11. Thomas R., Park I-K. International Journal of Molecular Sciences 2013, v.14 (8), p.15910.
12. Giouroudi I., Hristoforou E. Journal of Applied Physics 2018, v. 124, p. 030902.
13. Nasibova A.N., Fridunbayov İ.Y., Khalilov R.I. Journal of Biotechnology and Bioscience 2017, v.5 (3), p.14.
14. Khalilov R.I., Nasibova A.N., Gasimov R.J. News of Baku University, 2011, v. 4, p. 55.

THE FUNDAMENTAL PARAMETERS OF THE STAR HD164613(F2II)

ZA SAMEDOV[1,2], ZA ALIYEVA[1], GM HAJIYEVA[2] and UR RUSTAM[2]

[1]Department of Astrophysics, Faculty of Physics, Baku State University, Baku, Azerbaijan
[2]Division of Physics of stellar atmospheres and magnetism, Shamakhi Astrophysical Observatory of ANAS, Baku, Azerbaijan
E-mail: zahir.01@mail.ru zaminaaliyeva@bsu.edu.az

The atmosphere of *HD164613*(*F2II*) giant star of F spectral class was studied using the model and parallax methods. The effective temperature T_{eff} and acceleration of gravity *g* on the surface of the star were determined based on a comparison of the observed and theoretically calculated values of the photometric quantities [c_1], Q, and the equivalent widths of the spectral lines of the hydrogen Balmer series and the using of parallax. Based on the *FeII* lines the microturbulence ξ_t and the metallicity [Fe/H] were determined. In the atmosphere of the star, the metallicity is close to the metallicity of the Sun. This shows that the star we are studying and the Sun are formed from the same metallicity matter. This result is important from the point of view of the chemical evolution theory of the star.

Keywords: F spectral class, giant stars, fundamental parameters of stars
PACS: 95.30.−k, 95.75.Fg, 47.27.Ak

Introduction

In this work, the fundamental parameters of star-effective temperatures T_{eff}, acceleration of gravity g, microturbulent velocity ξ_t and metallicity [Fe/H] were determined. Knowing the effective temperature and acceleration of gravity the models of stellar atmospheres are calculated and on the basis of these models the chemical composition of stars is determined, also the evolutionary parameters of star-mass, radii, luminosity, age are calculated. In astrophysics, microturbulence is considered as a mechanism broadening of the spectral line. The equivalent width of the spectral line depends on microturbulence, therefore, to determine the chemical composition, it is necessary to know the microturbulent velocity. Metallicity is one of the main fundamental parameters of stars. According to the definition of this parameter, it is determined that the star and the Sun are formed the same or different metallicity matter, the problem of the correctness of the provisions of the modern theory of chemical evolution of stars is solved. It should be noted that from the considered star, only the metallicities of the star HD164613(F2II) are determined by other authors [1]. The acceleration of gravity g on the surface of the star, the microturbulence ξ_t, and the metallicity [Fe/H] were determined by us.

Observation material

The spectra of the star were obtained with the spectrograph of the CCD-matrix of the 2-meter telescope of the Shamakhi Astrophysical Observatory of ANAS (R=56000, S/N=150-400) [2].

The spectra were developed by the DECH program. The equivalent widths of spectral lines were measured.The equivalent widths of the lines of FeII atoms used are given in Table1.

Effective temperature and acceleration of gravity

The effective temperature T_{eff} and the acceleration of gravity g of the star were determined by the model and the parallax method. This method is described in detail in [3,4]. The

effective temperature and acceleration of gravity were determined based on a comparison of the observed and theoretically calculated values of the photometric quantities $[c_1]$, Q, and the equivalent widths of the spectral lines of the hydrogen Balmer series and the use of the parallax method. The parallax method is a completely new method and does not depend on models.

The index $[c_1]$ is defined as $[c_1]=c_1-0.2(b-y)$, in the uvby photometric system, and the Q index is defined as Q=(U-B)-0.72(B-V) in the UBV system.

Table 1. List of lines of FeII studied in the spectrum of the star HD164613(F2II)

λ, Å	E_{low}, eV	lg gf	W, mÅ	lg ε
4122,64	2,57	-3,67	103	7,25
4233,16	2,57	-1,88	237	7,4
4258,15	2,69	-3,93	103	7,6
4296,57	2,69	-3,32	148	7,6
4416,82	2,77	-2,57	168	7,28
4446,25	5,93	-2,12	27	7,34
4508,29	2,84	-2,33	183	7,3
4515,33	2,83	-2,5	215	7,26
4520,22	2,79	-3,17	206	7,56
4541,52	2,84	-2,83	87	7,26
4663,70	2,88	-4,42	54	7,6
5100,66	2,79	-4,22	63	7,46
5234,62	3,21	-2,14	177	7,22
5256,93	2,88	-4,33	36	7,27
5276,00	3,19	-2,06	184	7,2
5337,72	3,22	-3,99	58	7,52
5362,86	3,19	-2,84	149	7,47
5425,27	3,19	-3,35	85	7,2
5534,84	3,23	-2,92	86	7,25
6113,32	3,21	-4,2	29	7,25
6147,73	3,87	-2,73	110	7,37
6238,38	3,87	-2,64	117	7,36
6239,95	3,87	-3,44	35	7,2
6247,56	3,87	-2,34	132	7,25
6416,91	3,87	-2,75	106	7,33
6432,67	2,88	-1,11	87	7,26
6456,38	3,89	-2,09	165	7,44
6482,19	6,19	-1,84	41	7,54

These indices are released from the absorption effect in interstellar space. The observation values of the quantities $[c_1]$, Q are determined from the catalog [5]. The theoretically calculated values of the equivalent widths of the Balmer series are given in [6], theoretically calculated values of quantities $[c_1]$, Q in [7]. The parallax of the star was measured in [8]. The diagram defining Teff and logg is shown in Figure 1. Based on this diagram, HD164613(F2II) is

assigned to the star: Teff=6800K, logg=2.6.

Other authors have obtained the value: Teff=6874K [1] for HD164613 star. As can be seen, the value determined in [1] corresponds to the value determined by us.

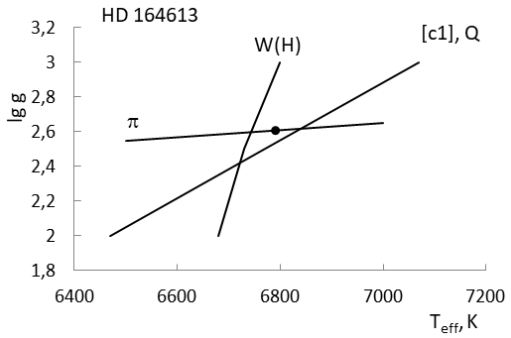

Fig. 1. T_{eff} – lg g diagram

The microturbulent velocity

The determination of the microturbulent velocity by the model method is based on the study of equivalent widths in a wide range of spectral lines of a neutral atom or ion of any element. Several values are given to the microturbulent velocity ξ_t, the equivalent widths W_λ of the spectral lines of the considered element are calculated and compared with the equivalent widths measured from observation. Based on each spectral line, the abundance of the element logε is calculated for different values of the microturbulent velocity ξ_t, the abundance of the element $log\varepsilon$ determines the microturbulent velocity ξ_t in the atmosphere of the studied star according to the graph does not depend on the equivalent widths W_λ of its spectral lines. Note that the deviation from LTT does not affect the $FeII$ line. Therefore, the microturbulent velocity ξ_t and the iron abundance are determined by *FeII* lines in the stellar atmosphere. Only the fairly weak lines are used when determining the microturbulent velocity ξ_t. These lines are formed in deep layers of the atmosphere, these layers are plane-parallel and in the LTT form. The main parameters - effective temperature $T_{eff} = 6800K$ and acceleration of gravity $logg = 2.6$. Knowing the effective temperature and acceleration of gravity of the star, we calculate its model using Kurucz ATLAS 9 program. Based on these models, the iron abundance $log\varepsilon(FeII)$ is calculated by giving different values to the microturbulent velocity ξ_t in the atmosphere of each star. The iron abundance is determined on comparison of the measured from observation and theoretically calculated values of the equivalent width of lines $FeII$. The atomic data of spectral lines are taken from the VALD 3 [*vald.astro.uu.se*].

In Fig. 2 is shown the dependence graph of the abundance $log\varepsilon(Fe)$ determined based on the different equivalent widths of $FeII$ on the equivalent widths W_λ- in the atmospheres of HD164613 star. As can be seen from Fig. 2 there is no correlation between $log\varepsilon(Fe)$ and W_λ for the star HD164613(F2II) at $\xi_t = 3$ km/sec. When analyzing the microturbulence on the basis of *FeII* lines, the abundance of the iron element *logε* (*Fe*) is simultaneously determined: $log\varepsilon(Fe)$=7.36±0.12. The abundance of iron in the sun is logε(Fe) =7.47 [9].

As is shown the metallicity of the studied star and the Sun is practically the same. This

shows that the star is studied and the Sun is formed from the same metallicity matter and this result is important from the point of view of the theory of the chemical evolution of stars.

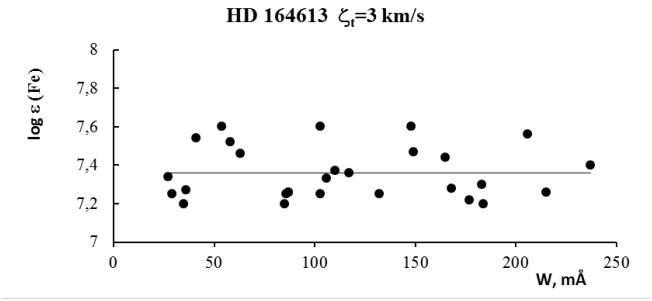

Fig. 2. Determination of microturbulent velocity

Main results

1. The effective temperatures and the accelerations of gravity of F spectral class HD164613 star have been determined by model and parallax methods.

2. The microturbulent velocity has been determined in the atmospheres of the star: $\xi_t = 3$ km/sec.

3. The metallicity was calculated in the atmosphere of the HD164613 star. It has been found that the iron abundance is close to the abundance in the Sun. This shows that the star is studied and the Sun is formed from the same metallicity matter. This result is important from the point of view of the chemical evolution theory of the stars.

Funding

This work was supported by the Sciense Development Foundation under the President of the Republic of Azerbaijan-Grant № EIF-ETL-2020-2(36)-16/03/1-M-03

References

1. Casagrande L., Schoenrich R., Asplund M., Cassisi S., Ramirez I., Melendez J., Bensby T. and Feltzing S. Astronomy and Astrophysics 2011, v. 530A (6-1), p. 138.
2. Mikailov Kh.M, Musaev F.A., Alekberov I.A., Rustamov B.N., and Khalilov O.V. Kinematics and physics of celestial bodies 2020, v. 36 (1), p. 22. DOI: 10.3103/S0884591320010043
3. Lyubimkov L.S., Rachkovskaya T.M., Poklad D.B. Astrophysics 2009, v. 52, p. 217. DOI: 10.1007/s10511-009-9060-x
4. Leonid S. Lyubimkov, David L. Lambert, Sergey I. Rostopchin, Tamara M. Rachkovskaya, and Dmitry B. Poklad, Mon. Not. R. Astron. Soc. 2010, v. 402, p. 1369. DOI:10.1111/j.1365-2966.2009.15979.x
5. Hauck B., Mermilliod M. Astron. Astrophys. Suppl. Ser. 1998, v. 129, p. 431.
6. Kurucz R.L., CD-ROM 13, ATLAS 9 Stellar Atmosphere Programs and 2 km/s grid./ Cambridge, Mass., Smithsonian Astrophys. Obs., 1993.
7. Castelli F., Kurucz R.L., in Piskunov N.E., Weiss W.W., Gray D.F., eds, Proc. IAU Symp. 210, Modelling of Stellar Atmospheres. Poster A20. Astron. Soc. Pac., San Francisco, 2003, p. A20.
8. 2018yCat.1345....0G - CDS/ADC Collection of Electronic Catalogues, 2018, p. 1345.
9. Scott P., Asplund M., Grevesse N., Bergemann M., Jacques Sauval A. Astron. Astrophys. 2015, v. A26, p. 573. http://dx.doi.org/10.1051/0004-6361/201424110

PROPERTIES OF ERYTHROCYTES IN PATIENTS WITH ANGINA IN DIFFERENT PERIODS OF THE 11-YEAR SOLAR CYCLE

S PARSHINA and L TOKAEVA

Saratov State Medical University n.a. V.I. Razumovsky of the Ministry of Health of Russia, Saratov, Russia
E-mail: 1parshinasvetlana@mail.ru

It is known that the short-term and long-term reactions of the human body to fluctuations in solar and geomagnetic activity may differ. For example, on the days of a geomagnetic storm, an increase in the daily frequency of acute myocardial infarction is observed, however, the analysis of the relationships between the daily amount of myocardial infarction and geomagnetic activity over longer periods sometimes yields conflicting results [1]. In the well-known works of Yu.I. Gurfinkel, the phenomenon of erythrocyte sludge (gluing) is noted during geomagnetic disturbances in patients with coronary heart disease [2]. The aim of this work was to assess the functional properties of erythrocytes (aggregation activity and deformability) in a longer period - in different phases of the 11-year solar cycle. In the 23rd 11-year cycle of solar activity, two periods were distinguished. The first half of the 11-year cycle (the period of increased solar activity) was characterized by high values of Wolf numbers (112.0 ± 2.9). The second half of the 11-year cycle (the period of decline in solar activity) was characterized by lower values of the Wolf numbers (62.4 ± 3.9). To estimate solar activity from Wolf numbers, we used data from the Institute for Space Research, Russian Academy of Sciences. We examined 115 patients with secondary unstable angina pectoris: during the period of increased solar activity - 64 people, and in the recession phase - 51 people. The growth phase of solar activity in patients with secondary unstable angina pectoris is characterized by a decrease in the aggregation activity of erythrocytes and an increase in their deformability, which indicates the activation of protective and adaptive mechanisms aimed at maintaining oxygen delivery to tissues. In the phase of decline in solar activity in the 11-year cycle, in comparison with the growth phase, the aggregation capacity of erythrocytes increases and their deformability decreases. Thus, the phase of the decline in solar activity in the 11-year cycle is characterized by a lower activation of the compensatory mechanisms of the blood rheology system. The results obtained indicate that fluctuations in solar activity act not only as activators of the pathogenetic mechanisms of cardiovascular pathology, but also as factors that activate the protective and adaptive reactions of the human body. Probably, evolutionarily, it is these features that ensure the existence of the human body as a component of the biosphere.

Keywords: erythrocytes, solar activity, 11-year solar cycle, secondary unstable angina
PACS: 26.65.+t, 52.72.+V, 97.20.Ec

Introduction

It is known that change in the solar activity (SA) causes variations in the Earth magnetic field. Whereas, this impacts the progress of cardio-vascular diseases including an ischemic heart disease (IHD) [1, 2].

The main factor in the developing of lethal complications in an IHD is the pathology of a haemostasis system [3, 4]. A significant role here plays a rheology blood condition, including functional properties of erythrocytes [5, 6]. In the famous works of Yu.I. Gurfinkel, the phenomenon of erythrocyte sludge (adhesion) is noted during geomagnetic disturbances in patients with coronary heart disease, leading to impaired blood flow in small vessels [7]. The course and outcome of angina pectoris (the most common form of coronary heart disease) and the development of acute myocardial infarction often depend on such microcirculation disorders. Violations of the rheological properties of blood under the influence of heliogeophysical factors are also observed in other vascular diseases [8].

Of particular interest is the change in the properties of erythrocytes under the influence of heliogeomagnetic factors in patients with unstable angina (UA) (which was previously called

the pre-infarction state), since it is external influences that can be a decisive factor contributing to an unfavorable outcome - the development of acute myocardial infarction.

The most common form of unstable angina is secondary unstable angina, which occurs against the background of additional provoking factors - exacerbation of arterial hypertension, anemia, respiratory failure, etc. [9]. Secondary unstable angina is characterized by significant changes in the functional properties of erythrocytes and blood viscosity [6]. However, information about hemorheological disorders in patients with unstable angina pectoris is very contradictory. A number of authors report a decrease in erythrocyte deformability (ED) [10], there is also information about a compensatory increase in ED with an increase in blood viscosity and aggregation of erythrocytes [6], it is also reported about the same ED values with stable angina pectoris, UA and myocardial infarction [11].

It cannot be ruled out that the reason for such contradictory data is that they were obtained in studies carried out in various phases of the 11-year solar cycle, since it has been established that the rheological properties of blood in patients with angina pectoris differ in the growth and decay phases of solar activity in the 11-year cycle (our work). Solar activity activates not only pathological changes leading to disruption of the coagulation system, but also protective and adaptive mechanisms that prevent the occurrence of thrombosis [12].

It is also known that the short-term and long-term reactions of the human body to fluctuations in solar and geomagnetic activity may differ. For example, on the days of a geomagnetic storm, an increase in the daily frequency of acute myocardial infarction is observed, however, the analysis of the relationships between the daily amount of myocardial infarction and geomagnetic activity over longer periods sometimes yields conflicting results [1]. Since it is known about an increase in the aggregation of erythrocytes during the occurrence of geomagnetic disturbances [7], it is of interest to assess the behavior of erythrocytes in a longer period - in the 11-year cycle of solar activity.

Objects and research methods

Solar activity (SA) in the 11-year cycle was estimated by Wolf numbers. In the 23rd SA cycle (from September 1996 to September 2007), we identified two periods. The first half of the 23rd 11-year cycle - the period of SA growth (from the 2nd to the 5th years of the solar cycle, inclusive) - was characterized by high values of Wolf numbers (112.0 ± 2.9). The second half of the 11-year solar cycle - the SA decay period (from the 6th to the 11th years of the solar cycle) - was characterized by lower values of the Wolf numbers (62.4 ± 3.9; $p < 0.05$ with the SA growth period)... To estimate SA by Wolf numbers, data from the Space Research Institute of the Russian Academy of Sciences (Moscow) were used.

A total of 115 patients with secondary unstable angina pectoris (NS) were examined: during the growth of SA - 64 people and in the recession phase - 51 people. The control group consisted of 80 healthy individuals (40 people each during the periods of growth and decline of the 11-year SA cycle).

The functional properties of erythrocytes - the erythrocyte aggregation index (EAI) and the erythrocyte deformability index (EDI) - were studied using an AKR-2 rotary viscometer.

The tissue oxygen delivery index, fibrinogen content and treatment efficacy were also assessed.

We also simulated vascular spasm using a cuff test [13] and studied EAI, EDI, oxygen delivery to tissues under spasm conditions at different periods of the solar cycle.

Statistical processing of the material was carried out using the "MED STAT" computer program, which has a quality certificate from the Ministry of Health of the Russian Federation.

Results

In patients with secondary UA, the functional properties of erythrocytes differed during the periods of growth and decline of the SA. The erythrocyte aggregation index in the SA growth phase was 1.15 ± 0.05 r.u. and was significantly lower than in the decay phase (1.43 ± 0.03 r.u., p <0.05) (table). The deformability of erythrocytes, on the contrary, in the growth phase of SA was increased in comparison with the phase of decline in SA (table). Thus, the SA growth phase of the 11-year solar cycle is characterized by lower aggregation and higher deformability of erythrocytes than the decline phase.

Oxygen delivery to the tissues of patients with secondary NS did not differ in different periods of the solar cycle (table), however, it was reduced in comparison with the indices of healthy individuals both in the growth phase and in the decay phase of the 11-year SA cycle. Thus, at the growth phase, the index of oxygen delivery to tissues in healthy individuals was 11.21 ± 0.35 r.u., which exceeded the same indicator in patients with secondary UA (6.23 ± 0.33 r.u., p <0.05). In the recession phase, the index of oxygen delivery to tissues was also higher in healthy individuals than in patients with secondary UA: 10.01 ± 0.23 r.u. and 6.53 ± 0.19 r.u. respectively (p <0.05).

Table. Functional properties of erythrocytes and oxygen delivery to tissues in patients with secondary unstable angina pectoris in different periods of the 11-year solar cycle

Parameters	SA growth phase	SA decline phase
EAI, r.u.	1,15±0,05 *	1,43±0,03
EDI, r.u.	1,68±0,10*	1,09±0,01
index of oxygen delivery to tissues, r.u.	6,23±0,33	6,53± 0,19

Note: * - the difference between the indicators of the SA growth phase and the SA decline phase is statistically significant, p<0,05.

Under conditions of vascular spasm in the growth phase of SA, the aggregation of erythrocytes did not change (1.15 ± 0.05 and 1.22 ± 0.07 r.u., p> 0.05), as well as their deformability (1.68 ± 0, 10 and 1.68 ± 0.14 r.u., p> 0.05). In the recession phase, the occurrence of vascular spasm also did not significantly affect the functional properties of erythrocytes: aggregation was 1.43 ± 0.03 and 1.43 ± 0.04 r.u. before and after spasm (p> 0.05), deformability - 1.09 ± 0.01 and 1.07 ± 0.01 r.u. before and after spasm (p> 0.05).

Thus, vascular spasm in patients with secondary unstable angina pectoris did not significantly affect the functional properties of erythrocytes either in the growth phase or in the SA decay phase in the 11-year cycle.

However, the index of oxygen delivery to tissues during the growth phase of the SA under conditions of vascular spasm decreased and amounted to 6.23 ± 0.33 r.u. and 5.18 ± 0.35 r.u. before and after spasm, respectively ($p < 0.05$). At the same time, during the SA decay phase, no significant change in the degree of tissue oxygenation under spasm conditions was revealed, the delivery index was 6.53 ± 0.19 r.u. and 6.42 ± 0.22 r.u. before and after spasm, respectively ($p > 0.05$).

Discussing

The increase in SA in the 11-year solar cycle in patients with secondary UA is accompanied by a decrease in the aggregation activity of erythrocytes and an increase in their deformability in comparison with the period of SA decline. These changes are of an adaptive-compensatory nature, since it is known that in patients with secondary unstable angina pectoris, blood viscosity during the period of growth of solar activity is increased in comparison with the period of decline [12].

The viscosity of blood and the functional properties of erythrocytes determine such an important indicator as the degree of oxygen delivery to the tissues. The tissue oxygen delivery index in our study did not differ during periods of growth and decline in solar activity in the 11-year cycle. Thus, the described adaptive mechanisms are effective, since they lead to the maintenance of oxygen supply to tissues during the period of SA growth at a level characteristic of the period of SA decay, despite an increase in blood viscosity.

At the same time, the tension of the adaptive hemorheological mechanisms revealed during the period of increased solar activity, aimed at preventing thrombosis and ischemia, turns out to be insufficient to restore tissue oxygenation to the level of healthy individuals. However, in patients with unstable angina pectoris, this disorder recovers for a very long time, persisting even with stabilization of the state, in patients with chronic forms of ischemic heart disease [14]. The breakdown of compensatory mechanisms with an increase in SA occurs in patients with secondary UA only under conditions of vascular spasm, when there is a further decrease in oxygen delivery to the tissues. During the period of SA decline, vasospasm is not accompanied by a significant change in the oxygen supply of tissues. The results obtained indicate that fluctuations in solar activity act not only as activators of the pathogenetic mechanisms of cardiovascular pathology, but at the same time as factors that activate the protective and adaptive reactions of the human body. Identified in the works of Yu.I. Gurfinkel [5] sludge of erythrocytes during geomagnetic disturbances in patients with ischemic heart disease is a hemorheological response to a sudden flare activity of the Sun, leading to the formation of magnetic storms. At the same time, the adaptive-compensatory mechanisms simply do not have time to develop in such a short period of time. On the contrary, a long period of increase in solar activity in the 11-year solar cycle allows the implementation of protective-compensatory mechanisms aimed at reducing the risk of thrombosis and tissue hypoxia in ischemic heart

disease. Probably, evolutionarily, it is these features that ensure the existence of the human body as a component of the biosphere.

Conclusions

1. The rhythm-setting influence of fluctuations in solar activity on the biosphere in the 11-year solar cycle consists in the activation of not only pathological, but also protective and adaptive mechanisms.

2. A decrease in aggregation and an increase in the deformability of erythrocytes is the leading mechanism for the heliological-biological adaptation of blood properties during the growth phase of the 11-year solar cycle.

3. Short-term reactions of the functional properties of erythrocytes during geomagnetic disturbances and long-term reactions during an increase in solar activity in the 11-year solar cycle do not coincide. During the growth phase, protective and adaptive mechanisms are activated, which evolutionarily ensure the existence of the human body as a component of the biosphere.

References

1. Vencloviene, J., Radisauskas, R., Vaiciulis. V. et al. Int. J. Biometeorol. 2020, v. 64 (7), p. 1207. DOI: 10.1007/s00484-020-01895-z
2. Uskov. V., Uskov. M.; Uskov. V. et.al. Cardio-vascular therapy and prevention 2008, v. 7 (6), Appendix 1, p. 376.
3. Virmani. R., Burke. A.P., Farb. A. Cardiovasc. Pathol. 2001, v. 10, p. 211. DOI: 10.1016/s1054-8807(01)00091-6
4. Ananeva. N., Khrenov. A., Hauzer. Sh. et.al. Thrombosis, haemostasis and rheology 2002, v. 2, p. 10.
5. Korkushko O., Lishnevskaya V. Clinical Haemostaseology and haemorheology in cardio-vascular surgery: Materials of the II Russian Scientific Conference with international participation, Mocsow, 2005, p. 176.
6. Lopatina. N. Features of the clinical course, anticoagulant protection and hemorheology in patients with unstable angina pectoris, PhD's abstract. Saratov 2004, 23 p.
7. Gurfinkel Lu. Coronary artery disease and solar activity, Mocsow, 2004, 170 p.
8. Sazanova. E., Ionova. V., Varahin. Iu. et.al. Thrombosis, haemostasis and rheology 2002, v. 2, p. 41.
9. Hamm C., Braunwald E. APACHE II: A classification of unstable angina revisited. Circulation 2000, v. 102, p. 118. https://doi.org/10.1161/01.CIR.102.1.118
10. Penco M., Romano S., Dagianti A. Clin. Hemorheology and Microcirculation 2000, v. 22 (2), p. 153.
11. Pfafferott C., Moessmer G., Ehrly A.M., Bauersachs R.M. Clin. Hemorheology and Microcirculation 1999, v. 21 (1), p. 35.
12. Parshina S., Tokaeva L., Dolgova E., Samsonov S. Features of hemorheology in healthy people and patients with ischemic heart disease at different periods of solar activity, Saratov, Saratov Resource, 2020, 129 p.
13. Baluda V., Lukianova T., Baluda M. Method for determining the antiaggregatory activity of the human vascular wall, Laboratornoe delo 1983, v. 6, p. 17.
14. Parshina S. Adaptive mechanisms of the hemostasis system and blood rheology in patients with various forms of angina pectoris, MD's abstract, Saratov 2006, 48 p.

BIOEFFECTIVENESS OF GEOMAGNETIC VARIATIONS IN THE PERIOD AND OUT OF THE PERIOD OF CORONAVIRUS INFECTION

S PARSHINA[1] and S SAMSONOV[2]

[1] Saratov State Medical University n.a. V.I. Razumovsky of the Ministry of Health of Russia, Saratov, Russia,
[2] Federal State Budgetary Scientific Institution, Yu.G. Shafer Institute of Cosmophysical Research and Aeronomy of Siberian Branch of the RA of Sciences, Yakutsk Scientific Center of the Siberian Branch of the RA of Sciences, Yakutsk, Russia
E-mail: 1parshinasvetlana@mail.ru

The impact of space weather factors on human health is being studied by many research teams, and in the context of the ongoing epidemic of coronavirus infection, it attracts special attention of modern researchers. The bioeffectiveness of geomagnetic variations in the minimum of the 11-year solar cycle was studied in a long-term 2-month monitoring of the cardiac sensitivity of healthy volunteers during the coronavirus pandemic (2020) and outside the pandemic (2019). Observation groups in 2019 and in 2020 consisted of the same volunteers. The conditions for the occurrence of direct and delayed (by 1-2 days) myocardial reactions were established, taking into account certain values of the Kp-index of geomagnetic disturbance, the dynamic pressure of the solar wind and the Bz-component of the interplanetary magnetic field both during the period of the coronavirus infection pandemic and outside this period.

Keywords: geomagnetic variations, solar wind, interplanetary magnetic field, cardiovascular system, cardiosensitivity, epidemic, Covid-19.
PACS: 91.25.-r, 94.30.Va, 95.85.Sz

Introduction

The bioeffectiveness of space weather factors, as shown in many studies, is realized primarily through the cardiovascular system of the human body [1-3]. Therefore, the vast majority of studies in this area are devoted to the influence of heliogeophysical factors on acute vascular events (myocardial infarction, stroke, hypertensive crises) [1-4]. At the same time, it is known that not all healthy people have cardiosensitivity to space weather factors [4, 5]. Among patients with cardiovascular pathology, the sensitivity to geomagnetic disturbance can also differ significantly and obeys a quasi-logarithmic relationship [6]. Therefore, the issues of studying the cardiosensitivity of healthy individuals are an important stage that makes it possible to assess the heliological-biological connections and the mechanisms of their effect on the cardiovascular system, since this is necessary for further understanding the influence of heliogeomagnetic disturbance on the state of patients with cardiovascular pathology.

It was found that, in addition to geomagnetic disturbances, stable quasi-sinusoidal geomagnetic pulsations Pc1 in middle and low latitudes and irregular geomagnetic pulsations Pi1 with periods of 0.5-3 Hz at subauroral latitudes [7, 8], dynamic pressure and solar velocity wind [2], beta plasma of the solar wind [1], variations of the components of the magnetic field vector [9].

At the same time, a number of authors believe that the influence of geomagnetic disturbance on the mortality rate from cardiovascular pathology is present, but is not significant in comparison with factors of a socio-economic nature [10] (Shumilov). The coronavirus pandemic that emerged in 2020 is a natural model for assessing the impact of changing social and psychological factors on sensitivity to space weather factors. Long-term multi-latitude monitoring "Heliomed-2" to assess the impact of space weather factors on the cardiovascular system [5], which has been ongoing since 2014, allows, thanks to a large database, to carry out a

comparative analysis of the bioeffectiveness of geomagnetic disturbances in different years and periods of the 11-year of the solar cycle, in volunteers at high and middle latitudes, in certain age groups, etc. That is why it was possible to analyze the effect of geomagnetic disturbances on the state of the myocardium and cardiosensitivity of healthy volunteer doctors to geomagnetic variations directly in the first year of the coronavirus pandemic [11].

It is known that in an epidemic, healthy individuals develop a state of psychological maladjustment [12], this is especially true for doctors [13], since their work is characterized by increased emotional and physical stress. Since the psychoemotional state and the functioning of the cardiovascular system are closely related, the study of the bioeffectiveness of geomagnetic disturbances and their effect on the myocardium of healthy individuals during the period of coronavirus infection (covid-19) and beyond this period will also allow us to assess how much the impact of space weather factors is modified by a sudden change social factors and the surrounding psychological environment.

Purpose of the work: to assess the response of the myocardium of healthy volunteers of middle latitudes to variations in the parameters of geomagnetic disturbance, solar wind, Bz-component of the interplanetary magnetic field, radio emission from the Sun with a wavelength of 10.7 cm outside the period and during the epidemic of coronavirus infection.

Objects and methods of the research

For a comparative assessment of the influence of space weather parameters on the state of the cardiovascular system of healthy volunteers during and outside the period of the coronavirus infection epidemic, the results obtained in 2019 (before the onset of the coronavirus infection epidemic) [14] and in 2020 (immediately during epidemic of coronavirus infection) [11]. 2019 and 2020 refer to the period of the minimum of the 11-year 24th solar cycle, therefore, they are characterized by similar heliogeophysical conditions.

The studies were carried out in mid-latitudes (Saratov) and included a simultaneous assessment of the parameters of space weather and the state of the cardiovascular system of volunteers in the same seasonal period - March-April 2019 and March-April 2020. Healthy people took part in the monitoring. volunteer doctors.

Initially, 18 people took part in the monitoring in 2019, 15 people completed the study. (83.3%), in the analysis of primary documentation 4 people. were excluded due to missing more than 3 days during the monitoring period. Thus, the group of 2019 volunteers included in the study consisted of 11 people.

In 2020, initially 21 people participated in the monitoring, but by the end of March, due to the COVID-19 epidemic and the transfer to remote operation, the group was reduced to 6 people. (28.6%) who completed the study. Thus, the 2020 group included 6 healthy volunteers.

For the daily assessment of geomagnetic activity, an indicator of global geomagnetic disturbance was used - the daily Kp-index, which best describes not only strong, but also weak geomagnetic disturbances, since it is based on a quasi-logarithmic measurement scale. Indicators of the daily Kr-index are more than 32 conv. units indicates a significant geomagnetic

disturbance, indicators from 16 to 32 r.u. - about weak disturbance of the Earth geomagnetic field.

The dynamic pressure of the solar wind (Flow Pressure), the Bz-component of the interplanetary magnetic field (IMF), changes in the temperature and density of the Sun by radio emission with a wavelength of 10.7 cm (F 10.7) were also analyzed. The indicated daily solar activity data were downloaded from the NASA website (https://omniweb.gsfc.nasa.gov). The solar wind and interplanetary magnetic field data were obtained by the WIND satellite located at the L1 Lagrange point.

The study of the state of the cardiovascular system of the volunteers was carried out daily in accordance with the algorithm adopted in the multi-latitude monitoring "Heliomed-2" and described in detail in [5]. The coefficient of symmetry of the T wave (TSC) in the phase portrait of the electrocardiogram (ECG) was estimated using an express cardiograph "Fazagraf" (Ukraine).

The assessment of the synchronization of the TSC with heliogeophysical parameters was carried out using a special interactive software package in the Python programming language to analyze the synchronization of the state of the myocardium with the parameters of space weather [15]. Volunteers who were cardiosensitive and cardiosensitive to changes in geomagnet disturbance were identified; persons in whom geomagnetic variations in more than 67% of cases caused a myocardial response according to TSC data were considered cardiosensitive [4, 5].

In addition, a comparative assessment of the state of the myocardium of volunteers was carried out outside the period and during the epidemic of coronavirus infection when analyzing the mean values of TSC for the monitoring period for each group of volunteers.

For the construction of graphs and statistical calculations, the Origin and Medstat programs were used.

The study was conducted in accordance with the ethical standards of the 1964 Declaration of Helsinki and its subsequent amendments. Voluntary informed consent was obtained from all study participants.

Results

The study periods are 2019 and 2020. were characterized by weak geomagnetic disturbance, there were no magnetic storms, the Kp-index fluctuated in 2019 from 2 to 20 r.u., in 2020 - from 4 to 22 r.u. (Fig. 1, Fig. 2). In 2019, geomagnetic variations with amplitude dynamics of 5-10 r.u. occurred every 3-4 days. In 2020, the dynamics of the amplitude of geomagnetic variations, which also occur quite often, amounted to 5-17 r.u. Thus, the periods of March-April, both in 2019 and in 2020, did not fundamentally differ from each other in terms of geomagnetic disturbance, a relatively calm state of the Earth's geomagnetic field was observed.

Volunteer groups 2019 and 2020 were comparable in gender (women) and age (36.0 ± 5.2 years in 2019 and 38.0 ± 6.4 years in 2020, $p > 0.05$). When analyzing the groups and comparing the monitoring participants, it was found that the 2019 group consisted of 54.6% of people who then took part in the 2020 study.

The average CST value in the groups of volunteers was 0.91 ± 0.09 r.u. in 2019 [14] and

0.840 ± 0.007 r.u. in 2020 [11], p> 0.05. Thus, the initial state of the myocardium of the volunteers who took part in monitoring outside the period and during the period of the coronavirus infection epidemic did not differ.

Comparative characteristics of groups of volunteers during and outside the period of the coronavirus infection epidemic are presented in the table.

Table. Characteristics of groups of volunteers and geomagnetic disturbance according to the Kp-index outside the period (2019) and during the epidemic of coronavirus infection (2020)

Characteristics	2019	2020	p
Daily Kp values for the monitoring period	from 2 to 20 r.u.	from 4 to 22 r.u.	
Inclusion in monitoring	18 ind.	21 ind.	
Finished monitoring	81,3%	28,6%	p<0,05
Included in the analysis (no missed days)	11 ind.	6 ind.	
Age	36,0±5,2 years	38,0±6,4 years	p>0,05
Sex	female	female	
Average TSC for the study period	0,91±0,09 r.u.	0,840±0,007 r.u.	p>0,05
Number of TSC measurements	462	246	
Cardiosensitive	9,1%	16,6%	p>0,05
Individual synchronization TSC-Kp	72,7%	75%	p>0,05
Cardiononsensitive	90,9%	83,4%	p>0,05
Delayed TSC-Kp responses	no	yes	

In 2019, out of all volunteers, only 1 person. demonstrated the presence of cardiosensitivity to geomagnetic variations, which is 9.1% of the group size [14]. The TSC-Kp synchronization was 72.7%. The remaining 90.9% of the volunteers in the 2019 group were classified as cardiosensitive, since they showed a CST response to a small amount of geomagnetic variations (from 0% to 41.7%). Thus, outside the period of the epidemic, the myocardium of the overwhelming number of volunteers did not respond to weak fluctuations in the Earth geomagnetic background.

In 2020, only one volunteer (16.6% of the size of the observation group) demonstrated cardiosensitivity to geomagnetic variations, his TSC-Kp synchronization was 75% [11]. The remaining 83.4% of the volunteers were cardiosensitive, with TSC-Kp synchronization occurring in less than 50% of all maxima of geomagnetic disturbance (from 0% to 50%). Thus, even during the epidemic, the myocardium of most volunteers was insensitive to weak geomagnetic variations.

Comparative analysis showed that the cardiosensitivity of volunteers outside the period and during the period of coronavirus infection did not differ (90.9% and 83.4%, respectively, p> 0.05) (table).

We also carried out a comparative analysis of groups of cardiosensitive volunteers outside the period and during the epidemic of coronavirus infection. In Fig. 1 [14] presents the averaged graphs of the TSC in cardiosensitive volunteers and fluctuations in the Kp-index, Bz-component of IMF, dynamic pressure of the solar wind and solar radio emission with a wavelength of 10.7 cm (10-22WM-2Hz-1) in the monitoring of 2019.

In Fig. 1, the abscissa shows the days of monitoring, on the top panel of the figure - changes in the daily values of the TSC (in r.u.), on the second panel from the top - fluctuations in the daily Kp-index (in r.u.), on the third - fluctuations in the IMF Bz component (nT), on the fourth from the top - fluctuations in the dynamic pressure of the solar wind (nPa), on the bottom panel - fluctuations in the solar radio emission with a wavelength of 10.7 cm (10-22WM-2Hz-1). In order to simplify the visualization of possible coincidences of the volunteers' TSC maxima with the maxima of space weather parameters, vertical dashed lines from the TSC maxima are drawn in the figures. Fig. 1 demonstrates that the synchronization of oscillations of the TSC with the Kp-index and with all other studied geophysical indicators in the monitoring of 2019 does not exceed 66.7%, which indicates the lack of sensitivity of the myocardium of volunteers to the studied parameters.

Thus, outside the period of the epidemic (2019), no response of the myocardium of volunteers to fluctuations in the Bz-component of the IMF, the dynamic pressure of the solar wind and radio emission from the Sun with a wavelength of 10.7 cm was revealed.

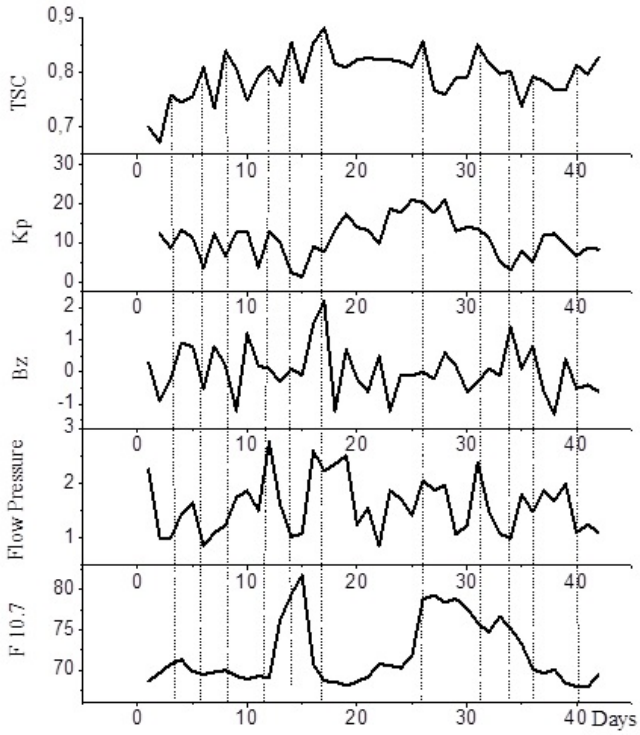

Fig. 1. TSC of a group of cardio-insensitive volunteers when changing parameters of space weather (2019 r.) [14].

In work [11], it was found that during the period of coronavirus infection (2020), cardio-sensitive volunteers have 1-2 days delayed myocardial reactions to changes in geomagnetic disturbance (Fig. 2), but only under certain conditions - with geomagnetic variations with Kp more than 20 r.u. and values of the solar wind dynamic pressure of more than 2.0 nPa in combination with negative values of the IMF Bz component. No connection with meteorological parameters was revealed during the observation period.

In Fig. 2, the abscissa shows the days of monitoring, on the top panel of the figure -

changes in the daily values of the Kp-index (in r.u.), on the second panel from the top - fluctuations in the TSC (in r.u.), on the third panel - fluctuations in the Bz-component IMF (nT), on the fourth from the top - fluctuations in the dynamic pressure of the solar wind (nPa), on the bottom panel - fluctuations in the solar radio emission with a wavelength of 10.7 cm (10-22WM-2Hz-1). In order to simplify the visualization of possible coincidences of the volunteers' CST maxima with the maxima of space weather parameters, vertical dashed lines from the Kp maxima are drawn in the figures.

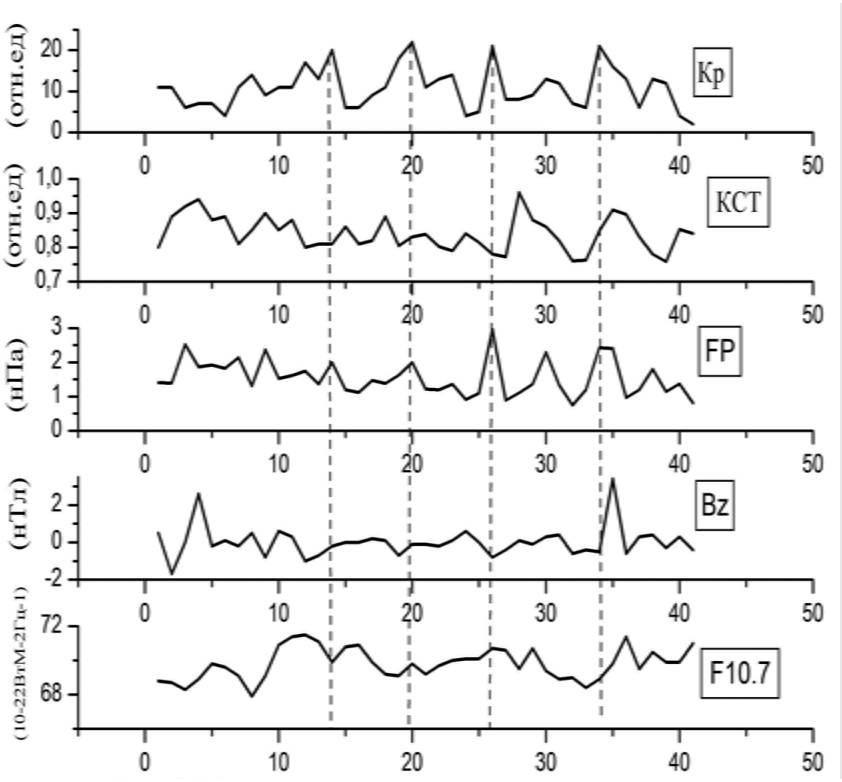

Fig. 2. TSC of a group of cardio-insensitive volunteers when changing parameters of space weather (2020 r.) [11].

Thus, in cardiosensitive volunteers, a certain combination of cosmophysical factors is capable of causing delayed myocardial reactions, which was observed in 2020, during the period of the coronavirus infection epidemic. In 2019, outside the period of the epidemic, no delayed myocardial reactions were recorded. The analysis of heliogeophysical parameters and their combinations for the studied period of 2019 showed that in 2019 geomagnetic variations were characterized by the absence of combinations of «Kp> 20 r.u. + dynamic pressure of the solar wind> 2 nPa + negative value of the IMF Bz component ". First of all, this concerned the values of the Kp-index, since during the monitoring period of 2019 no geomagnetic variations with Kp more than 20 r.u. were observed. Thus, one gets the impression that delayed myocardial reactions in cardiosensitive volunteers at mid-latitudes are associated not with the presence or absence of an epidemic, but with certain combinations of heliogeophysical factors that can induce responses of the cardiovascular system.

Discussing

The ongoing epidemic of coronavirus infection attracts special attention of modern researchers studying the influence of space weather factors on human health [16].

The coronavirus epidemic has significantly changed both social and psychological living conditions. By now, it is already known that the period of the COVID-19 pandemic significantly affects the psychoemotional state of the entire population, and a significant part of medical workers experience severe symptoms of professional burnout, depression, an increased level of anxiety and suicidal tendencies [13]. However, our assumption that the state of the myocardium of doctors in this case should be distinguished by more pronounced functional disorders in comparison with the period before the onset of coronavirus infection has not been confirmed. In our study, the state of the myocardium of volunteers when assessing the ECG in the phase space and analyzing TSC, as the most sensitive parameter to external influences [17], was characterized by the absence of significant differences before the epidemic and during the epidemic.

However, there are 2 factors to consider. Firstly, only healthy young volunteers were included in the survey, without damage to the cardiovascular system, therefore, the reserve capacity of the myocardium was high enough. Secondly, the study was carried out in the first months of the COVID-19 epidemic (March-April 2020), therefore, in such a short period of time, the depletion of myocardial reserves in healthy individuals has not yet occurred, despite the psycho-emotional stress. Perhaps a longer period of psychological stress will lead to a change in the functional state of the heart muscle.

Thus, the absence of differences in the state of the myocardium of volunteers in 2019 and 2020. increases the reliability of our results of a comparative study of cardiosensitivity to geomagnetic variations in the periods under study.

Conditions of geomagnetic disturbance in the studied periods of 2019 and 2020. also practically did not differ according to the data of the daily Kp-index of geomagnetic activity, dynamic pressure of the solar wind, Bz-components of the interplanetary magnetic field and radio emission from the Sun with a wavelength of 10.7 cm. The Earth's geomagnetic field was calm, there were no magnetic storms.

Thus, it became possible to assess the responses of the myocardium of healthy volunteers with the same type of weak variations in geomagnetic disturbance in homogeneous groups of subjects, but in different socio-psychological conditions.

It was found that the myocardium of the overwhelming majority of healthy volunteers was insensitive to weak geomagnetic variations, which did not depend on the onset of the coronavirus infection epidemic. 90.9% of volunteers outside the epidemic period and 83.4% during the epidemic period were cardi-sensitive to changes in geomagnetic disturbance. Thus, the bioeffectiveness of weak geomagnetic variations in the minimum of the 11-year solar cycle in healthy volunteers in mid-latitudes does not depend on the presence or absence of an epidemic of coronavirus infection. The low cardiosensitivity of healthy volunteers, detected at the minimum of the 24th solar cycle, is not modified by the occurrence of an epidemic of coronavirus infection.

In this work, we did not assess the psychoemotional state of the volunteers, however, the

absence of changes in cardiosensitivity to geomagnetic variations during the epidemic suggests that the responses of the cardiovascular system of healthy individuals to changes in space weather factors can be realized through independent mechanisms, and not secondarily due to changes in psychological fortunes of volunteers.

Currently, there is a stable point of view that social conditions have a stronger effect on the human cardiovascular system than the factors of space weather. Thus, in [10], the authors provide data indicating that in the case of cardiovascular diseases, the influence of geomagnetic disturbance on the mortality rate is present, but is not significant compared to factors of a socio-economic nature. Our data indicate that the modification of the influence of space weather factors by social conditions may differ in young healthy individuals and in patients with cardiovascular pathology, which requires further research.

Conclusions

1. The bioefficiency of geomagnetic variations in the minimum of the 11-year solar cycle in healthy volunteers in mid-latitudes does not depend on the presence or absence of a coronavirus epidemic.

2. At the minimum of the 11-year solar cycle, the myocardium of most healthy volunteers of middle latitudes is not sensitive to weak geomagnetic variations, fluctuations in the dynamic pressure of the solar wind, the Bz component of the interplanetary magnetic field, and radio emission from the Sun with a wavelength of 10.7 cm, regardless of the presence or absence of the coronavirus epidemic infections.

3. The presence of 1--2 days delayed myocardial responses to changes in geomagnetic disturbance in cardiosensitive volunteers is primarily associated with the peculiarities of the combination of space weather factors (combination of daily Kp values> 20 r.u., solar wind dynamic pressure> 2.0 nPa, negative value of the Bz-component of the interplanetary magnetic field), and not with the period of the epidemic.

4. Natural long-term mechanisms of synchronization of the functional state of the cardiovascular system of healthy individuals with space weather factors in the 11-year cycle of solar activity have a stronger effect in comparison with short-term, suddenly emerging social and psychological factors.

5. The lack of difference in myocardial responses to geomagnetic variations during a pandemic and outside a pandemic suggests that in healthy individuals the effect of space weather factors on the cardiovascular system is independent and not mediated through the psychoemotional state of a person.

References

1. Caswell. J., Carniello. T.,; Murugan. N. Int. J. Biometeorol. 2016; v. 60 (1), p. 9. DOI: 10.1007/s00484-015-1000-3
2. Vencloviene. J., Radisauskas. R., Vaiciulis. V. et al. Int. J.Biometeorol. 2020, v. 64 (7), p. 1207. DOI:10.1007/s00484-020-01895-z
3. Feigin. V. et al. Stroke 2014, v. 45, p. 1639. https://doi.org/10.1161/STROKEAHA.113.004577
4. Samsonov. S. Space weather parameters and the state of the human cardiovascular system: group and

population effects. In the book: Biotropic effects of space weather (based on the materials of the Russian-Ukrainian monitoring "Heliomed" 2003-2010). Ed. M.V. Ragulskaya. Moscow., Kiev – St.Petersburg: BBM, 2010, p. 69-90.
5. Parshina S., Samsonov S., Afanasyeva. T. et al. Biophysics 2020, v. 65 (6), p. 1161.
6. Samsonov S., Manykina V. Parshina. S. Electronic scientific and educational bulletin Health and education in the XXI century 2014, v. 16 (12), p. 5.
7. Kleimenova. N. et al. Biofizika 2007, v. 6, p. 1112. DOI:10.1134/S0006350907060152
8. Samsonov S., Kleimenova N., Kozyreva P., Petrova. Izvestiya Atmospheric and oceanic physics 2014, v. 50 (7), p. 719. DOI:10.1134/S0001433814040057
9. Bardak A., Borodin A., Kaliuzhin V., Kolesnik A. Tomsk State University Bulletin 2003, v. 278, p. 134.
10. Shumilov O., Kasatkina E., Cleimenova N. et.al. Geophysical Processes and the Biosphere 2020, v.19 (2), p. 45. https://doi.org/10.1134/S000143382008006X
11. Samsonov S., Parshina S. Izvestiya Atmospheric and Oceanic Physics 2021, v. 57 (8), p. 926–936.
12. Kisely S., Warren. N., McMahon L. et al. BMJ 2020. https://www.bmj.com/content/369/bmj.m1642 doi:10.1136/bmj.m1642.
13. Petrikov S., Holmogorova A., Suroegina A. et al. Counseling psychology and psychotherapy 2020, v. 28 (2), p. 8. DOI: https://doi.org/10.17759/cpp.2020280202.
14. Samsonov S., Parshina S. IOP Conf. Series: Earth and Environmental Science 2021, v. 853, p. 012025. DOI:10.1088/1755-1315/853/1/012025
15. Petrova P., Molchanov V., Samsonov S. et.al. The program for the analysis and visualization of the study data of the synchronization of the parameters of the repolarization of the myocardium of the ventricles (according to the symmetry coefficient of the T wave of the electrocardiogram) with the parameters of space weather, Certificate of state registration of a computer program 2021. № 2021610105.
16. Ragulskaya. M.; Tekutskaya. E. Solar activity global minimum and genogeographic features of the COVID-19 pandemic, 2021, IOP CS: EES. 853 012002 doi:10.1088/1755-1315/853/1/012002.
17. Vishnevskii V., Fai`nzil`berg L., Ragul`skaia M. Biomedical technologies and electronics 2003, v. 3, p. 3.

GLOBAL AND REGIONAL BIOEFFICIENCY OF SPACE WEATHER FACTORS IN SUBARCTIC AND MIDDLE LATITUDES

S SAMSONOV

Federal State Budgetary Scientific Institution, Yu.G. Shafer Institute of Cosmophysical Research and Aeronomy of Siberian Branch of the Russian Academy of Sciences, Yakutsk, Russia
E-mail: s_samsonov@ikfia.ysn.ru

The connection between geomagnetic disturbances and cardiovascular events has been actively studied both in the past and at the present time. It is known that the same geomagnetic disturbances cause different responses of the cardiovascular system of volunteers, depending on the region of residence. Based on the results of synchronous multi-latitude monitoring in subarctic (Yakutsk) and middle (Saratov) latitudes, the myocardium response to changes in space weather was estimated according to the T-wave coefficient in the ECG phase portrait. Measurements had been carried out daily for 2 months. The groups of volunteers in different regions were comparable in age and gender. The synchronization of the dynamics of the T-wave coefficient with the dynamics of the Kp-index of geomagnetic disturbance was analyzed. Two groups of geomagnetic disturbances were distinguished: Group 1 - disturbances to which the reaction of the myocardium was of the same type in subarctic and middle latitudes; Group 2 - disturbances that did not cause the same type of myocardial reaction in the surveyed volunteers from different regions. The differences in geomagnetic disturbances in groups 1 and 2 are analyzed for a set of indicators, including the values of the solar wind parameters, the Bz-component of the interplanetary magnetic field, the Kp-index of geomagnetic disturbance, and middle latitudes.

Keywords: geomagnetic variations, bioeffectiveness, cardiovascular system, arctic and subarctic latitudes
PACS: 07.87.+v, 91.85.-r, 07.57.-c

Introduction

The relevance of studying the relationship between geomagnetic disturbance and cardiovascular events remains unchanged, since both previous and the most recent studies demonstrate the influence of space weather factors on the occurrence of strokes, myocardial infarctions and the number of suicides [1-4]. A meta-analysis of 6 large population studies in Europe and Australia suggests that geomagnetic storms can trigger stroke [1]. At high latitudes, when assessing the 11-year cycle of solar activity, a relationship was established between the frequency of suicides and mortality from myocardial infarction with geomagnetic disturbance [4]. The risk of developing acute myocardial infarction in the Baltics during the days of a geomagnetic storm is associated with the western phase of the quasi-two-year cycle, the dynamic pressure of the solar wind and the speed of the solar wind [2]. Mortality from hypertension in Canada (as well as sudden infant death syndrome) depends on the beta plasma of the solar wind [3]. Thus, the global mechanisms of the impact of space weather on the cardiovascular system are beyond doubt, while the issue of regional sensitivity to space weather factors remains insufficiently studied.

There is evidence that volunteers of the same type in high and middle latitudes respond only to 43% of geomagnetic disturbances, the bioeffectiveness of the remaining 57% of geomagnetic disturbances is different for volunteers, depending on the region of residence [5]. Currently, there are no convincing explanations for such a phenomenon; a few published works on this topic indicate that the regional sensitivity to heliogeophysical factors and, as a consequence, the bioeffectiveness of geomagnetic variations at different latitudes, may be

associated with geomagnetic pulsations [6]. The comparative bioeffectiveness of geomagnetic variations in subarctic and middle latitudes has not been previously studied.

The aim of our work was to study the features of geomagnetic variations in subarctic and middle latitudes, causing and not causing the same type of myocardial responses in healthy volunteers in subarctic and middle latitudes at the maximum of the 11-year solar cycle.

Objects and methods

At the maximum of the 24th 11-year solar cycle (2014) for 60 days (March-April), synchronous monitoring of space weather parameters and indicators of the cardiovascular system of healthy volunteers was carried out in the subarctic (Yakutsk) and middle (Saratov) latitudes. The complex of analyzed heliogeophysical parameters included the daily Kp-index of geomagnetic disturbance, the speed, density and dynamic pressure of the solar wind, the Bz-component of the interplanetary magnetic field (Bz IMF).

Groups of healthy volunteers in subarctic latitudes included 15 people, in middle latitudes - 31 people. The groups were matched for age and gender.

The study of the cardiovascular system of the volunteers included an assessment of the symmetry coefficient of the T wave (TSC, r.u.) in the phase portrait of an electrocardiogram (ECG) using an express cardiograph "Fazagraf" [7]. TSC reflects the processes of repolarization of the ventricular myocardium and of all ECG parameters is the most sensitive in assessing the effect of geomagnetic disturbance on the heart muscle [8, 9]. The measurement of the phase portrait of the ECG of the volunteers was carried out daily for 60 days of multi-latitude monitoring; blood pressure was also assessed.

Based on the results obtained, cardiosensitive volunteers were identified in each of the groups (in the subarctic and middle latitudes) [5, 9]. At the next stage, for each region, the synchronization of space weather parameters with TSC in a group of cardiosensitive volunteers was assessed using a data processing program created to solve the project's problems [10]. Variations of geomagnetic disturbance, causing the response of the myocardium of volunteers according to the TSC data, were considered bioeffective.

For the construction of graphs and statistical processing of the material, the Origin and Medstat programs were used.

Results

During the period under study, geomagnetic activity was characterized by variations in the daily Kp-index with an amplitude of 2 to 20 r.u., there were only 2 maximum Kp with an amplitude of more than 20 r.u. In total, 7 maxima of the Kp-index were recorded (Fig.).

The synchronization of geomagnetic variations and the state of the myocardium of volunteers in the subarctic and middle latitudes is shown in the figure: the upper graph is the dynamics of the TSC during 60 days of monitoring in the group of volunteers in the subarctic latitudes, the middle graph is the dynamics of the TSC in the group of volunteers in the middle latitudes, the lower graph is the dynamics of the Kp -index for the same period. Dashed lines show the maxima of the Kp-index and the corresponding TSC values in groups of volunteers

in subarctic and middle latitudes.

In subarctic latitudes, the TSC-Kp synchronization was noted at the 1st, 2nd, and 5th maxima of the Kp-index (Kp1, Kp2, Kp5). The volunteers reacted late to the 3rd, 4th and 7th maximums of Kp (Kp3, Kp4, Kp7), the response maximum of the TSC appeared on Kp3 and Kp4 the next day, on Kp7 - after 1 day. At the 6th maximum Kp, there was no response from the TSC of the volunteers. Thus, at 42.9% of the maxima of geomagnetic variations, the response of the myocardium occurred directly on the day of geomagnetic variation, by 42.9% - 1-2 days later, by 14.2% - it was absent.

The data obtained indicate that in subarctic latitudes there are two variants of the response of the myocardium of volunteers to changes in geomagnetic disturbance: direct - on the day of geomagnetic variation and delayed - 1-2 days later. The response of the myocardium was caused by 6 geomagnetic variations out of 7, that is, 85.7% of geomagnetic variations were bioeffective, of which 50% cause direct responses of the cardiovascular system and 50% - delayed ones.

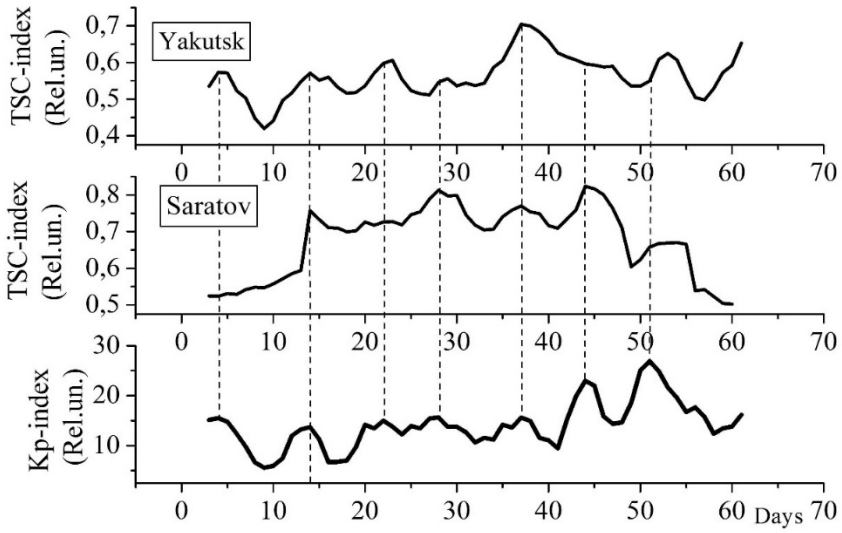

Fig. 1. Synchronization of the Kp-index of geomagnetic disturbance and the state of the myocardium according to the TSC data in the phase portrait of an ECG in volunteer of subarctic and middle latitudes.

In middle latitudes, the TSC-Kp synchronization was noted in the 2nd, 4th and 5th, 6th, 7th maxima of the Kp-index and was absent in the 1st and 3rd maxima of the Kp-index. There were no delayed reactions. Thus, in the middle latitudes, 71.4% of geomagnetic variations were bioeffective.

The myocardium of volunteers from subarctic and middle latitudes reacted in the same way (on the day of geomagnetic variation) to the 2nd and 5th maxima of Kp, that is, to 28.6% of geomagnetic variations. The remaining 5 Kp maxima, that is, 71.4% of geomagnetic variations, had regional features of the volunteers' myocardial responses associated with the latitude of residence.

Thus, at the 1st maximum of the Kp-index (Kp1) in subarctic latitudes, a direct TSC reaction was noted, in the middle latitudes there was no TSC response. Kp3 did not evoke a TSC

response in middle latitudes, and volunteers in subarctic latitudes reacted, but with a delay of 1 day. At Kp4 in subarctic latitudes, the TSC reaction also occurred with a delay of 1 day, but in the middle latitudes the volunteers reacted with the maximum TSC directly on the day of the geomagnetic variation. Kp6 elicited a myocardial response from volunteers in middle latitudes on the day of geomagnetic variation, but did not elicit a TSC response in volunteers from subarctic latitudes. Kp7 evokes a TSC response in mid-latitudes on the day of geomagnetic variation, in subarctic latitudes - with a 2-day delay. The difference in myocardial responses to Kp1-7 in subarctic and middle latitudes is presented in the table.

Table. Space weather parameters and cardiovascular responses in volunteers in subarctic and mid-latitudes

№ of the Kp maximum in the 60 days monitoring	**Kp (r.u.)**	**Solar wind**			**Bz-component IMF (nT)**	**Myocard response TSC-Kp**		**Types of response in subarctic and middle latitudes**
		velocity (km/sec)	**density (p/cm³)**	**pressure (nPa)**		**subarctic latitudes**	**middle latitudes**	
1	16	370	5.2	1.36	0.6	есть	нет	regional
2	14	451	2.4	0.97	0.7	есть	есть	global
3	15	433	4.5	1.62	3.3	есть с задержкой	нет	regional
4	16	426	2.6	0.91	0.5	есть с задержкой	есть	regional
5	17	380	6.2	2.21	2.1	есть	есть	global
6	24	351	6.3	1.57	-3.3	нет	есть	regional
7	28	590	6.6	5.03	2.7	есть с задержкой	есть	regional

Thus, only the direct responses of the myocardium on the day of maximum geomagnetic disturbance are of the same type for subarctic and middle latitudes. Regional features of the response of the cardiovascular system in volunteers of subarctic latitudes are characterized by the presence of delayed myocardial responses that occur 1-2 days later after the maximum of geomagnetic variation.

We analyzed the values of the Kp-index of geomagnetic disturbance, solar wind parameters and the Bz-component of the IMF on days of geomagnetic variations that cause and do not cause the same type of myocardial responses in volunteers in subarctic and middle latitudes (table). It was found that the values of the Kp-index, velocity, density and dynamic pressure of the solar wind, the Bz-component of the IMF in the group of geomagnetic variations causing global effects and in the group causing regionally determined effects do not have significant differences ($p > 0.05$)... It was also not possible to identify differences in the Kp-index, solar wind parameters and Bz-component of the IMF of geomagnetic variations that cause immediate and delayed reactions of the myocardium of volunteers in subarctic latitudes ($p > 0.05$). Thus, the regionally determined bioeffectiveness of geomagnetic variations in middle and subarctic latitudes is not related to the Kp-index of geomagnetic disturbance, the solar wind, and the Bz-component of the IMF.

It cannot be ruled out that regional effects of geomagnetic disturbance may be associated

with Pc1 pulsations at mid-latitudes or with the participation of Pi1 pulsations at high latitudes, since there is information about the participation of Pc1 and Pi1 pulsations in biotropic effects of space weather [6, 11]. In addition, meteorological factors can also affect the regional bioefficiency of geomagnetic disturbances, since a number of authors believe that the degree of influence of geomagnetic activity depends on the state of the earth's weather [12]. And, finally, the sensitivity to geomagnetic disturbances can be different depending on the initial state of the human cardiovascular system. Investigation of these reasons will probably make it possible to clarify the reasons for the regional bioeffectiveness of geomagnetic variations in subarctic and middle latitudes.

Conclusions

The bioefficiency of geomagnetic variations at the maximum of the 24th solar cycle is 85.7% for healthy volunteers in subarctic latitudes and 71.4% for volunteers in mid-latitudes. Similarly, the myocardium of volunteers from subarctic and middle latitudes reacts only to 28.6% of geomagnetic variations, this is manifested by the direct reactions of TSC on the day of geomagnetic variation. Regional features are manifested in response to the remaining 71.4% of geomagnetic variations and are not associated with the Kp-index of geomagnetic disturbance, solar wind parameters and the Bz-component of the interplanetary magnetic field. In the subarctic region, a feature of the response of the cardiovascular system to geomagnetic disturbance is the presence of myocardial reactions delayed by 1–2 days. Delayed reactions occur in 50% of all bioeffective impacts in the subarctic region.

References

1. Feigin V. et al. Stroke 2014. v. 45, p. 1639.
2. Vencloviene J., Radisauskas R., Vaiciulis. V. et al. Int. J. Biometeorol. 2020. v. 64 (7), p. 1207. DOI: 10.1007/s00484-020-01895-z
3. Caswell J., Carniello T., Murugan N. Int. J. Biometeorol. 2016. v. 60 (1), p. 9. DOI: 10.1007/s00484-015-1000-3
4. Shumilov O., Kasatkina E. Geophysical processes and biosphere 2020. v.19 (2), p. 45.
5. Parshina S., Samsonov S., Afanasyeva T. et al. Biophysics 2020. v. 65 (6), p. 1161.
6. Samsonov S., Kleimenova N., Kozyreva O. Izvestiya Atmospheric and oceanic physics 2014. v. 50 (7), p. 719. DOI:10.1134/S0001433814040057
7. Fainzilberg L. Information Technologies for Processing Signals of Complex Forms, Theory and practice. Kiev: Naukova Dumka 2008, 333 p.
8. Vishnevskii V., Fainzilberg L., Ragulskaia M. Biomedical technologies and radioelectronics 2003, v. 3, p.3.
9. Samsonov S. Space weather parameters and the state of the human cardiovascular system: group and population effects, In the book: Biotropic effects of space weather (based on the materials of the Russian-Ukrainian monitoring "Heliomed" 2003-2010). Ed. M.V. Ragulskaya. Moscow., Kiev – St.Petersburg: BBM, 2010, pp. 69-90.
10. Petrova P., Molchanov V., Samsonov. S. et.al. The program for the analysis and visualization of the study data of the synchronization of the parameters of the repolarization of the myocardium of the ventricles (according to the symmetry coefficient of the T wave of the electrocardiogram) with the parameters of space weather, Certificate of state registration of a computer program 2021. № 2021610105.
11. Kleimenova N., et al. Biofizika 2007, 6, p. 1112. DOI:10.1134/S0006350907060152
12. Gurfinkel. Y., Sasonko. M, Ozheredov. V,, Breus. T. Biophysics 2018, 63 (2), p. 299.

SYNTHESIS OF SNS NANOCRYSTALS AND SNS/CDZNS STRUCTURES

SA JAHANGIROVA

Baku State University, Baku, Azerbaijan
E-mail: sona_aliqizi@mail.ru

Nanocrystalline SnS powder has been prepared using tin chloride ($SnCl_2$) as a tin ion source and sodium sulfide ($Na_2S_2O_3$) as a sulfur ion source on glass substrate by electrochemical deposition at room temperature. The detailed structural and optical properties confirmed the orthorhombic SnS structure and a strongly blue shifted direct band gap (1.74-1.76 eV), for synthesized nanoparticles, after heath treatment. The advanced technology in the electrochemical deposition of thin films of SnS on the surface conductivity CdZnS allowed for the first time a photo converter heterojunctions CdZnS/SnS, showing the possibility to realize high conversion efficiency of solar radiation on the substrates SnS large areas.

Keywords: nanocrystalline powder, electrochemical deposition, heterojunctions, solar cell
PACS: 61.46.+w, 61.72.Vv, 72.10.Di

Introduction

Quantum confinement effect in semiconductor nanomaterials has been of special interest during the last decades. Quantum confined semiconductor nanocrystals, which exhibit properties different from bulk materials, are a new class of materials that hold considerable attention for numerous applications in the field of optoelectronics [1-3]. Modification of molecular design and morphology of such nanostructures provides a powerful approach to control their electronic and optical properties. Among the extensively studied IV-VI semiconductor materials, tin sulfide is very important narrow gap material because of its low toxicity and wide applications as an absorber layer in solar cells, near infrared materials, holographic recording media and solar control devices [4-6]. The optical properties of SnS vary depending on the synthesizing or fabrication method. In order to obtain nanostructured SnS, the following methods are used: spray pyrolysis of the water solution, chemical vapor deposition, electrochemical deposition, microwave assisted synthesis, mild solution route, modified solution dispersion method, solvothermal process, successive ionic layer adsorption and reaction, hydrothermal synthesis, and molecular beam epitaxy [7-9]. SnS is an important optoelectronic material. Chemical bath deposition can be used to deposit SnS films. SnS can be deposited in superstrate or substrate configurations, but the best efficiencies were obtained in the substrate configuration where it is possible to separate between absorber deposition and junction formation. [10-12].

In this paper we report the preparation, morphological, optical and structural properties of SnS nanocrystals and heterojunction CdZnS/SnS by electrochemical deposition.

Experimental details

Depositions were carried out potentiostatically from a de-aerated aqueous solution containing 0.2M solution of tin chloride ($SnCl_4$), $Na_2S_2O_3$ (0.2M). and PVA-400. To optimize the stoichiometry of the deposit, electrochemical baths with different compositions, obtained mixing different volumes of the above-mentioned solutions, were tested. The final pH was about 5, it was obtained adding lactic acid and NaOH (10M). Electrodeposition was performed

at a potential of -1.05V vs. saturated calomel electrode (SCE); electrochemical experiments were performed using a PAR potentiostat/galvanostat (model PARSTAT 2273). The role of PVA is to stabilize the nanostructures preventing them from coagulation.

For the manufacture of photosensitive heterostructures CdZnS/SnS in the process of film deposition was used CdZnS 0.05M solution of cadmium chloride $CdCl_2$, 0.05M solution of zinc chloride $ZnCl_2$, 0.15M solution of $Na_2S_2O_3$, 12M ammonium hydroxide NH_4OH solution and distilled water. Dosed application of the working solution was carried out at room temperature on a pre-prepared surface of the substrate. The substrates used in film-coated ITO glass plate and the plate with the film CdZnS thickness 0,2 microns.

Morphological analyses were performed by scanning electrode microscopy (SEM), (model QUANTA 200F). Atom Force microscopy (AFM) images of the sample were taken on a Philips performing at an accelerating voltage of 100 kV. Films were also characterized by XRD analysis, using an Ital. Structures (APD2000) diffractometer having the Cu Kα radiation (λ= 0.154nm). A computerized 619 Electrometer/Multimeter was used to measure the current-voltage (I-V) characteristics of the resulting solar cells using a solar simulator with light intensity corrected to a power density of 100 $mW \cdot cm^{-2}$ (AM1.5). The results of the materials characterisation and device assessment are presented and discussed in the next section.

Results and discussion

Cyclic voltammetry (CV) was carried out in a three-electrodesystem to evaluate the catalytic activities of the as prepared SnS film. Fig. 1a shows the cyclic voltammograms of Pt and SnS CEs. The Epp values for SnS and Pt CE are 607 and 456 mV, respectively, which indicates that CoSP made SnS is not a prominent electrocatalyst for reduction of I3. The cyclic voltammetry did notchange and shows very stable anodic and cathodic peak current densities as shown in Fig. 1b.

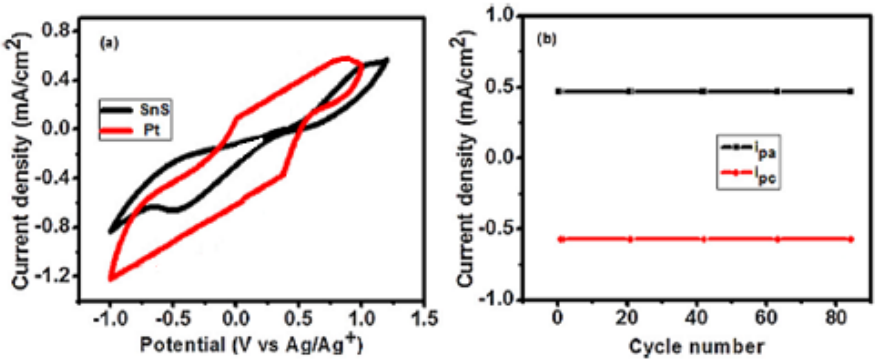

Fig. 1. (a) CV curves of the triiodide/iodide redox couple for SnS and Pt electrode at a scan rate of 100 mV/s, (b) the relation of anodic (ipa) and cathodic (ipc) peak current densities vs. number of cycles.

The morphology of the as-prepared products was studied by SEM. The SEM image (Figure 2) show that the product is consisting of very small spherical SnS nanocrystallites aggregated in the form of polydispersive nanoclusters with sizes smaller than 100 nm.

In order to further elucidate the morphology and the size of nanoparticles, Atom Force Microscopy (AFM) image was taken and is shown in Figure 3. Comparison of SEM and AFM

images confirms the formation of very small spherical SnS nanoparticles which most of them aggregated together in the form of polydispersive nanoclusters.

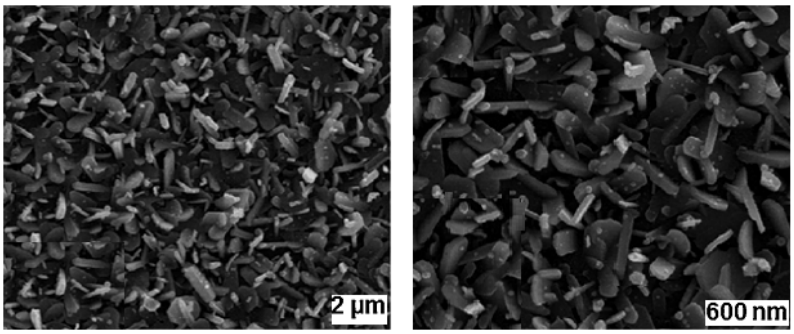

Fig. 2. SEM image of the as-prepared SnS nanocrystals

The detection and measurement of the nanoparticles (segmentation) on this type of samples is difficult because thickness changes locally, and diffraction from different crystal orientations introduce large contrast variations. Secondly, the SnS nanoparticles were segmented using a semiautomatic procedure which combines interactive segmentation with adaptative thresholding, obtaining an mean particle diameter of 3.2 nm with a standard deviation of 1.9 nm.

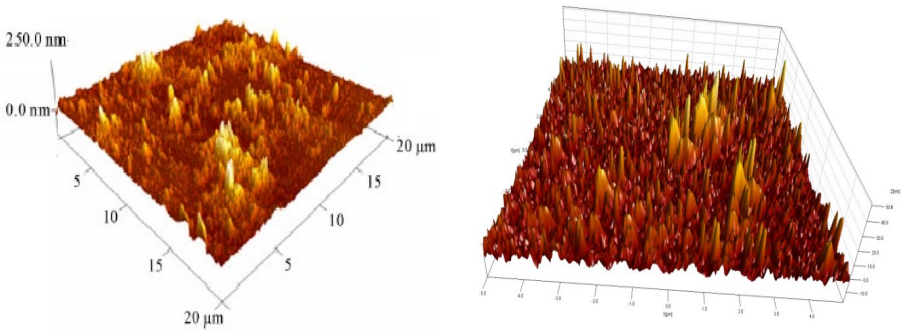

Fig. 3. Typical AFM image of SnS and CdZnS nanocrystals

Figure 4 show the XRD pattern of as-prepared SnS nanocrystals. Several peaks corresponding to diffraction of orthorhombic SnS appear clearly in the figure. All the diffraction peaks are indexed to theorthorhombic crystalline phase of SnS (JCPDS file No. (39-354)). It is observed that the peak (1 0 1) is strongly dominating indicatinga preferred orientation along this direction.

No other phases of SnS were found from the XRD analysis. The sharp and narrow (1 0 1) peaks indicate that as-grown nanostructures are highly crystallineand consist of only a single phase of SnS. The peaks observed at 2θvalues of 32.83, 45.86, and 54.92 were found to match with reflections from (200), (220), and (311) crystallographic planes of orthorhombic phase of SnS respectivitely. The average crystalline size is estimated by Sherer formula: $D = K\lambda/\beta\cos\theta$. Where λ is the wavelength of CuKα radiation (0.154 nm), k = 0.9 is the shape factor, θ is the Bragg angle and β is the experimental full-width at half maximum on the respective diffraction peak. The micro strain ε can be obtained by using the relation $\varepsilon = \beta\cos\theta/4$. From the below

table shows the average crystalline size of different samples is about 32.0 nm.

Fig. 5a shows the absorption spectrum of SnS thin films. In order to know the band gap energy of SnS films,the optical absorption measurements were done in the wavelength range of 400–1300 nm. The absorption of SnS films starts at wave-length of ~989 nm and reaches a maximum value at a wavelengthof 400 nm. Fig. 5b shows $(\alpha hv)^2$ versus $(\mathrm{h}\nu)$ with a straight line fitting,indicating a direct band gap of 1.70 eV.

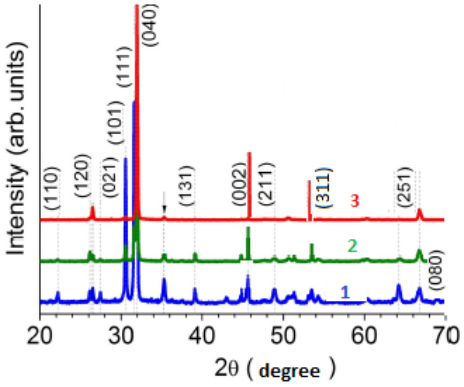

Fig. 4. XRD pattern of the as-prepared SnS nanocrystals, before (1) and after HT at temperatures 300^{0}C (2) and 350^{0}C (3).

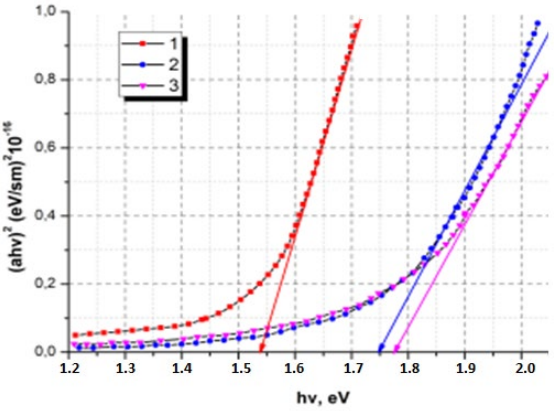

Fig. 5. Plot of $(\alpha hv)^2$ versus (hv) and UV-visible absorption spectrum of the as-prepared SnS nanocrystals before (1) and after HT at temperatures 300^{0}C (2) and 350^{0}C (3).

These values were used to determine absorption coefficient α. The curve has a good straight line fit with higher energy range above the absorption edge, indicating a direct optical transition edge. Based on Figure 5, the direct energy gap of the sample has been calculated as 1.74-1,76 eV which is blue shifted in comparison the bulk band gap.

The residual resistance of the obtained heterojunctions n-CdZnS/SnS usually reaches $R_0 \approx 10^4$-10^5 ohms at a temperature T = 300K, and is mainly determined by the electrical properties of the substrate CdZnS. The current-voltage characteristics I (U) in the structures CdZnS / SnS, are shown in Fig. 6a. Reverse branch of the current-voltage characteristics of structures obey the power law I α Um with an exponent of m ≈ 1 to voltages U 2B, which is typical for tunneling of charge carriers, or characteristic of currents limited by space charge, in the saturation velocity of carriers. The growth of the reverse current is observed in the investigated heterojunctions CdZnS/SnS with increasing bias voltage can also be attributed to imperfections in the periphery. Typical for the obtained heterojunctions A load characteristic structure CdZnS/SnS before and after heat treatment is shown in Figure 6b.

CdZnS/SnS spectral dependence of the relative quantum efficiency of photoconversion η(hv), representing the ratio of short-circuit to the number of incident photons, shown in Fig. 7. These spectra for the structures obtained were similar, indicating a high local homogeneity of the substrates used.

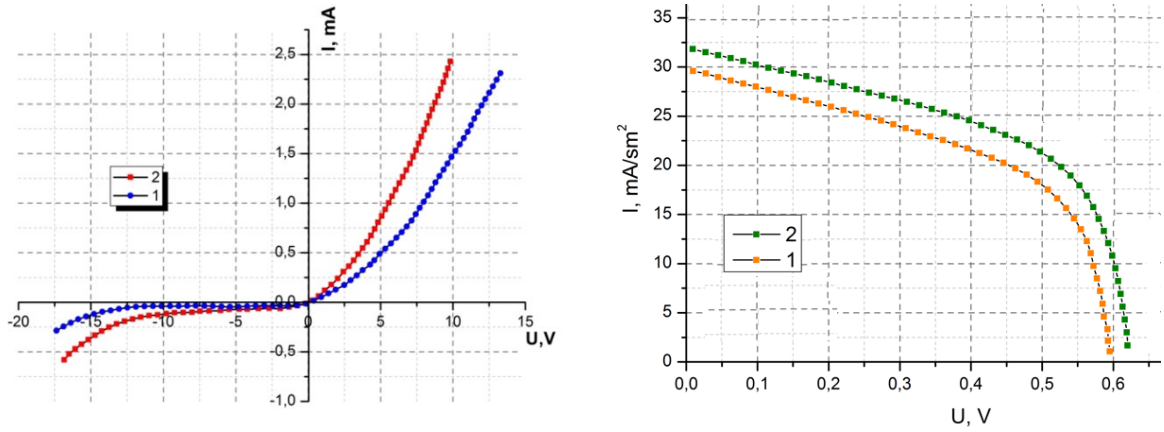

Fig. 6. Static current-voltage characteristic of the heterojunction CdZnS/SnS.(a) and Load characteristic structures (b) CdZnS/SnS before (1) and after (2) heat treatment at temperatures 200^{0}S for 10 min.

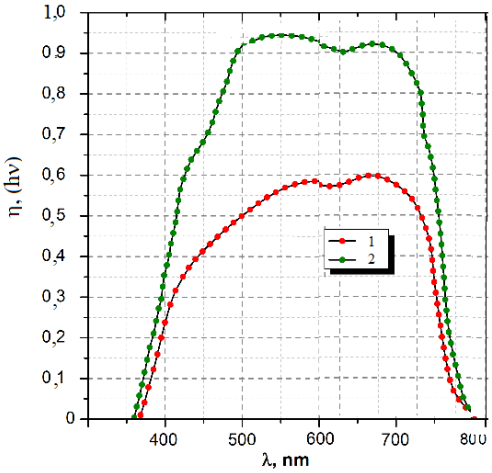

Fig. 7. CdZnS/SnS spectral dependence of the relative quantum efficiency of photoconversion η(hv).

The sharp increase in long-wave η in such heterojunctions in their coverage of the film CdZnS (d ≈ 100 nm) occurs in a relatively narrow spectral range hv =1.74-1.75 eV. The value of η reaches a maximum near hv ≈ 1.75 eV, which agrees with the energy of direct interband transitions in SnS. It is important to note that the resulting structures CdZnS/SnS, photosensitivity in a wide range of photon energies in their coverage of the film CdZnS maintained at a high level. This fact indicates that the developed method of applying thin films of SnS on the surface of the substrate CdZnS provides enough advanced heterojunction. Reproducibly observed decline in η (hv) in the obtained heterojunctions CdZnS/SnS, begins at hv ≥ 2.45 eV, and the spectral contour observed the decline in the η (hv) was similar to the spectral dependence of optical transmittance of the films n-CdS, used in the formation of heterojunctions. The total width of the spectra η (hv) at half-maximum of the obtained heterostructures δ ≈ 1.1-1.2eV, which is higher than the corresponding parameters of heterojunctions and indicates a high degree of perfection created in this study compared with the structures known.

Thus, the advanced technology in the chemical surface deposition of thin films of SnS on the surface conductivity CdZnS allowed for the first time a photo converter heterojunctions

CdZnS/SnS, showing the possibility to realize high conversion efficiency of solar radiation on the substrates CdZnS large areas.

Conclusion

In conclusion, for the first time, using a novel, very simple and not expensive procedure, SnS nanocrystals have been synthesized via ultrasonic waves at normal laboratory conditions. The as-synthesized SnS nanoparticles were quantitatively analyzed and characterized in terms of their morphological, structural and optical properties. The SnS nanocrystals appear strongly blue shifted direct band gap energy with a value 1.74-1.76 eV. The advanced technology in the electrochemical deposition of thin films of SnS on the surface conductivity CdZnS allowed for the first time a photo converter heterojunctions CdZnS/SnS, showing the possibility to realize high conversion efficiency of solar radiation on the substrates SnS large areas.

References

1. Azizian-Kalandaragh Y. & Khodayari A. Mater. Sci. Semicond. Process. 2010, v. 13, p. 225. DOI:10.1016/j.mssp.2010.10.018
2. Azizian-Kalandaragh Y., Khodayari A., & Behboudnia M. Mater. Sci. Semicond. Process. 2009, v. 12, p. 142. DOI:10.1016/j.mssp.2009.09.006
3. Azizian-Kalandaragh Y., Khodayari A. Physica Status Solidi a, 2010, v. 207 (9), p. 2144. DOI:10.1002/pssa.200925484
4. Bashkirov S.A., Gremenok V.F., Ivanov V.A. Fizika i Tekhnika Poluprovodnikov 2011, v. 45, p. 765. https://doi.org/10.1134/S1063782611060030
5. Bhattacharyya S. & Gedanken A. Microporous Mesoporous Materials 2008. v. 110, p. 553. DOI:10.1016/j.micromeso.2007.06.053
6. Biswas S., Kar S. & Chaudhuri S. Appl. Surf. Sci. 2007, v. 253, p. 9259. DOI:10.1016/j.apsusc.2007.05.053
7. Ghosh B., Das M., Banerjee P. Das S. Appl. Surf. Sci. 2008, v. 254, p. 6436-6440. DOI:10.1016/j.apsusc.2008.04.008
8. Goharshadi E.K., Ding Y., Jorabchi M.N. & Nancarrow P. Ultraso. Sonochem. 2009, v. 16, p. 120. https://doi.org/10.1016/j.ultsonch.2008.05.017
9. Gontard L.C., Ozkaya D. & Dunin-Borkowski R. Ultramicroscopy 2011, v. 111, p. 101. DOI: 10.1016/j.ultramic.2010.10.011
10. Liu H., Liu Y., Wang Z., & He P. Nanotechnology 2010. v. 21, p. 105707.
11. Mahendia S., Tomar A.K., Chahal R.P., Goyal P. & Kumar S. J. Phys. 2011, v. D 44, p. 205105.
12. Ning J., Men K., Xiao G., Wang L., Dai Q., Zou B., Liu B. & Zou G. Nanoscale 2010, v. 2, p. 1699. https://doi.org/10.1039/C0NR00052C

ENHANCING PERFORMANCE OF TRIBOELECTRIC NANOGENERATORS BY USING TITANIUM OXIDE/POLYVINYLCHLORIDE NANOCOMPOSITE FILMS

O GULAHMADOV, R MIRSULTANOVA, MB MURADOV and J KIM

Baku State University, 23 Zahid Khalilov Street, AZ1148, Baku, Azerbaijan
E-mail: kjiseok@bsu.edu.az

In this study, nanocomposite films which are made of polyvinylchloride (PVC) and titanium oxide (TiO_2) nanoparticles are used as triboelectric films for triboelectric nanogenerators (TENGs) to convert wasted mechanical energy into electrical energy. Nanocomposite films are fabricated by the hotprssing method in which a mixture of melted PVC and TiO_2 nanoparticles are compressed with heating. TENGs are fabrcated by assembling the PVC nanocomposite film and a nylon film. And performance of TENGs is investgated according to the concentration of TiO_2 nanoparticles in the PVC nanocompostie film. TiO_2 nanoparticles with high dielectric constant and high meechanical strength provide positive effect for performance of TENGs. As a result, the charge density on the surface of the PVC nanocomposite triboelectric film is enhaced according to the concentration of TiO_2 nanoparticles. And electrical outputs of TENGs such as the open-circuit voltage and the short-circuit current increase as the concentration of TiO_2 nanoparticles that are dispersed into the PVC matrix. PVC-TiO_2 nanocomposite films show enhancement of the mechanical property of TENGs because of the strong interfacial interaction between TiO_2 nanoparticles and the polymer matrix through the hotpressing method. Mechanically robust TENGs with high electrical outputs are demonstrated by using PVC-TiO_2 nanocomposite films.

Keywords: energy harvesting, triboelectric nanogenerator, titanium oxide nanoparticle, polyvinylchloride, nylon, dielectric constant

PACS: 41.20. Cv, 77.55.-g, 85.35.-p, 77.84. Bw, 77.84. Lf, 88.05. Np, 45.20. dg

Introduction

Using the energy of the fossil fuel is well recognized to cause the global climate change which significantly threatens sustainability of the ecosystem and human society [1]. Therefore, there has been lots of effort to harness eco-friendly and renewable energy sources. In recent years, triboelectric nanogenerators (TENGs) have attracted interest of researchers as a promising way to collect energy efficiently and comfortably from the environment since the first TENG was reported by Zhang et al. in 2021 [2]. The TENG is a versatile technology to harvest energy from various sources from our surrounding environment, including human mechanical motions [3–8], raindrops] [9,10], water waves [11–14] and wind [15–20]. Even a TENG which harnesses the thermal energy has been also reported [21]. TENGs generate electricity from mechanical motions through contact electrification and electrostatics [22]. The surface of one material is charged positive and that of the other material is charged negative when two materials contact and separate. And the induced charges stay on the surface of materials as electrostatic charges when the two materials are non-conductive. Electric current flows when they are connected to an electric circuit including electrodes and electric wires. TENGs have such a simple mechanism of operation compared to other energy harvesting systems and can harvest electric energy from all the mechanical energy sources. And triboelectricity is generated theoretically when any two materials, even two same materials, contact and separate because the actual transfer of charges occurs in the nano scale contact [23–25]. Thus, TENGs can be produced very cheap. TENGs have been usually suggested to harvest energy for

small-scale electronic devices such as portable electronic devices [26–30], self-powered sensors [31–33], active air filtration systems [34–36] and water-splitting [37–39].

In this study, a nanocomposite of polyvinylchloride (PVC) and titanium oxide (TiO_2) was used as a triboelectric dielectric film. TiO_2 is well known high dielectric material. A mixture of TiO_2 nanoparticles PVC were cast into a film. This nanocomposite film was assembled with a nylon film into a TENG. The TENG with the PVC-TiO_2 nanocomposite was compared to a TENG with a PVC film without TiO_2 nanoparticles. The TENG with PVC- TiO_2 nanocomposite showed much enhancement on generation of electrical outputs in comparison to the PVC film only.

Experiments

PVC and nylon (nylon socks, nylon 90% and other polymer 10%, 15D; thread diameter 43 µm) were used as triboelectric pairs. TiO_2 nanoparticles were first dispersed in dimethylformamide (DMF) with help of ultrasonication. PVC powder was dissolved in mixture of TiO_2 and DMF for 4 hrs. The PVC-TiO_2 nanocomposite film was prepared by drop casting on a piece of aluminum (Al) foil. The prepared PVC-TiO_2 nanocomposite film was cut into a rectangular in 5 cm by 3 cm. A nylon film was prepared by cutting nylon socks into patches and attaching patches to Al foil with a thin double-sided tape. The Al foil with the PVC-TiO_2 nanocomposite film was attached by a double-sided tape to a thick paper substrate as the nanocomposite film faced up. And the nylon film was also attached to a thick paper substrate. And two films were assembled in a TENG as the nanocomposite film was placed against the nylon film with 1 cm distance.

Electrical outputs such as voltage and current from the PVC-TiO_2 nanocomposite TENG were measured by a digital multimeter (DMM6500 6-1/2-digit multimeter, Keithley). Temperature and relative humidity during the analysis were 30°C, 45%, respectively.

Results and discussion

PVC was slowly dissolved in DMF. It took around 4 hours for PVC to be dissolved completely. The mixture of PVC and TiO_2 nanoparticles was poured onto a piece of Al foil as shown in Fig. 1.

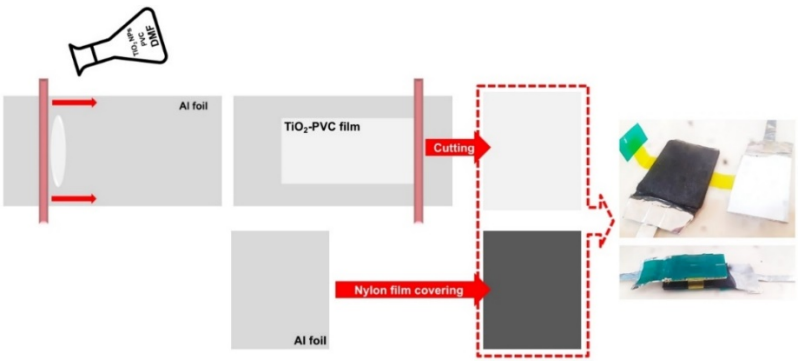

Fig. 1. The schematic represents of fabrication of PVC-TiO_2 nanocomposite film and TENGs

Then, Meyer's rod was rolled over the drop and the film was dried overnight. The PVC-TiO_2 nanoparticle nanocomposite thin film was easily obtained. The nanocomposite thin film

and the nylon film were put together as shown in Figure. They were connected through a pair of bridges which keeps relative distance between two films after compression. In this way, the prepared TENG operates and generates electrical outputs such as voltage and current as two triboelectric films repeat contact and separation

First, two triboelectric films contact to each other by compression as shown in Fig. 2.

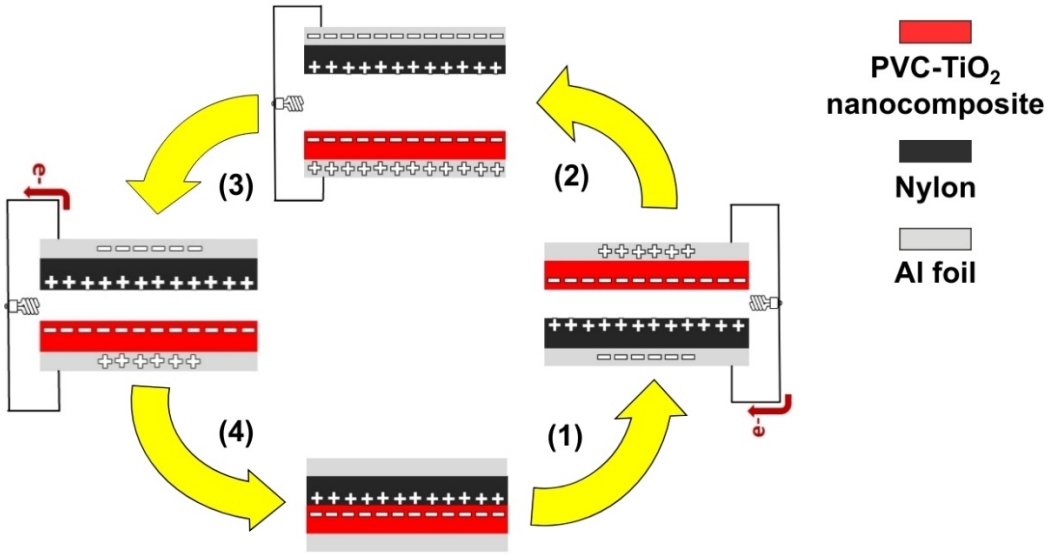

Fig. 2. The operation principle of the fabricated TENG

Then, negative charges are moved into the surface of the PVC-TiO_2 nanocomposite film and the surface of the nylon film becomes positive. (1) Two triboelectric films start to separate by the restoring force of bridges. Electrons start to flow into the Al electrode on the nylon film to compensate for positive charges. Current flows from the nylon film to the nanocomposite film. (2) Then, the positive charge and the negative charge balance out each other. (3) The triboelectric films come close again. And charges repel the opposite charge from surfaces thus electrons flow into the electrode on the nanocomposite film. Current flows from the nanocomposite film to the nylon film. (4) Two films contact again and then, the cycle is repeated, which results in an alternating current. Repeated up-and-down motions were applied for analyzing TENGs.

The current is induced by the operation of the TENG according to the following Maxwell equation.

$$J = \varepsilon_r \varepsilon_0 \frac{dE}{dt} + \frac{dP}{dt} \tag{1}$$

J is current density, ε_r dielectric constant, ε_0 permittivity of free space, E electric field, P polarization, t time.

Thus, the current density generated by the TENG increases as the dielectric constant of the triboelectric film. TiO_2 has large dielectric constant of 300 compared to PVC which has dielectric constant of 3. Thus, two TENGs were prepared with PVC films with and without TiO_2 nanoparticles to see the effect of TiO2. One TENG was prepared with a PVC film without TiO_2 nanoparticles while the other was prepared with a PVC film with TiO_2 nanoparticles in 5 wt%.

And they were compared. Results are shown in Fig. 3.

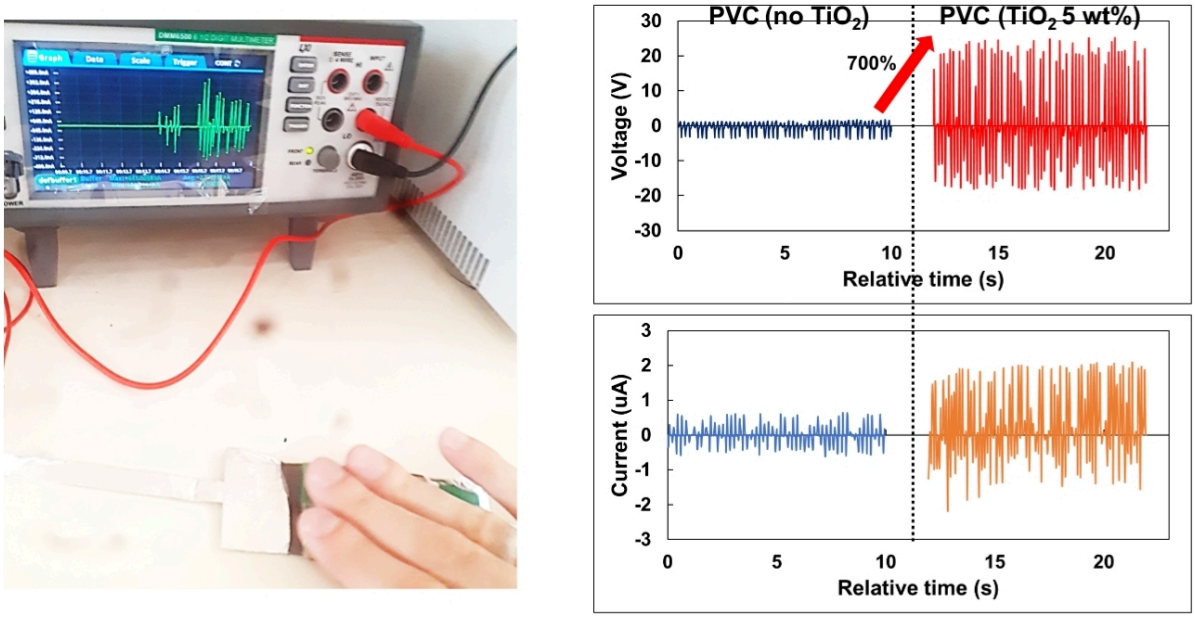

Fig. 3. Operation of TENGs and electrical outputs from TENGs with PVC-TiO_2 nanocomposite film and PVC film only, respectively.

The TENG with only PVC generated voltage of 3 V and current of 0.5 μA. The TENG with PVC with 5 wt% of TiO_2 nanoparticles generated much more electrical outputs, voltage and current were 21 V and 2 μA, respectively. The TENG with PVC-TiO_2 nanocomposite film showed as much as 700% enhancement on performance compared to that without TiO_2 nanoparticles.

Conclusions

In this study, TENGs were fabricated with PVC-TiO_2 nanocomposite thin films. The nanocomposite film was prepared by drop-casting of mixture of PVC and TiO_2 nanoparticles onto Al foil as an electrode. The nanocomposite film was put against a nylon film with distance of 1 cm for a TENG. A TENG with PVC film only was also prepared for comparison to confirm the effect of TiO_2 nanoparticles. The TENG with the PVC-TiO_2 nanocomposite film showed 700% increase in electrical outputs comparted to the TENG with PVC only. This increase attributes to the high dielectric constant of TiO_2. Thus, nanocomposite films with nanoparticles of high dielectric constant such as TiO_2 are promising for enhancement of performance of TENGs.

Acknowledgements

We appreciate Baku State University for help with facilities.

References

1. Perera F. Int. J. Environ. Res. Public Health 2018, v. 15, p. 16.
2. Fan F.R., Tian Z.Q., Lin Wang Z. Nano Energy, 2012, v. 1, p. 328.
3. Zhu G., Bai P., Chen J., Lin Wang Z. Nano Energy, 2013, v. 2, p. 688.

4. Xie Y., Wang S., Niu S., Lin L., Jing Q., Yang J. Adv. Mater., 2014, v, 26, p. 6599.
5. Chen J., Zhu G., Yang J., Jing Q., Bai P., Yang W. ACS Nano 2015, v. 9, p. 105.
6. Rasel M.S.U., Park J.Y. Appl. Energy 2017, v. 206, p. 150.
7. Zhang H., Zhang J., Hu Z., Quan L., Shi L., Chen J. Nano Energy, 2019, v. 59, p. 75.
8. Wang S., Tai H., Liu B., Duan Z., Yuan Z., Pan H. Nano Energy 2019, v. 58, p. 312.
9. Sun Y., Huang X., Soh S. Chem. Sci. 2015, v. 6, p. 3347.
10. Zhao L., Liu L., Yang X., Hong H., Yang Q., Wang J. J. Mater. Chem. A 2020, v. 8, p. 7880.
11. Yang X., Chan S., Wang L., Daoud W.A. Nano Energy 2018, v. 44, p. 88.
12. Chen B.D., Tang W., He C., Deng C.R., Yang L.J., Zhu L.P. Mater. Today 2018, v. 21, p. 88.
13. Liang X., Jiang T., Liu G., Xiao T., Xu L., Li W. Adv. Funct.Mater. 2019, v. 29, p. 1807241.
14. Feng Y., Jiang T., Liang X., An J., Wang Z.L. Appl. Phys. Rev. 2020, v. 7, p. 021401.
15. Yang Y., Zhu G., Zhang H., Chen J., Zhong X., Lin Z. ACS Nano 2013, v. 7, p. 9461.
16. Li S., Wang S., Zi Y., Wen Z., Lin L., Zhang G. ACS Nano 2015, v. 9, p. 7479.
17. Yong H., Chung J., Choi D., Jung D., Cho M., Lee S. Sci. Rep. 2016, v. 6, p. 33977.
18. Lin H., He M., Jing Q., Yang W., Wang S., Liu Y. Nano Energy 2019, v. 56, p. 269.
19. Ren Z., Wang Z., Liu Z., Wang L., Guo H., Li L. Adv. Energy Mater. 2020, v. 10, p. 2001770.
20. Jiang D., Liu G., Li W., Bu T., Wang Y., Zhang Z. IEEE Trans. Power. Electron. 2020, v. 35, p. 25.
21. Zhu S., Yu A., Yu G., Liu Y., Zhai J., Dai W. Appl. Phys. Lett. 2017, v. 111, p. 153901.
22. Wu C., Wang A.C., Ding W., Guo H., Wang Z.L. Adv. Energy Mater. 2019, v. 9, p. 1802906.
23. Baytekin H.T., Patashinski A.Z., Branicki M., Baytekin B., Soh S., Grzybowski B.A. Science, 2011, v. 333, p. 308.
24. Lin S., Xu L., Xu C., Chen X., Wang A.C., Zhang B. Adv. Mater. 2019, v. 31, p. 1808197.
25. Pan S., Zhang Z. Friction 2019, v. 7, p. 2.
26. Niu S., Wang X., Yi F., Zhou Y.S., Wang Z.L. Nat. Commun. 2015, v. 6, p. 8975.
27. Tian Z., He J., Chen X., Wen T., Zhai C., Zhang Z. RSC Adv. 2018, v. 8, p. 2950.
28. Dudem B., Kim D.H., Mule A.R., Yu J.S. ACS Appl. Mater. Interfaces 2018, v. 10, p. 24181.
29. Pu X., Liu M., Chen X., Sun J., Du C., Zhang Y. Sci. Adv. 2017, v. 3, p. e1700015.
30. Zhang K., Wang X., Yang Y., Wang Z.L. ACS Nano 2015, v. 9, p. 3521.
31. Chen X., Song Y., Chen H., Zhang J., Zhang H. J. Mater. Chem. A 2017, v. 5, p. 12361.
32. Lin Z., Wu Z., Zhang B., Wang Y.C., Guo H., Liu G. Adv. Mater. Technol. 2019, v. 4, p. 1800360.
33. Jiang Y., Dong K., Li X., An J., Wu D., Peng X. Adv. Funct. Mater. 2020, v. 31, p. 2005584.
34. Gu G.Q., Han C.B., Lu C.X., He C., Jiang T., Gao Z.L. ACS Nano 2017, v. 11, p. 6211.
35. Liu G., Nie J., Han C., Jiang T., Yang Z., Pang Y. ACS Appl. Mater. Interfaces 2018, v. 10, p. 7126.
36. Bai Y., Han C.B., He C., Gu G.Q., Nie J.H., Shao J.J. Adv. Funct. Mater. 2018, v. 28, p. 1706680.
37. Tang W., Han Y., Han C.B., Gao C.Z., Cao X., Wang Z.L. Adv. Mater. 2015, v. 27, p. 272.
38. Wei A., Xie X., Wen Z., Zheng H., Lan H., Shao H. ACS Nano 2018, v. 12, p. 8625.
39. Ren X., Fan H., Wang C., Ma J., Li H., Zhang M. Nano Energy 2018, v. 50, p. 562.

THE POTENTIAL BARRIER HEIGHT AND PROFILE OF SURFACE STATES OF Re/n-GaAs SCHOTTKY BARRIER DIODE

IM AFANDIYEVA[1] and RF BABAYEVA[2]

[1]Institute for Physics Problem, Baku State University (BSU), acad.Z.Khalilov str. 23, Baku, Azerbaijan;
[2]Department of Engineering and Applied Science, Azerbaijan State University of Economics, Istiglaliyyat str.6, AZ1001 Baku, Azerbaijan
E-mail: afandiyeva@mail.ru

The forward and reverse bias current–voltage $(I-V)$, capacitance–voltage $(C-V)$ and conductance–voltage $(C/\omega-V)$ characteristics of Re/n-GaAs Schottky barrier diodes (SBDs), fabricated by the using PLD technique, were measured at room temperature. The zero bias barrier height (BH) Φ_{B0}, series resistance (R_s) and the ideality factor n were obtained as 0.6eV, 3.9 Ω and 1.8, respectively by the using the thermionic emission theory. Using the impedance characteristics of SBDs in the frequency range from 10kHz to 5MHz dependence profiles of surface states N_{ss} on voltage and frequency were evaluated from the low-high frequency capacitance $(C_{LF}-C_{HF})$ and Hill-Coleman methods. In addition, the changing of R_s from 3 Ω to 38 Ω with increasing frequency have been revealed. The result of analysys for Re/GaAs Schottky diode clearly shows that the contribution of surface state charges decreased at high frequencies, because N_{ss} cannot follow the *ac* signal at high frequencies. The influence of surface states on the electrical parameters of Re/n-GaAs SBDs has been revealed.

Keywords: Re/n-GaAs Schottky barrier diodes (SBDs), basic electrical parameters of SBDs, impedance spectroscopy, frequency dependence, surface states
PACS: 73.30.+y, 73.40.Qv, 73.40.Ns

Introduction

Currently the operation of electronic devices is based on principles as transmission, processing and storage of information. Increased speed and performance any electronic device achieved by reducing the size electrical circuit elements. Schottky diodes are often used as a driving diode in field effect transistors. The main parameters, characteristics, and reliability of diodes on the Schottky barrier depend on the choice of contacting materials, their crystal structure, and the homogeneity of the metal-semiconductor interface [1-3]. It should be noted that GaAs -based SBDs are an important element of integrated circuits, semiconductor lasers, some radar systems, solar batteries, due to high electron mobility, high voltage electrical breakdown, high radiation resistance [4-6]. At the same time GaAs is characterized by a high density of surface states.

On the other hand, rhenium is also an interesting material. The advantages of rhenium are stability at high temperatures, a low temperature coefficient of resistance, a slight change in resistance with increasing film thickness [7-10]. Initially, rhenium is recommended for the fabrication of thin-film resistors. Besides there is no experimental information in the literature about Re/n-GaAs SBDs, practically [11-12]. The aim of this study is to investigate the main parameters of Re/n-GaAs SBDs based on measured $I-V$, *C-V* and *G/ω-V* characteristic at room temperature.

Experiments and methods

The Re/n-GaAs SBDs were fabricated by the using n-type single crystal n-GaAs wafer with (100) surface orientation thikness and carrier concentration of which 625 mm and (2.2-3.1)10^{18} cm^{-3} respectively. The GaAs wafer was degreased for about (5-7)min in organic

solvent of trichloroethylene, acetone and methyl alcohol and was etched in a sequence of sulfuric acidand hydrogen peroxide, 20% hydro fluoricacid (HF), a solution of nitricacid (6HNO3): 1HF:35 H2O, 20% HF and finally followed by a quench in de-ionized water of resistivity of 18.2 MΩcm.After some procedure of degreasing and etching of the GaAs wafer the low resistance ohmic contacts to n-GaAs wafer was made by using highpurity (99.999%) Au with a thickness of about 2000 Å in high vacuum system of about 10^{-6}Torr [12]. The rectifying contacts in about (200-250) nm thickness were deposited by PLD technique on the front surface of n-type GaAs wafer using Rhenium (Re) metal with a 99.99% purity as a target material. The distance between the target and the substrate was 40 mm. To increase the homogeneity of the contact area both the Re target and the n-GaAs substrate were rotated at a speed of 10-15 rev/min. Rectifying contacts were deposited on n-type GaAs under high vacuum. To produce rectifying contacts with 1.5 mm diameters a metal shadow mask was used. Deposition time was about 2 hours depending on the required contact material thickness. The current-voltage ($I-V$) measurements in the range from -5.0 V to +5.0 V with 5 mV steps were performed by using a Keithley 2410 Source Meter at room temperature.

Results and discussion

The most important parameters of contact as Φ_{B0} and n can be determined by various methods [13-15]. In the present work Re/n-GaAs SBD parameters have been calculated by the using I-V and C-V characteristics and compared.

The Re/n-GaAs SBD current-voltage characteristic measured at forward and reverse biased regions (±5V) has indicated in Fig. 1 in a semi-logarithmic scale. The forward bias $I-V$ characteristics at intermediate bias voltage region show a linear behavior. Coefficient of straightening $\left(I_{for}/I_{rev}\right)$ for Re/n-GaAs SBD at 0.4V is 1.12x10^2. At high bias voltage the slope deviated from linear due to series resistance. The experimental $I-V$ data for Re/n-GaAs diode have been analyzed by the well-known equation for SBDs with a R_s and R_{sh} and obey the thermionic emission model as:

$$I = I_s exp\left[\frac{q(V-IR_S)}{nkT}\right]\left\{1-exp\left[-\frac{q(V-IR_s)}{kT}\right]\right\}+\frac{q(V-IR_s)}{R_{sh}} \quad (1)$$

where, n is the ideality factor, T is the temperature in Kelvin, V is the applied voltage, $V-IR_s$ is the voltage on the Schottky junction, q is the electron charge, k is the Boltzmann constant [1, 2]. I_s is the saturation current and is given by using Eq. 2

$$I_s = AA^*T^2 exp\left(-\frac{q\Phi_{B0}}{kT}\right) \quad (2)$$

where A and A^* are the area of Re/n-GaAs SBD and the Richardson constant for n-GaAs which equals to 3.14x10^{-2} cm^2 and 8.16 A/cm^{2}K^2, respectively. Φ_{B0} is zero bias BH calculated by using the following equation:

$$\Phi_{B0} = \frac{kT}{q} ln\left[\frac{AA^*T^2}{I_s}\right] \quad (3)$$

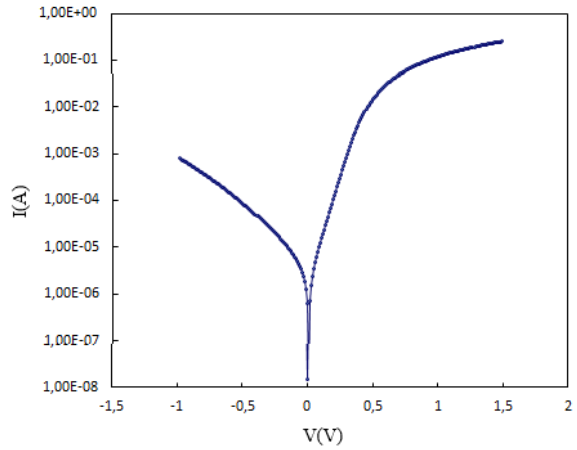

Fig. 1. The $I-V$ characteristic of Re/n-GaAs SBD at room temperature.

The saturation current I_s has been derived from an intercept of a straight line of $ln(I)$ at zero bias. Φ_{B0} of Re/n-GaAs SBD has been calculated on the basis of linear region of $\ln(I-V)$ as is shown in Eq.(1). Moreover, the ideality factor has been obtained as is shown below in Eq.(4):

$$n = \frac{q}{kT}\frac{dV}{dln(I)} \tag{4}$$

Due to the existence of the R_s the value of n greater than unity. On the basis of investigated of $I-V$ characteristic Φ_{B0}, I_s and n of Re/n-GaAs Schottky diode at room tempearture have been calculated as 0.602 eV, 2x10^{-6} A and 1,84, respectively.

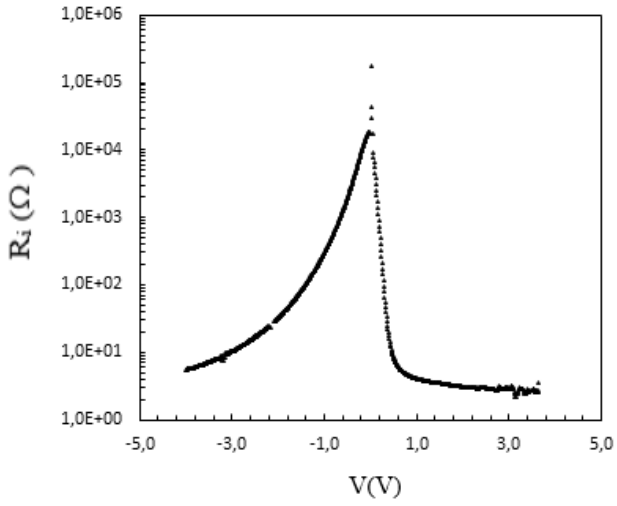

Fig. 2. The voltage dependent resistance profile of Re/n-GaAs SBD at room temperature

With the aim of the calculate the basic parameters of Re/n-GaAs SBD the capacitance-voltage ($C-V$) and conductance-voltage ($G/\omega-V$) characteristics have been measured at room temperature in a bias voltage and wide frequency range of +-1,2eV and from 10kHz to 5000 kHz, respectively (Fig,3 a, b).

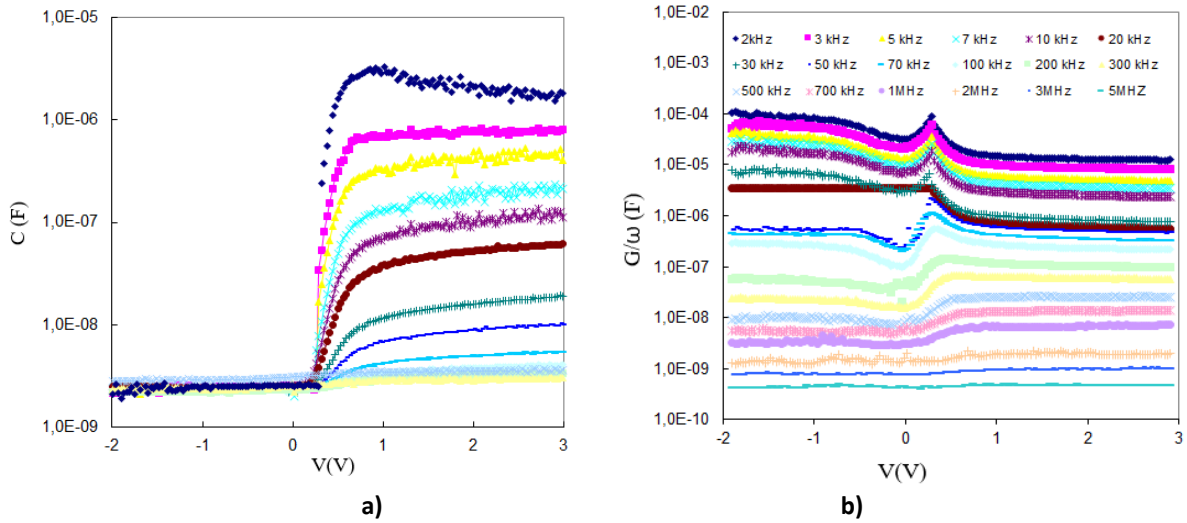

Fig. 3. The measured C-V (a) and G/ω-V (b) characteristics for Re/n-GaAs SBD at various frequencies (T=300K)

So, figure 3 shows for Re/n-GaAs SBD the dependence of C(a) and G/ω (b) value vs. voltage at different frequencies of test signal. It should be noted, that decreasing of values of C and G/ω at height frequencies can be attributed to the carrier charges at surface states/traps and their relaxation time (τ), due to the influence of the recharging of surface states.

With the aim of the study the parameters of Re/GaAs the real series resistance of the diode according to a method presented by Nicollian and Brews has been calculated [16-18]. The method considers the influence R_s on $C-V$ and $G/\omega-V$. As is known, the voltage and frequency dependence R_s can be determine from measured $C-V$ and $G/\omega-V$ dependence at different frequencies from 10 kHz to 3MHz. Therefore, the frequency and voltage dependence can be determined from the measured impedance (Z_{ma}) at strong accumulation region [19]:

$$Z_{ma} = \frac{1}{G_{mi} + j\omega C_{mi}} \tag{5}$$

Based on comparing the real and imaginary part of the impedance can be obtained R_s as

$$Y = G + j\omega C \tag{6}$$

$$R_s = \frac{G_{ma}}{G_{ma}^2 + (\omega C_{ma})^2}, \tag{7}$$

where ω (=2πf) is the angular frequency, C_{mi} and G_{mi} are the measured capacitance and conductance values for any voltage in strong accumulation region at different frequencies, respectively.

The dependence of R_s for any voltage and frequency evaluated according to formula (7) based on the measurements C_m-V-f and $G_m/\omega-V-f$ has been analyzed and shown in Fig. 4. Due to the charge of surface states cannot follow an ac-signal at high frequencies the value of R_s decreased when frequency increased. The magnitude of peak in the R_s–ln(f) plots changed with increasing frequency.

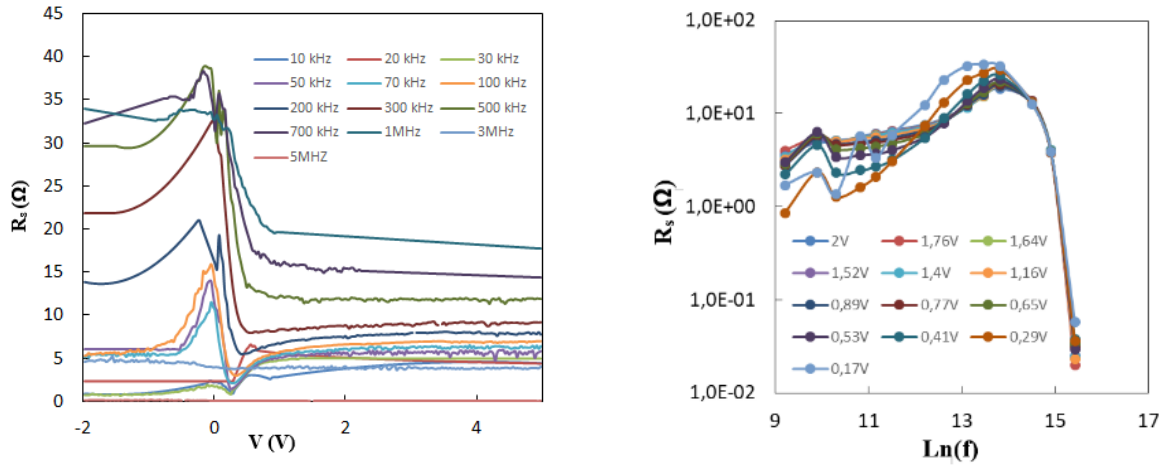

a) **b)**

Fig. 4. The dependence series resistance of Re/GaAs SBD on voltage (a) and frequency (b)

As is shown in Fig. 4 (a) $R_s - V$ characteristics gives peaks in the range -0,1÷ 0,5 V, which decreased with increasing of the frequency. The value of R_s for high frequencies (≥500 kHz) in strong accumulation region corresponds to the real value of R_s of the structure. Therefore, this dependence can be explained by the presence of charge of traps and surface states which cannot follow an external ac signal [19,20]. The peaks in the $R_s - V$ dependence in the displacement range -0,1÷ 0,5 V and the non-uniform frequency dependence show the contribution of surface states with different relaxation times.

In this connection, the interface state density N_{ss} has been evaluated as follows [21,22]:

$$N_{ss} = \frac{1}{qA}\left[\left(\frac{1}{C_{LF}} - \frac{1}{C_{ox}}\right)^{-1} - \left(\frac{1}{C_{HF}} - \frac{1}{C_{ox}}\right)^{-1}\right] \quad (8)$$

where C_{LF} and C_{HF} are measured capacitance at low (10 kHz) and high (5MHz) frequencies, respectively. Based on above obtained results has been revealed that the charges in traps and surface states cannot follow ac-signal at high frequencies. As can be seen from Fig. 5 the plot of distribution of surface states ($N_{ss} - V$) gives a peak at around 0,47 V.

By the using of Hill-Coleman method [23], has been obtained the dependence of surface sates distriburion on frequencies as follows:

$$N_{ss} = \frac{2}{qA}\frac{\left(G_{m,max}/\omega\right)}{\left(G_{m,max}/\omega C_{ox}\right)^2 + (1 - C_m/C_{ox})^2} \quad (9)$$

As can be seen (Fig. 6) this result for Re/GaAs Schottky diode clearly shows that the contribution of surface state charges decreased at high frequencies, because N_{ss} cannot follow the ac signal at high frequencies.

To explain the obtained results, it should be taken into account that the ratio of the lattice parameters of the metal and semiconductor plays a significant role in the formation of a contact [3]. It is known, that lattice parameters are a = 0.565nm for GaAs and a=2.761nm, c=4.456 nm for Re, respectively [24,25]. Due to lattice mismatch between the metal and GaAs in the subsurface region of semiconductor elastic stresses can be appear. When a metal is deposited

on a semiconductor surface, mutual diffusion of metal and semiconductor atoms is possible, which affects the formation of a barrier and surface states [26-27]. The resulting dependence of C-V, $G/\omega - V$ characteristics and R_s values on frequency can be explained by the presence of surface states due to the influence of lattice mismatch between Re and GaAs.

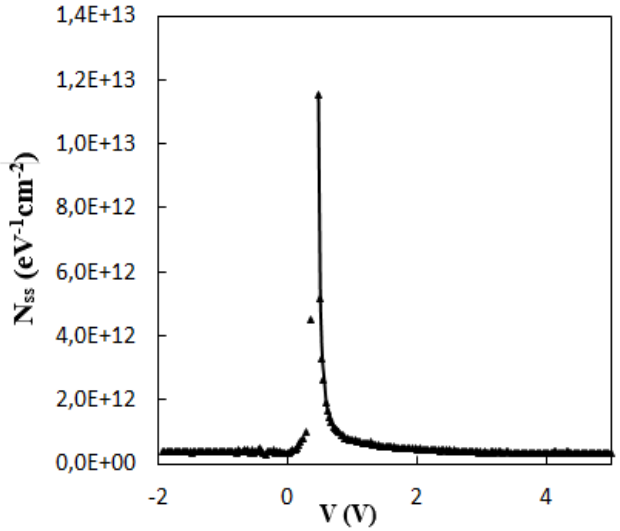

Fig. 5. The dependence of the distribution profile of surface states on voltage by the using high-low frequency capacitance method for Re/GaAS Schottky diode.

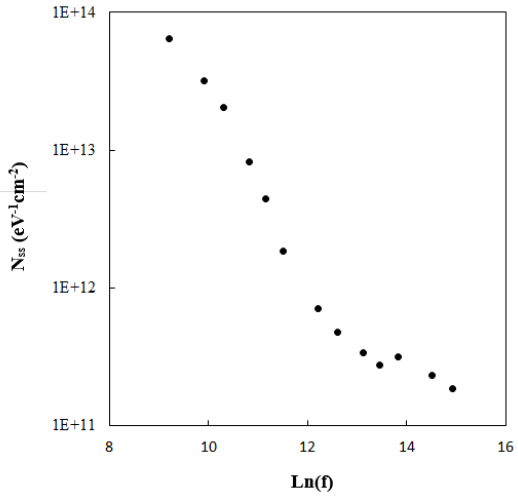

Fig. 6. The depe1ndence of surface sates distriburion for Re/GaAs SBD on frequencies at 300K

Conclusion

The measurements of $I-V$ characteristics of Re/n-GaAs SBD in the voltage range from -5.0 V to +5.0 V were performed at room temperature. The basic characteristics parameters such as Φ_B, n and R_s, have been calculated by using $I-V$, $C-V$ and $G/\omega - V$ characteristics measured at room temperature and frequency of test signal from 10 kHz to 3Mhz. The depending of R_s values on frequency can be attributed to influence of surface states at low frequencies. Revealed profile $N_{ss} - \ln(f)$ of surface states can be connected to the influence of lattice mismatch between the Re and GaAs on the formation of the barrier and surface states.

References

1. Rhoderick E.H., Williams R.H. Metal–Semiconductor Contacts. Clarendon Press: Oxford, England, 1988.
2. Sze S.M. Physics of Semiconductor Devices, John Wiley & sons: New York, USA, 1981.
3. Afandiyeva I. M., Altındal Ş., Abdullayeva L.K., Bayramova A.I. Journal of Semiconductors 2018, v.39 (5), p.054002-1. DOI: 10.1088/1674-4926/39/5/054002 EEACC: 4320J
4. Taghizadeh F., Van Rensburg P.J., Janse Ostvar K. et al. Materials Science in Semiconductor Processing 2019, v.99, p. 23. DOI: 10.1016/j.mssp. 2019.04.012
5. Kirezli B., Ahmetoglu (Afrailov) M., Kara A. Journal of Molecular Structure 2019, v. 1192, p. 258. DOI:10.1016/j.molstruc. 2019.04.072
6. Vezzoli Andrea, Brooke Richard J., Ferri Nicolo et al. Faraday Dıscussıons 2018, v. 210, p. 397.
7. Contelot Fanny, Thomas Robert J., Seaman John C. Environment International 2019, v. 128, p. 379. DOI: 10.1016/j.envint.2019.05.001.
8. Littleton, Joshua A. H., Secco, Richard A., Yong, Wenjun et.al. Journal of Applied Physics 2019, v. 125 (13),

p. 135901. DOI: 10.1063/1.5066103.
9. Tian Bian, Yu Qiuyue, Zhang Zhongkai et.al. Ceramics International 2018, v.4, p.15. DOI: 10.1016/j.ceramint.2018.08.334.
10. Hasanli Nijat, Gauquelin Nicolas, Verbeeck Johan. Dalton Transactions 2018, v. 47 (44), p.15783.
11. Chia-Chien Lin. Journal of Applied Physics 1999, v. 85, p.3893.
12. Durmus H., Yildirim M., Altindal S. Journal of Materıals Scıence-Materıals In Electronıcs 2019, v. 30 (9), p. 9029. DOI:10.1007/s10854-019-01233-z Corpus ID: 140766411.
13. Kudryk Ya.Ya., Shynkarenko V.V., Slipokurov V.S. et al. Semiconductor Physics, Quantum Electronics & Optoelectronics 2014. v.17 (4), p. 398.
14. Norde H.A. J. Appl. Phys. 1979, v. 50, p. 5052.
15. Cheung S.K., Cheung N.W. Appl.Phys.Lett. 1986, v. 49 (2), p. 85. doi:10.1063 /1.97359.
16. Moloi S.J., McPherso M. Radiation Physics and Chemistry 2013, v. 85, p.73. DOI: 10.1016/j.radphyschem.2012.12.002.
17. Yahiya I.S., Zahran H.Y., Alamri F.H., Aslam M. Physica B: Condensed Matter 2018, v. 543, p. 46. https://doi.org/10.1016/j.physb. 2018.05.011
18. Nicollian E.H. and Brews J.R. MOS (Metal Oxide Semiconductor) Physics and Technology. Wiley: New York, USA, 1982, p. 117–129.
19. Ersoz Gulchin, Yucedag Ibrahim, Azizian-Kalandaragh Yashar, et al. IEEE Transactions on Electron Devices 2016, v. 63 (7), p. 2948. DOI: 10.1109/TED.2016.2566813
20. Parlakturk F., Altındal S., Tataroglu A. et al. Microelectronic Engineering 2008, v. 85 (1), p. 81. DOI: 10.1016/j.mee. 2007.03.012
21. Castagné R., Vapaille A. Surf. Sci. 1971, v. 28, p. 157.
22. Hung K.K., Cheng Y. C. J. Appl. Phys., Jul. 1987, v. 62, p. 4204. https://doi.org/10.1063/1.339091.
23. Hill W. A., Coleman C. C. Solid-State Electron. 1980, v. 23, p. 987. https://doi.org/ 10.1016/0038-1101(80)90064-7.
24. Krylov P.N. Journal of Udmurt University 2006, v. 4, p.125 (in Russian).
25. Shaskolskaya M.P. Crystallography. Visshaya shkola: Moscow, 1984 (in Russian).
26. Calandra C., Santoro Giorgio. Journal of Physics C Solid State Physics 2001, v. 8 (6), p. L86. DOI: 10.1088/0022-3719/8/6/002

STUDY OF HIGGS BOSON INTERACTION WITH TOP QUARKS AT THE LHC

NA HUSEYNOV

Institute of Physics, ANAS Baku, Azerbaijan
E-mail: nguseynov@jinr.ru

Top quark is the heaviest elementary particle of the Standard Model. Hence, its interaction with the Higgs boson attracts a particular interest, since the New Physics phenomena are likely to manifest themselves in the sector of top-Higgs interaction. Within this acticle we will study the Higgs boson production in association with one (pp→tH). The latter reaction is sensitive to the absolute value of the top Yukawa coupling y_t, while the former one allows a determination of the y_t complex phase. An opposite sign of y_t would increase pp→tH event yield by an order of magnitude with respect to the Standard Model prediction, thus providing an unambiguous evidence of New Physics.

Keywords: Higgs boson, top quark, Yukawa coupling, LHC
PACS: 13.66.Fg, 14.65.Ha, 14.80.Bn

Introduction

Currently, the Large Hadron Collider (LHC), built at CERN (Geneva), is a flagship of high-energy physics. A record high energy (proton-proton collision energy of 13 TeV was achieved) and high luminosity made it possible to obtain a huge number of new scientific results. Research includes both the precise study of known particles and the search for new particles and phenomena beyond the scope of the Standard Model. After the discovery of the Higgs boson by ATLAS [1] and CMS [2], the SM is now a complete theory. However, the SM is not able to fully describe the observed structure of matter, since it does not provide answers to some of the most fundamental questions - for example, the existence of dark matter, the hierarchy problem, the small masses of neutrinos, and others. On the other hand, there are many BSM models. Of particular interest is the interaction of the Higgs boson with the top quark, which is the heaviest SM particle. It is widely believed that the BSM phenomena of New Physics can manifest themselves in the sector of Higgs-top interaction.

In this article we will study the Higgs-top interaction in the production channels pp→tH. The analysis will use the complete Run-2 data (140 fb^{-1} integrated luminosity). In the Standard Model, this channel is characterized by an extremely small production cross section, about 70 fb. The channel pp → tH has not yet been observed in the experiment. In the pp→tH channel the amount of background from the fake leptons will be determined with a data-driven method using the Matrix Method (MM). The main challenge of the analysis is to reduce the enormous pp→tt background (at the preselection level the signal is about 100 events, while the background is 200,000 events), making use of the kinematical, topological and event-shape variables. Several methods of event selection will be explored. A simpler one, Sequential Cut Analysis and a more sophisticated method: Gradient Boosted Decision Tree(GBDT) and Deep Neural Network Analysis (DNN) making use of all variables and their correlations. The DNN method is more challenging in understanding the input features and correlations, ordering the features in order to reduce their number. Also, the DNN method requires an optimization of the DNN structure and determining the optimal working point to maximize the performance. A systematic comparison of the DNN performance with the Sequential Cut Analysis

allows gaining confidence in the DNN analysis and determining the performance enhancement.

Associative production of the Higgs boson with a single top quark

The channel with a single top quark pp→tH can be studied in the decay modes H→bb, H→γγ, and H→ττ, as well as in the multilepton channel. In this article, the channel H→bb will be investigated. In this case, the semi-leptonic decays of the top quark are selected, t→bW→blv, Such events are characterized by the presence of a charged lepton with a large transverse momentum, an energetic neutrino detected as an imbalance of the transverse momenta of the reconstructed particles, and at least three b-jets. When using the standard working point for identifying b-jets with an efficiency of 70%, the requirement of having three b-jets reduces the signal by approximately a factor of three, but it can significantly reduce the background from pp→tt events. Even with this selection, the tt background is still many times higher than the signal level [3]. Background events pass the selection due to the fact that in decays t→bW→bcs the jet from the charmed quark is identified with a probability of the order of 10% as the third b-jet. In addition, the pp→ttbb events, which are QCD corrections to the pp→tt process, make a significant contribution to the background. The pp→tH channel has not been previously studied in the ATLAS experiment. Therefore, at the first stage of the analysis, the simulated data at the generator level will be investigated, without modeling the response of the detector. The signal and background processes will be simulated taking into account the effects of parton showers and hadronization. On the basis of this simulation, the kinematics of the corresponding processes will be studied, the observable sensitive to signal/background separation will be established, the most effective criteria for event selection will be developed. The results obtained at the generator level will be applied to the ATLAS experimental data, as well as to simulated data that takes into account the response of the detector. The selection criteria will be adjusted taking into account the features of the experimental setup. Based on these criteria, a preliminary selection of events will be made. The signal pp→tH predicted by the Standard Model is characterized by an extremely small production cross section. The background ttH exceeds the signal by a factor of 10, and the background tt by 10 thousand times. Even after applying the selection criteria, the background will still be many times higher than the signal level. Reliable signal isolation will require the use of machine learning algorithms. It should be noted that existing event generators rather poorly model QCD corrections involving heavy quarks, in particular, the process pp→ttbb, which makes an important contribution to the overall background level. In addition, the background process pp→ttH has so far been studied with rather low experimental accuracy. Thus, it will not be enough to divide all events into only two categories, “signal’ and “background”. Such an approach would lead to large systematic errors, since the ratio of the various components of the background is modeled rather poorly. In this project, it is supposed to apply the FOAM algorithm, which allows one to divide events into several classes. The result of the algorithm will be the classification of events received after preliminary selection in the categories “signal”, “background ttH”, “background tt”, “background ttbb”, “other background”.

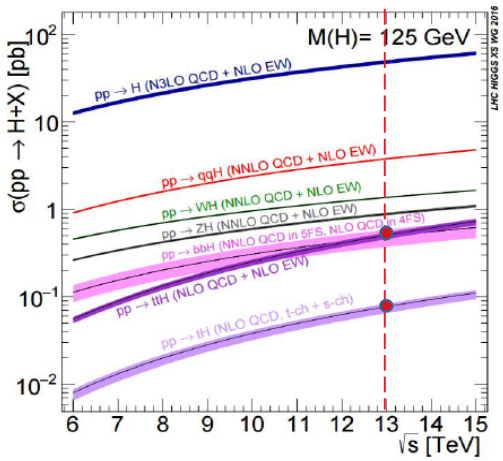

Fig. 1. Energy dependence of the cross section of the Higgs boson production in proton-proton collisions.

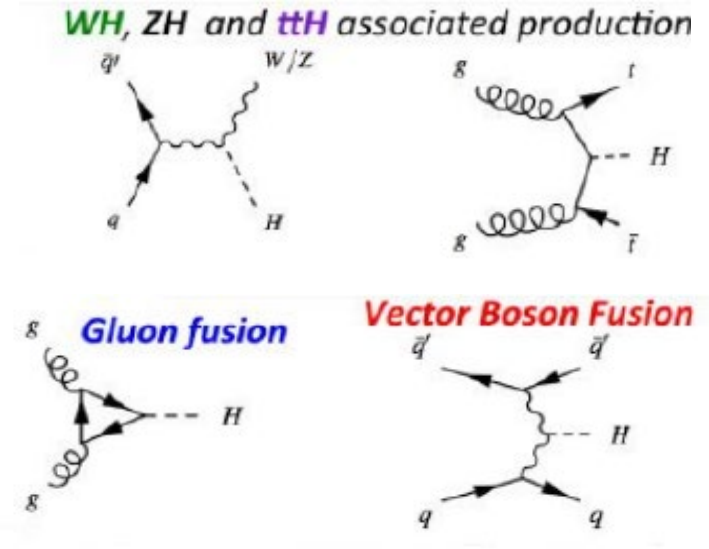

Fig. 2. Main Higgs boson decays mode in proton-proton collisions.

The experimental observable studied at the LHC are the Higgs boson mass, spin and parity, decay branching, kinematics of production, cross sections of exclusive production modes [4].

Figure 1 shows the energy dependence of cross sections for different production modes of the Higgs boson. So far, 4 most abundant production modes have been observed at the LHC (Figure 2):

- gluon fusion (87%, gg → H), b-tagging works reliably from 50 GeV
- vector boson fusion (7%, VV → H, where V is W or Z boson)
- vector boson associated production (4%, pp → H + V)
- top pair associated production (1%, pp → ttH).

A production of Higgs boson in association with a single top quark was not observed yet. For this production mode (which we call “signal” hereafter) the Standard Model predicts much smaller cross section than for the Higgs boson production in association top quark pair. In this article we discuss the prospects of the signal discovery at the LHC.

The signal process

The dominant mechanisms of Higgs boson production in association with a single top quark are described by the two leading-order Feynman diagrams presented in Figure3. Both processes result in the tHqb final states with a single top quark, a b-quark from the gluon splitting and a light quark (q) from the incoming beam.

One of these diagrams is sensitive to the Higgs boson coupling to the W boson (WWH vertex), another to the Higgs boson coupling to the top quark (ttH vertex). In the Standard Model there is a strong destructive interference between these two leading diagrams. As a result, the cross section of the signal process is very small, approximately 71 fb [5]. Such rare process can not be observed even after collection of the full LHC Run-2 statistics (several times bigger statistics is required to observe the SM process). An observation of the signal would be a clear indication of a new physics beyond the Standard Model. The signal is sensitive not only to the couplings of the Higgs boson, but also to the relative phase between the WWH and ttH vertices.

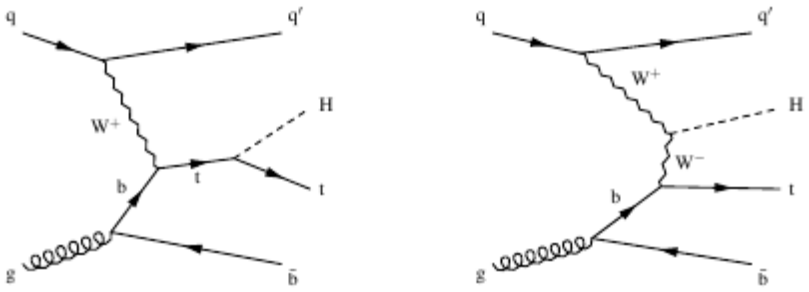

Fig. 3. Feynman diagrams of the leading order signal processes.

One of the key properties of the top quark is the top Yukawa coupling Yt. The magnitude of the top Yukawa coupling has been already measured (indirectly) at LHC with O(10%) precision. However, the pp→tHqb signal is the only process sensitive to the sign of Yt, or, more generally, the phase difference between the WWH and ttH vertices.

In particular, the signal cross section is dramatically increased in the Inverted Top Coupling (ITC) scenario [6]. In ITC all couplings are assumed to have the Standard Model magnitude, however the top Yukawa coupling is assumed to have an opposite sign with respect to SM. The interference between WWH and ttH vertices becomes constructive rather than destructive, increasing the tHqb production rate by an order of magnitude. The resultant signal cross section (739 fb at 13 TeV) makes it possible to observe a signal evidence with the statistics which is expected to be collected in 2016-2018 in the LHC Run-2.

Cut-based selection of single top Higgs signal

While the mainstream analysis is based on a MVA approach, a cross-check event selection was performed using sequential cuts on the kinematic variables (“Cut-and-Count”, or C&C analysis) [7]. The goal of the analysis was to achieve the highest possible signal significance, which was calculated as $Z=S/\sqrt{(B+S)}$, where S is the number of signal events which survive all

the cuts and B is the total background. The analysis started with the Preselection Region where the signal significance was 0.15 for the SM signal and 2.36 for the ITC (Yt = −1) signal.

All the variables were ranked according to the Signal/Background separation power which was calculated with TRexFitter. The variables with highest separation power are listed in Table 1.

Table 1. List of highest-ranking variable and their Signal/Background separation power.

Variable	Separation power
Number of jets with CBT=5	14.5%
Mass of hadronically decaying top	11.9%
Sphericity	11.7%
Aplanarity	11.0%
Mass of hadronically decaying W	10.8%
Number of jets with CBT=1	10.5%
Mass of H and the maximum pT non-b jet	10.3%
Mass of 3 maximum pT jets	9.8%
Rapidity gap between the top and the forward jet	8.3%
Number of central jets	6.6%

Starting from the variables of the highest separation power, each variable was tested for a possible improvement of the signal significance. A “scan” was performed for a given variable by applying different cuts, from very loose to very tight ones. If no cuts were able to improve the signal significance, then the variable was removed from the C&C analysis and the next-ranking variable was tested. If there was an improvement, then the optimal cut with highest signal significance was applied to the events, and the next-ranking variable was tested using only the events that passed the cuts on the variables with higher ranking. It should be noted that there is no one-to-one correspondence between the separation power of a variable and the possibility to improve the signal significance applying a cut on this variable. Several variables with high separation power provided no improvement of the signal significance, while this was achieved with variables of lower separation power. The optimal selection cuts are summarized in Table 2 for the SM signal.

Table 2. Cut and Count analysis with the Standart Model signal.

Variable	Optimal cut	Signal significance
Preselection		0.15
Forward jets	$N_{fwd} > 0$	0.16
Mass of hadronic top	M < 130 GeV or M > 200 GeV	0.178
Spherisity	Sp < 0.15	0.185
Inv.mass of 3 highest pT jets	$M_{jjj} > 250$ GeV	0.187
Central jets	$N_{cent} < 6$	0.201
Number of CBT jets	$N_{CBT=1} < 2$ and $N_{CBT=5} > 1$	0.211

The final significance of the SM signal was found to be 0.21, to be compared with 0.15 in the preselection region. The number of signal and background events was reduced from 72.6 and 228000 in the preselection region to 21.3 and 10120 after the Cut and Count analysis. For the ITC signal the significance was improved from 2.36 (preselection) to 3.32. The number of signal and background events was 397 and 14590, to be compared with 1147 and 228000 for the preselection.

Conclusions

In the single top quark Higgs analysis where Higgs boson decays to pair of b-quarks the machine learning algorithms was decided used as baseline analysis technics. Two algorithms were applied in current analysis are Gradient Boosted Decision of Tree(GBDT) and Deep Neural Network(DNN). In additional the Cut and Count analysis was used as cross check of machine learning algorithms. The data-driven Matrix Method method was used for fake light leptons estimation in this analysis. The expected limit from Asimov fit stands at $\mu<17.9$ @95% CL at present time.

Acknowledgments We are grateful to Igor Romanovich Boyko, Oksana Aleksandrovna Koval for valuable discussions and the referee for useful comments.

References

1. ATLAS Collaboration, Physics Letters B 2012, v. 716, p. 1.
2. CMS Collaboration, Physics Letters B 2012, v. 716, p. 30.
3. ATLAS Collaboration, Journal of Instrumentation 2016, v. 11, p. 04008.
4. F. Demartin et al. European Physical Journal 2015, v. 75, p. 267.
5. CMS Collaboration, CMS Note 2017, p. 369.
6. J. Alwall et al. Journal of High Energy Physics2014, v. 7, p. 79.
7. Mohamed Aly. An overview of the tH(bb) Analysis. HTop Workshop, CERN, Switzerland, 2021.

EFFECTS OF GEOMAGNETIC STORMS ON THE MID-LATITUDE D-REGION OF THE IONOSPHERE

EV BAYRAMOVA[1], FR MUSTAFA[1] and R ISMAYILLI[2]

[1]Shamakhy Astrophysical Observatory named after Nasraddin Tusi, Azerbaijan National Academy of Sciences, Shamakhy, Azerbaijan

[2]KU Leuven, Belgium

E-mail: elista.bayramovaa@gmail.com

The response of D Layer Preparation Time (DLPT) depth to geomagnetic storms during 2008-2011 is studied to investigate the effect of geomagnetic storms on the D layer of the ionosphere. The Very Low Frequency (VLF) signal at 19.6 kHz transmitted from the GBZ transmitter station Anthorn, UK (54^{o}N, 3^{o}W) and recorded by the AWESOME receiver at the Shamakhy Astrophysical Observatory named after N.Tusi, Shamakhy, Azerbaijan (40^{o}N, 48^{o}E) is used for analysis. Five geomagnetically disturbed days (Ap>26) are studied. A decrease in DLPT depth is observed for the storm day on October 11, 2008, while an increase is observed for all other storms.

Keywords: D layer preparation time, VLF wave propagation, geomagnetic storms
PACS: 91.25.-r, 92.60.Qx, 94.20.Bb

Introduction

Earth's ionosphere plays a significant role in radio communication by reflecting the wave owing to electrical conductivity. Radio waves first penetrate the D layer (60-90 km) when they propagate in the ionosphere and are exposed to attenuation. Therefore, fading of signals is strongly dependent on the ionization level of this layer. Space weather events, adversely affect radio communication, radio navigation systems, and satellite communication by increasing the ionization level of the ionosphere. Substantial enhancement of electron density, particularly in the auroral zone, during geomagnetic storms, increases radio wave attenuation, which causes the disappearance of radio signals in MH/HF ranges [1].

VLF (3-30 kHz) remote sensing method is considered the best technique to detect space weather effects on the lower ionosphere. VLF signals are transmitted from around the world to the ionosphere and received at Sudden Ionospheric Disturbances (SID) monitoring stations. They propagate with little attenuation on the cavity called the Earth-Ionosphere Waveguide (EIWG) between ionospheric D-layer and ground [2]. Amplitude and phase of the waves are much sensitive to changes in the electrical conductivity of the ionosphere on the propagation path [3]. EIWG height is 70 km during the daytime and 85 km during the nighttime, depending on the diurnal variation of the ionosphere [4]. The impacts of solar flares on VLF signals propagation have been discussed by many investigators [5-11]. They determined that enhanced X-ray radiation when a solar flare occurs increases the ionization of the D-layer, which results in a sudden anomaly in amplitude and phase of the VLF signals. Solar flares affect the entire daytime ionosphere, while geomagnetic storms primarily affect the high-latitude ionosphere; the effect extends to low and equatorial latitudes [2].

A geomagnetic storm is a temporary disturbance of Earth’s magnetosphere in response to changes in solar wind parameters and interplanetary magnetic field (IMF) conditions. Magnetic storms lead to energetic electron precipitation into the ionosphere associated with magnetospheric substorms. In order to penetrate below the 100 km altitude, electrons must have energies exceeding 20 keV [12]. Lastovicka [1] opined that at high latitudes, enhancement in

electron density and radio wave absorption is caused by energetic electron precipitation from the magnetosphere in the storm main phase. Cummer et al. [13] mentioned that energetic precipitating electrons penetrate the lower ionosphere, where they can cause extra ionization. Consequently, as the auroral electrojet crosses a VLF signal propagation path, this electron precipitation results in variations in amplitude and phase of the signal. Observing a decrease or increase in the amplitude at the receiving station depends on the modal mixture of the signal [14]. Clilverd et al. [15] observed that the amplitude of the very low-frequency signal transmitted from the NAA (24.0 kHz, 44°N, 67°W, L = 2.9) received at Sodankyla increased during geomagnetic activity. They showed ground-based electron precipitation flux (>100 keV) calculated from the NAA amplitude corresponds with the variation of electron fluxes determined by the POES satellite. From the analysis of two severe geomagnetic effects on the D-layer at low-equatorial latitudes, Kumar et al. [16] observed that for the March 2015 storm, VLF signal amplitude decreased on the primary phase and recovered one day after the storm. For June 2015 storm, they observed amplitude decreased in the storm recovery phase.

The effect of geomagnetic storms on the lower ionosphere is characterized in terms of “primary storm effect,” “after-storm effect,” “post-storm effect.” “Primary storm effect” describes signal anomaly during the main phase of the storm, whereas “after-storm effect” describes anomaly during the storm recovery period and subsequent days. The “Post-storm” effect, on the other hand, is observed due to excess ionization when the magnetic perturbations have abated [17, 18].

In this work, the influence of geomagnetic storms during 2008-2011 on the mid-latitude D region of the ionosphere via VLF signal amplitude was studied.

Research methodology and observational results

Fig. 1. Map showing the location of transmitter and receiver stations, geographical coordinates, and VLF signal propagation path along TRGCP.

Narrowband VLF signals transmitted from the transmitter (call sign is GBZ) located in Anthorn, UK (54^{o}N, 3^{o}W) and operating at 19.6 kHz stabilized frequency, received at Shamakhy, Azerbaijan (40^{o}N, 48^{o}E) are used for analysis. VLF signals are recorded with AWESOME (Atmospheric Weather Electromagnetic System for Observation Modeling and Education) receiver provided by Stanford University and installed at Shamakhy Astrophysics Observatory

named after Nasraddin Tusi (Figure 2). Transmitter-Receiver Great Circle Path (TRGCP) is shown in Figure 1. The distance between the GBZ transmitter and the receiving station is 4065 km.

(a) (**b**)

Fig. 2. (**a**) AWESOME receiver and (**b**) VLF antenna

Ap index was utilized for determining geomagnetically disturbed days. A geomagnetic storm is classified as minor when the activity level is Ap<50, moderate when the storm is 50≤Ap<100, and severe when Ap≥100. Magnetic storms with Ap index above 26 were selected for analysis. Ap index data is taken from the website mentioned in the reference section [19]. Detailed information on geomagnetic storms is given in Table 1.

The VLF DAQviewer (Data Acquisition Viewer) Matlab program was used to view VLF signal data. The DLPT depth parameter was utilized to investigate the effect of geomagnetic storms on the D-layer. A Diurnal variation of VLF signal is given in Figure 3. Sunrise Maxima, Sunrise Minima, Afternoon Maxima, Sunset Minima, and Sunset Maxima are marked with points A-E, respectively [20]. The change in amplitude between A and B points is taken as "D Layer Preparation Time (DLPT) depth." DLPT depth was evaluated on the storm day, four days before, and four days after for each geomagnetic storm. In this way, nine days variation of DLPT depth was obtained.

Figure 4 represents the variation of DLPT depth with bars and Ap index values with lines for all events. There was an increase in DLPT depth on the storm day for the September 2008 and October 2011 events, whereas there was an increase in the storm recovery period for the August 2010 and May 2010 events. Only for the October 11, 2008 storm, a dramatic decrease by 7dB was observed in DLPT depth on the storm day.

Table 1. Properties of geomagnetic storms considered in the study

Event Date	Daily Averaged Ap index	Ap max	Start time
04 Sep 2008	31	80	04 Sep 2008 00:00 UT
11 Oct 2008	34	94	11 Oct 2008

			06:00 UT
29 May 2010	28	56	29 May 2010 06:00 UT
04 Aug 2010	49	111	03 Aug 2010 18:00 UT
25 Oct 2011	38	154	24 Oct 2011 18:00 UT

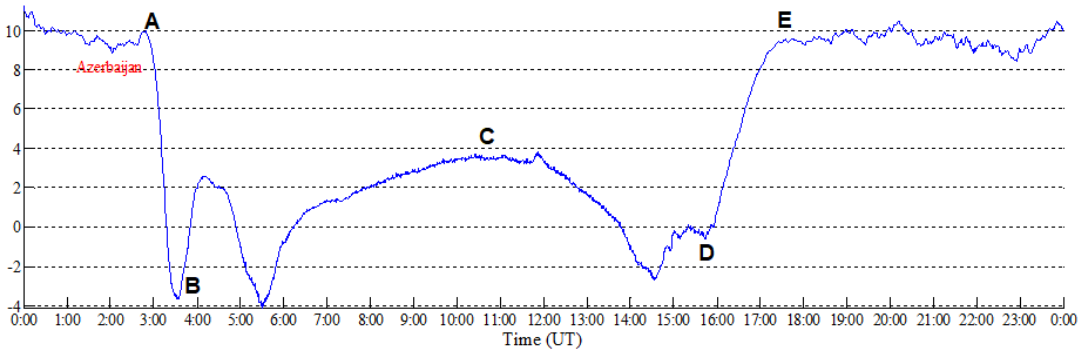

Fig. 3. A diurnal variation of GBZ signal amplitude. A-Sunrise Maxima, B-Sunrise Minima, C-Afternoon Maxima, D-Sunset Minima, E-Sunset Maxima

Discussion and conclusions

The present paper investigated the effect of geomagnetic storms on the D layer of the ionosphere using the DLPT depth parameter of the VLF signal. The “primary storm effect” was observed on the DLPT depth parameter for three magnetic storms, but the “after-storm effect” was observed for the remaining two storms. Clilverd et al. [21] found that phase advance on signal recorded at mid-latitudes is associated with magnetospheric substorms. They suggested that the phase advance is related to triggering energetic electron precipitation during the substorm, concerning electromagnetic ion cyclotron (EMIC) wave-particle interaction. Additionally, the cause of the after-storm effect at mid-latitudes is the loss of energetic electrons from Earth’s radiation belt during the recovery phase of the storm [12, 18].

In this study, DLPT depth showed an increase for all geomagnetic storms, apart from one storm. An increase in DLPT depth resulted from decreased amplitude during the morning terminator with respect to the previous day. This depression of amplitude can be related to a storm-induced increase in electron concentration of the D-layer, which is to say more electron-molecule collisions and consequently leads to absorption of the signal. In the previous works, researchers discussed geomagnetic storm effects on DLPT depth. Kumar and Singh [2] studied a severe geomagnetic storm effect on the D region for the mid-equatorial-low path using VLF signals transmitted from GBZ and NWC transmitters. They observed that DLPT showed an increase during the recovery phase of the storm. Naidu et al. [22] investigated the change of DLPT depth during intense magnetic storms for mid-latitude path and observed an increase in DLPT depth on the storm day, except for one event. They explained that an increase in DLPT depth could be due to a reduction in the reflection height of VLF waves resulting from the enhanced electron concentration of the D layer. Nevertheless, from the study of DLPT depth variation for low-latitude path, Choudhury et al. [20] reported that during

long-duration geomagnetic storms, DLPT depth decreases due to decreased day-night asymmetry caused by increased electron density.

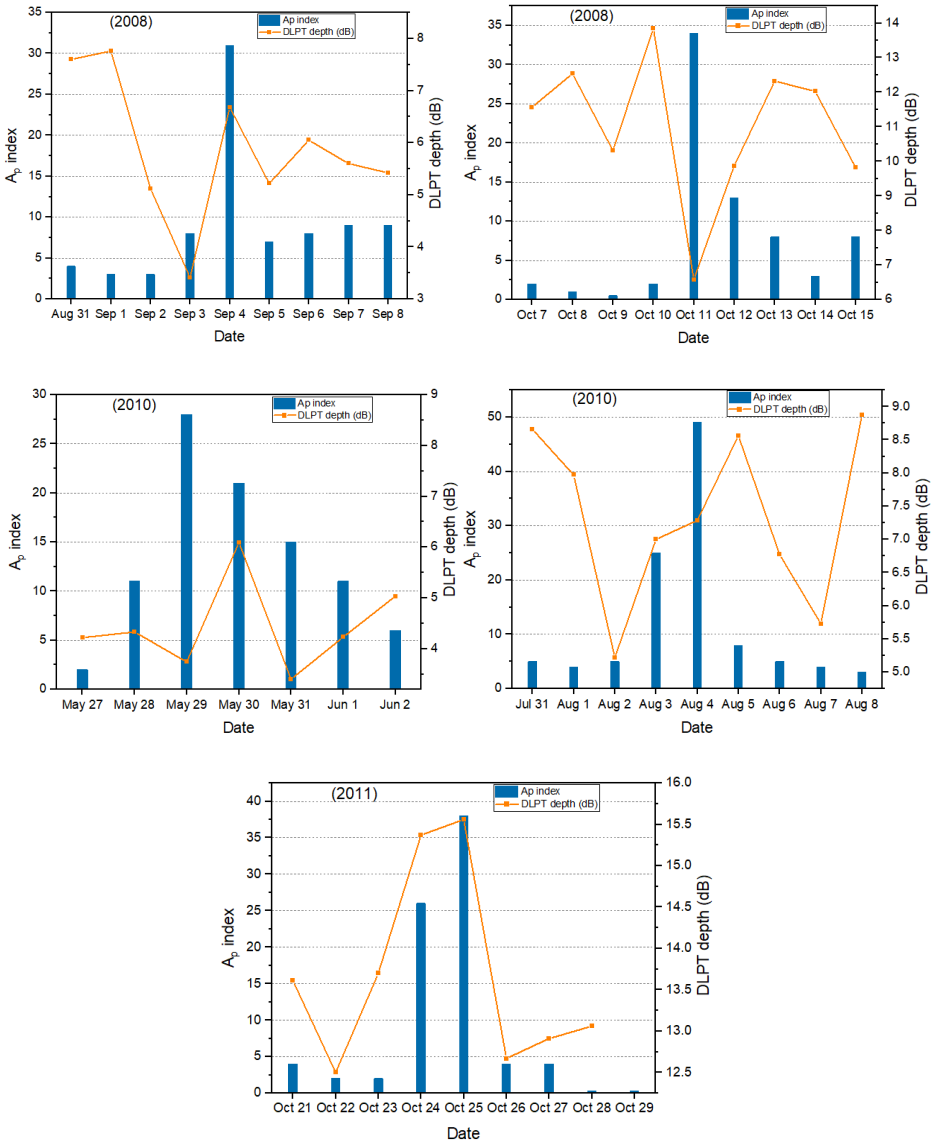

Fig. 4. Nine days variation of DLPT depth and Ap index values for all geomagnetic storms considered in the study

Obtained results showed that the response of the D region to geomagnetic storms varies from storm to storm. We will investigate separately the influence of geomagnetic storms on the D region originating distinct solar and interplanetary sources in the future.

Acknowledgments

This research was funded by the Science Development Foundation under the President of the Republic of Azerbaijan, 1st Azerbaijani-Russian Joint Grant Competition (EİF-BGM-4-RFTF-1/2017). We are grateful to the website of https://omniweb.gsfc.nasa.gov/form/dx1.html for Geomagnetic data.

References

1. Lastovicka J. J. Atmos. Terr. Phys. 1996, v. 58, p. 831. DOI:10.1016/0021 9169(95)00106-9.
2. Kumar A., Singh R. St. Patrick's day geomagnetic storm effect on mid-low-equatorial D-region ionosphere using very low-frequency radio waves. 2nd URSI AT-RASC, Gran Canaria, 28 May – 1 June 2018.
3. Peter W. B., Chevalier M. W., Inan U. S. J. Geophys. Res. 2006, v. 111, p. A03301. DOI:10.1029/2005JA011346
4. Thomson N. R. J. Atmos. Terr. Phys. 1993, v. 55, p. 173.
5. Kumar A., Kumar S. Planets and Space 2014, p. 66-76. DOI:10.1186/1880-5981-66-76
6. Selvakumaran R., Kumar A., Gokani S. A., et al. J.Atmos. Terr. Phys. 2015, v. 123, p. 102. http://dx.doi.org/10.1016/j.jastp.2014.12.009.
7. Bouderba Y., NaitAmor S., Tribeche M. J. Geophys. Res. 2016, v. 121, p. 6799. DOI:10.1002/2015JA022233.
8. Hayes L. A., Gallagher P. T., McCauley J., Dennis B. R., Ireland J., Inglis A. J. Geophys. Res. Space Physics 2017, v. 122, p. 9841-9847. DOI:10.1002/2017JA024647
9. Sreckovic V. A., Sulic D.M., Vujcic V., Jevremovic D., Vyklyuk Y. J. Geogr. Inst. Cvijic. 2017, v. 67, p. 221. DOI: https://doi.org/10.2298/IJGI1703221S
10. Korsakov A. A., Kozlov V. I., Karimov R. R. 24th International Symposium on Atmospheric and Ocean Optics: Atmospheric Physics, Tomsk, Russian Federation, 13 December 2018, Matvienko, G. G.; Romanovskii, O.A. DOI: 10.1117/12.2504428.
11. Sharma, A. K., More C. T. J. Space Sci. & Technol. 2018, v. 6, p. 2321. https://www.researchgate.net/publication/322600215.
12. Spjeldvik W. N., Thorne R. M. J. Atmos. Terr. Phys. 1975, v. 37, p. 777.
13. Cummer S. A., Bell T. F., Inan U. S., Zanetti L. J. J. Geophys. Res. 1996, v. 101, p. 5381. DOI:10.1029/95JA03409.
14. Rodger C. J., Clilverd M. A., Thomson N. R. et al., J. Geophys. Res. 2007, v. 112, p. A11307. DOI:10.1029/2007JA012383
15. Clilverd M. A., Rodger C.J., Gamble R. J. et al. J. Geophys. Res. 2010, v. 115, p. A12304. DOI:10.1029/2010JA015638
16. Kumar A., Venkatesham K., Kumar S., Singh R., Tiwari P., Singh A. K. J. Geophys. Res. Space Physics 2018, v. 123, p. 6836. DOI:10.1029/2018JA025536
17. Araki T. J. Geophys. Res. 1974, v. 79, pp.4811.
18. Larsen T. R., Reagan J. B., Imhof W.L., Montbriand L. E., Belrose J.S. J. Geophys. Res. 1976, v. 81, p. 2200. DOI:10.1029/JA081i013p02200
19. OMNIWeb. https://omniweb.gsfc.nasa.gov/form/dx1.html
20. Choudhury A., De B. K., Guha A., Roy R. J. Geophys. Res. Space Physics 2015, v. 120, p. 778. DOI:10.1002/2014JA020738
21. Clilverd M. A., Rodger C. J., Brundel, J., Bahr J., et al. J. Geophys. Res. 2008, v. 113, p. A103311. DOI:10.1029/2008JA013220
22. Naidu P. P., Madhavilatha T., Devi M. I. Ann. Geophys. 2020, v. 63 (2), p. GM214. DOI:10.4401/ag-8127

SOLAR – TERRESTRIAL RELATIONS AND BIOSPHERE: FROM EARLY EARTH TO PRESENT

M RAGULSKAYA

Department of Solar Physics and Solar-Earth Relations Institute of Terrestrial Magnetism and Radio Wave Propagation, Russian Academy of Sciences, 108840 Moscow, Russia
E-mail: ra_mary@mail.ru

The report considers the influence of space weather factors and the solar dynamics on the biosphere of the early and modern Earth. The verification of the available theoretical models of the formation of the Solar system and physical conditions on the early Earth is carried out from the point of view of the possibility of the modern form life development. The emergence of the biosphere and the geomagnetic field was determined not only by the conditions on the Earth itself, but also by the dynamics of the early Sun, the migration of giant planets and the formation of the Earth-Moon system. Prospects for expanding the search for bacterial life on Mars, on satellites of outer planets and exoplanets are being considered. The development of flu pandemics 1880-2020 and genogeographic features of the pandemic COVID-19 in conditions of low solar activity are being discussed.

Keywords: galactic processes and Solar system, early Sun and Earth, solar dynamics and pandemics, solar UV-radiation and biosphere
PACS: 96.40.-z, 96.90.+c, 98.62.-g

Sun and biosphere

Galactic processes, the dynamics of the Sun and factors of space weather have had a significant impact on the development of the biosphere and physical conditions into the heliosphere and on the Earth during the entire existence of the solar system. At present, the search area for life (in its bacterial form) has expanded significantly. The cradle of life can be molecular galactic clouds and protoplanetary disks, volcanoes and oceans of the Earth, Mars and planets - satellites of giant planets, as well as exoplanets outside the solar system. The luminosity of the parent star and the intensity of radiation on the planet's surface are the main factors for the existence and development of life on our planet, terrestrial planets, satellites of giant planets or exoplanets. For the Earth, it is necessary to consider the dynamics of activity and magnetic fields of the Sun, as well as solar and galactic cosmic rays (Fig 1).

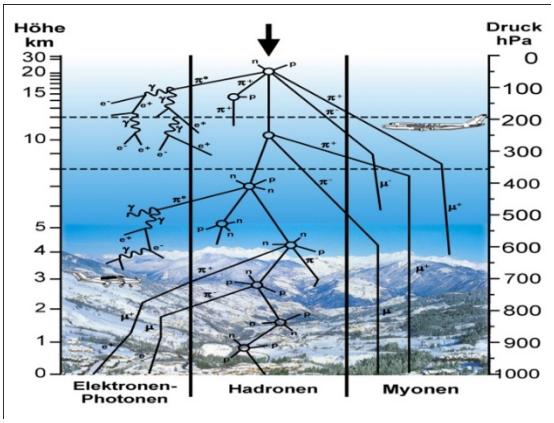

Fig. 1. Cosmic rays in the Earth's atmosphere, height distribution.

For satellites of gas giant planets, these factors are also joined by the radiation of accelerated particles of the main planet. The intensity of solar and galactic cosmic rays (SCR and

GCR) is in antiphase; therefore the activity of the Sun is a determining factor in the radiation safety of both ancient and modern biospheres. Intensity of galactic cosmic rays exceeds the intensity of SCR by several orders of magnitude. GCR have a serious effect on the biosphere, especially at the minima of solar activity.

The early Sun was more active and dimmer at the same time. Flares in the early Sun occurred up to 500 times more often and lasted up to 20 times longer than modern flares. The total luminosity of the early Sun was almost 1.5 times less than the modern one. However, the surface temperature of the early Earth significantly exceeded modern values. The article discusses ways to solve this paradox, and proposes to consider a combination of solar and terrestrial factors. The dynamics of the Sun has a serious impact on the modern biosphere. For example, all influenza pandemics over the past 270 years have occurred at the extrema of the 11-year solar cycle. The COVID-19 pandemic also began at a deep low in both 11-year and quasi-100-year solar cycles. A feature of this pandemic is the large difference in relative mortality and morbidity in countries with different genetic makeup of the population. The most affected in Europe is the R1b haplogroup.

Galactic factors and the solar system. The sun is the main source of energy for all planets in the solar system (SS). Its dynamics modulates all spatio-temporal regularities of the interplanetary medium in the heliosphere. Solar activity affects all shells of the Earth (ionosphere, atmosphere, biosphere and even the lithosphere). The formation of the solar system was not uniform and simultaneous. Theories about the formation of the solar system in a dense stellar association with the presence of nearby massive stars are now being discussed especially actively. The SS formation process took place with the possibility of repeated injections of matter into the pro-planetary disks due to supernova star explosions about 4.66 billion years ago.

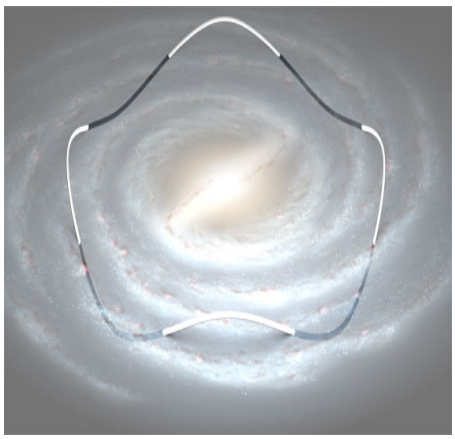

Fig. 2. The trajectory of the Sun around the center of our Galaxy

The solar system (SS) moves around the center of the Milky Way (Fig. 2). The intersection of the SS arms of the Galaxy can lead to an increase in the flux density of galactic cosmic rays up to 5-6 times relative to the current state. This situation could take place 20 to 80 times during the existence of the biosphere It is possible that mass extinctions of biological species are partially associated with this effect.

The distance from the Sun to the center of the Galaxy has fluctuated (Fig 2).The sun makes a complete revolution around the center in about 200-250 million years (1 galactic year). Now the interstellar gas in the immediate vicinity of the Sun (but outside the heliosphere) has a density of several tenths of a particle in a cubic centimeter, the degree of ionization is about 50%. The Sun is located in a cavern of warm gas in the Local Galactic Overshell near the edge of the hot gas. The movement of the Sun through gas of different temperatures and densities also significantly affects the physical conditions in the solar system and on the terrestrial planets. The Sun has passed through interstellar clouds about 130 times with a concentration of particles 150 times greater during its existence (7-8 times per galactic year). And about 16 times the solar system has passed through clouds with a concentration of particles 1500 times greater. The number of anomalous subrelativistic cosmic rays increased hundreds of times during these passages, which could affect the development of the biosphere.

Pre-biological evolution of organic matter. Living organisms are made from the most abundant elements in the universe (H, O, N, C, P, S). All biological matter is a product of the stars of previous generations. The modern composition and balance of chemical elements has developed somewhere around half the time of the existence of the Universe. Therefore, the chemical possibility of the emergence of life appeared not earlier than 7-8 billion years ago (the age of the Universe is about 14, billion years). It was by this time that the stars in the process of their birth, development and death produced a sufficient amount of heavy elements.

Experimental material on the chemical composition of molecular clouds in interstellar space suggests the presence of active prebiological synthesis of complex organic substances already in the process of formation of stellar and planetary clusters. Ion-neutral (or ion-molecular) reactions are widespread in interstellar molecular chemistry.

Cosmic rays provide the primary ionization of the process (Vibe D, [25]). At present, the number of known interstellar and circumstellar molecules is approaching 200 (excluding isomers and isotopomers). The largest molecules identified have 12 atoms (CH3OC2H5, C3H7CN). More complex organic structures - fullerenes, aromatic compounds - are also present in the interstellar medium. A list of experimentally detected interstellar and circumstellar molecules can be viewed at http://astrochymist.org/. It is necessary to admit the possibility of multiple "drift" of organic matter to the early Earth with meteorites, as well as multiple occurrence and destruction of various earthly biological structures proper. It can be assumed that the ready-made organic pre-biological material was synthesized in catalytic cauldrons of astronomical sizes and energies in the protoplanetary cloud. Later, these organic “bricks” became the foundation for the construction of our own terrestrial biosphere.

In works on artificial irradiation of bacterial communities of V. Cheptsov [6] with ionizing radiation at a dose of 1 MGy, it was shown that bacterial colonies can survive in open space under the cover of meteorite matter for up to 3.5 million years.

Traces (fossilis) of eukaryotes are found in meteorites of the age of the solar system. Micro-fossilis from the Orgei meteorite and their modern terrestrial counterparts are shown in

Fig. 3. Based on these data, the head of the Russian astrobiology program, ac. RAS A. Yu. Rozanov assumes the possibility of the existence of the primary world of RNA up to 7 billion years ago, i.e. as early as 2.5 billion years before the emergence of the Earth [22].

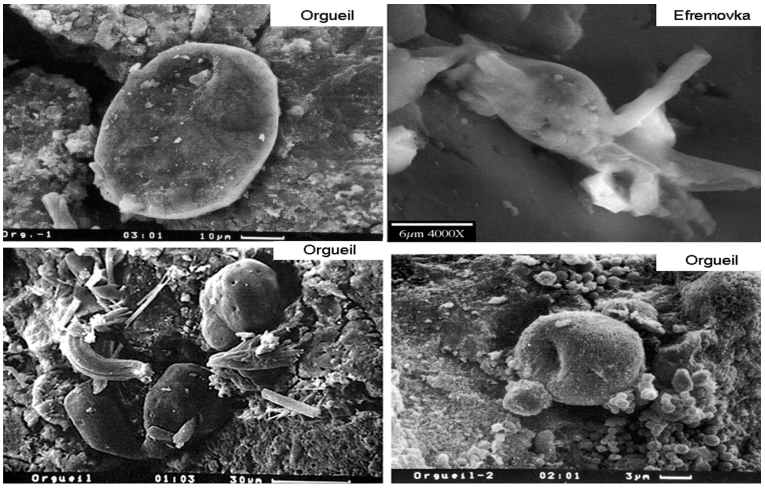

Fig. 3. Micro-fossilis from the Orgei meteorite

The homochirality of biological molecules can also indirectly indicate the involvement of cosmophysical factors in the formation of earthly life. Selective homochirality is characteristic of earthly life. For example, deoxyribose and ribose, which are part of unique DNA and RNA, are right-rotational D-isomers), and proteins contain only L-amino acids. The existing organization of terrestrial life could have arisen even during the formation of the planetary system under the influence of the polarized radiation of the progenitor star of our star cluster. If this supernova emitted light with a degree of circular polarization, then the racemic set of molecules of the protoplanetary disk exposed to such irradiation acquired a slight predominant chirality. Subsequent chemical reactions and intense ultraviolet irradiation can enhance the effect, including under conditions of a protoplanetary disk [15-20].

Young Sun and early Earth

The general picture of ideas about the structure and evolution of solar-type stars, the Sun itself and the first 0.5-1 billion years of its existence is based on observations of sun-like stars. The young Sun (up to 1 billion years) had a period of rotation around its axis of 5-10 days (now 27-29). The mass of the young Sun was greater, up to 103% of the modern one. In that era, the activity of the Sun was higher than it is now, but less regular. The electromagnetic radiation of the Sun at these stages of evolution in the optical range changed insignificantly, but in the soft X-ray range of 0.15 - 4 KeV (shorter than 90 A), the ratio of the X-ray luminosity of the young Sun to its total luminosity was 1000 times higher than the luminosity of the modern Sun at the maximum of the solar cycle. The dimensions of the heliosphere changed significantly during the evolution of the solar system from the early Sun to the present day, as well as depending on changes in the parameters of the galactic environment of our star (Fig 4).

According to the standard model, the luminosity of the young Sun should have been 30% lower than the current one. The Standard Solar Model is the result of calculating the evolution of a star with a mass of 1 solar mass, provided that at an age of 4.6 billion years, the luminosity and radius of the star are equal to modern solar values. The calibration is carried out by fitting 2 parameters: the parameter of the helium content (which cannot be determined from observations) and the parameter of the theory of convection. Some simplifications are also used: complete spherical symmetry of the problem is assumed, the absence of accretion and mass loss, without mixing outside the convection regions, etc. The low luminosity of the young Sun formed a lack of energy input to the young Earth.

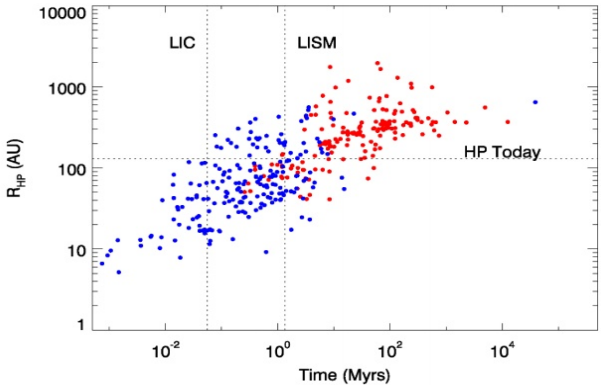

Fig. 4. Evolutionary dynamics of the heliosphere (Bochkarev N, 2017)

At the same time, according to paleoclimatic data, the temperature of the Earth's surface in the first billion years even exceeded modern values [Rozanov A]. This discrepancy formed the basis of the "paradox of the weak young sun." While maintaining the current albedo and emissivity values, the Earth should have spent half of its life without liquid water on the surface. The freezing point of the Earth's ocean water is about 271 K, which corresponds to 0.84 of the modern luminosity of the Sun. The luminosity of our star reached this value only about 2 billion years ago. On the other hand, according to paleontological data, the ancient biosphere and geological rocks available for study were formed in the presence of a large amount of liquid surface water. The assumed surface temperature was at least +60 C.

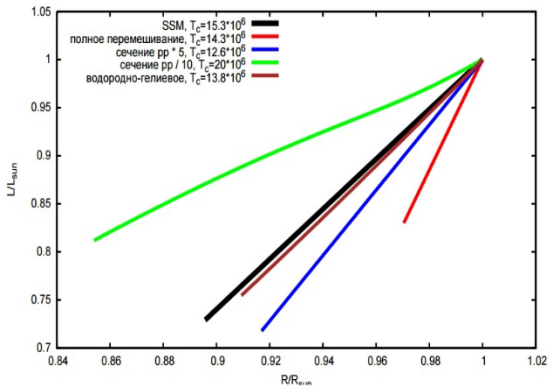

Fig. 5. Non-standard models of the Sun

Factors leveling the weak young Sun paradox can be: 1. Variations of the solar constant in models for the young Sun; 2. Increased mass of the young Sun; 3. Reduced distance between the Sun and the Earth in the early Solar system; 4. Significantly lower albedo of the young Earth; 5. Unaccounted for additional energy sources of the Earth; 6. More powerful greenhouse effect; 7. Primary biosphere of the Earth as an active planetary factor.

Most likely, the required heating of the young Earth's surface provided a combination of several of the considered effects at once, since individually they do not reach the required heating values for the Earth's surface. To compensate for the "paradox of the weak young Sun", the loss of the star's mass must be at least 7%. However, theoretical models can explain the evolutionary loss of no more than 3% of the Sun's mass.

Non-standard models of the Sun provide maximum compensation for no more than 5% of the 30% missing luminosity (Fig.5). However, solar activity not only reduces GCR (and, as a consequence, albedo), but also directly affects the greenhouse effect, stimulating the synthesis of various greenhouse gases, depending on the composition of the planetary atmosphere. Geothermal activity is also an insufficient compensation factor. Another location of the early Earth and Mars apparently did take place during the formation of the SS in connection with the migration of Jupiter and Saturn, but only in the first 50 million years.

The greenhouse effect may be the largest contributor to the heating of the planet. But the increase in the greenhouse effect is limited by an increase in the concentration of carbon dioxide in the atmosphere of the early Earth by no more than 3 times (according to geological data). This amount is clearly not enough to provide the desired effect. For Mars, the required surface heating could provide the greenhouse effect of the ancient atmosphere, consisting mainly of carbon dioxide (90%), methane and its decay products (5–10%). As shown in [Wordsworth et al, 2017], collisions between carbon dioxide and methane molecules alter their probability of absorbing photons. The atmosphere of a mixture of these gases retains heat much better. The greenhouse effect in this scenario is much stronger than previously thought. It could heat Mars to zero degrees Celsius even in the weak sunlight of the young Sun, ensuring the existence of ancient oceans.

Consideration of the primary biosphere of the Earth as an active planetary factor is a promising area of research. E. Khramova [18] proposed the hypothesis of oceanic films. Oceanic films could be a constant donor of greenhouse gases, increase the temperature of the ocean, form new organic compounds under the influence of UV radiation from the young Sun, and at the same time protect the primary oceanic biosphere from the aggressive radiation of the young Sun.

Habitable zone

The main criteria for the existence of the terrestrial biosphere are: 1. The presence of sources and energy gradients necessary to maintain biochemical processes, including in the form of chemical energy; 2. The presence of a large number and gradient of various organic compounds; 3. The presence of protective shells in the celestial body - the carrier of life; 4. The presence of liquid water on a space object for a long geological period of time.

Possible habitable zones (according to NASA materials) are shown in the Fig 6.

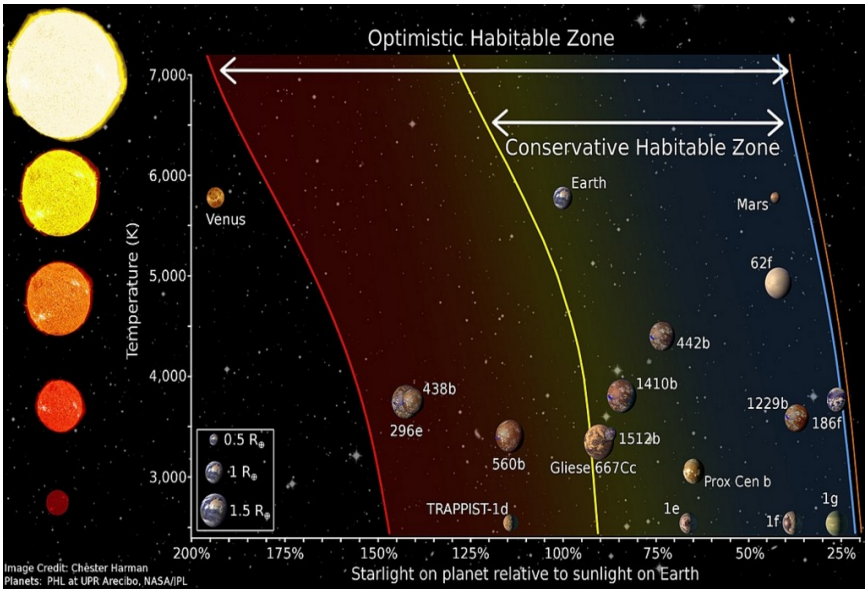

Fig. 6. Conservative and optimistic Habitable zone (NASA)

Mars is included in both the conservative and optimistic habitability zones. At present, a complex of physicochemical conditions, which is extreme for terrestrial organisms, has formed on Mars. Low temperatures and atmospheric pressure, high intensity of ionizing and ultraviolet radiation, the presence of strong oxidants, low availability of water are characteristic of this planet now. However, early Mars had all the ingredients for possible life. There were oceans (comparable in volume to the earth's water) and a large amount of organic matter. Also present were energy sources, a magnetic field and a dense protective atmosphere. Most of the meteorites known to us are Martian, so Mars cannot be excluded from the possible sources of the earth's biosphere. The possibility of the survival of microorganisms during ultra-high-speed impacts in the composition of meteorites and in open space is being actively discussed.

Venus does not enter the optimistic habitable zone due to the high temperatures and pressure on its surface, as well as the chemically extremely aggressive environment. But recently, work on catalytic chemistry has appeared, which shows that it is precisely such a set of conditions that can allow the formation of life based on nitrogen instead of carbon. In V. Snytnikov's model it is shown that on Venus many functions of water can be performed by a supercritical fluid of carbon dioxide [12].

The formation of the complex of protective shells of the Earth, thanks to which the modern biosphere exists, was completed not so long ago. At present, the Earth's biosphere is protected from active galactic and solar influences: 1. The heliosphere (the Sun's magnetosphere). 2. Hydrosphere (oceans). 3. The Earth's magnetic field (Earth's magnetosphere). 4. Atmosphere (moreover, the ionosphere and ozonosphere should be separated from the atmosphere, each of which protects from different types of external influences and radiation). 5. Lithosphere.

Radiation of the young Sun and the early biosphere of the Earth. The origin of the first terrestrial living systems is a controversial and controversial issue. The age of the Earth itself is 4.5 billion years, the existence of the first terrestrial ecosystems dates from 3.8 billion years ago (according to optimistic estimates - 4 billion years ago). The gene constructor of the modern earth's biosphere consists of 4 nitrogenous bases (A, C, G, T). They are maximally resistant to UV radiation. Apparently, it was the spectrum and intensity of radiation of the young Sun and cosmic rays that determined such a composition of terrestrial genes (and even more so than the physical conditions on the early Earth).

Recall that the young Sun did not have an ordered dynamics of activity and the usual 11-year cycle of solar activity, its orbital period was much shorter (3-8 days instead of the current 27), and the intensity of sporadic radiation in the X-ray and UV ranges was orders of magnitude higher present. Life on Earth is associated with complex carbon-based molecules. For them, the most important is radiation in the range of less than 350 A. In this range, there is a powerful resonance line of ionized helium (He II) 304A and numerous weak lines of highly ionized atoms that form in the solar corona. At present, the total radiation in this range changes during the 11-year cycle of activity by 5-7 times, and during flares - by 2-3 orders of magnitude. The total radiation of the young Sun (1 billion years old) in the region of 200 - 350 A was constantly higher than the modern one by 10 - 30 times, and during flares - up to 1000 times more. Therefore, the resistance of biological structures and communities to the intense sporadic radiation of the young Sun in the X-ray and UV ranges was the governing factor of Earth emerging biosphere evolution. The optimal system for collecting and storing biological information, which is maximally resistant to ultraviolet radiation from the young Sun, has become a single genetic code for all living organisms on Earth.

Many evolutionary milestones in the development of the biosphere are not biological, but physical in nature. For example, the emergence of multicellular organisms and topologically "more densely packed" twisted forms of proteins allows biological objects to more successfully withstand destructive external UV and X-ray radiation and cosmic rays even with partial destruction of the outer shell of a living structure. The emerging biological structures and ecological systems had to simultaneously "be able to use" ultraviolet radiation as an energy source, effectively protect themselves from it, and also undergo selection for resistance to the destructive effects of radiation from the young Sun.

The biosphere also adjusted to changes in the magnetic fields of the Sun. In the early Sun, the magnetic fields had a more closed structure, and the bulk of the mass removal was carried out due to flare processes. After 2-2.5 billion years of existence, dipole configurations of magnetic fields began to prevail on the Sun, the dynamics of the Sun became periodic, and the outflow of mass was determined mainly by the outflow of matter from coronal holes. The solar wind has played the role of a serious factor affecting the biosphere of the Earth now. Individual living organisms and species as a whole react to both solar cycles and fluctuations in solar wind parameters. For example, in the work of S. Samsonov and S. Parshina it is shown that the human cardiovascular dynamics (the symmetry coefficient of the T-wave) depends on the speed of the solar wind flow [23].

The modern sun and pandemics. The dynamics of the Sun has a serious impact on the modern biosphere. For example, all influenza pandemics over the past 270 years have occurred at extrema of the 11-year solar cycle (Fig 7).

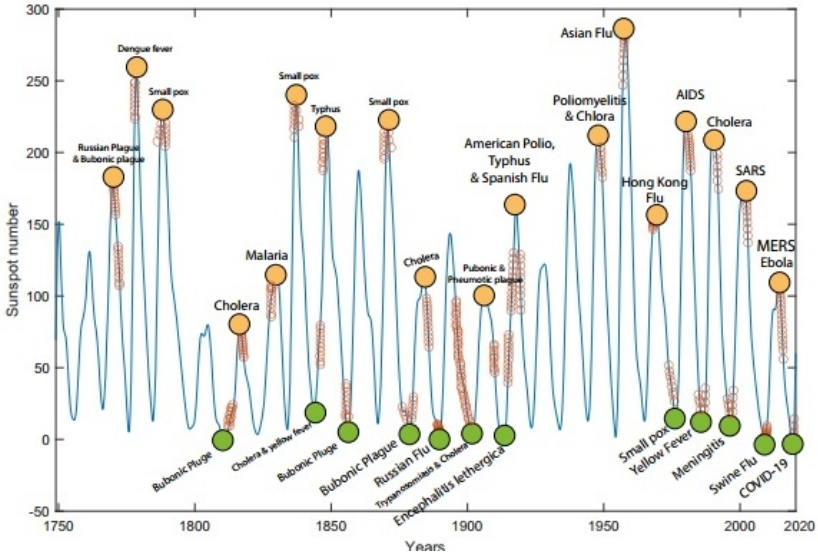

Fig. 7. The number of sunspots and pandemics 1750-2020

The COVID-19 pandemic also began at a deep low in both 11-year and quasi-100-year solar cycles. The methods of modern medicine and most of the drugs were developed in the conditions of high solar activity in the 20th century. They have proven to be ineffective in a pandemic that occurs during prolonged low levels of solar activity. A feature of the COVID-19 pandemic is the large difference in relative mortality and morbidity in countries with different genetic makeup of the population. The COVID-19 pandemic is most severe in countries with a dominant haplogroup R1b (the relative number of deaths per million is more than 12-25). Local COVID-19 epidemics were more easily in countries with a dominant haplogroup N (relative number of deaths less than 3). The incidence per million people in haplogroups R1b: R1a: N has a ratio of about 7: 2: 1. This ratio no depends of the pandemic waves and the population vaccinated rate. Vaccination effectiveness may depend on the population's genetic characteristics too.

Conclusion

The emergence and development of the Earth's biosphere was accompanied by such powerful physical factors as galactic and solar cosmic rays, as well as the magnetic field of the Sun, the protoplanetary disk and the Earth. The processes of the emergence of life could begin already at the stage of the formation of star clusters from molecular clouds or in protoplanetary clouds. The resistance of biological structures and communities to the intense sporadic radiation of the young Sun in the X-ray and UV ranges was one of the governing factors that determined the direction of Earth emerging biosphere evolution. The early Sun was more active and dimmer at the same time. Outbreaks occurred up to 500 times more often and lasted up to 20 times longer than modern outbreaks. The total luminosity of the early Sun was almost

1.5 times less than the modern one. However, the temperature of the Earth's surface significantly exceeded modern values. Explaining this paradox requires a comprehensive consideration of solar and planetary factors, since they do not separately explain the physical conditions on the early Earth. The modern Sun has become calmer and more orderly, protective shells of the Earth (atmosphere, ozonosphere, magnetosphere, hydrosphere) have appeared. At the same time, biological organisms have retained the mechanisms of adaptation to solar activity and space weather factors. For the survival of an individual organism, it is important to be able to adapt to short-term changes in the external environment, comparable to its own time scales (minutes, days, years). For the biosphere as a whole, it is necessary to preserve programs of protection and adjustment to space weather factors on long time scales: 1. Adaptation is required to strong UV radiation, X-rays and cosmic rays during periods of increase or decrease in solar activity (characteristic time - several times per millennium); 2. It is necessary to adjust to the reversals of the Earth's magnetic field (the characteristic time is several times in a million years). 3. It is also required to preserve the programs of adaptation to the increase in the level of galactic cosmic rays when the Solar system passes through the dense arms of the Galaxy (several times in a billion years). When looking for possible life on exoplanets, the intensity of cosmic rays, radiation from the parent star and radiation from gas giant planets are the main factors that simultaneously limit and stimulate the development of life. The peculiarities of the course of viral pandemics also significantly depend on the combination of 11-year and 100-year cycles of solar activity.

References

1. Atri D., Melot A. A P 2014, v. 53, p. 186.
2. Austin, N. et al. JVI 2020, v. 94. DOI: 10.1128/JVI.00510-20.
3. Belisheva N. K., Lammer, H. at al. ASST 2012, v. 8, p.7.
4. Bochkarev N. Astronomy Reports 2017, v. 61 (4), p. 307.
5. Cheptsov V et al. Geosciences 2018, v. 8, p. 298.
6. Dergachev V. A. GA 2015, v. 55, 2, 139-51
7. Dizdaroglu, M. 2012, C L, 327, p. 26.
8. Gaucher, E. et al. Nature 2008, v. 451 (7179), p. 704.
9. Güdel, M. LRSP, 2007, v. 4 (1), p. 137.
10. Ishkov, V. S R 2017, v. 55, p. 391.
11. Ksanfomality L., Zeleny L., Parmon V., Snytnikov V. Advances in Physical Sciences 2019, v. 189 (4), p. 403.
12. Manzella N., Bracci M., Ciarapica V. 2015, Bioelectromagnetics, v. 36 (4), p. 294.
13. McComas, D. J. et al. ApJ 2013, v. 779, p.2.
14. Mironova, I. A. et al. JASTP 2016, v. 149, p. 146.
15. Obridko V. N., Nagovitsyn Yu. A. Solar activity, cyclicity and forecasting methods Press VVM 2017.
16. Obridko V., Ragulskaya M., Khramova E. JASTP 2020, v. 208, id. 105395.
17. Ragulskaya M, Obridko V, Khramova E. Biophysics 2020, v. 65 (4), p. 686.
18. M. V. Ragulskaya. The sun and the biosphere: billions of years together. M, Radiotekhnika, 2019. http://www.izmiran.ru/pub/izmiran/Ragulskaya-Sun-2019.pdf
19. Ragulskaya M. V. JNPPR 2020, v. 7(1), p. 031.
20. Ragulskaya M., Tekutskaya E. IOP CS: EES 2021, v. 853, p. 012002. doi:10.1088/1755-1315/853/1/012002

21. Rozanov A. Yu., Hoover R.B., Krasavin E. A. at al. 2020. Meteorite Orhei (atlas of microfossils). Moscow: PIN RAN.
22. Samsonov S, Parshina S. IOP Conf. Series: Earth and Environmental Science 2021, v. 853, p. 012028.
23. Tekutskaya, E. E., Baryshev, M. G., Gusaruk, L. R., Ilchenko, G. P. Biophysic 2020, v. 65, p. 564.
24. Vibe D, Avedisova V, Surdin V. Galaxies. M. Fizmatlit, 2019.

ELECTRICAL PROPERTIES OF p-Si/$Cd_{1-x}Zn_xS(Se)_{1-y}Se(Te)_y$/ZnO HETEROJUNCTIONS

HM MAMEDOV[1], MA JAFAROV[1], SI SHAH[2], EF NASIROV[1], DN PIRIYEVA[1], SV GANBAROVA[1] and AR RASULOVA[1]

[1]Baku State University, Baku, Azerbaijan
[2]Delaware University, USA
E-mail: dilara.piriyeva@bsu.edu.az

Electrical properties of p-Si/$Cd_{1-x}Zn_xS(Se)_{1-y}Se(Te)_y$/ZnO heterojunctions deposited by the method of electrodeposition from aqueous solution were analyzed. The results indicate that, optimizing the composition of $Cd_{1-x}Zn_xS(Se)_{1-y}Se(Te)_y$ films, substrate surface and heat-treatment conditions, one can obtain *p*-Si/$Cd_{1-x}Zn_xS(Se)_{1-y}Se(Te)_y$ heterojunctions suitable for the fabrication of rectifier diodes with high-rectification coefficient. However, the increase in band width with the addition of Zn leads to an increase in the contact potential difference in the p-Si/$Cd_{1-x}Zn_xS$ heterostructures and a decrease in the conduction band difference in the conduction band (in thin layers with x=0.8, ΔE_c=2.22 eV, Si with CdS contact ΔE_c=2.7 eV) which increases their applicability in solar energy converters. The investigation of p-Si/$Cd_{1-x}Zn_xS(Se)_{1-y}Se(Te)_y$ heterostructures by a scanning electron microscope shows that after 11-13 minutes of heat-treatment in an argon environment at 410^0C the near conduction band becomes sharper and the metal /semiconductor excess in the transition region decreases sharply. Electron-molecular processes and recrystallization occur not only on the surface of thin layers, but throughout the volume during heat-treatment have been established.

Keywords: electrochemical deposition, thin film, heterojunction, heat treatment, solar cell, rectifier diodes
PACS: 71.55.Gs; 78.20.-e; 85.30.-z; 85.60.Dw

Introduction

Unique chemical, mechanical, electrical, thermal, optical and photoelectrical properties of silicon contribute to its wide application in various fields of electronics and semiconductor manufacturing of a special purpose. However, single crystals of Si are well studied materials; therefore, their use at manufacturing of heterojunctions p-Si/$A^{II}B^{VI}$ will be good way of deep studying of electrical properties of films $Cd_{1-x}Zn_xS_{1-y}Se_y$, $Cd_{1-x}Zn_xS_{1-y}Te_y$ and $Cd_{1-x}Zn_xSe_{1-y}Te_y$. There are many techniques used to synthesize of thin films of $A^{II}B^{VI}$ compounds such as thermal evaporation, chemical bath deposition, successive ionic layer absorption and reaction (SILAR), magnetron sputtering, MOVPE etc [1-20]. Of all these methods electrochemical deposition is preferred due to it's relatively ease, not expensive and suitable technique for the deposition of high quality and large area films [1-6]. The aim of the work is to determine the electrical characteristics of the dominant transfer mechanism, charge carriers of heterojunctions deposited by the method of electrodeposition from aqueous solution.

Result and Discussion

After direct deposition, all compositions of heterostructures type p-Si/$A^{II}B^{VI}$ have the property of rectification (Fig. 1). Rectification direction corresponds to the case where a positive potential is applied to p-Si. It can be seen from Figure 1a, the value of the direct current at the electrical contact of Si with CdS decreases with the addition of Zn to the composition. As the Cd/Zn ratio in the thin layers of $Cd_{1-x}Zn_xS$ increases, the value of the direct

current increases, while the current decreases sharply. The best rectification (k = 60) is observed in heterostructures based on thin layers of x = 0.6 (Figure 2a), which shows the compatibility of the lattice parameters of p-Si with those thin layers. The decrease in the rectification coefficient with the addition of Zn can be explained by the increase in the resistivity of the thin layers $Cd_{1-x}Zn_xS$ and consequently, the insufficient separation of the electron-hole pair. However, the increase in band width with the addition of Zn leads to an increase in the contact potential difference in the p-Si/$Cd_{1-x}Zn_xS$ heterostructures and a decrease in the conduction band difference in the transition region (in thin layers with x=0.8, ΔEc=2.22 eV, Si with CdS contact ΔEc=2.7 eV) which increases their applicability in solar energy converters. Also, the high resistance of $Cd_{1-x}Zn_xS$ thin layers to deformation allows them to be widely used in flexible solar panels. In order to control the lattice parameter, the resistivity of the thin layers and accordingly, the zone difference in the heterojunctions (ΔEc and $\Delta E\vartheta$), the optical emission factor, the series resistance of the transition, etc., by taking the width of band gap constant (or vice versa), we tried to make electrical contact with p-Si of thin layers of solid solutions $Cd_{1-x}Zn_xS_{1-y}Se_y$, $Cd_{1-x}Zn_xS_{1-y}Te_y$ and $Cd_{1-x}Zn_xSe_{1-y}Te_y$ by adding Se or Te at a certain concentration to the thin layers of $Cd_{1-x}Zn_xS$. Thus, such contacts stimulate both the creation of new types of alternative diode structures, as well as the study of physical processes in thin layers of complex structure based on the parameters of Si known in the scientific literature and, consequently, the creation of a new section of micro- and nanoelectronics based on complex semiconductors would have given.

As shown in Figures 1c and 1d, the addition of a small amount of Se (y= 0.1; 0.2) to the thin layers of $Cd_{1-x}Zn_xS$ results in a decrease in the specific resistance and an increase in the rectification coefficient. Components x = 0.6 and 0.7 of the four-component thin layers of $Cd_{1-x}Zn_xS_{0.9}Se_{0.1}$ and $Cd_{1-x}Zn_xS_{0.8}Se_{0.2}$ show the best rectification at electrical contact with p-Si (k = 1800). In the subsequent increase in the amount of zinc in the thin layers, the increase in the resistivity of the layers and, accordingly, the successive resistance results in a sharp decrease in the rectification coefficient. Also, despite the decrease in resistivity with increasing amount of Se in the composition, the difference in their lattice parameters with Si leads to a decrease in the rectification coefficient and even the acquisition of Ohmic contacts in some compositions. When adding Te, the rectification coefficient in $Cd_{1-x}Zn_xS_{0.9}Te_{0.1}$ compositions has the maximum value at the values of Zn with x=0.9 (k = 9000). In the subsequent increase of Te, a sharp decrease in the rectification coefficient is observed. When Se is added at a small concentration (x = 0.1) to the thin layers of CdS, the direct current decreases sharply compared to the thin layers of $Cd_{1-x}Zn_xS$ (Figure 1b). However, with increasing the concentration of selenium to x = 0.2, a relative increase in the direct current is observed, and vice versa, a decrease in the current. By increasing the concentration of selenium in the composition to $x<0.8$ a decrease in the rectification coefficient is observed in p-Si/$CdS_{1-x}Se_x$ heterojunctions and a sharp increase (k=2200) is observed in the rectification coefficient in x = 0.8 (Figure 2a). With further increase in the concentration of selenium in the composition, the rectification weakens again. All this shows that the dependence of the lattice parameter on the composition of the thin layers $CdS_{1-x}Se_x$ does not follow Vegard's linear rule.

That is, the electrical contacts with the p-Si of the thin layers $CdS_{1-x}Se_x$ containing x = 0.2 and x = 0.8 can be applied as rectifier diodes. In the electrical contacts of thin layers of solid solutions of the CdSe-ZnTe system with p-Si, both the mechanism of current transfer and the value of rectification vary significantly compared to previous thin layers. Thus, p-$Si/Cd_{0.05}Zn_{0.95}Se_{0.9}Te_{0.1}$ heterostructures exhibits $k \approx 4200$ rectification after direct precipitation.

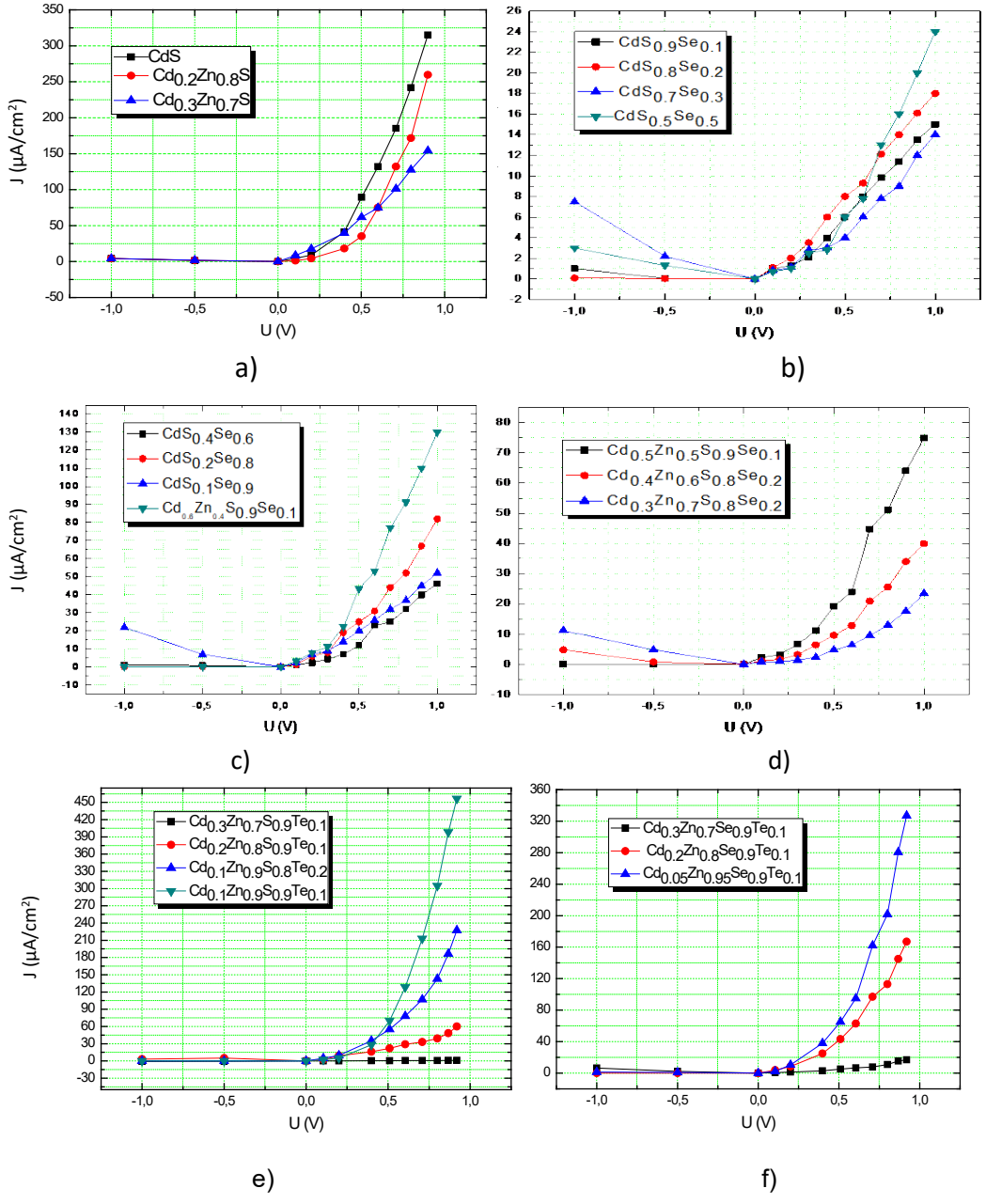

Fig. 1. Dark VAC of p-Si/$A^{II}B^{VI}$ heterostructures at room temperature after direct deposition.

As can be seen from the figure, the direct current up to voltages U≤0.6 V increases exponentially with the known expression:

$$I = I_0\left[\exp(\frac{qU}{nkT}) - 1\right] \quad (3)$$

Here, I_0 – is the saturation current flowing through the diode, q is the charge of electron, k-Boltzmann's constant, T- temperature, n - non-ideality coefficient of VAC of studied structure. The values calculated based on the expression of the non-ideality coefficient $n = \frac{q}{kT}\frac{\Delta U}{\Delta ln J}$ using the figure are shown in Table 1 As can be seen, the value of n in the wide voltage range is very high in CdS-based heterocurrents.

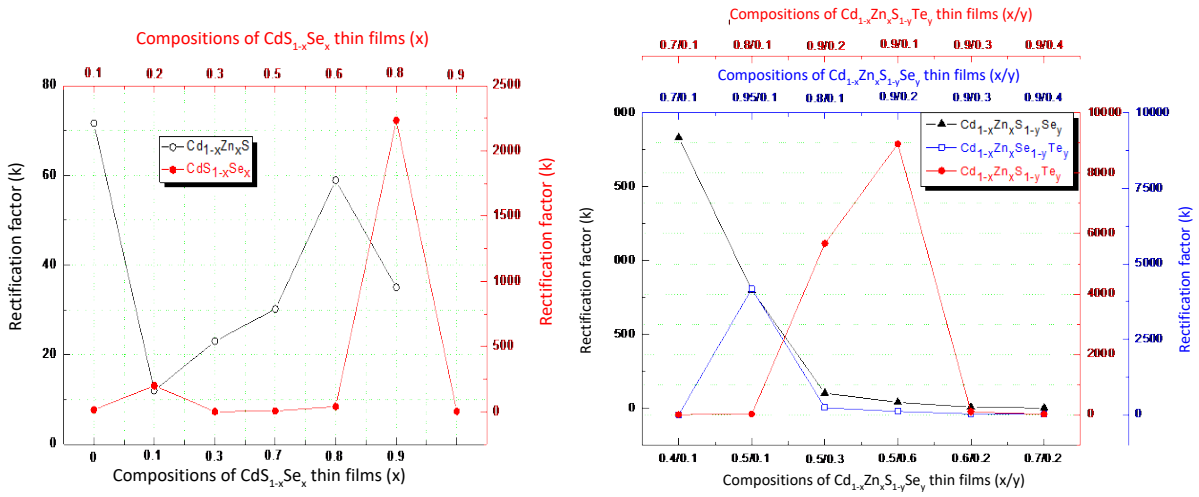

a) b)

Fig. 2. Dependence of the rectification coefficient on the components of thin films in p-Si/n-$A^{II}B^{VI}$heterostructures immediately after deposition

Figure 3 illustrates the VAC on a semi-arithmetic scale in the direct direction of several thin film-based heterojunctions. This is due to the large recombination acts of both carriers in the bulk area due to the mismatch of the Si and CdS lattice parameters, and the stepped emptying of the defect centers with increasing voltage (weak crosswalks and tunnel crossings due to the high value of ΔE_c proves once again that it is dominant [4-5]. The predominance of tunneling currents results in insufficient photoelectric parameters of solar cells based on Si/CdS diode structures. The addition of Zn, Se, or Te to CdS changes the structure and energy structure of the transition region. Thus, with the addition of Zn, the non-ideality coefficient decreases to n=1.8 in small values of external voltage (U≤0,2V). This shows that with the addition of Zn, the lattice parameters of the thin layers of $Cd_{1-x}Zn_xS$ match with Si, however, at the same time the increasing of successive resistance of Si/$Cd_{1-x}Zn_xS$ heterostructures results in the predominance of recombination currents at low voltages in thin films, because of main part of the external voltage falls on thin layers, not on the bulk area. The decrease in the value of n with increasing external voltage (in the potentials of 0,2≤U≤0,5V the value of n decreases till the 1,4) and temperature (Appendix Figure 3) indicates that the recombination centers are donor-type centers. In our opinion, these centers are mobile (levels that can be controlled by external influences) levels associated with the degree of polycrystallization of thin layers and the metal/semiconductor vacancies in them.

Table 1. Electrical parameters of p-Si/$A^{II}B^{VI}$ type heterostructures after direct deposition

Sample	Non-ideality coefficient (U≤0,2 V)	Non-ideality coefficient (0,2≤U≤0,5V)	Rectification factor	Opposite saturation current (A)	Series resistance (Om) for 1 cm^2 area	Contact potentials' difference (eV) (Calculated on VAC)	Contact potentials' difference (eV) (Calculated on VFC)	Current carrying mechanism	Differences in conduction zone ΔE_c (eV)
Si/CdS	2,5	**2,5**	72	$4,6 \cdot 10^{-7}$	1	0,45		Tunnel-recombination in the bulk area due to both carriers	2,74
Si/$Cd_{0.4}Zn_{0.6}S$	1,8	**1,4**	60	$2,3 \cdot 10^{-8}$	5,6	0,57	0,58	U≤0,2 V voltages: Tunnel recombination due to the holes At 0,2≤U≤ 0,5V voltages: Diffusion	2,24
Si/$CdS_{0.2}Se_{0.8}$	2,1	**1,8**	2200	$\approx 10^{-8}$	2	0,5	0,52	Tunnel-recombination in the bulk area due to both carriers	2,57
Si/$Cd_{0.3}Zn_{0.7}S_{0.8}Se_{0.2}$	1,6	**1,3**	1800	$1,2 \cdot 10^{-8}$	6,3	0,63	0,6	U≤0,2 V voltages: Tunnel recombination due to electrons At the voltages of 0,2≤U≤ 0,5V: Diffusion	2,34
Si/$Cd_{0.1}Zn_{0.9}S_{0.8}Te_{0.2}$	1,5	**1,45**	9000	$4,2 \cdot 10^{-8}$	4,2	0,6	0,64	Recombination+Diffusion	2,15
Si/$Cd_{0.05}Zn_{0.95}Se_{0.9}Te_{0.1}$	1,2	**1,2**	4200	$\approx 10^{-9}$	0.8	0,58	0,611	Diffusion	2,28

Thus, with the increase of the external stress in the plane, as a result of filling the recombination centers of the holes injected into the transition zone from Si, the cross-links are already predominant, which results in a decrease in the value of n. Also, with the addition of Zn a decrease in the value of ΔEc and an increase in the contact potential difference (Table 1) reduce the probability of tunnel transitions which indicates that the photoelectric parameters of Si/$Cd_{1-x}Zn_xS$ heterojunctions will be better than those of Si/CdS heterostructures.

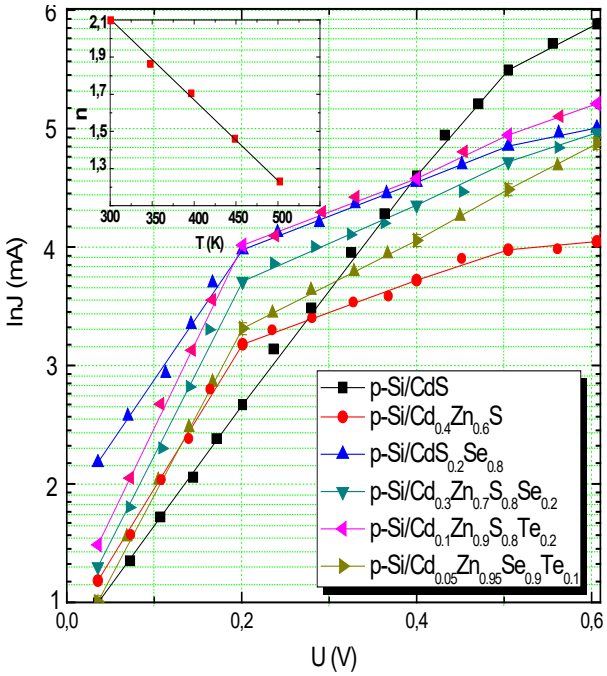

Fig. 3. Semi-logarithmic VAC of p-Si/n-$A^{II}B^{VI}$heterojunctions after deposition.

Although the addition of Se to CdS reduces the mismatch of the lattice parameters, the value of the non-ideality coefficient does not decrease significantly (Table 1) up to the values of the external voltage U≤0,5V. Tunnel-recombination currents predominate in Si/$CdS_{1-x}Se_x$ heterojunctions. As we know the addition of Se reduces the specific resistance of thin layers, but vacancies (most likely both donor and acceptor type) associated with an excess of metal / semiconductor on the surface and increase in the degree of polycrystalline of thin layers with the addition of selenium increase recombination acts of both types of carriers in the transition area that leads to a violation of the exponential dependence of the direct current from the external voltage on the cross-links.

As can be seen, the addition of Zn to CdS increases the concentrations of donor-type vacancies, with the addition of Se increases the concentrations of acceptor-type vacancies at low concentrations and donor-type vacancies at high concentrations. In order to control the concentration ratio of donor/acceptor type vacancies, we added both metal (Zn) and semi-metal (Se, Te) to the CdS at the same time. The resulting thin layers of solid solutions of all three types of four-component compounds ($Cd_{1-x}Zn_xS_{1-y}Se_y$, $Cd_{1-x}Zn_xS_{1-y}Te_y$ and $Cd_{1-x}Zn_xSe_{1-y}Te_y$) tunnel-recombination currents in electrical contacts with Si are sharply reduced. Of course, the value of n that does not decrease to the unit indicates that the concentration of defects is not fully compensated, however, the predominance of diffusion currents, increasig of the contact potential difference, and decreasing of the difference between the conductive zones (Table 1) indicate that four-component compounds are more promising.

In general, the scientific literature also suggests a method of deposition of a high or low resistance middle layer to the junction in order to control the concentration of defects in the transition area. Thus, the middle layer allows to reduce the height of the potential barrier in accordance with the defects caused by the difference between the lattice parameters and the

coefficients of thermal expansion of the materials brought in contact and to minimize excess tunneling currents. In this work, in order to minimize the value of excess tunneling currents in Si-based heterojunctions and, as a result, to improve the electrical and photoelectric parameters of heterojunctions, high and low resistance thin layers with different chemical compositions (CdS, CdTe, CdSSSe, CdZnS) were obtained. As a result, it was determined that it is possible to control the concentration of transient defects by changing the chemical composition, percentage, crystal structure, thickness and specific electrical conductivity of the middle layer. It should be noted that only generalized results are described in this article, as the topography of the transition zone with the middle layer can be controlled by the choice of the environment and mode of thermal processing, and physical processes occur with almost the same regularity.

As can be seen from the table, the lowest values of the non-ideality coefficient are observed in p-Si/n-$Cd_{1-x}Zn_xS_{1-y}Te_y$(x=0.9; y=0.2) and p-Si/$Cd_{1-x}Zn_xSe_{1-y}Te_y$(x=0.95; y=0.1) heterojunctions which indicates that they are closer to the ideal heterojunction properties. For a more detailed analysis of the transition region of the studied heterojunctions, we studied the capacitance-voltage (VFC) and capacitance-frequency (VTC) characteristics of the transition in them. Figure 4 shows graphs of the dependence of junction capacitance from external voltage for heterojunctions of different compositions. As can be seen from the figure, in heterostructures based on thin layers of four-component solid solutions, the junction capacity varies more sharply depending on the external voltage, and the value of the transition capacity is greater at U = 0.

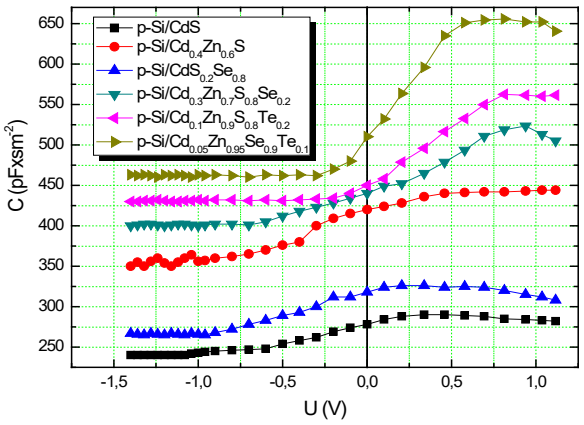

Fig. 4. Volt-farad characteristics for different compositions of p-Si/n-$A^{II}B^{VI}$ heterojunctions after direct deposition.

Using the graphs, the C^{-n}=f(U) dependencies were constructed for heterojunctions of different compositions (Figure 5).

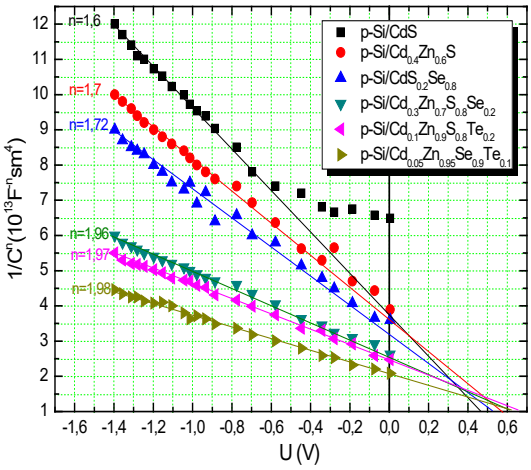

Fig. 5. After direct deposition volt-farad characteristics of p-Si/n-$A^{II}B^{VI}$ heterojunctions in the C^{-n}=f(U) scale.

As can be seen from the graphs, for CdS-based heterojunctions, the graph line is close to the linear function when n = 1.6, which proves once again that the frequency dependence of the capacitance for these different components is not sharp in bulk boundaries and has recombination centers in the transition area. In heterojunctions based on thin layers of four-component solid solutions $n \approx 2$ (1,96-1,98) and the frequency dependence of the capacitance in these heterojunctions (Figure 6) is weaker, which proves that their transition region is close to ideal. According to Figure 6, the transition capacitance of all composite heteroconductors up to $f \approx 40$ kHs is almost constant.

At higher frequencies, the capacity decreases. As can be seen, the reduction is weaker in heterojunctions based on four-component compounds with a low concentration of transition states. It is clear that the sharpness of the decreasing region in the frequency characteristics of the capacity determines the addition of the defect level to the total capacity of the transition. Based on the temperature dependence of the electrical capacity, it was determined that as the temperature increases, the height of the decreasing region observed in the characteristics decreases due to the discharge of recombination levels. In order to calculate the energy depth of the defect levels, firstly, the characteristic frequency (ω_t) of those levels was determined. For this reason graphs at different temperatures $\frac{dC}{d\omega} = f(\omega)$ were used Based on the characteristic frequencies determined from the graphs $\ln\left(\frac{\omega_t}{T^2}\right) = f\left(\frac{1000}{T}\right)$ the Arrenius curves were constructed and the energy depth of the defect levels was calculated based on these curves (E_1= 0.157 eV (for $Cd_{0.05}Zn_{0.95}Se_{0.9}Te_{0.1}$ thin films) and E_{II}= 0.276 eV (in all type heterojunctions)).

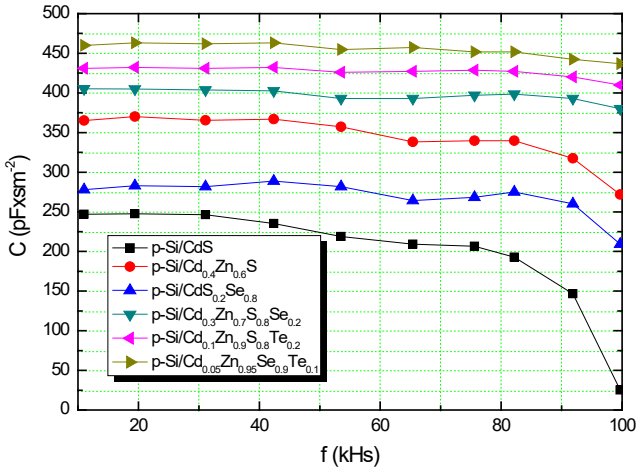

Fig. 6. Frequency dependence of capacitance for different compositions of p-Si/n-$A^{II}B^{VI}$heterojunctions after direct deposition.

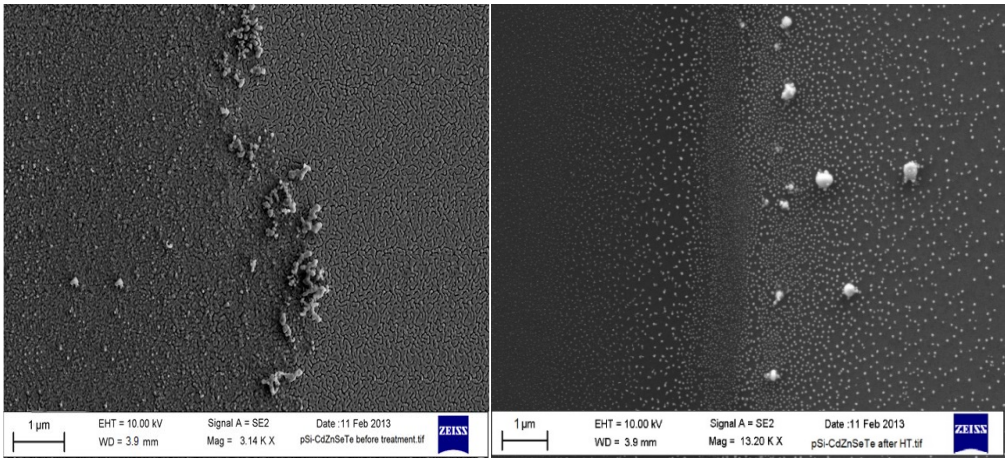

Fig. 7. SEM images of transition zone of the p-Si/$Cd_{0.05}Zn_{0.95}Se_{0.9}Te_{0.1}$ heterojunctions

Note that although the activation energy of the E1 levels varies depending on the deposition regime of the thin layers, the activation energy of the E2 levels has the same value for all the thin layers studied. All these results allow us to say that the first group of levels is only due to the excess of chalcogen atoms (S, Se and Te) on the surface and in the volume of the layers during the reaction, which evaporate easily.

Deeper E2 group levels (in our opinion they are acceptor levels) are related to vacancies $\left[(V_{Cd,Zn} - O)^{+} - (Zn)Cd_i^{+}\right]^{++}$ created by oxygen absorbed into the surface of thin layers after removal from the reaction solution.

The physical and chemical processes occurring on the surface and volume of $A^{II}B^{VI}$ type thin films during thermal annealing (TA) in open air, oxygen and argon environments change all their electrical, optical and photoelectric properties. As a result of our detailed research, it was determined that in order to obtain optimal electrical parameters of different types of heterojunctions based on $A^{II}B^{VI}$ type thin films, they must be thermally annealed in the optimal environment and mode. Thus, depending on the environment and mode of TA, either physical or chemical processes occur on the surface of thin layers and in the transition region of

heterojunctions. We commented on the results of studies conducted in the open air, oxygen and argon environments for a comparative analysis of the electrical properties of p-Si/$A^{II}B^{VI}$ type heterojunctions.

The transition region of heterojunctions was scanned with a scanning electron microscope (SEM) before thermal processing and after TA in an argon environment. Figure 7 shows images of the transition section for p-Si/$Cd_{0.05}Zn_{0.95}Se_{0.9}Te_{0.1}$ heterostructures under a scanning electron microscope. As can be seen from the figure, the boundary of the transition section before TA is not sharp, i.e., the heterojunction is not fully formed. However, after 11-13 minutes of TA in an argon environment at 410^0C the near transition part becomes sharper and the metal/semiconductor excess in the transition region decreases sharply. As can be seen, during TA, electron-molecular processes and recrystallization occur not only on the surface of thin layers, but throughout the volume.

TA sharply changes not only the crystal structure and degree of crystallization of all types of p-Si/$A^{II}B^{VI}$ heteroconductors studied in this work, but also all electrical parameters and the mechanism of current transfer. Thus, Figure 8 shows graphs of the change in the non-ideality coefficient of VAC (n) depending on the TA temperature in open air (a), oxygen (b) and argon (c) environments. As can be seen from the graphs, the change in the non-ideality coefficient at the initial temperatures occurs with the same regularity, regardless of the TA environment. At initial TA temperatures (up to the 150^0C) the value of n decreases for all thin layers. This decrease is due to the evaporation of unreacted (unbound) metal/semiconductor residue during deposition on the surface and volume of thin layers. As can be seen from the figures, in four-component compounds, this reduction occurs more weakly, which may be due to the lower metal/semiconductor excess. As can be seen from figure, the mode of TA for the optimal values of all electrical parameters is different for different thin layers. As can be seen from the figures, the dependence of TA on temperature and regime decreases with increasing amount of Zn and Te in thin layers, regardless of the environment of TA. The weakest dependence is observed in tellurium compounds, which indicates that they are more resistant to the environment. That is, diode structures based on tellurium compounds may exhibit weaker degradation during operation. Depending on the composition, the value of n and the series resistance continue to decrease during TA at temperatures up to 300-390^0C and have a minimal value, which indicates that heterostructures are fully formed during TA at these temperatures. Heterostructures after TA exhibit maximum rectifying in the specified temperature range, regardless of the environment in which they are conducted; in all types of heterojunctions, the value of $C^{-n}=f(U)$ is $n\approx2$ which indicates that after TA, their bulk boundaries sharpened, i.e., they are strong heterojunctions; the dependence of the capacity on the frequency of the external field is not observed; series resistance gets a minimum value. Scanning electron microscopy images of the transition region, surface images of thin films under an atomic force microscope, and changes that occur after TA, in our opinion, are directly related to the degree of polycrystalline thin layers obtained after deposition. Thus, after direct deposition, the transition region of heterojunctions consists of nanoheterostructures with different electrical properties and very small geometric dimensions and each of these

nanoheterostructures has a different orientation direction (Figure 9 a). In each of these nanoheterostructures in the external electric field, the nature of the field distribution in the field of bulk region and the mechanism of current transfer are of a different nature. That is, the electrical properties of a common heterojunction matrix are determined by the properties of such nanoheterojunctions. Recrystallization at high temperatures (300-390^{0}C) leads to the aggregation of polycrystals along the entire volume of thin layers, reduction of electric field fluctuations in the transition region (bulk area) and the formation of a single system, which results in the getting of optimal electrical parameters (Figure 9 b).

While all the electrical properties of heterojunctions during thermal processing at low temperatures do not depend on the type of environment in which the TA is conducted, both the mechanism and value of changes in electrical parameters during TA at higher temperatures (t≥400^{0}C) depend sharply on the type of environment. This shows that in the case of low temperatures physical processes occur on the surface and volume of thin layers during TA, however also chemical processes occur at high temperatures. Thus, as can be seen from Figure 8, the value of the non-ideality coefficient of VAC increases again and decreases sharply during TA at 400-415^{0}C in the open air and in an oxygen environment. The change in the value of n is becomes more clear in the oxygen environment (Figure 8 b). At an temperature of 400-415^{0}C in an argon environment, almost no change occurs during TA. We think that Cd and Zn, which did not react during chemical deposition on the surface and volume of thin films during TA in the open air and oxygen environment, combine with oxygen in the environment at high temperatures to form $Cd_{1-x}Zn_xO$ type semiconductor compounds on the surface of thin films and as a result, the formation of p-Si/$A^{II}B^{VI}$/$Cd_{1-x}Zn_xO$ type heterojunctions leads to changes in all electrical parameters (non-ideality coefficient of VAC, series resistance, potential barrier's height, rectification coefficient, etc.).

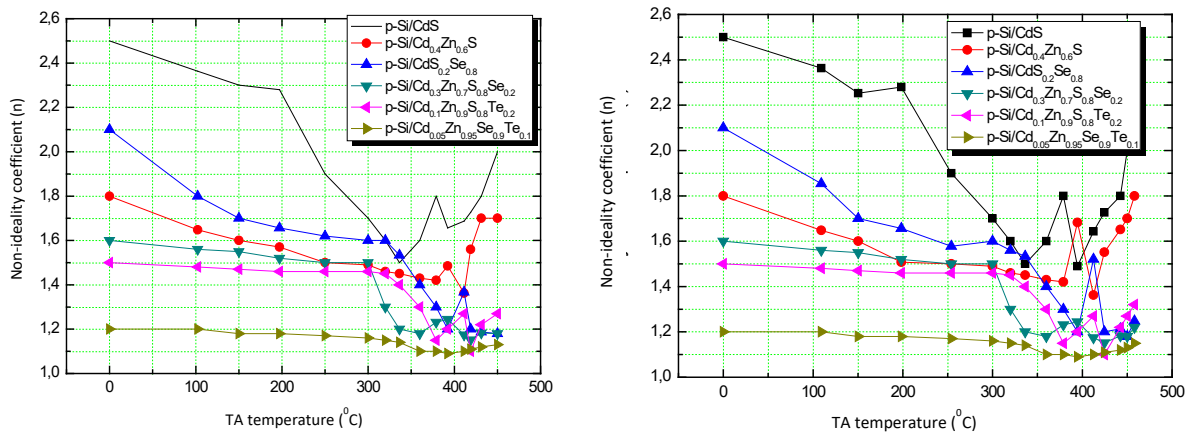

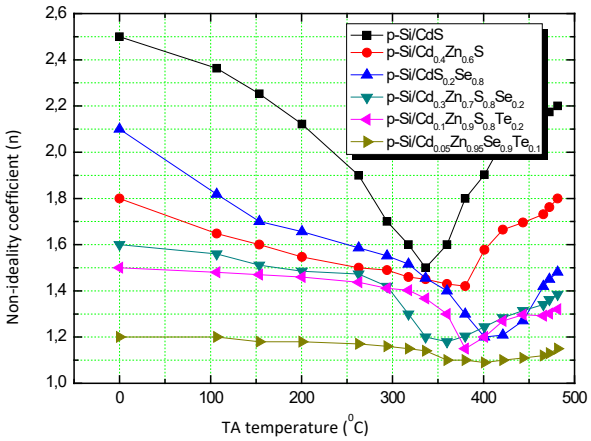

Fig. 8. Variation of the non-ideality coefficient (n) of VAC in p-Si/$A^{II}B^{VI}$ heterojunctions of different compositions depending on the temperature of TA in open air (a), oxygen (b) and argon (c) environments. The duration of TA was 11 minutes.

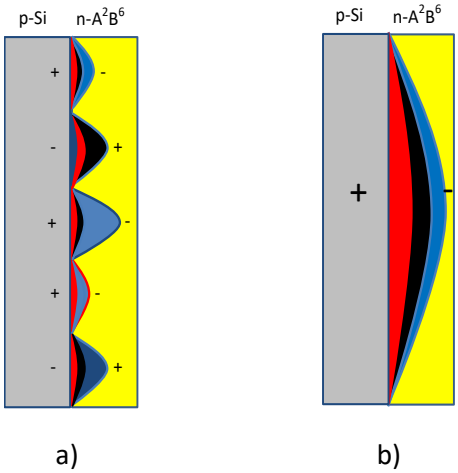

Fig. 9. Assumed diagram of the transition area of heterojunctions before (a) and after (b) TA.

As can be seen from Figure 8 a, b, c, the electrical parameters of heterojunctions based on selenium-tellurium thin layers have remained almost unchanged, although the electrical parameters of heterojunctions based on sulfur-tellurium compounds have changed little, regardless of the environment in which the thermal processing has taken place. This confirms that they are more environmentally stable. As can be seen from the figure, at higher temperatures of TA (in all three TA environments), the value of n increases sharply in all types of heterojunctions, which can be explained by physical phenomena such as intensive evaporation of thin layers and destruction of the transition.

All electrical parameters of the heterojunctions were calculated depending on the TP environment and temperature and an energy diagram was constructed for the heterojunctions based on the optimal compositions.

Conclusions

The present results indicate that, optimizing the composition of $Cd_{1-x}Zn_xS_{1-y}Se_y$, $Cd_{1-x}Zn_xS_{1-y}Te_y$ and $Cd_{1-x}Zn_xSe_{1-y}Te_y$ films and heat-treatment conditions, one can obtain *p*-Si/ $Cd_{1-x}Zn_xS_{1-y}Se_y$, $Cd_{1-x}Zn_xS_{1-y}Te_y$ and $Cd_{1-x}Zn_xSe_{1-y}Te_y$ heterojunctions suitable for the fabrication

of rectifier diodes with high-rectification coefficient. Adding Te, the rectification coefficient in $Cd_{1-x}Zn_xS_{0.9}Te_{0.1}$ compositions has the maximum value at the values of Zn with x=0.9 (k = 9000). The lowest values of the non-ideality coefficient are observed in p-Si/n-$Cd_{1-x}Zn_xS_{1-y}Te_y$ (x=0.9; y=0.2) və p-Si/$Cd_{1-x}Zn_xSe_{1-y}Te_y$ (x=0.95; y=0.1) heterojunctions which indicates that they are closer to the ideal heterojunction properties.

The transition region of heterojunctions was scanned with a scanning electron microscope (SEM) before thermal processing and after TP in an argon environment. The investigation of p-Si/$Cd_{0.05}Zn_{0.95}Se_{0.9}Te_{0.1}$ heterostructures by a scanning electron microscope shows that after 11-13 minutes of thermal processing in an argon environment at 410^0C the near transition part becomes sharper and the metal/semiconductor excess in the transition region decreases sharply. During thermal processing, electron-molecular processes and recrystallization occur not only on the surface of thin layers, but throughout the volume.

Acknowledgement

This research was funded by the Science Development Foundation under the President of the Republic of Azerbaijan (EİF-ETL-2020-2 (36) -16 / 01/1-M-01).

References

1. Abdinov A.Sh., Mamedov H. M., Amirova S.I., Thin Solid Films 2006, v. 511-512, p. 140.
2. Mamedov H.M., Muradov M.B., Konya Z. Kukovecz A., Kordas K., Shah S.I., Mamedova V.C., Ahmedova K.M., Tagiyev E.B., Mamedov V.U. Photonics Letters of Poland 2018, v.10, p. 73.
3. Mamedov H.M, Kukevecz A., Konya Z., Kordas, K., Shah S.I., Mamedov V.U., Ahmedova K.M., Mamedova V.J., Rzaev R.M., Shamilova Sh.A., Khanmamedova E.A., Agazade L.E. Russian Journal Of Applied Physics 2018, v. 61, p. 96.
4. Mamedov H.M., Mamedov V.U., Mamedova V.J., Ahmedova K.M., Tagiyev E.B., Agazade L.E. Journal of Optoelectronics and Advanced Materials 2018, v. 20, p. 468.
5. Mamedov H.M., Shah S.I., Chirakadze A., Mamedov V.U., Mamedova V.J., Ahmedova K.M. Photonics Letters of Poland, 2018, v. 10, p.26.
6. Mamedov H.M., Hasanov H.A., Amirova S.I. Thin Solid Films, 2005, v.480-481, p.388.
7. Albassan A.A. Solar Energy Mater. Sol. Cells, 1999, v.57, p. 323.
8. Baykul M. C. Thin Solid Films, 2010, v.518, p.1925.
9. Mamedov H., Hasanov H., Proc. SPIE 2005, v. 5834, p. 264.
10. Mamedov H., Amirova S. Proc. SPIE, 2007, v. 6636, p. 121.
11. Primachenko V.E., Kononets J.F., Bulakh B.M., Venger E.F., Kaganovich É.B., Kizyak I.M., Kirillova S.I., Manoilov É.G., Tsyrkunov Y.A., Semiconductors 2005, v. 39, p. 565.
12. Shevchenko O.Yu., Goryachev D.N., Belyakov L.V., Sresli O.M. Semiconductors 2010, v. 44, p. 642.
13. Xu Y.K., Adachi S. Journal of Applied Physics, 2007, v. 101, p. 10.
14. Laukaitis G., Lindroos S., Tamulevičius S., Leskelä M., Račkaitis M., Appl. Surf. Sci. 2000, v. 161, p.396.
15. Yamaguchi T., Yamamoto Y., Tanaka T., Demizu Y. and Yoshida A. Thin Solid Films 1996, v. 281-282, p.375.
16. Chu T.L., Chu S.S., Britt J., Ferekids C., Wu C.Q. J. Appl. Phys. 1991, v. 70, p. 2688.
17. Chandra S., Pandy R.K., Agrawal R.C. J. Phys. D. Appl. Phys. 1980, v. 13, p. 1757.
18. Chopra K.L., Das S.R. Thin Film Solar Cells, Plenum Press, New York, 1983.
19. Ezema F.I., Ezugwu S.C., Osuji R.U., Asogwa P.U., Ezekoye B.A., Ekwealor A.B.C., Ogbu, M.P. Non-Oxide Glasses 2010, v. 1, p. 45.
20. Yah C.I., Zulkarnain Z., Anuar K., Wan M. Int. J. Electrochem. Sci. 2011, v. 6, p. 2898.

DEUTERON PROFIL FUNCTION IN HARD-WALL MODEL OF ADS/QCD

NJ HUSEYNOVA and ShA MAMEDOV

Department of Theoretical Physics, Institute for Physical Problems, Baku State University, Baku, Azerbaijan
E-mail: nerminh236@gmail.com, sh.mamedov62@gmail.com

One of two stable isotopes of hydrogen is Deuterium (D), which also is known as a heavy hydrogen. The nucleus of a deuterium atom, called a deuteron consists of one proton and one neutron, whereas the far more common Protium has no neutrons in the nucleus. Deuterium is destroyed in the interiors of stars faster than it is produced. Deuterons are formed chiefly by ionizing deuterium (stripping the single electron away from the atom) and are used as projectiles to produce nuclear reactions after accumulating high energies in particle accelerators. A deuteron also results from the capture of a slow neutron by a proton, accompanied by the emission of a gamma photon. We present profile function of the deuteron in the framework of hard-wall AdS/QCD model. First, we construct an effective bulk action, which describes the interaction for free deuteron fields. Guided on this action according to classical field theory, we write Lagrange-Euler equation for the free deuteron field. Appling Kaluza-Klein decomposi-tion from the Euler-Lagrange equation we obtain an equation over the additional coordinate for the deuteron wave function. Having solved the equation of motion we find profile function for the deuteron in the framework of hard-wall model of AdS/QCD.

Keywords: profile function; hard-wall; bulk; boundary
PACS Number(s): 12.40.Yx, 12.40.Nn

Introduction

Deuteron is studied in the framework experimental and theoretical approaches of elementary particle physics. In this work, profile function of deuteron is studied in hard-wall model of the Anti-de Sitter (AdS)/Quantum Chromodynamics (QCD), where the confinement and chiral symmetry breaking propers of QCD and finiteness condition of the 5D action is constructed by cut off the AdS space at Infrared boundary.

The AdS/QCD models was successfully described the phenomenological properties of hadron physics, such as couplings and decay constants, form-factors, mass spectra and etc. during recent decades. One of the main interesting branch of hadronic physics is the study of deuteron [1-5]. In the framework of soft-wall model AdS/QCD the profile function and electromagnetic form-factors of deuteron is calculated [5], but in hard-wall model they was not carry out yet. So, in this work we study profile function of deuteron in hard-wall model of AdS/QCD.

The hard-wall model

The metric of d+1 dimensional AdS space is given by

$$ds^2 = g_{MN}dx^M dx^N = e^{2A(z)}\left(dz^2 + \eta_{\mu\nu}dx^\mu dx^\nu\right) = \\ = \frac{1}{z^2}\left(-dz^2 + \eta_{\mu\nu}dx^\mu dx^\nu\right) \quad \mu,\nu = 0,1,2,\dots,d-1 \ , \tag{1}$$

where $\eta_{\mu\nu} = diag(1,-1,-1,-1)$ is a 4-dimensional Minkowski metric.

The mesons are described by 5D fields propagating with the action given by

$$S = \int \mathrm{d}^5\mathrm{x}\,\sqrt{\mathrm{G}}\,\mathcal{L}\,, \tag{2}$$

where $\mathcal{L}$ is Lagrangian density and $g = |detg_{MN}|$ (M,N=0,1,2,3,z) . The z variable extend from 0, which is called the ultraviolet boundary, to z_m , which is called the infrared boundary.

For describing the nucleon doublet in the boundary QCD, it is necessary to introduce two bulk fermions N_1 and N_2 having opposite signs of M and $\phi\bar{\Psi}\Psi$ term, then eliminate extra chiral components at the UV boundary by the boundary conditions. For demonstrating profile function for the fermion field $\Psi_1(x,z)$ in the bulk of the AdS space, we need to write action for fermion field, where was not considered interaction with the gauge fields as follows:

$$S_{F_1} = \int d^5x \sqrt{g} \left(\frac{i}{2}\bar{\Psi}_1 e_A^N \Gamma^A D_N \Psi_1 - \frac{i}{2}(D_N\Psi_1)^+ \Gamma^0 e_A^N \Gamma^A \Psi_1 - m_5\bar{\Psi}_1\Psi_1\right) \quad (3)$$

where $e_A^N = z\delta_A^N$ is the inverse vielbein and the covariant derivative is: $D_N = \partial_N + \frac{1}{8}\omega_{N\,AB}[\Gamma^A, \Gamma^B]$.

Non-zero components of spin connection are: $\omega_{\mu zv} = -\omega_{\mu vz} = \frac{1}{z}\eta_{\mu v}$.

5-dimensional matrices obey the anticommutation relation $\{\Gamma^A, \Gamma^B\} = 2\eta^{AB}$ and are defined as $\Gamma^A = (\gamma^\mu, -i\gamma^5)$ [5].

From the action (9) the equation of motion was obtained as follow:

$$(ie_A^N \Gamma^A D_N - m_5)\Psi_1 = 0 \quad . \quad (4)$$

The second order differential equations for the profile function was obtained from (4) as below:

$$\begin{cases} \left(\partial_z^2 - \frac{4}{z}\partial_z + \frac{(6+m_5-m_5^2)}{z^2}\right) f_{1L} = -|P|^2 f_{1L} \\ \left(\partial_z^2 - \frac{4}{z}\partial_z + \frac{(6-m_5-m_5^2)}{z^2}\right) f_{1R} = -|P|^2 f_{1R} \end{cases}. \quad (5)$$

The n-th normalized Kaluza-Klein mode $f_{L,R}^{(n)}(z)$ of the solutions $f_{L,R}$ with $p^2 = m_n^2$ may be expressed in terms of Bessel functions $\mathcal{J}_{m_5 \mp \frac{1}{2}}(pz)$:

$$f_{1L} = cz^{\frac{5}{2}}\mathcal{J}_{m_5 \mp \frac{1}{2}}(pz), \; m_5 = \frac{5}{2}$$

Similarly we find that

$$f_{1L}^n = c_1^n z^{\frac{5}{2}}\mathcal{J}_2(pz), \quad f_{1R}^n = c_1^n z^{\frac{5}{2}}\mathcal{J}_3(pz),$$
$$f_{2L}^n = -c_2^n z^{\frac{5}{2}}\mathcal{J}_3(pz), \quad f_{2R}^n = c_2^n z^{\frac{5}{2}}\mathcal{J}_2(pz), \quad (6)$$

where $\propto$ parameter is related with 5-D mass as follow:

$$\alpha = M + \frac{1}{2}$$

and normalization constants n_{1L} and n_{1R} are found from

$$\int_0^{z_m} \frac{dz}{z^5} f_{1L}^{(n)}(z) f_{1L}^{(m)}(z) = \delta_{nm}$$

normalization condition like this:

$$|c_{1,2}^n| = \frac{\sqrt{2}}{z_m \mathcal{J}_2(m_n z_m)} \quad (7)$$

$M = \frac{5}{2}$ and thus $\propto = 3$. The profile functions of the first and second bulk fermion fields are related each other like follow[3]:

$$f_{1L} = f_{2R}$$
$$f_{1R} = -f_{2L} \quad (8)$$

Deuteron profil function in hard-wall model of ADS/QCD

In this work, the main idea in hard-wall model is based on an effective action including 5D (five-dimensional) fields propagating in the bulk of AdS space, which are correspond to the deu-teron and electromagnetic field. In this case, an effective action for the free deuteron field is written like below [5]:

$$S = \int_0^{z_M} d^4x\, dz\, \sqrt{G}\, [-D^M d_N^+(x,z)\, D_M d^N(x,z) + d_M^+(x,z)\mu^2\, d^M(x,z)], \quad (9)$$

where z_M – is a IR (infrared) boundary of a AdS space, z – is a fifth variable, $\sqrt{G} = e^{5A(z)}$ – is a modulus of the determinant of the metric tensor AdS space $g_{MN} = \frac{R^2}{z^2}\eta_{MN}$, R – is the AdS radius, $A(z) = \log(\frac{R}{z})$, $D^M = \partial^M - ieV^M(x,z)$ – is a covariant derivative, $V^M(x,z)$ – is a dual to the electromagnetic field, $\mu^2 = \frac{(\Delta-1)(\Delta-3)}{R^2} = \frac{(\tau+L-1)(\tau+L-3)}{R^2} = \frac{(L+5)(L+3)}{R^2}$ – is the 5D mass, $\Delta = \tau + L$ – is the dimension of the $d^N(x,z)$ field, L – is the orbital angular momentum, $d^N(x,z)$ – is a fit to the Fock component contributing to the deuteron with twist $\tau = 6$.

For simplicity we use axial gauge condition for both vector fields $V^z(x,z) = 0$ and $d^z(x,z) = 0$. As the deuteron field is a free field , so in our case $D^M \equiv \partial^M$.

First we write Lagrange-Euler equation of motion (EOM) for the (1) Lagrangian, notice that $\partial_\alpha \partial_\beta F^\nu \eta^{\alpha\beta} = -M^2 F^\nu$,

$$\left\{-\frac{d^2}{dz^2} + \frac{1}{z}\frac{d}{dz} + \frac{(L+4)^2-1}{z^2}\right\} F^\nu(x,z) = M^2 F^\nu(x,z)\ , \quad (10)$$

Then we carry out Kaluza-Klein (KK) decomposition for the vector field dual to the deuteron field:

$$d^\nu(x,z) = e^{-\frac{A(z)}{2}} \sum_n d_n^\upsilon(x)\Phi_{\mathrm{n}}(\mathrm{z}), \quad (11)$$

where $F_n^\upsilon(x)$ is tower of a KK fields dual to the deuteron fields with twist-dimension $\tau = 6$ and radial quantum number n .

Thus we perform Schrodinger-type equation of motion for the $\Phi_{\mathrm{n}}(\mathrm{z})$ bulk profile :

$$\left\{-\frac{d^2}{dz^2} + \frac{4(L+4)^2-1}{4z^2}\right\} \Phi_{\mathrm{n}}(\mathrm{z}) = M^2 \Phi_{\mathrm{n}}(\mathrm{z})\ , \quad (12)$$

After the solving analytically (4) EOM , we get expression for the bulk profile function of the deuteron like as:

$$\Phi_{\mathrm{n}}(\mathrm{z}) = \mathrm{c}_1\sqrt{z}\,\mathrm{Bessel}\,\mathcal{J}_5(\mathrm{Mz}) + \mathrm{c}_2\sqrt{z}\mathrm{Bessel}\,\mathrm{Y}_5(\mathrm{Mz}), \quad (13)$$

where $\mathrm{Bessel}\ \mathcal{J}_5(\mathrm{Mz})$ – is a Bessel function of the first kind and $\mathrm{Bessel}\ \mathrm{Y}_5(\mathrm{Mz})$ – is a Bessel function of the second kind.

Discussion and conclusions

In conclusion we return again the main resluts of our work. In the framework hard-wall model AdS/QCD we get analytical expression for the deuteron profile function in terms of first and second kind Bessel function, which help us to calculate interaction parametrs, couplings and etc. for the deuteron in future researches.

References

1. Garcon M. and Van Orden J. W., Adv. Nucl. Phys. 2001, v. 26, p.293.
2. Abbott D. et al. (JLAB t20 Collaboration), Eur. Phys. J. A 2000, v. 7, p. 421.
3. Kohl M., Nucl. Phys. A 2008, v. 805, p. 361.
4. Holt R. J. and Gilman R., Rep. Prog. Phys. 2012, v. 75, p. 086301.
5. Gutsche T., Lyubovitskij V.E., Schmidt I. and Vega A., Phys. Rev. D 2015, v. 91, p. 114001.

DEUTERON IN THE FRAMEWORK OF SOFT-WALL MODEL ADS/QCD

NJ HUSEYNOVA, ShA MAMEDOV, VH BADALOV

[1]Department of Theoretical Physics, Institute for Physical Problems of Baku State University, Baku, Azerbaijan
E-mail: nerminh236@gmail.com, sh.mamedov62@gmail.com, badalovvatan@yahoo.com

Deuterium is used in heavy water moderated fission reactors, usually as liquid D2O, to slow neutrons without the high neutron absorption of ordinary hydrogen. In research reactors, liquid D2 is used in cold sources to moderate neutrons to very low energies and wavelengths appropriate for scattering experiments. Experimentally, deuterium is the most common nuclide used in nuclear fusion reactor designs, especially in combination with tritium, because of the large reaction rate (or nuclear cross section) and high energy yield of the D–T reaction [1-4]. In present work, the profile function of deuteron is described in the framework of Anti-de Sitter (AdS)/Quantum Chromodynamics (QCD), where the nonperturbative aspects of QCD and finiteness condition of the 5D action is provided by multiplying an extra exponential factor (called Dilaton field) to the Lagrangian in the action. We introduce deuteron field as a twist 6 vector field and write action in this bulk. Using this action, we write Lagrange-Euler equation for deuteron field and obtain an equation over the z coordinate. Solving this equation, we find profile function for deuteron, in the framework soft-wall model AdS/QCD. We also perfome integral expression over the Q^2 momentum square for the magnetic form-factor of the deuteron.

Keywords: deuteron; soft-wall model; form-factor; magnetic
PACS: 12.40.Yx, 12.40.Nn

Introduction

An effective action which involve all interaction Lagrangians in the bulk of AdS space, between vector and deuteron fileds are presented in literature as below [5]:

$$S = \int_0^\infty d^4x\, dz\, e^{-k^2z^2}\sqrt{G}\,[-\frac{1}{4}F_{MN}(x,z)F^{MN}(x,z) - D^M d_N^+(x,z)\, D_M d^N(x,z) - \\ -ic_2F^{MN}(x,z)d_M^+(x,z)d_N(x,z) + \frac{c_3}{4M^2}e^{2A(z)}\partial^M F^{NK}(x,z)(iD_K d_M^+(x,z)\, d_N(x,z) - \\ -d_M^+(x,z)iD_K d_N(x,z) + H.c.) + d_M^+(x,z)(\mu^2 + U(z))\, d^M(x,z)], \quad (1)$$

where z – is a fifth variable, z_M – is a Dilaton parameter, $\sqrt{G} = e^{5A(z)}$ – is a modulus of the determinant of the metric tensor AdS space $g_{MN} = \frac{R^2}{z^2}\eta_{MN} = e^{2A(z)}\eta_{MN}$, R – is the AdS radius, $F^{MN}(x,z) = \partial^M V^N(x,z) - \partial^N V^M(x,z)$ – is the stress tensor of the vector field $V^M(x,z)$, $A(z) = \log(\frac{R}{z})$, $D^M = \partial^M - ieV^M(x,z)$ – is a covariant derivative, $V^M(x,z)$ – is a dual to the electromagnetic field, $\mu^2 = \frac{(\Delta-1)(\Delta-3)}{R^2} = \frac{(\tau+L-1)(\tau+L-3)}{R^2} = \frac{(L+5)(L+3)}{R^2}$ – is the 5D mass, $\Delta = \tau + L$ – is the dimension of the $d^N(x,z)$ field, L – is the orbital angular momentum, $d^N(x,z)$ – is a fit to the Fock component contributing to the deuteron with twist $\tau = 6$, $U(z) = \frac{\varphi(z)}{R^2}U_0$- is the confinement potensial.

Profil function of a deuteron in the framework soft-wall ADS/QCD model

From the (1) effective action we get the Scrodinger-type equation of motion (EOM) for the bulk deuteron field as below:

$$\left\{-\frac{d^2}{dz^2} + \left(2k^2z + \frac{1}{z}\right)\frac{d}{dz} + \left(\frac{(L+4)^2-1}{z^2} + k^2U_0\right)\right\}F^\nu(x,z) = M^2F^\nu(x,z)\,, \quad (2)$$

where we notice that, $\partial_\alpha\partial_\beta F^\nu\eta^{\alpha\beta} = -M^2F^\nu$.

After substitution

$$d^{v}(x,z) = e^{-\frac{A(z)}{2}} \sum_n d_n^{v}(x)\Phi_{\mathrm{n}}(\mathrm{z}), \tag{3}$$

Kaluza-Klein (KK) decomposition for the vector field dual to the deuteron field in formula (2),

where $F_n^{v}(x)$ is tower of a KK fields dual to the deuteron fields with twist-dimension $\tau = 6$ and radial quantum number n , Schrodinger-type equation of motion for the $\Phi_{\mathrm{n}}(\mathrm{z})$ bulk profile is follow:

$$\left\{-\frac{d^2}{dz^2} + k^4z^2 + k^2U_0 + \frac{4(L+4)^2-1}{4z^2}\right\}\Phi_{\mathrm{n}}(\mathrm{z}) = M^2\Phi_{\mathrm{n}}(\mathrm{z}). \tag{4}$$

By helping Mathematica Program we solved EOM (4) and thus find formula for the bulk profile function of the deuteron in the framework soft-wall model AdS/QCD as below:

$$\Phi_{\mathrm{n}}(\mathrm{z}) = \frac{e^{-\frac{1}{2}k^2z^2}C[1]\mathrm{HypergeometricU}\left[\frac{-8k^2-M^2+k^2U_0}{4k^2}, -4, k^2z^2\right]}{4z^{\frac{9}{2}}} + \\ + \frac{e^{-\frac{1}{2}k^2z^2}C[2]\mathrm{LaguerreL}[-\frac{-8k^2-M^2+k^2U_0}{4k^2}, -5, k^2z^2]}{4\,z^{\frac{9}{2}}}, \tag{5}$$

where the first kind of term is a hipergeometric function and equal zero from the boundary condition. Thus, the profile function of the deuteron in the framework soft-wall model AdS/QCD is expressed with generalized Laguerre polynomials:

$$\Phi_{\mathrm{n}}(\mathrm{z}) = \frac{e^{-\frac{1}{2}k^2z^2}C[2]\mathrm{LaguerreL}[-\frac{-8k^2-M^2+k^2U_0}{4k^2}, -5, k^2z^2]}{4\,z^{\frac{9}{2}}}. \tag{6}$$

Magnetic form-factor of a deuteron in the hard-wall ADS/QCD model

In literature there are three interaction Lagrangian between bulk fields that contribute to the Deuteron electromagnetic form-factors. They called minimal coupling term and magnetic gauge coupling terms. We use from the magnetic gauge coupling term, which are as follow:

$$S = \int_0^{z_M} d^4x\, dz\, \sqrt{G}\, [-ic_2F^{MN}(x,z)d_M^{+}(x,z)\, d_N(x,z)], \tag{7}$$

We use from the Kaluza-Klein(KK) decomposition for the 5D deuteron field correspond to the vector field as follow:

$$d^{\mu}(x,z) = e^{-\frac{A(z)}{2}} \sum_n d_n^{\mu}(x)\Phi_{\mathrm{n}}(\mathrm{z}), \tag{8}$$

where $F_n^{v}(x)$ is tower of a KK fields dual to the deuteron field with twist-dimension $\tau = 6$ and radial quantum number n and for the simplicity we use axial gauge condition for both vector fields $V^{z}(x,z) = 0$ and $d^{z}(x,z) = 0$. As the deuteron field is a free field, so in our case $D^{M} \equiv \partial^{M}$.

We also comply the Fourier transform for both vector and deuteron fields:

$$V_{\mu}(x,z) = \int \frac{d^4q}{(2\pi)^4} e^{-iqx}V_{\mu}(q)\, V(q,z), \tag{9}$$

$$d_\mu(x) = \int \frac{d^4p}{(2\pi)^4} e^{-ipx} \epsilon_\mu(p), \tag{10}$$

$$d_\mu^+(x) = \int \frac{d^4p^{"}}{(2\pi)^4} e^{ip'x} \epsilon'_\mu(p'), \tag{11}$$

where, $V(q,z) = \frac{\pi}{2} Qz[\frac{K_0(Qz_m)}{I_0(Qz_m)} I_1(Qz) + K_1(Qz)]$ – is a bulk profile function of a vector field.

After using expressions (8),(9),(10) and (11) in expressions (7) and integrating over x and z , we get expression for the matric element of the $d + \gamma \to d$ transition, from which we obtain formula for the Deuteron magnetic form-factor $G_M(Q^2)$.

$$S = \int_0^{z_M} d^4x\, dz\, \sqrt{G}\, c_2[i\partial_v V_\mu(q) F^{\mu+}(x,z) F^{\nu}(x,z) - i\partial_\mu V_v(q) F^{\mu+}(x,z) F^{\nu}(x,z)] =$$
$$= (2\pi)^4 \int \frac{d^4p}{(2\pi)^4} \int \frac{d^4p'}{(2\pi)^4} \int \frac{d^4q}{(2\pi)^4} \delta^4(p+q-p') V_\mu(q) M^\mu(p,p') , \tag{12}$$

where, $M^\mu(p,p') = -c_2 \int dz\, V(q,z) \Phi^2(z)\, \{\varepsilon^\mu(p) \epsilon^+(p') q - \epsilon^{+\mu}(p') \varepsilon(p) q\} =$
$$= -G_2(Q^2)\{\varepsilon^\mu(p)\, \epsilon^+(p') * q - \epsilon^{+\mu}(p') \varepsilon(p) * q\} . \tag{13}$$

Thus, the form-factor $G_2(Q^2)$ which constitute magnetic $G_M(Q^2)$ form-factor are equal :

$$G_2(Q^2) = c_2 \int dz\, V(q,z) \Phi^2(z), \tag{14}$$

From (13) we easily get expression for the magnetic $G_M(Q^2)$ form-factor of deuteron as below:

$$G_M(Q^2) = G_2(Q^2) = c_2 \int dz\, V(q,z) \Phi^2(z), \tag{15}$$

where $\Phi(z)$ – is a bulk profile function of the deuteron in the framework of hard-wall model like as:

$$\Phi(z) = a \sqrt{z}\, \mathrm{Bessel}\, \mathcal{J}_5(Mz) + b \sqrt{z} \mathrm{Bessel}\, Y_5(Mz), \tag{16}$$

The $\mathrm{Bessel}\, \mathcal{J}_5(Mz)$ – is a Bessel function of the first kind and $\mathrm{Bessel}\, Y_5(Mz)$ – is a Bessel function of the second kind and $c_2 = G_M(0) = 1.714$ constant is find within soft-wall model of AdS/QCD.

Discussion and conclusions

Using soft-wall model AdS/QCD we get analytical expression for the deuteron profile function in terms of Laguerre polynomials, which help us to calculate coupling constants and form-factors of deuteron in next works. We also calculate the deuteron magnetic form-factors in the frame-work of hard-wall model AdS/QCD, which coincide with the results of soft-wall model AdS/QCD.

References

1. Garcon M. and Van Orden J. W. , Adv. Nucl. Phys. 2001, v. 26, p. 293.
2. Abbott D. et al. (JLAB t20 Collaboration), Eur. Phys. J. A 2000, v. 7, p. 421.
3. Kohl M., Nucl. Phys. A 2008, v. 805, p. 361.
4. Holt R. J. and R. Gilman, Rep. Prog. Phys. 2012, v. 75, p. 086301.
5. Gutsche T. , Lyubovitskij V.E., Schmidt I. and Vega A., Phys. Rev. D 2015, v. 91, p. 114001.

TEMPERATURE AND SURFACE STATES INFLUENCE ON THE IDENTIFYING OF SCHOTTKY DIODE PARAMETERS

IM AFANDIYEVA[1], RF BABAYEVA[2], ChG AKHUNDOV[1]

[1]Baku State University, Institute for Physics Problem, Baku, Azerbaijan
[2]Department of Engineering and Applied Science, Azerbaijan State University of Economics (UNEC), Baku, Azerbaijan
E-mail: babaeva-rena@yandex.ru

Both the capacitance-voltage $(C-V)$ and conductance–voltage $(G/\omega-V)$ characteristics of Pd_2Si/n-Si(111) SBDs have been investigated in the wide temperature range of 79-360 K and ± 1V for 500 kHz. On the basis of the temperature dependent characteristics potential barrier height (Φ_B), the doping concentration of donor atoms (N_D), the Fermi energy level (V_n), series resistance (R_s), distribution of applied bias voltage and the role of surface states (N_{ss}) were analyzed. The value of Φ_B was irregular changed between 0.46 and 0.69 eV with temperature. Such behavior in Φ_B with temperature was attributed to the influence of surface states and electrons exchanging between surface states and semiconductor or metal under temperature and voltage effects. In this work Nicollian - Brews and Hill-Coleman methods have been used to calculating of R_s and N_{ss} vs the voltage for each temperature.

Keywords: Pd_2Si/n-Si(111) Schottky barrier diode, $C-V-T$ and $G/\omega-V-T$ characteristics, temperature dependence of electrical parameters, surface states and series resistance
PACS: 73.30.+y, 73.61.-r, 67.40.Pm

Introduction

This presented work is devoted to the study of the electro-physical parameters of Pd_2Si/n-Si(111) SBDs. The great interest shown in Pd_2Si/n-Si(111) SBD based on Schottky barriers is caused by the formation of palladium silicide (Pd_2Si) [1-4]. Palladium reacts with silicon to form silicide's at very low temperatures (about 473 K). The activation energy (E_a) for this process is in the range of 1,1-1,5 eV. A characteristic feature of Pd_2Si is a very loose structure, which facilitates the diffusion process. Palladium silicide (Pd_2Si) also characterized by volume diffusion. In these structures (Pd_2Si/n-Si(111)) the formation of the potential barrier of the space-charge region in the semiconductor caused to the electronic properties of the surface of the semiconductor and localized states in the band gap of semiconductor.

The specific purpose of the selection of multicomponent metallization is to protect silicon from diffusion of aluminum, which is usually used as an ohmic contact. Deffects, arising as a result of the chemical interaction of Pd with silicon can play a significant role in electronic phenomena in diode structures, affect the properties of Schottky barriers, change the distribution profiles of carrier concentration in the near-contact region. In addition, a decrease in the geometric dimensions of the diodes increases the likelihood of fluctuations in the parameters. The choice of contact structures of small sizes, the study of fluctuations of parameters, the identification of legitimacy in their occurrence and alternation are of interest for creating multifunction devices with well-known characteristics.

All these factors determined the reason for this investigation of Pd_2Si/n-Si(111) SBDs. Firstly, palladium was deposited on a silicon surface by thermal spraying, because the used technological method does not violate the initial properties of substrate surface. Secondly,

the formation of a silicide film on the surface of silicon shifts the interface into a semiconductor. Thirdly, to prevent the penetration of aluminum, as a diffusion barrier was used an amorphous alloy TiW. Besides, we investigated small diodes, areas of which about 10^{-6} cm^2.

The selected silicon in the (111) direction has the smallest work function. In addition, all the minima of the conduction band in this direction make the same contribution to the current; the effective Richardson constant reaches its maximum value. The above characteristics can determine the homogeneous surface of the natural cleavage, the highest potential barrier and current stability. In addition, due to the silicon band gap, it is possible to create elements based on it that are resistant to elevated temperature [5-8].

The main aim of this study is two-fold: first, the study of the temperature influence on the functionality of Pd_2Si/n-Si (111) SBDs. Second, the analyze of the identified physical phenomena for the fabrication of new multifunctional devices.

Materials and Methods

For fabrication of Pd_2Si/n-Si(111) SBDs as a semiconductor substrate a 2 inch(=2,5 cm) diametr n-type silicon single crystal (P doped) wafer with a resistivity of 0.7 Ohm·cm, 3.5 μm thickness and a surface orientation of (111) was used. The diode matrix contained 14 SBDs, the areas of which varied from 1×10^{-6} cm^2 to 14×10^{-6} cm^2 [5,7,9].

Investigated diodes was fabricated by using the method planar technology based on the method of photolithography. Prior to the deposition of the metal film, the silicon (n-Si) substrate was cleaned in a mix of a peroxide – ammoniac solution for 10 minutes using two stages of chemical purification. Then, the substrate was washed for a long time in deionized water until the resistivity of water became 18 $M\Omega cm$. The dielectric mask (SiO_2) was obtained by thermal oxidation at a temperature of 1320 K in O_2+H_2+HCl vapors. Prior to the deposition of palladium, the silicon wafers were annealed in a system chamber at a vacuum of 6×10^{-5} Torr and a temperature of 573 K for 300 seconds. The palladium film was applied by thermal spraying. For fabrication a homogeneous Pd_2Si film the wafer (Pd_2Si/n-Si(111)) was annealed at $6x10^{-5}$ Torr at 773K for 10 minutes. Then, the structure was annealed in a special ampoule with the furnace at 783K for 30 minutes in atmosphere of the gases N_2 and H_2. To prevent the penetration of Al to Pd_2Si the amorphous TiW alloy was deposited between Al and Pd_2Si as diffusion barrier. All processes were carried out in a clean room of class 100 [5,6,9,10].

The capacitance-voltage $(C-V)$ and conductance –voltage $(G/\omega-V)$ characteristics of the fabricated Pd_2Si/n-Si(111) SBDs were measured in the temperature range of 79 K-360 K by using a HP 4192A LF impedance analyzer. Small sinusoidal test signal of 20 mV_{p-p} (500 kHz) was applied from the external pulse generator. The temperature dependence measurements were performed in a Janes VPF-475 cryostat with a Lake Shore model 321 auto-tuning temperature controllers in a vacuum at about $5x10^{-4}$ Torr. All measurements were carried out with the help of a microcomputer through an IEEE-488 ac/dc converter card. In this paper the results of measurements of diode with the area of $8x10^{-6}cm^2$ are presented.

Results and discussion

A set of $(C-V)$ and $(G/\omega-V)$ characteristics of Pd_2Si/n-Si(111) SBD was measured in the temperature range of 79K-360K and voltage ± 1V and given in Fig.1 and Fig.2, respectively. This is very important to get more information on the conduction mechanisms and the formation of BH between metal and semiconductor. Because, when these measurements were carried out only at one or narrow voltage and temperature range cannot supply enough information on them.

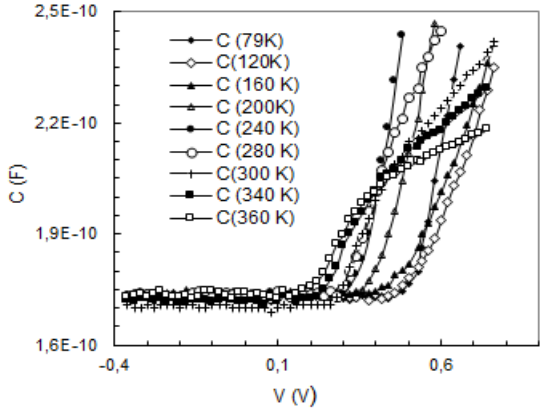

Fig. 1. The measured $C-V$ characteristics of Pd_2Si/n-Si(111) SBD at various temperatures.

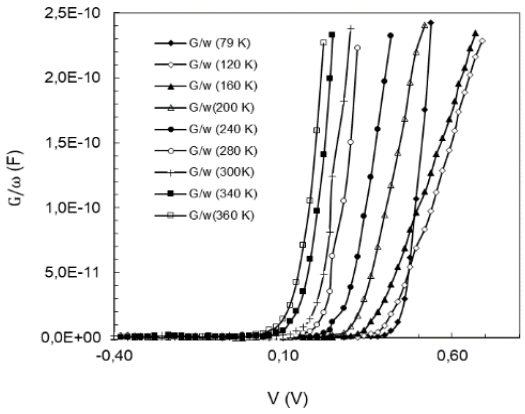

Fig. 2. The measured $G/\omega-V$ characteristics of Pd_2Si/n-Si(111) SBD at various temperatures.

As can be seen from these figures, dependences of $C-V$ and $G/\omega-V$ characteristics of Pd_2Si/n-Si(111) diode on temperature are different for different regions of temperature. One of the reasons for such temperature dependence is the existence of surface states and their life-times recharging [11,12].

To assess the values of the V_n , N_d and Φ_B and factors affecting the parameters of Pd_2Si/n-Si(111) SBD the reverse bias $(A/C)^2-V$ plots have been obtained for each temperature (Fig.3).

The value of N_D was calculated by using following relation [13,14]:

$$\frac{d(A/C^2)}{dV}=\frac{2}{\varepsilon_s\varepsilon_0 q N_D} \quad (1)$$

where ε_s and ε_0 are the permittivity of the semiconductor (11,8 for Si) and the permittivity of free space charge (ε_0= 8.85x10^{-14} F/cm), respectively. N_D is the doping concentration of n-type semiconductor Si, A is the diode contact area [13,14].

The experimental value of N_d was calculated by using Eq. 2 for each temperature (Fig.3)

$$N_d = \frac{2dV}{\varepsilon_s \varepsilon_0 q d(A/C^2)} \tag{2}$$

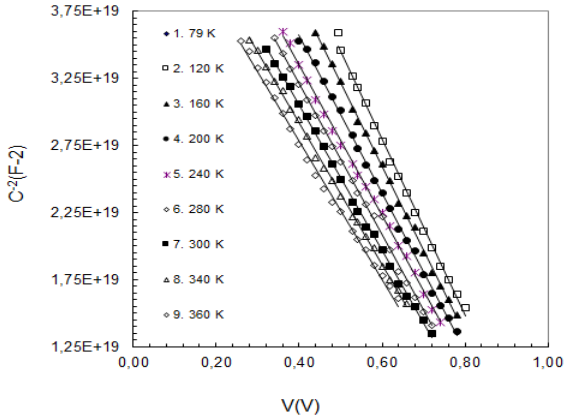

Fig. 3. The $(C/A)^{-2} - V$ characteristics of Pd_2Si/n-Si(111) SBD at various temperatures.

The value of Φ_B of Pd_2Si/n-Si(111) SBD has been also calculated using the intercept voltage $(A/C)^2 - V$ plot as function of the temperature by using the following equation [12,15,17-24]:

$$\Phi_B = q(V_0 + V_n) \tag{3}$$

where V_0 is diffusion potential, which has been determined from intersection of linear part of $(A/C)^2 - V$ characteristics with V axis.

The values of V_n , according to Ref.[15], has been obtained as

$$V_n = \frac{kT}{q} ln\left(\frac{N_c}{N_D}\right) \tag{4}$$

with

$$N_c = 4{,}82x10^{15} T^{3/2} \left(\frac{m_e^*}{m_0}\right)^{3/2} \tag{5}$$

where N_c is the effective density of states in non-degenerated Si conductance band, m_e^*=1,09m_0 is the effective mass of the density of states of silicon [9,11,12,14,15]. The obtained temperature dependent experimental values of V_0, N_D, V_n, and Φ_B from the reverse bias $(A/C)^2 - V$ plot for various temperatures have been calculated. It was revealed the non-uniform dependence of these parameters on temperature. Besides, potential barrier height (Φ_B) of Pd_2Si/n-Si(111) Schottky barrier diode irregularly depends on temperature (Fig.4).

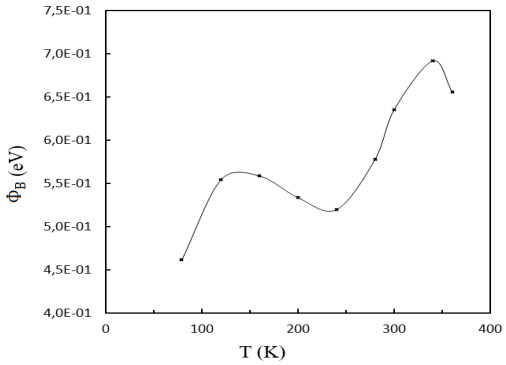

Fig. 4. The dependence of Φ_B for Pd_2Si/n-Si(111) SBD on the temperature.

The value of R_s is also more effective on the $C-V$ and $G/\omega-V$ characteristics especially at accumulation region and also it may be more dependent both on the temperature and frequency. The value of R_s were calculated by using Nicollian and Brews [16] method for each temperature as function of applied bias voltage by using following relation:

$$R_s = G_{ma}(\, G_{ma}^2 + (\omega C_{ma}\,)^2)^{-1} \tag{6}$$

where C_m and G_m are measured capacitance and conductance respectively, ω is angular frequency ($\omega = 2\pi f$). As is shown in Fig.5 the $R_s - V$ plot has a peak for each temperature position of which changes irregularly with increasing of temperature. This behavior implies the existence of surface states and their recharging. Moreover, it is known that the processes of transfer and accumulation of charges are temperature activated processes.

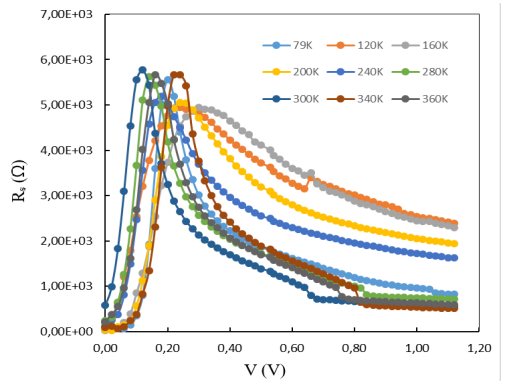

Fig. 5. The dependence of series resistance of Pd_2Si/n-Si(111) SBD on voltage at different temperatures.

By the using of Hill-Coleman method [17*], has been obtained the dependence of surface sates distriburion on voltage for each temperature (Fig.6):

$$N_{ss} = \frac{2}{qA}\frac{(G_{m,max}/\omega)}{(G_{m,max}/\omega C_{ox})^2 + (1 - G_m/C_{ox})^2}$$

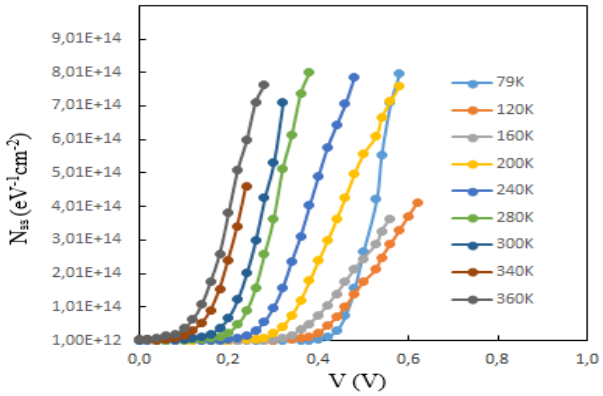

Fig. 6. the distribution of surface states profile on voltage.

It is known, that the electronic processes of real physical contact models are much more complicated than for an idealized model [11,12]. This complexity is determined by two factors: the presence of a dielectric gap and the presence of surface states, which are actively involved in electronic processes. The charge of the space charge region is compensated by the charge of the metal, as well as the charge of the surface states [11,12,18,19]. It should be noted, that silicon, being a covalent semiconductor, characterized by a high density of surface states. Moreover, between the current and voltage there is a phase shift caused by recharging of the surface states. In addition, the formation of metal film on the surface of Si depends on the ratio of crystallographic parameters of the contacting materials [9,20,21].

Due to the mismatch of the lattice parameters of Si and Pd_2Si is very small (2%), the appearance of quantum wells is excluded. Therefore, the temperature dependence of a parameters of Pd_2Si/n-Si(111) SD, can be explained by the presence of a thin dielectric gap and the enhanced role of surface electronic states at the interface. The nonlinear characteristics$(A/C)^2 - V$ and value of Φ_B on temperature confirmed the contribution of surface states .

The observed changes of investigated parameters with temperature can be attributed to the influence of recharging surface states. The weak dependence of R_s on temperature, which give a peak near 0.1 V, the big value of N_{ss} and minimal value of Φ_B at 240K can be connected with reconstruction and recharging of surface states, the distribution of applied voltage between dielectric interlayer and depletion layer and charge exchange between a surface state with a metal or semiconductor. Due to the influence of temperature and recharging of surface states has been determined the effective value of potential barrier height Φ_{Beff}. Above results can be taken into account in the fabrication of new multifunctional devices.

Conclusion

A set of capacitance-voltage $(C - V)$ and conductance-voltage $(G/\omega - V)$ characteristics of Pd_2Si/n-Si(111) Schottky barrier diode with the using of a small sinusoidal test *ac* signal of 20 mV peak to peak amplitude at 500 kHz were measured in the temperature range 79-360K to get more information on their conduction mechanisms and BH. On the basis of measured characteristics the values of V_0, Φ_B, N_D, V_n and R_s have been investigated as function of temperature and applied bias voltage. Obtained result was attributed to the presence of

dielectric gap between metal and semiconductor and recharging of surface states. The voltage dependent profile of R_s obtaned by Nicollian and Brews method for each temperature. In conclusion, the observed changes of investigated parameters with temperature can be attributed to the influence of surface states under temperature and voltage of electric field.

References

1. Kircher C.J. Solid State Electronics 1971, v. 14 (6), p.507. DOI:10.1016/0038-1101(71)90061-X
2. Shepela A. Solid State Electronics 1973, v. 16 (4), p. 477. DOI:10.1016/0038-1101(73)90185-8 Corpus ID: 98371943
3. Poate J.M., Tu K.N., Mayer J.W. Thin films – Interdiffusion and Reactions. Wiley-Interscience, New York , USA, 1978, https://doi.org/10.1002/pol.1979.130170107
4. Murarka S P, Silicides for VLSI: Application.: Academic Press, New York 1983.
5. Afandiyeva I.M., Askerov S.G., Abdullayeva L.K, et al. Solid Stae Electronics 2007, v. 51, p. 1096. DOI:10.1016/j.sse.2007.05.021
6. Sakurai Y., Takeda Y., Ikeda S, et al. Phys Status Solidi C 2014, v. 11 (9/10), p. 1423. https://doi.org/10.1002/pssc.201300621
7. Dokme, I., Altındal, Ş., Afandiyeva, I.M. Semiconductor Science and Technology 2008, v. 23, p. 035003. DOI:10.1088/0268-1242/23/3/035003
8. Sze S.M, Physics of Semiconductor Devices. John Wiley and Sons, New York 1981.
9. Afandiyeva, I.M., Altındal,Ş, Abdullayeva,L.K., et al. Journal of Semiconductors 2018, v. 39 (5), p. 054002. DOI: 10.1088/1674- 4926/39/5/054002
10. Kwak J.S., Kang K.M., Park M.J., et al. Sci. Adv. Mater, 2014, v. 6 (10), p.2249. DOI: https://doi.org/10.1166/sam.2014.2075.
11. Buzanyova E V. Microstructures of integrated electronics., Radio i svyaz, Moscow, 1990 (in Russian).
12. Strikha V.I, Buzanyova E.V, Radziyevskiy I.A. Semiconductor devices with the Schottky barrier, Sovetskoye radio, Moskow, 1974 (in Russian)
13. Moloi S.J., McPherso M. Radiation Physics and chemistry, 2013, v. 85, p. 73. DOI: 10.1016/j.radphyschem.2012.12.002
14. Yahiya I.S., Zahran H.Y., Alamri F.H., Aslam M. Physica B: Condensed Matter, 2018, v. 543. p. 46. DOI:10.1016/j.physb.2018.05.011.
15. Rajan L., Periasamy C., Sahula V. Perspectives in Science, 2016, v. 8, p. 66. https://doi.org/10.1016/j.pisc.2016.03.011.
16. Nicollian,E.H., Brews, J.R., MOS Physics and Technology, Wiley, New York, USA, 1982.
17. Hill,W.A., Coleman,C.C., Solid-State Electronics 1980, v. 23, p. 987. https://doi.org/10.1016/0038-1101(80)90064-7.
18. Strikha, V. I. Theoretical bases of metal–semiconductor contact work., Naukova Dumka, Kiev, 1974 (in Russian).
19. Bardeen J. Phys. Rev. 1947, v. 71 (10), p. 717.
20. Krylov P N. Journal of Udmurt University, Fizika 2006, v. 4, p. 125 (in Russian).
21. Shaskolskaya M P. Crystallography. Visshaya shkola, Moscow,1984 (in Russian).
22. Murygin V.I., Fattakhdinov A.U., Loktev, D.A. et al. Fizika I tekhnika poluprovodnikov 2007, v. 41 (10), p.1207 (in Russian).

CHARACTERIZATION OF Sn DOPED ZnS THIN FILMS SYNTHESIZED BY CBD

MA JAFAROV, AH KAZIMZADE, EF NASIROV and SA JAHANGIROVA

Baku State University, Institute for Physics Problem, Baku, Azerbaijan
E-mail: maarif.jafarov@mail.ru

Zinc sulphide (*ZnS*) thin film were prepared using chemical bath deposition (CBD) process and tin (*Sn*) doping was successfully carried out in *ZnS*. Structural, morphological and microstructural characterization was carried out using XRD, TEM. XRD pattern confirms presence of hexagonal phase. The particle size of prepared hexagonal wurtzite *ZnS* was around 14-18 nm with average size of ~16.5 nm. The bandgap of the film increases from ~ 3.69 eV for *ZnS* to ~ 3.90 eV for 5% *Sn* doped *ZnS* film which might be due to more ordered hexagonal structure as a result of tin incorporation. PL study shows variationof intensity with excitation wavelength and a red shift is noticed for increasing excitation wavelength.

Keywords: CBD, Sn:ZnS thin film, XRD, TEM, Particle size, Optical band gap
PACS: 68.37.-d, 68.47.Fg, 34.50.Dy

Introduction

Zinc sulfide *ZnS* is one of the direct II–VI semiconductorcompounds with large band gap energy of ~3.65 eV at room temperature [1-3]. The material crystallizes in both cubic and hexagonal forms and is a material of reference to test several theoretical models in condensed matter physics. The material has huge potential application in both bulk and thin film form in various photovoltaic andoptoelectronic devices [4,5]. It is used as key material for solar control coating, optoelectronic devices, electroluminescence devices, sensors and others. *ZnS* is a prospective material to be used in solar cell as passivation layer for better photovoltaicproperties. Due to its high refractive index (n ~ 2.3), it canbe used as an antireflective coating. *ZnS* is also an important phosphor host lattice material used in electroluminescent devices (ELD). Various physicaland chemical techniques have been used by researchers todeposit *ZnS* thin films. While physical deposition methods such as sputtering, metal organic chemical vapor deposition (MOCVD), molecular beam epitaxy (MBE) and atomic layer epitaxy (ALE) demand the use of either vacuum conditions and/or complex equipment, chemical techniques are simpler and cost effective [6]. The technique of CBD (also known as chemical solution deposition) is simple, inexpensive and can be adaptable tolarge area processing with low fabrication cost. Also doping with metal ions at low temperatures can be conveniently carried out at this technique. For tin doped *ZnS* nanoparticles with thiourea as capping agent, quantum confinement effect leading to blue shift in band gap has been reported [7]. Detail information regarding effect of tin incorporation on microstructure of ZnS is not available. This was the key motivation behind this work. In the present study we report the synthesis of ZnS and Sndoped ZnS thin films by CBD and their microstructural andoptical properties.

Experimental

ZnS and Sn doped ZnS thin film was deposited on well treated microscope glass slide substrates as substrate treatment plays an important role in deposition of thin film by CBD process. The substrate cleaning steps involved overnight keeping in chromic acid followed by rinsing in distil waterand ultrasonic cleaning in equivolume acetone and alcoholfor about 20

minutes. The glass substrates were lightly rubbed before immersion for better adherence and dipped vertically in the bath solution. All the chemicals and reagents used to prepare the reacting bath were of analytical reagent grade. 80 ml 0.2 M zinc acetate [$Zn(CH_3COO)_2.2H_2O$] and 160 ml 0.2 M thiourea [$(NH_2)_2CS$] was added and stirred properly at room temperature. Then 0.66 M tri-sodium citrate as complexing agent was mixed properly in the solution. After that, ammonia solution was added to make the pH 11 of the bath. The substrates were immersed in the bath solution for 24 hours and a white colored film with a faint shadow of blue appears over the surface of the substrate. To obtained *Sn* doped *ZnS* thin film, 0.1 M tin chloride ($SnCl_2$, $2H_2O$) was added in proper ratio with the solution. In this process *ZnS*, 2.5% *Sn: ZnS* and 5% *Sn: ZnS* thin films were prepared. Attempts to prepare films with more than 5% resulted in instability of the acetate bath resulting in non-uniform films with pinholes. Film thickness measured using gravimetric weight difference method[22-23] was approximately ~1300 nm for *ZnS* and ~1400 nm for 5% *Sn: ZnS*.

The phase identification and crystalline properties of undoped and doped samples were studied by X-ray diffraction (XRD) method employing a Bruker (D8 advance) x-ray diffractometer with Ni-filtered CuK_α radiation (λ=1.5418 Å). The Transmission electron microscopy (TEM) investigation was carried out using Tecnai F30 microscope operating at 200 kV accelerating voltage. The sample was separated from the substrate carefully and dispersed in ethanol by ultrasonication process. Then they were mounted on a carbon coated copper grid, dried, and used for TEM measurements. The optical absorption measurements were carried out using a Schimatzu dual beam UV-Vis spectrophotometer (Model No: UV-1800). The spectrum was recorded by using a similar glass slide as reference and hence the absorption due to the film only was obtained. The band gap of the films was calculated from the absorption edge of the spectrum.

Results and discussions

The X-ray diffraction patterns of undoped *ZnS* and *Sn* doped *ZnS* films are shown in Figure 1. The materials were scanned in the range 20-70°. Intensity in arbitrary units is plotted against 2θ in Figure 1. It is seen from Figure 1 (a) that peaks appears at 26.42°, 28.38°, 30.35º and 47.65° respectively. The diffractogram of the sample reveals that all the peaks are in good agreement with the Joint committee on powder diffraction standard (JCPDS) data belonging to hexagonal *ZnS* structure (Card No. 36-1450). The corresponding reflecting planes are (100), (002), (101) and (110) respectively. The (101) peak appears with maximum intensity at 30.35°. The major peak along with the other peaks is shifted slightly towards lower angles for tin doped films. The peak positions for 5% *Sn: ZnS* films are 26.32°, 28.3°, 30.20° and 47.50° respectively. For pure *ZnS* film, the ratio is ~0.32 and it increases to ~0.79 for 5% *Sn: ZnS*. Such enhanced ordering of structure possibly also facilitates film growth rate and enhanced thickness due to tin doping.

Figure 2 shows optical absorbance spectrum [absorbance (*A*) as a function of wavelength (λ)] for *ZnS* and *Sn* doped *ZnS* films. The absorbance coefficient increases with increasing *Sn* doping for the entire wavelength range. Increase of absorbance implies decrease of transmittance which might be due to enhanced thickness due to *Sn* incorporation. This might be attributed to increase of film thickness due to tin enrichment. Although no systematic thickness measurement

was carried out in our work, a rough and ready gravimetric technique (measuring the weight change of the substrate due to film deposition and dividing this by area of film deposition and known density of the material) shows increase of thickness with tin enrichment (~1300 nm for pure ZnS to ~1400 nm for highest tin content film). Band gap energy (E_g) was derived from the mathematical treatment of the data obtained from the absorbance vs. wavelength spectrum for direct band gap ZnS using Tauc's relationship: $(\alpha h\nu)^2 = A(h\nu - E_g)$ where v is the photon frequency, A is a function of index of refraction and hole/electron effective masses and h is the Planck's constant. Absorption coefficient (α) was evaluated from the relation A = 2.303αt and using the measured values of thicknesses (t) for ZnS and Sn doped ZnS films.

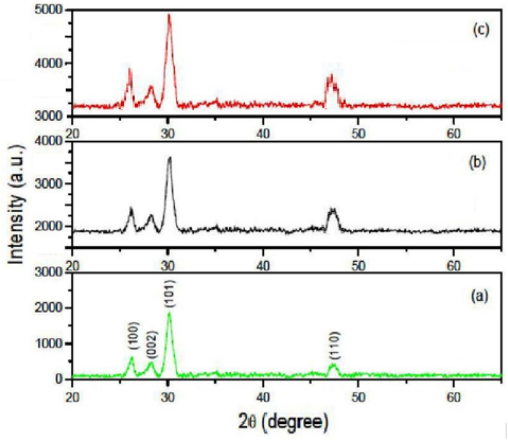

Fig. 1. X-ray diffraction pattern of (a) *ZnS*, (b) 2.5% *Sn: ZnS* and (c) 5% *Sn: ZnS.*

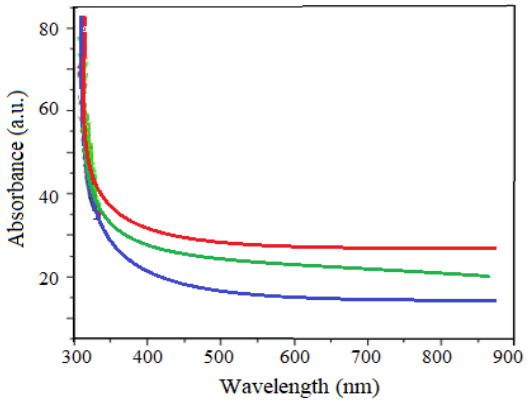

Fig. 2. Absorbance versus photon wavelength for (a) *ZnS*, (b) 2.5% *ZnS:Sn* and (c) 5% *ZnS:Sn*.

Figure 3 shows the plot of $(\alpha h\nu)^2$ as a function of photon energy $h\nu$. Extrapolation of the line to the base line, where the value of $(\alpha h\nu)^2$ is zero, gives band gap E_g. The sharp absorption edge corresponding to the band gap confirms the good quality of the films. The band gap energy increases from ~3.69 eV for *ZnS* to ~ 3.90 eV for 5% *Sn: ZnS* indicating a blue shift. Incidentally the band gap of tin sulphide is much lower than that of zinc sulphide and thus incorporation of tin should have caused red shift in band gap. Thus it appears that a particle size reduction of ~15% only cannot lead to such enhancement in band gap. Since the particle sizes observed are much higher than the *ZnS* Bohr exciton radius, quantum confinement effect is obviously not the reason

behind such a blue shift. The only other possible reason might be enhancement of relative intensity of the major diffraction peak corresponding to hexagonal wurtzite structure (100 plane). Such enhancement of relative intensity implies more ordered structure and a band gap closer to bulk value. Thus the enhancement in band gap may be ascribed enhancement of structure ordering resulting from enhancement of relative intensity of the major diffraction peak of hexagonal wurtzite structure. In hexagonal wurtzite structure, the band gap can even reach a very high value of ~4.4 eV.

Dependence of photoluminescence (PL) spectra of *ZnS* films on the excitation wavelength (λ_{ex}) has been investigated. Figure 4 shows the PL intensity spectrum is plotted against wavelength for different excitation wavelength (340-420 nm). A redshift has been observed with increase of excitation wavelength which may be due to different contribution of excitonic emissions and their phonon replicas[32]. The intensity of the peaks decreases with excitation wavelength.

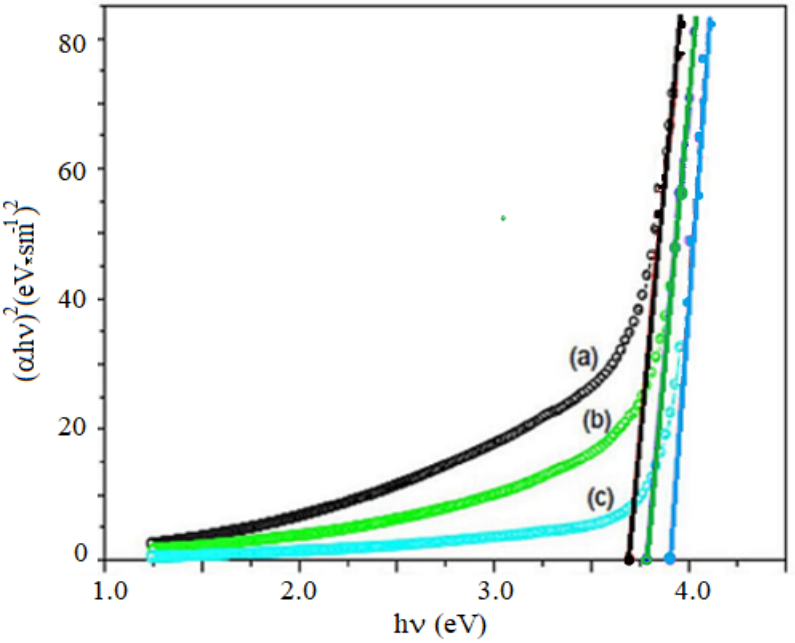

Fig. 3. Plot of $(ahv)^2$ versus *hv* for (a) *ZnS*, (b) 2.5% *ZnS*: *Sn* and (c) 5% *ZnS*: *Sn*.

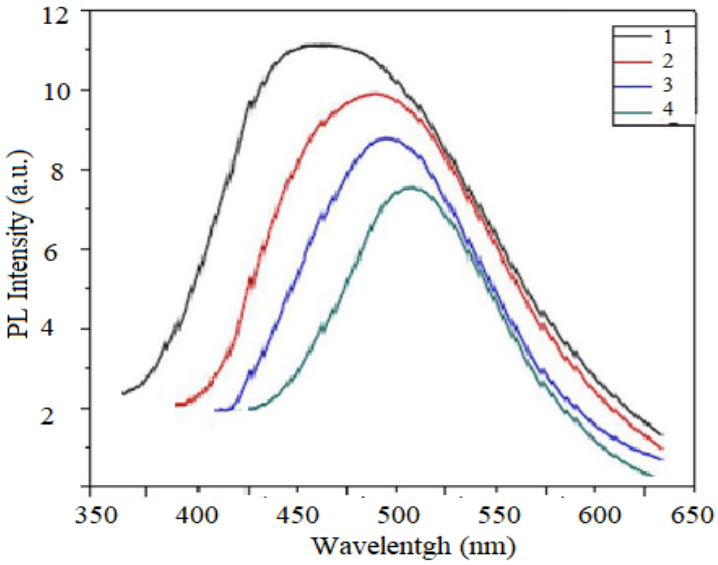

Fig. 4. PL spectrum of *ZnS* film for different excitation wavelengths, λ:1-300, 2-320, 3-340, 4-380.

Conclusion

The primary aim of the present investigation was to explore the possibility of doping *ZnS* with tin by CBD method. *Sn* doped *ZnS* films with different percentage of *Sn* content (2.5% and 5%) could be successfully synthesized through this technique for the first time to the best of our knowledge. The average particle size of ~15-18 nm for *ZnS* evaluated by X-ray technique is on the lower side compared to TEM observation (~16.5 nm). The crystal structure is hexagonal as confirmed by XRD and TEM. *Sn* doping increases the fundamental absorption edge. The band gap energy increases from ~ 3.69 eV for *ZnS* to ~ 3.90 eV for 5% *ZnS:Sn*. The materials are therefore useful for configurations that involve bandgap engineering.

References

1. Ozutok F, Erturk E, Bilgin V. Acta Physica Polonica A 2012, v. 121, p. 221.
2. Rawlins T.G.R., Woodward R.J. Journal of Materials Science 1972, v. 7 (3) p. 257.
3. Nasr T.B., Kamoun N., Kanzari M., Bennaceur R. Thin Solid Films 2006, v. 500 (1-2), p. 4.
4. Shinde M.S., Ahirrao P.B., Patil I.J., Patil R.S. Indian Journal of Pure & Applied Physics 2011, v. 49 (11), p. 765.
5. Thi T.M., Hien N.T., Thu D.X., Trung V.Q. J.of Experimental Nanoscience 2012, v. 8 (5), p. 694.
6. Hachiya S., Shen Q., Toyada T. Journal of Applied Physics 2012, v. 111 (10), p. 104315.
7. Tec-Yam S., Rojas J,, Rejón V., Oliva A.I., Materials Chemistry and Physics 2012, v. 136 (2-3), p. 386.

NANOSTRUCTURED POR Si-CdSTe THIN FILMS

HM MAMEDOV[1], MA JAFAROV[1], A KUKOVECZ[2], Z KONYA[2], EF NASIROV[1], VU MAMMADOV[1] and GM EYVAZOVA[1]

[1]Baku State University, Baku, Azerbaijan
[2]University of Szeged, Szeged, Hungary
E-mail: maarif.jafarov@mail.ru

Nanostructure CdSTe thin film was fabricated by electrodeposition technique. To manufacture the heterojunctions, p-type *c*-Si wafers of (100) orientation were used as a substrate. Before anodization, the surface of the *c*-Si substrates were etched in an aqueous solution of HF and further washed in distilled water (at temperature of 80°*C* and ethyl alcohol and then dried in air. The current-voltage characteristics of the CdSTe /PS solar cell under dark conditions show that forward bias current variation approximately exponentially with voltage bias. The capacitance for Nano- CdSTe /PS Solar Cell decreases with the increase of the reverse bias voltage and with the increasing of etching time of nPS layers.

Keywords: CST, Thin Films, electrochemical deposition, current-voltage characteristics
PACS: 34.50.Dy, 85.60.pg, 52.59.Mv

Introduction

Compound semiconductors such as CdSTe are important because of their photovoltaic, photoelectrochemical, and electroluminescent applications and, thus, they have much attention. Recently, there have been many efforts to produce nanosized materials, because electrical and optical properties can be varied via chemical control over the size, stoichiometry, and interparticle separation. These materials have been synthesized by various techniques including pyrolysis of organometallic compounds and sol gel synthesis. In recent years, there has been considerable interest of using thin films in solar cells [1-3]. Photoelectrical properties of these heterojunctions have found practical application in phototransistors and in solar cells. However, the physics and technology of heterojunctions have also other prominent aspect - creation, research and practical application of non-ideal heterojunctions. The big set of various effects and phenomena in non-ideal heterojunctions related to various properties of semiconductors on both junction regions of heterocontacts have been observed [4-6]. Perspectivity of practical application of the non-ideal heterojunctions is related first to more economic technology of creation of polycrystalline heterostructure in comparison with the monocrystalline [7-9].

Porous silicon has attracted great attention due to its room temperature photoluminescence in the visible light range. As we know that, the bulk crystalline silicon has an indirect gap at 1.1 eV at room temperature, which results in a very inefficient radiative recombination and produced light in the infrared region. Therefore, the strong visible light emission in porous silicon is quite surprising and such structure can exhibit a large variety of morphologies and particles sizes. The precise control of porosity and thickness allows the tailoring of optical properties of porous silicon and has opened the door to a multitude of applications in optoelectronics technology [10-12]. Such structures consist of silicon particles in several nanometer size separated by voids. Hence, porous silicon layers are regarded as nanomaterials, which can be obtained by the electrochemical etching of silicon wafer. In section two, the synthesis and characterization of electrochemically anodized nanocrystalline

porous silicon layers is done, then, the setup was used in fabrication as a device of Nano-CdSTe/PS heterojunction solar cell, and investigating the electrical properties of the heterojunction [13,14] . This paper is devoted to studying the CdSTe /por-Si/p-Si heterostructure.

Experimental

CdSTe thin films were electrodeposited potentiostatically on ITO and por.Si substrates supported by polyethylene terephthalate (PET). To manufacture the heterojunctions, p-type *c*-Si wafers (2.5 $Ohm \cdot cm$ resistivity and 0.2 ÷ 0.3 *mm* thickness) of (100) orientation were used as a substrate. Before anodization, the surface of the *c*-Si substrates were etched in an aqueous solution of HF and further washed in distilled water (at temperature of 80*°C*) and ethyl alcohol and then dried in air. The anodization of *c*-Si substrate surface was carried out in Teflon chamber with Pt cathode. HF: ethanol solution (1:1) were used for the porous silicon formation. The anodization voltage, current density and anodization time were 30*V*, 40-70 mA/cm^2 and 30–1800 *sec*, correspondingly. Depending on the anodization current and time porous-Si with porous size of 7-50 *nm* were prepared on the surface of *c*-Si.

Depositions were carried out potentiostatically under nitrogen atmosphere at room temperature from a de-aerated aqueous solution containing $CdSO_4$ (0.01M), TeO_2 (0.01M), and $Na_2S_2O_3$ (0.2M). To optimize the stoichiometry of the deposit, electrochemical baths with different compositions, obtained mixing different volumes of the above-mentioned solutions, were tested. The final pH was about 5, it was obtained adding lactic acid and NaOH (10M). Electrodeposition was performed for 45 min, at a potential of -1.05V vs. saturated calomel electrode (SCE); electrochemical experiments were performed using a PAR potentiostat/galvanostat (model PARSTAT 2273).

Morphological analyses were performed by scanning electrode microscopy (SEM), using a FEI field-emission gun (FEG) environmental scanning electron microscope (model QUANTA 200F). Films were also characterized by XRD analysis, using an ItalStructures (APD2000) diffractometer having the Cu Kα radiation (λ= 0.154nm) as the source, with a step of 0.02° and a measuring time of 0.5s for each step. A computerized 619 Electrometer/Multimeter was used to measure the current-voltage (I-V) characteristics of the resulting solar cells using a solar simulator with light intensity corrected to a power density of 100 $mW \cdot cm^{-2}$ (AM1.5). The results of the materials characterisation and device assessment are presented and discussed in the next section.

Results and discussion

The morphology of PS was investigated using SEM. SEM data indicate that the increase of anodization current density leads to the increase of the resulting pore size and a significant surface flattening between the pores. In order to achieve a more direct insight into the surface structural features of the films, SEM imaging had been performed. SEM images of CdSTe thin films deposited at potential of 0.86 *V* onto the *c*-Si/PS (with pores size of 10; 20 and 30 *nm*) are shown in Figure 1.

The size of the grains was different from each other, indicating irregular growth rate of the grains. The pass direction corresponds to positive polarity of the external bias on the *c*-Si layers. Rectification increases from 180 up to 1100, with increasing the pores size from 10 to 20 *nm*. It is assumed that the change in rectification factor value depending on the pore size is due to the oxygen or nitrogen molecules, because in order to remove excess water from pores and films, heterojunctions were dried in air, just after the deposition (as-deposited heterojunctions).

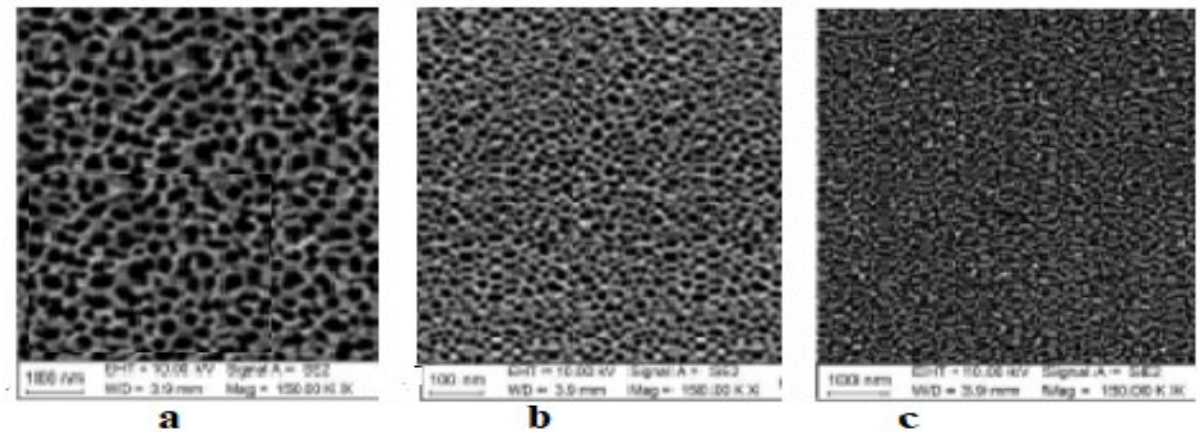

Fig. 1. SEM images of porous silicon prepared at different regimes of anodization: 30*V*; 70 *mA/cm*^{2}; 1800 *sec*(a); 30V; 55 *mA/cm*^{2}; 1800 *sec*(b); 30 *V*; 40 *mA/cm*^{2}; 400 *sec*(c).

Depending on composition of electrolytic bath used for the deposition process, it was possible to obtain different CdSTe deposits, characterized by different chemical compositions. It was necessary to investigate different baths prior to find the best experimental conditions leading to CdSTe films with suitable composition for solar cell applications. We have checked the influence of bath composition on the kinetics of deposition and on film morphology and composition, varying the volumes of mixed initial solutions. A compact enough CdSTe layer covering uniformly all substrate area exposed to the solution was obtained. Thermal treatment would vary the structure of the film, but we didn't perform it because of ITO/PET substrate, which could not be exposed at high temperatures (PET decomposes at about 340°C). In fact, annealing would be efficient at temperatures higher than 400°C and, thus, it is necessary to change the substrate.

The prefered orientation of the structure is in the <002> direction with the corresponding XRD peak at 2θ = 26.3°. However, the (002) peak was not used for estimating the crystallite size since it coincides with an İTO peak. As a result, the next higher peak which is the (101) peak at 2θ ~ 28.1° was used for this purpose. The estimated crystallite sizes using Scherrer equation were ~21 nm and 63 nm before and after annealing respectively. The d-spacing obtained for the annealed sample was 3.186 Å. The corresponding 2θ and d-spacing for the reference file are 28.2° and 3.164 Å respectively. Figure 2 shows that the electrodeposited CdSTe is highly oriented in the <111> direction with a cubic structure.

Atomic force microscopy (AFM) is one of the effective ways for the surface analysis of p-Si/10 *nm porous*-Si/ CdSTe; thin films due to its high resolution and powerful analysis software (Fig.2.).

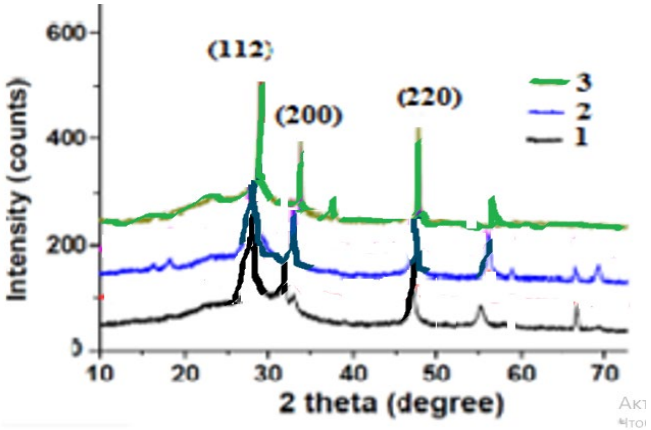

Fig. 2. X-ray diffraction patterns of electrodeposited polycrystalline CdSTe highly oriented thin layers on Por-Si substrates, before (1,2) and after (3) annealing respectively.

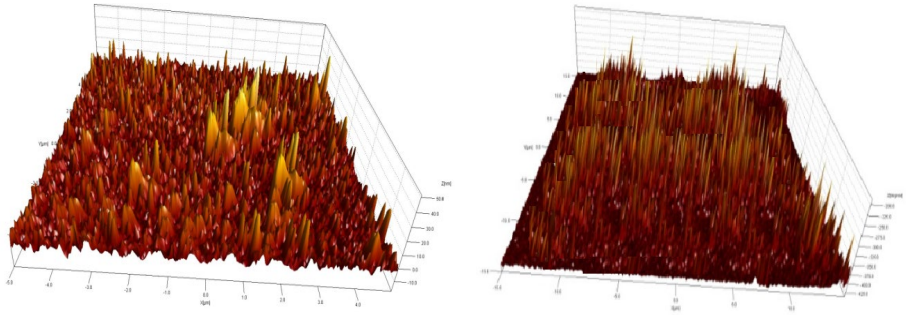

a b

Fig. 3. AFM images of electrdeposited films : (a) p-Si/20 *nm porous*-Si/ CdSTe; (b) p-Si/10 *nm porous*-Si/ CdSTe.

The current-voltage curves are the most commonly used characterization tool for the devices. In this technique, the current is measured as a function of voltage of the heterojunction, in both dark and light. Figure 4 represents I-V characteristics under illumination with power intensities room temperature of the Nano- CdSTe /PS heterojunction, containing nPS layers prepared at different etching times (10 and 20) *min*.

In this case, adsorbed oxygen or nitrogen molecules to the silicon pores creates the acceptor states in junction region and thus increase recombination acts. It is established that the degree of adsorption depends on pores size. To confirm this fact, heterojunctions were heated in vacuum at 50 -70°*C* and *J-V* characteristics were taken in vacuum. It is established that rectification in heterojunctions with pore size of 10 and 20 *nm* remained almost unchanged.

Also, the reverse bias current contains two regions in the voltage region the current increases with increasing the applied voltage, and the generation current dominates. In addition, the current-voltage characteristics exhibit rectification behavior may be due to the

hetrojunction potential barrier at the CdSTe /PS interface.The rectification factor indicates the ratio between forward and reverse current at a certain applied bias voltage. Due to the high density of states of the nPS layer which will result in screening of internal field inside the nPS layer, this field would be nearly homogenously distributed through the nPS layer at higher voltages ($V > 1$ V), therefore, the forward bias characteristics will be controlled by the PSi layer resistance. This result explains the lowering of flow current in forward bias with the increasing of etching time of nPS layers, since the porosity of nPS layer increases with etching time and hence the resistance of nPS layer becomes too high which leads to low forward current. The photocurrent has been observed in reverse bias only, and we can see from this figure, that the presence of the light illumination strongly increases the reverse current. The photocurrent is always in the reverse bias direction due to it increases by increasing the depletion region width. The increasing of the reverse bias voltage leads to the increase in the internal electric field, which leads to an increasing in the probability of the separated electron-hole pairs.

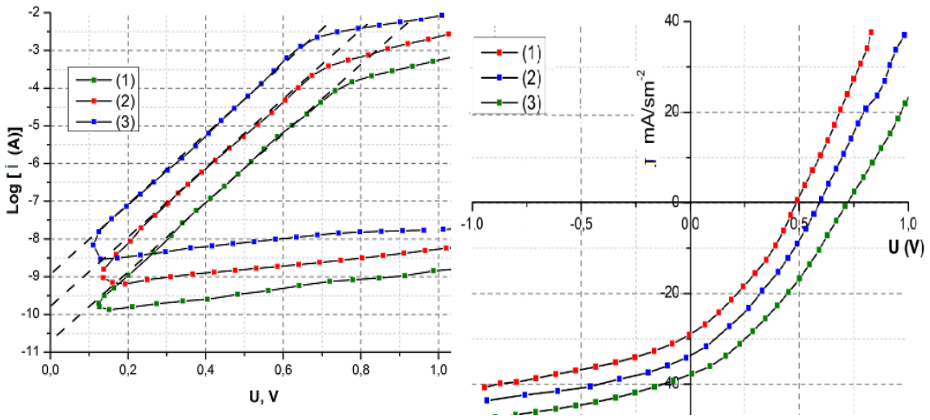

Fig. 4. I-V characteristics at dark (a) at forward and reverse bias voltage and under illumination conditions (b) for heterojunction Nano- CdSTe /PS before (1-20 nm, 2-10nm) and after (3-10nm) HT

The effect of preparation conditions of nPS layer such as etching time has very important effect on the photocurrent characteristics of the device, where one can observe from Figure 4, that the photocurrent is reduced with the increasing of etching time. This result can be explained since the porosity of nPS layer increases with the increasing of etching time. The increasing of porosity leads to increase the resistivity of nPS layer; therefore, the photocurrent will decrease.

The capacitance-voltage characteristics have been studied in this work. The variation of capacitance as a function of reverse bias voltage in the range of (0-1) V for Nano- CdSTe /PS heterojunction, which prepared before (1-20 nm, 2-10nm) and after (3-10nm) HT are shown in Figure 5. It is observed from this figure that the capacitance decreases with increasing the reverse bias. This decreasing was non-linear, that the capacitance becomes constant approximately at high voltages. The relation between inverse capacitance squared (C^{-2}) against the reverse bias at different values of etching time are shown in Figure 5. A linear relationship between C^{-2} and reverse bias voltage was obtained for the structure, this linear relationship represents that the junction was abrupt type. The interception of the straight line

with voltage axis at ($1/C^2$ = 0), represents the built-in voltage. Assuming that the resulting junction is one-sided junction, these data were calculated according to Anderson model

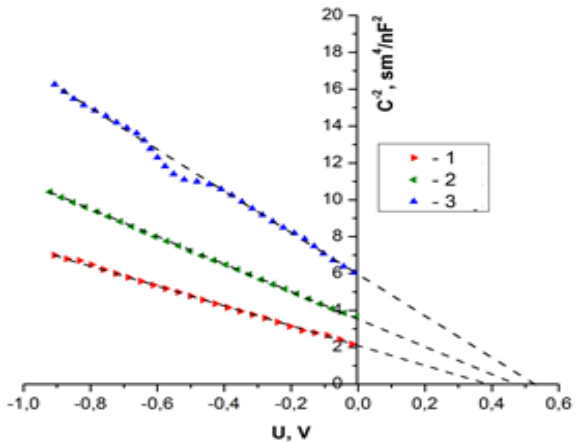

Fig. 5. The variation of $1/C^2$ as a function of reverse bias voltage for heterojunction Nano- CdSTe before (1-20 nm, 2-10 nm) and after (3-10 nm) HT.

Conclusion

Nanostructure CdSTe thin film was fabricated by electrodeposition technique. To manufacture the heterojunctions, p-type *c*-Si wafers of (100) orientation were used as a substrate. Before anodization, the surface of the *c*-Si substrates were etched in an aqueous solution of HF and further washed in distilled water (at temperature of 80*℃* and ethyl alcohol and then dried in air. The current-voltage characteristics of the CdSTe /PS solar cell under dark conditions show that forward bias current variation approximately exponentially with voltage bias. The capacitance for Nano- CdSTe /PS Solar Cell decreases with the increase of the reverse bias voltage and with the increasing of etching time of nPS layers.

Acknowledgement

This research was funded by the Science Development Foundation under the President of the Republic of Azerbaijan (EİF-ETL-2020-2 (36) -16 / 01/1-M-01).

References

1. Lincot D., Guillemoles J.F., Taunier S., Guimard D., Sicx-Kurdi J., Chaumont A., Roussel O., Ramdani O., Hubert C., Fauvarque J.P., Bodereau N., Solar Energy, 2004, v. 77, v. 6, p. 725. doi:10.1016/j.solener.2004.05.024
2. Bamiduro O., Chennamadhava G., Mundle R., Konda R., Robinson B., Bahoura M., Pradhan A.K. Solar Energy, 2011, v. 85 (3), p. 545. https://doi.org/10.1016/j.solener.2010.12.025
3. Ribeaucourt L., Savidand G., Lincot D., Chassaing E. Electrochimica Acta 2011, v. 56, p. 6628. https://doi.org/10.1016/j.electacta.2011.05.033.
4. Scragg J.J., Dale P.J., Peter L.M., Zoppi G., Forbes I. Physica Status Solidi (b), 2008, p. 1772. https://doi.org/10.1002/pssb.200879539.
5. Katagiri H., Jimbo K., Yamada S., Kamimura T., Maw WS, Fukano T., Ito T, Motohiro T. Applied Physics Express 2008, 1 (article number 041201, 2 pages). https://doi.org/10.1143/APEX.1.041201.
6. Jimbo K., Kimura R., Kamimura T., Yamada S., Maw W.S., Araki H., Oishi K., Katagiri H. Thin Solid Films. 2007, v. 515 (15), p. 5997. DOI:10.1016/j.tsf.2006.12.103

7. Merdes S., Abou-Ras D., Mainz R., Klenk R., Lux-Steiner M.C., Meeder A, Research and Applications 2012, v. 21 (1), p. 88. https://doi.org/10.1002/pip.2165
8. Prakash G.V., Singh R., Kumar A., et al. Mater Lett. 2006, v. 60 (13/14), p. 1744.
9. Zhang L., Chen Z., Tang Y., et al. Thin Solid Films, 2005, v. 492 (1/2), p. 24. DOI 10.1016/j.tsf.2005.06.028
10. Mamedov H., Muradov M., Konya Z., Kukovecz A., Kordas K., Shah S.I. Photonics Letters of Poland 2018, 10 (3), p. 73. DOI: 10.4302/plp.v10i3.813
11. Mamedov H.M., Mammadov V.U., Mammadova V.J., Ahmadova Kh.M., Journal of Optoelectronıcs and Advanced Materıals 2015, v. 17 (1-2), p. 67.
12. Tregulov V.V. , Litvinov V.G., Ermachikhin A.V., Semiconductors 2018, v. 52 (7), p. 891.
13. Ibiyemi A. A., Tech M., Awodugba A. O. The Pacific Journal of Science and Technology, 2012, v. 13 (1), p.149.
14. Yoshikawa K., Kawasaki H., Yoshida W., Irie T., Konishi K., Nakano K., Uto T., Yamamoto K. Nature energy 2017, v. 2, p. 17032. DOI: https://doi.org/10.1038/nenergy.2017.32

ELECTRICAL AND OPTICAL PROPERTIES OF ZnSTe THIN FILMS PREPARED BY CHEMICAL BATH DEPOSITION

EA KHANMAMMADOVA

Azerbaijan State University of Oil and Industry, Baku, Azerbaijan
E-mail: dadashovaelmira@mail.ru

Semiconductor ZnSTe thin films have been deposited by a chemical bath deposition (CBD) on a glass substrate at 80 °C with different deposition time (4, 6 and 8 h). The film thicknesses have been calculated between 200 – 800 nm by using gravimetrical analysis. The specific resistivity values (ρ) of the films are found to be between 1.08×10^5–1.01×10^6 Ω·cm and exhibit an *n*-type conductivity. The optical transmittance values of ZnSTe thin films in the visible region of the electromagnetic spectrum have been found to be between 50–90%. The calculations indicate that the refractive index (*n*) in the visible region is between 1.40 and 2.45. The optical band gaps (*E*g) of thin films have been calculated between 3.61–3.88 eV while the band edge sharpness values (*B*) are varied between 6.95×10^9–8.96×10^{10} eV/cm^2.

Keywords: ZnSte, Thin film, CBD, Optical properties, Electrical properties
PACS: 61.14.Qp, 68.35.Ja, 51.50+v

Introduction

Semiconductor zinc sulfide (ZnS) thin films play important role in terms of their utility in optoelectronic and photovoltaic devices. Among II-VI semiconductor compounds, ZnS holds a rather wide band gap (3.8 eV) and a high refractive index (2.3) with an *n*-type conductivity [1-4]. ZnSTe semiconductor thin films have been recently utilized as a promising materials in applications such as solar panel window materials, information storage, data transfer, and UV-sensitized coatings [5]. The reason of utilizing ZnSte in solar panel windows can be explained in terms of having wide band gap of the ZnS electronic structure inducing reduction of absorbance losses, and increasing in the short-circuit current [6]. ZnSTe thin films show a high refractive index, and have a dielectric filter along with its high transmittance values in the visible region of the light spectrum utilizing them in optical reflector applications [7]. It should be noted that those films can also be used in blue and UV light emitting diode (LED) applications [8]. ZnS thin films require a high quality growth in order to use them in electroluminescence and solar cell applications. Additionally, the technique is suitable for large surface semiconductor coatings with low cost, which can also be taken into account in terms of its advantages over other technique.

In this study, the effects of deposition time on optical and electrical properties of ZnSTe thin films are deeply investigated by using various experimental techniques. The experimental results showed that ZnSTe thin films are highly promising materials to utilize the optoelectronic device technology.

Experiment

ZnSTe thin films are deposited by chemical bath deposition (CBD) on a glass substrate. Prior to the deposition, the glass substrate with dimensions of 75×25×1 mm^3 is cleaned in a systematical order. The substrate is kept in diluted chromic acid for 5 min, and rinsed in tap water afterwards. Subsequently, the cleaning is further carried out with detergent only to be

rinsed again in deionized water (Purelab flex 3, water purity: 18.2 MΩ at 25 °C). In the last step of the cleaning process, the substrate is kept in ethyl alcohol (99.9% purity) for 10 min and rinsed with deionized water. The drying of the glass substrate is completed in an oven set at 100 °C for 2 h. The chemical constituents and materials for the ZnSTe thin film processing are selected with great care considering their function in the solutions. The ZnSTe thin film process solution consists of 1 M $ZnSO_4$, 2.5 mL NH_3/NH_4Cl buffer solution (pH=10.7), 0.8 mL 0.66 M K_2TeO_3, 2.5 mL 1 M N_2H_4CS (thiourea), and 0.5 mL 3.75 M $N(CH_2CH_2OH)_3$ (TEA) mixed with 12 mL of deionized water. The solutions are then transferred to 25 mL sterilized crucibles in order to start the mixing process. The mixing is achieved using a magnetic stirrer until a point of complete homogenization. In the next step, the clean glass substrates that are specified to particular dimensions as mentioned (75×25×1 mm^3), are dipped into the solution perpendicularly. The deposition time is kept at 4, 6, and 8 h for one immersing. The temperature is kept at 80 °C at all times during the process of the thin film production.

The thickness measurements of the thin films are performed by a Denver instrument TP-214 model gravimetrical analysis tool that has a sensitivity of 0.1 mg, and capable of weighing loads up to 210 g. Specific resistivity measurements of thin films are obtained with Hall measurements at room temperature. The specific equipment utilized for these measurements is an Ecopia Hall effect measurement system HS-3000.The optical properties of the thin films are then determined by the Perkin Elmer UV-Vis Lamda 2S spectrophotometer in the region of h =300– 1100 nm wavelength. It should also be mentioned that the UV-Vis analysis is carried out at room temperature to obtain the absorbance (*A*) and optical transmittance *T*) values. Initially a correction of the sort is made on the substrate and the incident beam/radiation that pass through the glass is normalized in a degree of 100%. With those room temperature optical transmittance values, they are let free of their dependency on the absorbance of substrate material.

Results and discussion

The determination of electrical properties of ZnSTe thin films is accomplished and all measurements are carried out at room temperature. The values of specific resistivity (ρ), mobility (μ) and carrier density (n) for ZnS thin films The mathematical correlation between specific resistivity (ρ), mobility (μ) and carrier density (n) is indicated. The specific resistivity values of the thin films are found to be 1.08×10^5 , 4.83×10^5 and 1.01×10^6 Ω·cm at 80 °C for 4, 6 and 8 h, respectively. It should also be noted that the films exhibit an n-type behavior.

Thin films deposited by the chemical bath deposition method at 80 °C and 4, 6, and 8 h time durations are measured in terms of their thickness with the gravimetrical analysis.

The thickness values of the thin films deposited in 4, 6, and 8 h, are measured as 210, 775 and 1375 nm, respectively. Figure 1 shows the variation of ZnSTe film thickness as a function of the deposition time. As clearly seen in Fig. 1, the film thickness increases linearly with deposition time. The optical transmittance (*T*%) and absorbance (*A*) values for the ZnSTe thin films between λ = 300–1100 nm region are given in Fig. 2(a, b).

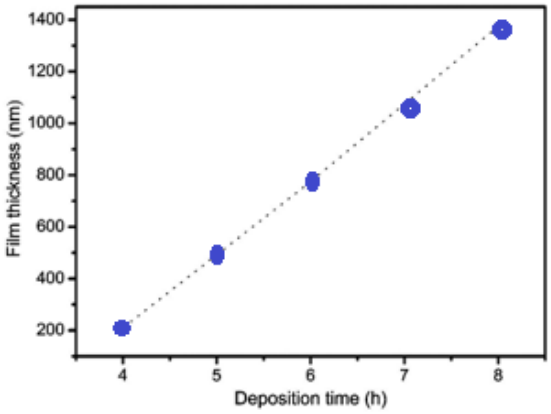

Fig. 1. Film thickness as a function of the deposition time for 4, 6, 8 h.

The examination of the transmittance and absorbance values yields a correlation between the film thickness and optical transmittance. The results reveal that an increase in the film thickness leads to a decline in the optical transmittance by 50% to 90%. Again, the evaluation of the absorbance values indicates that there is a sharp turn of events in the 300-330 nm region when compared to others as seen in Fig. 2(b), while the deposition time appears to increase the absorbance of the films. The absorbance band edge are initialized at ~ 310, 320, and 330 nm, for 4, 6, and 8 h deposition intervals, respectively.

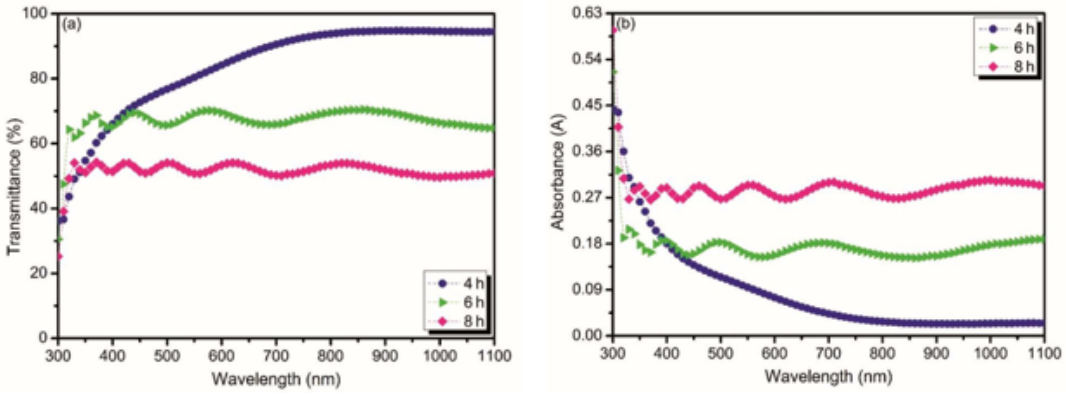

Fig. 2. Optical (a) transmittance and (b) absorbance spectra of 4, 6 and 8 h samples at 80 °C.

As clearly seen in Fig. 3, the deposition time causes an increase in the refraction values due to an increase in the film thickness, and the data from the other measurements such as the optical transmittance and absorbance is also proof regarding the deductions. Figure 4(a) indicates that the refractive index (*n*) values for the thin films are between relationship between the film thickness and the refractive index.

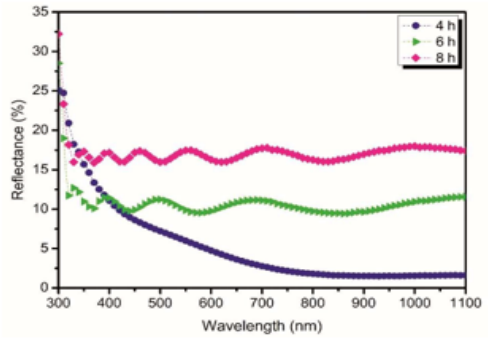

Fig. 3. Reflection spectra of ZnSTe deposited for 4, 6, and 8 h at 80 °C.

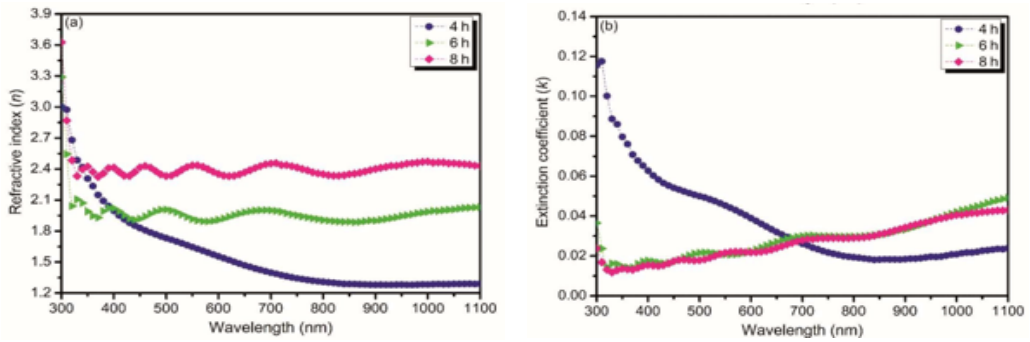

a) b)

Fig. 4(a) Refractive index and (b) extinction coefficient values of ZnS thin films deposited for 4, 6, and 8 h at 80 °C.

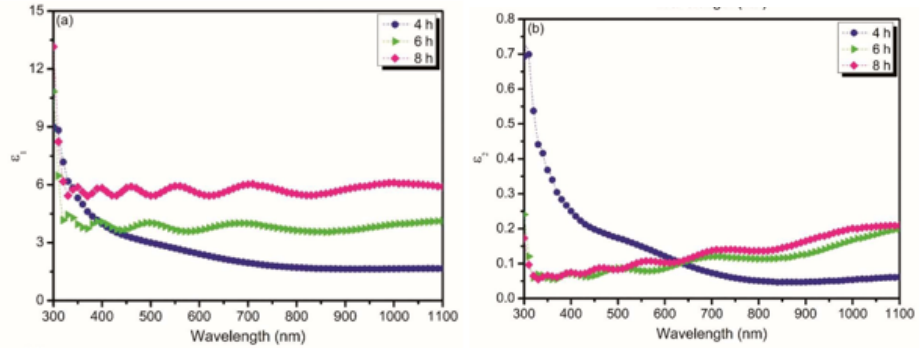

Fig. 5 (a) Real and (b) imaginary dielectric constant of ZnSTe thin films deposited for 4, 6, and 8 h at 80°C.

The dielectric constant values of the different films are calculated as demonstrated in Fig. 5(a, b). It is observed in Fig. 5(a) that the real dielectric constant of the thin films increases as the deposition interval widens with the effect of the increasing film thickness. increases, which is expected given the prior evaluations on these thin films. It can be said that the analysis from Fig. 4(a,b) indicates the relationship between the wavelength dependent refractive index values and extinction coefficient and real/imaginary dielectric constant analysis, complement to each other.

The determination of *E*g is accomplished by the determination of the point where *h* axis is cut at a point where $(ahv)^2 = 0$ as given in Fig. 6. The band edge sharpness (*B*) is determined via the slope in the linear region of $(ahv)^2 – hv$.

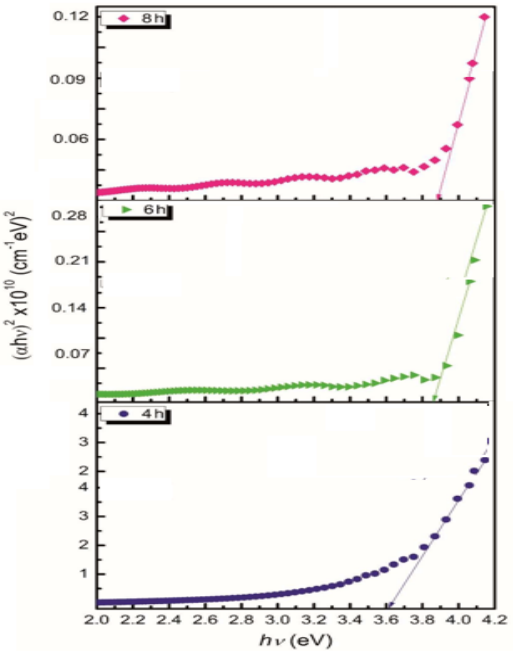

Fig. 6. Plots of $(\alpha h\gamma)^2$ vs $h\gamma$ for the ZnS thin films deposited at 80 ℃ with different depositi time (4, 6, and 8 h).

References

1. Zhang L., Chen Z., Tang Y., et al. Thin Solid Films, 2005, v. 492 (1/2), p. 24. DOI 10.1016/j.tsf.2005.06.028
2. Yokogawa T., Narusawa T., Journal of Crystal Growth, 1992, v. 117 (1-4), p. 480. DOI:10.1016/0022-0248(92)90796-L
3. Altosaar M., Raudoja J., Timmo K., Danilson M., Grossberg M., Krustok J., Mellikov E. Physica Status Solidi (a), 2008, v. 205 , p. 167. https://doi.org/10.1002/pssa.200776839
4. Nabiyouni G., Sahraei R., Toghiany M., Majles Ara M.H., Hedayati K. Rev Adv Mater Sci., 2011, v. 27, p. 52.
5. Mamedov H.M., Mammadov V.U., Mammadova V.J., Ahmadova Kh.M., Journal of Optoelectronıcs And Advanced Materıals, 2015, v. 17 (1-2), p. 67.
6. Najeeb M.A., Abdullah Sh.M., Aziz F.A., Zubair Sh.R. A., Mohamed A.M.A, Khalil, Uzma, Swelm, Wageh, Al-Ghamdi, Ahmed A., Sulaiman Kh. J Nanopart Res. 2016, v. 18 (12), p. 384.
7. Ibiyemi A.A., Tech M., Awodugba A. O. The Pacific Journal of Science and Technology 2012, v. 13 (1), p.149.
8. Yoshikawa K., Kawasaki H., Yoshida W., Irie T., Konishi K., Nakano K., Uto T., Yamamoto K. Nature energy, 2017, v. 2, p. 17032. DOI: https://doi.org/10.1038/nenergy.2017.32
9. Mike Cooke, J. Semiconductor Compounds, Advanced Silicon 2013, v. 8 (10). http://apex.jsap.jp/link?APEX/6/112102.

SPECIFICS OF ENHANCING SAFETY OF CANCER TREATMENT DURING PANDEMICS USING NANOPARTICLE MIXTURES

A CHIRAKADZE[1], G CHUBINIDZE[2], G PHICHKAHIA[2], Z BUACHIDZE[1], K CHIGOGIDZE[3], A GIGINEISHVILI[1], N KHUSKIVADZE[1] and M GULASHVILI[1]

[1]Department of Engineering Physics, Faculty of Informatics and Control Systems, Georgian Technical University, Tbilisi, Georgia
[2]Faculty of Medicine, Caucasus International University, Tbilisi, Georgia
[3]Faculty of Humanitarian and Social Sciences, Caucasus University, Tbilisi, Georgia
E-mail: achirakadze@gtu.ge; chubinidzegeorge@gmail.com; giorgi.phichkhaia@tsu.ge; jbuachidze@gmail.com; ketevan_chigogidze@yahoo.com; kakogigineishvili@yahoo.com; nanakhuskivadze53@gmail.com; marigulashvili25@gmail.com

Certain forms of cancer, along with other special conditions, chronic illnesses and addictions, significantly increase the risk of Covid-19 and severity of the disease. In the foreseeable future there will be a fairly large category of especially vulnerable groups of the population, having an acute need in specific treatment and antiviral protection modalities and tools. Several active complex combinations based on nanoparticles and nanocomposites, photosensitizers, liquid crystals and dyes, supposed to have a high and broad-spectrum activity against viruses (including new coronavirus), have been chosen in combination with reactive oxygen species (ROS) as a prospective antiviral treatment and protection modality. Their biological effectiveness against the strains of microorganisms of the American Type Culture Collection (ATCC) S. aureus, P. aeruginosa, E. coli, B.cereus, B. Subtilis was studied according to EN 13727 and EN 14476 standard methods. It was found that the strains of S. aureus, P. aeruginosa, E. coli and B. subtilis were completely deactivated, while the number of active B. cereus spores decreased by 10-12 times. Upon direct addition and homogenization of the synthesized nanoparticles in a nutrient medium at a concentration of 80-100 μg/ml, and further incubation, complete deactivation of B. cereus spores was observed. The acute toxicity of the developed combinations has been determined and a number of highly effective tools of Individual and Collective protective means has been proposed and tested.

Keywords: Covid-19; vaccination, nanoparticles, antiviral, toxicity
PACS: 61.46. +w;87.19.xj; 74.62.Bf

Introduction

Certain forms of cancer and its treatments, along with many other special conditions, chronic illnesses and addictions, significantly increase the risk of Covid-19 and severity of the disease. Despite the huge efforts of the developers and manufacturers of vaccines against the SARS-Cov2 virus, the prospect of final control over Covid-19 is becoming more distant, and the repetition of cycles of infection and mortality raise is becoming more common. It is already obvious that "boosting" is becoming a permanently repeated routine procedure, and the appearance of more and more aggressive strains due to mutations casts doubt on the reality of a sharp and sustained decrease in morbidity and mortality. The progress and results of vaccination are difficult to assess unequivocally. By mid-August 2019, 32% of the world's adult population had received at least one dose of the vaccine, and 24% were fully vaccinated [1]. At the same time, only 1.3% of adults in low-income countries received at least one dose. A serious problem is also associated with the so-called "anti-waxers" and "vaccine hesitance", which often find a considerable support in the mass media. Therefore, the provision of reliable and objective information is an important condition for a successful fight against pandemica?. According to the WOSCC (Web od Science Core Collection database), by September 2021, at least 110,000 studies have been devoted to the COVID-19 problem. Several vaccines have been approved for full marketing and use, but with the recurring waves and ongoing mutation

of the virus, there is an urgent need worldwide for new, safe and effective vaccines. As of August 20, 2021, there are 296 candidate vaccines in development, of which 112 are in the clinical research stage. Vaccine platforms include protein sub-units, viral vector (replicating or non-replicating), DNA, RNA, and inactivated virus. A peak of research also was focused on the side effects after vaccination. The most common side effects are injection site reactions, headache, fatigue, fever and chills. The reported rates of anaphylaxis for the Pfizer-BioNTech and Moderna vaccines are 5.0 cases per million and 2.8 cases per million, respectively. Polyethylene glycol, which is present in lipid nanoparticles, has been suggested as one of the causes of drug allergy, although it is still far from the final definition of the main mechanism of the anaphylactic shock caused by vaccination.Recently it was reported that vaccination with ChAdOx1nCov-19 can lead to the development of induced immune thrombocytopenia (VITT). In addition, cases of shingles or pityriasis (PR), PR-like rash, Guillain-Barré syndrome and myocarditis have been observed following vaccination with COVID-19 mRNA [1]. The largest number of studies has been conducted in the United States, England, China and Germany, with frequent partnerships between the United States, China, England and Canada. The University of Maryland and Ugur Sahin of the Johannes Gutenberg University Medical Center were the most cited institution and author, respectively.

For a long period of time, the primary and exclusive protection strategy has been to reduce direct contact, disinfect surfaces, physical barriers, physical distancing, respiratory hygiene, and the use of masks at droplet distance. Higher degrees of protection were used only for therapeutic procedures with the formation of aerosols. In our opinion, this largely contributed to the rapid spread of the new viral infection, primarily among medical personnel, patients and other specific groups of the population. At the same time, it has been proven that the droplet pathway is not the only, and possibly not the main pathway for the spread of the SARS-Cov-2 virus [2]. Consequently, reducing and suppressing the spread of SARS-CoV-2 requires measures to prevent inhalation of infectious aerosols, including ventilation, filtration and air disinfection, as well as a higher degree of protection for medical and frontline personnel. Medical grade portable HEPA purifiers have been found to be the most suitable treatment for airborne SARS-CoV-2 in indoor and public areas including hospitals, schools, dormitories, university auditoriums, kindergartens, shopping malls, supermarkets and markets, hotels, restaurants, cinemas, theaters, sports and concert halls, airports, railway stations, sea and river stations and ports, airplanes, urban transport, passenger trains, passenger ships, factories and plants, barracks, prisons and other places of detention, all large premises with a large crowd of people, etc. [3]. At the same time, an urgent need in new approaches and new highly effective medications against the SASRS-CoV-2 virus and Covid-19 disease is a crucial requirement of the current day, especially for cancer patients and other high-risk groups which cannot be vaccinated.

Development and toxicity testing of antivirsl nanoparticles and fabrics for the active protection and surgery masks, protection and isolation gowns and aweralls

Copper oxide semispherical nanoparticles, zinc oxide tetrapod nanoparticles, copper hydroxide and zinc hydroxide nanoparticles were synthesized according to methods given in [4-7], enhanced with 2.45 GHz microwave as a heating source. Microwave enhancement provided a 15-20% improvement in synthesis temperature reduce, crystallinity and monodispersity rate of the developed nanomaterials, which were vacuum-impregnated and fixed in the non-woven polypropylene fabrics by means of a 0.1 m^3 80 W handmade ultrasonic reactor. The biological effectiveness (acute toxicity) of both the developed nanomaterials and coated fabrics was tested against the following strains of microorganisms American Type Culture Collection (ATCC) S. aureus, P. aeruginosa, E. coli, B. cereus and B. Subtilis. Testing was carried out in the Richard Lugar Laboratory in Georgia according to EN 13727 standard (Quantitative suspension test for the evaluation of bactericidal activity in the medical area) and to EN 14476 standard (Quantitative suspension test for evaluation of virucidal activity in the medical area), with nanoparticle concentrations in the aqueous solution of 10-50 μg /ml and exposure times of 5 min, 15 min and 30 min.It was found that in case of copper and zinc oxides the strains of S. aureus, P. aeruginosa, E. coli and B. subtiliswere deactivated for 92-94 %, while the number of active B. cereus spores decreased by 9-10 times. The effectiveness of hydroxides was for 15-20 % higher. Upon direct addition and homogenization of the synthesized nanoparticles in a nutrient medium at a concentration of 80-100 μg/ml and further incubation, complete deactivation of B. cereus spores was observed for both oxides and hydroxides. The next step was the study of polypropylene fabrics with the impregnated and ultrasound-fixed nanoparticles in comparison with the identic fabrics without impregnated ones. The tests clearly showed that the survival time of the strains on the fabrics impregnated with nanoparticles was for an order shorter.

Development and testing of the antiviral air filtration and disinfection units based on the copper and zinc oxide and hydroxide nanomaterials impregnated in the oak charcoal micro-particles

The next stage of the study was the vacuum impregnation of copper and zinc oxide and hydroxide nanoparticles into the charcoal micro-particles and testing of their acute toxicity to the same strains of microorganisms. The above listed oxide and hydroxide nanoparticles were vacuum impregnared into the micro-particles of the activated oak tree charcoal with typical pores size 0.1 -100 μkm and their acute toxicity to the above listed strains of microorganisms was found to be about 4-6 times higher than of the nanoparticle dispersions and impregnated fabrics. After that, a simple experimental model of an antiviral filter for air sampling and pollution monitoring based on two HEPA-13 “Kaercher”filters, a vacuum cleaner and an intermediate layer of the activated chaircoal with impregnated nanoparticles was designed and prelliminarily tested. It shoved a 8-10-fold increase in the effectiveness of filtering due to the adition of chaircoal layer with impregnated and fixed active agents.

Fig. 1. Experimental model of an antiviral filter for air sampling and pollution monitoring based on two HEPA-13 "Kaercher" filters, a vacuum cleaner and an intermediate layer of the activated charcoal with impregnated nanoparticles.

Testing of the acute toxicity of the developed antiviral and air filtering materials

One of the most important characteristics of insecticides is their acute toxicity to the warm-blooded mammals. On the other hand, requirements for the standards of humane treatment of test animals (which should exclude the death of animals, causing them severe pain, significant deterioration of health, prolonged forced immobility, whole body anesthesia, etc.) are becoming increasingly stringent, and the modern methods of animal testing must be fitted to all modern 4 R (replace, refine, reduce, responsibility) principles of humane treatment of laboratory animals.The acute toxicity of developed drugs was tested using an original methodology developed and tested at the Georgian Technical University and Ivane Beritashvili Center for Experimental Biomedicine [8-10]. Methodology is based on the observation of the behavioral and physiological parameters of white rats in a standard branched training maze consisting of lighted and darkened sections. In addition to behavioral and mental characteristics, the four indicators, measured by means of the veterinary system of non-invasive blood pressure measurement of rodents "Systola", the non-contact infrared thermometer for animal research BIO-IRB153, the Free Radical Analytical System FRAS5 for measuring oxidation stress caused by reactive species and reactive oxygen species and the pulse oxymetertransflectance sensor NONIN 2000T were used for characterization of the general acute toxicity of insecticidal formulations to the exposed animals. The acute toxicity of commercially available SPIONs on the first day after exposure was taken as a 50% value.

Taking into account that the toxicity (biological effectiveness) of SPIONs against all the above strains was practically negligible, the acute toxicity of the developed highly effective copper and zinc oxides and hydroxides must be characterized as perfectly acceptable.

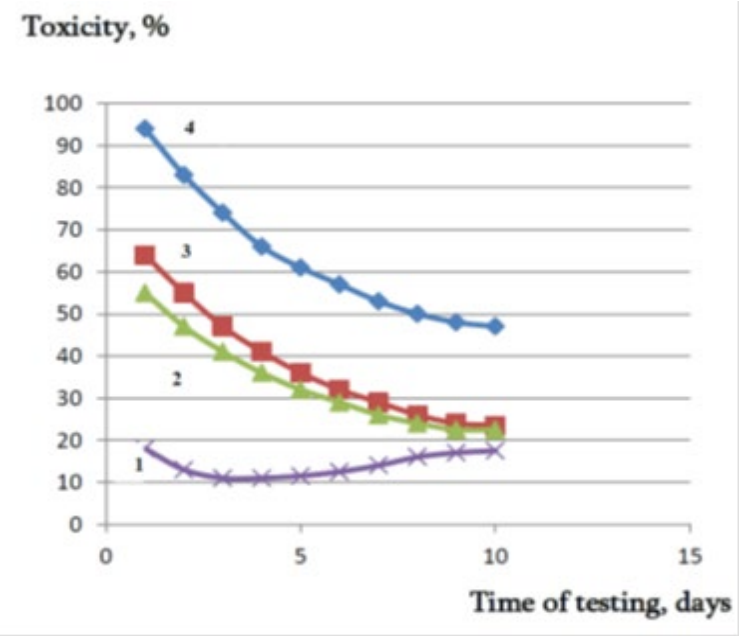

Fig. 2. Toxicity of copper oxide (1), zinc oxide (2), copper hydroxid and zinc hydroxide nanoparticles.

Discussion and conclusions

Despite the expected success of mass vaccination, the problem will still remain crucially relevant, since in the foreseeable future there will be a fairly large category of especially vulnerable groups of the population, such as elderly people, pregnant women, hypersensitive, patients with many chronic diseases, cancer patients, patients with psychological problems, etc. In this regard, our group has chosen several priority areas for the purpose of development, testing and implementation of the active complex combinations based on nanoparticles and nanocomposites, photosensitizers, liquid crystals and dyes with high antiviral activity (including the new coronavirus infection COVID-19). To date, the laboratory work on the development and testing of a UV generator of reactive oxygen species (ROS) based on titanium dioxide nanoparticles and photosensitizers porphyrins and phthalocyanines) has been carried out in cooperation with the Institute of cybernetics. Biological effectiveness of the generated ROS in combination with zinc and copper oxide/hydroxide nanoparticles was preliminary tested and showed ansynergystic super-additive effect. Currently, an intensive research on application of ROS in combination with biologically active nanoparticles is an urgently relevant area in antiviral and anticancer research, actively developed in the Georgian Technical University and partner organizations in Azerbaijan, Ukraine, India and Russia.

The developed copper and zinc oxide nanomaterials and HEPA filters were found to be the highly effective antiviral agents that can be the main components of the active personal and collective protection equipment including protective and surgery masks, isolation gowns and overalls and air filtration units. A very important characteristic of the developed materials is the high ratio of their biological effectiveness against pathogenic microorganisms to their acute toxicity to mammals. Apparently, the massive use of all these developed and tested modalities in combination with reactive oxygen species generators can make a significant

contribution to limiting the spread of the virus and protecting high-risk groups that cannot be vaccinated for various important reasons.

References

1. Xu Z.H., Qu H. Infection and Drug Resistance 2021, v. 14 (14), p. 4237.
2. Greenhalgh T., Jimenez J. The Lancet, 2021. DOI:https://doi.org/10.1016/S0140-6736(21)00869-2
3. Liu D.T., Phillips K.M. Otolaryngology. Otolaryngology–Head and Neck Surgery 2021. DOI: 10.1177/01945998211022636/http://otojournal.org.
4. Felix S., Chakkravarthy R.B.P. IOP Conf. Series: Materials Science and Engineering 2015. DOI:10.1088/1757-899X/73/1/012115. S.
5. Ramzuz I.N.M., Zakaria N. International Journal of Biosensors & Bioelectronics 2021, v.6 (3), p. 48.
6. Devamani H.P., Alagar M. Nano Biomedicine and Engineering 2013, v. 5 (3), p.116.
7. Saghatforoush L.A., Mehdizadeh R. Acta Chim Slov 2012, v. 59 (4), p. 863.
8. Mitagvaria N., Chirakadze A. Bulletin of the Georgian National Academy of Sciences 2021, v. 15 (1), p. 91.
9. Chirakadze A., Mitagvaria N. Bulletin of the Georgian National Academy of Sciences 2021, v.15 (2), p.120.
10. Chirakadze A., N. Mitagvaria. Annals of Agrarian Science 2021, v. 19 (4), p. 37.

MOLECULAR MODELING APPLIED TO THE BIOLOGICALLY ACTIVE SUBSTANCES

GA AKVERDİEVA, SD DEMUKHAMEDOVA, NA AKHMEDOV

Institute for Physical Problems, Baku State University, Baku, Azerbaijan
E-mail: gulnaraakverdieval@bsu.edu.az, http://orcid.org/0000-0003-1851-2234

In the represented work the role and possibilities of molecular modeling methods in modern research on the development of new drugs are discussed. The possibilities of a theoretical study of the spatial molecular structure are demonstrated on the example some biologically active substances. By molecular mechanics, molecular dynamics, quantum chemistry, molecular docking methods with application of modern programs the conformational profiles, geometry, structural, electronic and spectral parameters, molecular and physical properties of the biology active molecules have been established. Using received results and data of SAR studies the bioactive conformations for the investigated molecules were assessed and the pharmacophore models for their interaction with the specific receptors were constructed. An estimation of the arrangement of pharmacophore elements of the investigated molecules can be used for design of the peptidomimetics. The results of research create the prospects for the purposeful synthesis of steady medical products.

Keywords: Biologically active substances, molecular modeling, pharmacophore
PACS: 36.20.Ey, 36.20.Fz, 36.20.Hb

Introduction

The development of the representations on the interaction mechanism of pharmaceutical substance with the receptor and the understanding its electoral ability are possible owing to the structure-functional investigations. Many experimental works are devoted to the structure-functional investigations of the biologically active molecules. Note that none of these used methods led to a sufficient clarity, and even more so to a reasonable quantitative representation of the structure of such molecules. Moreover, developing a new drug is a very complex process which can take many years and can be very costly. Therefore, the search for new substances with specific biological activity is a problem that requires the use of modern molecular modeling techniques. One of the global challenges facing molecular modeling is to learn how to solve the problem of drug design using the structure of ligands and receptors. At present, the use of various theoretical calculation methods, the recent achievements of the computer technology, including programs with a graphic representation of spatial structures, allows researchers to construct all possible models of the pharmaceutical substance under study and its complex with specific receptore. The research work conducted on the basis of molecular modeling within the framework of the pharmacophore concept is most relevant. Pharmacophore-based designs can be used to control chemical modifications of molecules to improve receptor recognition and increase biological activity. This can be useful to provide some insight into the nature of the functional groups in the receptor responsible for binding to established drugs.

In this work the possibilities of a theoretical study of the spatial molecular structure are demonstrated on the example of biologically active substances - melanotropins, antiviral, opioid and immunomodulatory drugs studied in Biophysics Department of Institute for Physical Problems of Baku State University. By molecular mechanics, molecular dynamics,

quantum chemistry, molecular docking methods with application of modern programs the conformational profiles, geometry, structural, electronic and spectral parameters, molecular and physical properties of the mentioned molecules have been established. As result the conformational-electronic peculiarities, which are important for the functional activity of these peptides are revealed. Using received results and data of SAR studies the bioactive conformations for some of the investigated molecules were assessed and the pharmacophore models for their interaction with the specific receptors were constructed. An estimation of the arrangement of pharmacophore elements of the investigated molecules can be used for design of the peptidomimetics.

Calculation methods

The conformational possibilities of the invetigated molecules were investigated within molecular mechanics framework as described using a program for calculating of molecular conformations [1,2]. A comparison of conformation profiles of molecules was carried out on the basis of an analysis of the values of the root-mean-square deviations (RMSD) of the coordinates of atoms and the interatomic distances calculated under the optimal alignment of the compared structures.

The electronic structure of the some molecules was investigated by quantum-chemistry methods [3], used the demonstration version of software package HyperChem (http:// www.hyper.com). The geometry optimization of thymogen molecule was computed within the framework of DFT using the hybrid density functional B3LYP with extended basis set for the polarization and diffuse functions 6-31+G(d, p) of Gaussian09 software package [4] and GaussView 6.0 [5]. The molecular docking of thymogen and its receptor was performed by AutoDock Vina software [6]. PyMol [7] was used to visualize and analyze the ligand-receptor 3D interactions.

Discussion and conclusions

Using molecular modeling, the comparative structural analysis of α-melanotropin (H–Ser1–Tyr2–Ser3–Met4–Glu5–His6–Phe7–Arg8–Trp9–Gly10–Lys11–Pro12–Val13–OH), β-melanotropin (H–Asp1–Ser2–Gly3–Pro4–Tyr5–Lys6–Met7–Glu8–His9–Phe10–Arg11–Trp12–Gly13–Ser14–Pro15–Pro16–Lys17–Asp18-OH) and γ-melanotropin, (H-Tyr1–Val2–Met3–Gly4–His5–Phe6–Arg7–Trp8–Asp9–Arg10–Phe11–Gly12–OH), which stimulate physiological and morphological changes of skin and hair coloration was performed, the conformational-electronic peculiarities, which are important for the functional activity of these peptides are revealed [8-10]. Since the peptide and its active analogues have similar functions, it is likely to assume that these molecules interact with the specific receptors by the same pharmacophore elements.The bioactive conformations of the investigated peptides were assessed by a comparative conformational analysis by pairwise cross comparisons of the low energy conformations found for melanotropins and their active analog H-His-Phe-Arg-Trp-OH, corresponding to their physiologically active segment (Figure 1a) [11]. The structures exhibits an rmsd between residues 6–9 of α-melanotropin of 0.75 Å, between residues 9-12 of β-

melanotropin of 0.82 Å, between residues 5-8 of ϒ-melanotropin 0.79 Å at comparison with mentioned active analog. It was found the helical conformation of H-His-Phe-Arg-Trp-OH is realized in the optimal conformations of melanotropin molecules. It was found the stability of spatial structure of melanotropins is defined by mutual position of the functional groups of this tetrapeptide segment and is characterized by a specific distribution of electron density, that plays an important role in the interaction with the receptor. The conformational-electronic siimilarity of the "common fragment" His-Phe-Arg-Trp of melanotropins suggests that the helical structure of this tetrapeptide provides the specificity of melanotropin-receptor interaction. On the basis of the received calculation results and data of SAR studies the pharmacophore model of melanotropins for its interaction with the specific receptor was constructed (Figure 1b).

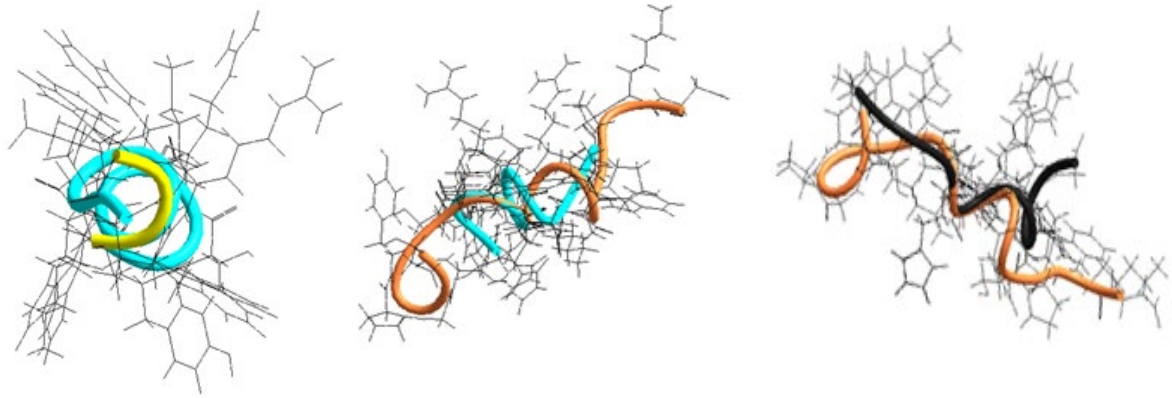

(a)

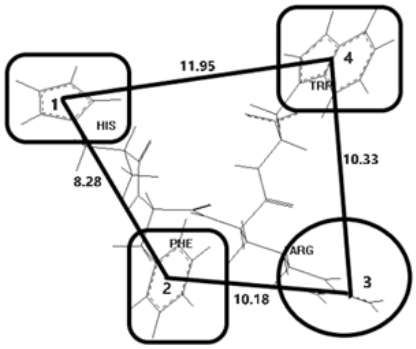

(b)

Fig. 1. Superimpositions (a) of the putative bioactive conformations of α-melanotropin (in cyan), β-melanotropin (in orange) melanotropin, γ – melanotropin (in black), that exhibits the smaller rmsd with the helical structure of active analog H-His-Phe-Arg-Trp-OH (in yellow) and its pharmacophore model (b) for the binding to specific reseptor

The relative geometric arrangement of pharmacophore groups of melanotropins is shown in Å. This pharmacophore model contains four moieties. The pharmacophore moiety 1 is the imidazole side chain of histidine residue, which can participate in the ionic contacts and H-bonding interactions with the receptor, the pharmacophore moieties 2 and 4 are the aromatic

rings of the phenylalanine and triptophan nonpolar residues, which can participate in the hydrophobic interactions with the receptor residues, the pharmacophore moiety 3 is the positive charged guanidino group of the arginine residue, which can participate in the ionic contacts and H-bonding interactions with negative charged aminoacid residues of receptor.

Comparison of the conformational characteristics of peptide T (H-Ala1-Ser2-Thr3-Thr4-Thr5-Asn6-Tyr7-Thr8-OH), showing the therapeutic effect against a HIV, its active and inactive analogs allowed to assess the bioactive conformation of peptide T, to reveal the structural features necessary for its biological activity [12-14]. In order to characterize the bioactive conformation, the structures of the peptide T and its analogs with relative energy not higher than 5 kcal / mol were compared in pairs. The visual inspection of superimposed pairs of conformations showed that the cyclic conformation could be considered similar to peptide T and its active analogues (4-8) peptide T and [D-Ala1]- peptide T amide and therefore was evaluated as bioactive (Figure 2a). The performed calculations and SAR studies of peptide T allowed us to construction the pharmacophore model for its interaction with the CD4 receptor (Figure 2b). The relative geometric arrangement of pharmacophore groups of peptide T is shown in Å. The proposed model contains five moieties which are occupied by pharmacophore elements marked by numbers 1-5. Important elements of this pharmacophore are the carbonyl group of the CO of the Thr4 residue, the alcoholic group CH3 in the side chain of the Thr5 residue, the amide NH2 in the side chain of the Asn6 residue, the aromatic ring of the side chain of the residue of Tyr7, the carboxyl group of the terminal Thr8 residue. Note that these atomic groups can serve, respectively, as donors and H-bond acceptors, and the remaining atoms of these residues are able to participate in hydrophobic interactions with the receptor.

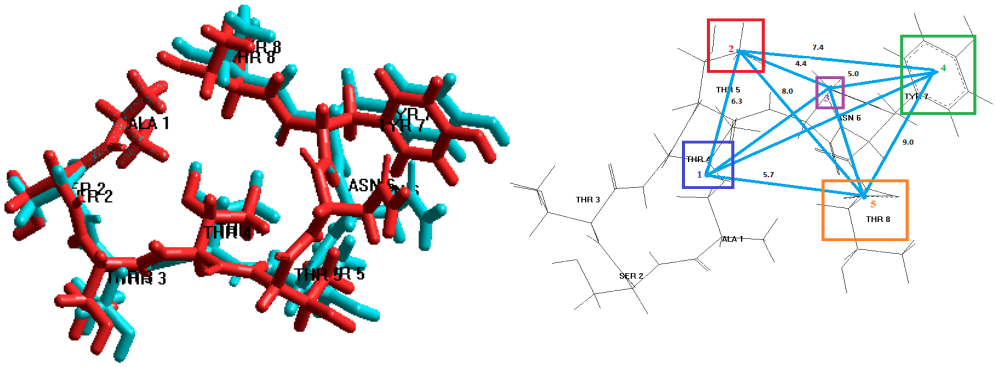

(a) (b)

Fig. 2. Superimposition (a) of proposed bioactive conformations of peptide T (blue color) and its active analogue [D-Ala1] - peptide T amide (red color) and the pharmacophore model (b) for the binding of peptide T to the CD4 receptor

The bioactive conformation of the dermorphin opioid peptide (H-Tyr-DAla-Phe-Gly-Tyr-Pro-Ser-NH_2) was assessed by pairwise cross comparisons of the low energy conformations found for dermorphin and its tetrapeptide active analogs- strong analgesics (1-4) dermorphin and [D-Arg2]-(1-4)demorphin [15,16]. In order to characterize the bioactive conformation of the dermorphin, the conformation of dermorphin with a relative energy not higher than 2

kcal/mol was compared in pairs with the optimal conformations of its active analogs. The RMSD were calculated for all atoms of the main chain of four N-terminal peptide residues. Comparison of the optimal structures of dermorphin with a set of optimal structures common to its active analogs revealed conformations with standard deviations in the range from 0.09 to 1.35 Å. A visual inspection of the superpimposed pairs of conformations showed that conformations with standard deviations below 0.8 Å can be considered similar (Figure 3a). It was found that α - amino group and the side chains of tyrosine and phenylalanine residues are in the same positions in space relative each other in the conformations of dermorphin, which are characterized by the α-helical structure of its physiologically active N-terminal tetrapeptide fragment. These conformations of the studied molecules were evaluated as bioactive. Conformational stability of the mentioned tetrapeptide sequence, apparently, plays important role in functional activity of dermorphin molecule and defines the specificity of its interaction with the opiate receptors. It was revealed that the distribution of charges on the atoms of the α - amino group and atoms of the side chains of tyrosine and phenylalanine reidues are similar for bioactive conformation of dermorphin and its active analogs, that may be correlate with their biological activity-ability to participate inligand-receptor interactions. On the basis of the received calculation results and data of SAR studies the pharmacophore model of dermorphin for its interaction with the μ-opioid receptor was constructed (Figure 3b). The relative geometric arrangement of pharmacophore moieties of dermorphin is shown in Å.

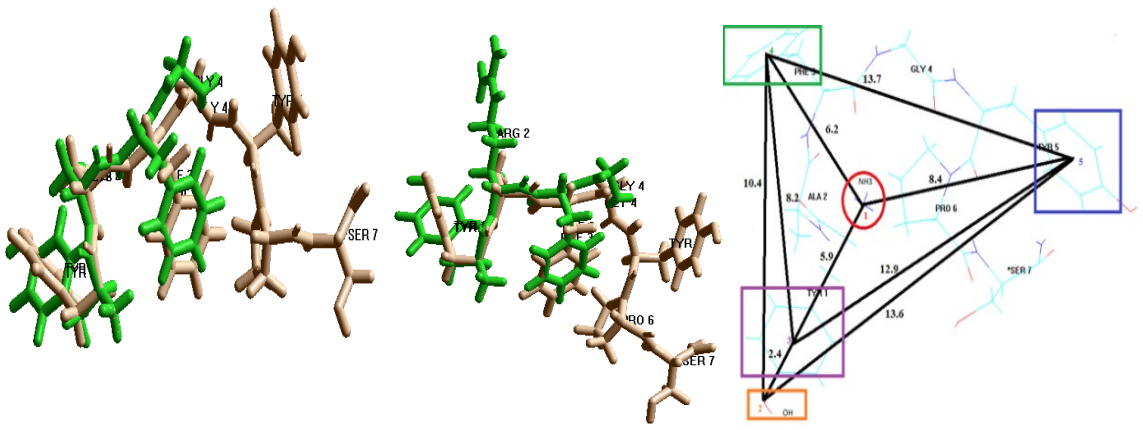

(a) (b)

Fig. 3. Superimposition (a) of proposed bioloactive conformations of dermorphin and its active analogues (1-4) dermorphin, [D-Arg2](1-4) dermorphin and the proposed pharmacophore model (b) for the binding of dermorphin to the μ-receptor.

The proposed model contains five moieties which are occupied by pharmacophore elements marked by numbers 1-5: an α - amino group, namely, the protonated nitrogen atom participating in electrostatic interaction with negatively charged residue of opioid receptor and in the formation of hydrogen bond with participation of protonated nitrogen atom; hydroxyl group of the side chain of residue Tyr1, participating in the transition of a charge as the donor of electronic density and in the formation of the hydrogen bond, a phenolic ring of

residue Tyr1 and an aromatic ring of residue Phe3, participating in the hydrophob interactions, a phenolic ring of the residue Tyr5 participating as in hydrophob interactions and in the formation of hydrogen bond, that defines the selectivity of this ligand.

Thymogen (H-Glu-Trp-OH), immunoactive dipeptide also was investigated by molecular modeling methods [17]. It was found that the conformation with extended form of backbone is optimal for this molecule. Moreover, the optimized structure of thymogen was docking onto the T-cell receptor (pdb:4MNH). The calculated binding energy and rmsd one can conclude that thymogen is potentially selective ligand for TCR and the optimized structure of thymogen complements well a cleft on the surface: the molecule undergoes only a slight displacement from its initial position and no significant conformational changes are observed, rmsd values on the backbone atoms of the minimized complex in respect to the initial ones are of 0.3Å.The hydrogen bonds between the hydrogens of of α-amino group and the carbonyl oxygen of Glu and the hydrogen bonds between NH group of Trp and oxygen atoms of the C-terminal carboxyl group stabilizing the thymogen conformation, are maintained after minimization.

In order to understand the stability of the complex obtained, the important contacts in the thymogen-TCR 4MNH complex were analyzed. We revealed that thymogen binds at the active site - β-chain and insignificantly α-chain of the complementarity-determining region (CDR) loop of the receptor by nonpolar, polar and ionic contacts. Moreover the residues of thymogen take part in intermolecular H-bonding interactions and forms also salt bridges with the receptor atoms. The obtained data allow to assess this structure as bioactive conformation of thymogen (Figure 4a). On the basis of the received results the model of pharmacophore of thymogen for its interaction with T-cell receptors was proposed (Figure 4b), the distances between the centres of pharmacophore moieties are given in Å. This pharmacophore model contains four moieties. The pharmacophore moiety 1 is the α-amino group, which can participate in the ionic contacts and H-bonding interactions with negatively charged residues of T-cell receptors. The pharmacophore moiety 2 is carboxyl group of the side chain of Glu residue, which can participate in the ionic contacts and H-bonding interactions with positive charged aminoacid residues of T-cell receptors. The pharmacophore moiety 3 is indole ring of Trp residue, it can participate in nonpolar interactions with residues of T-cell receptors. The pharmacophore moiety 4 is carboxyl group of the C-terminal part of this molecule, which can participate in the ionic contacts and H-bonding interactions with positevely charged residues of T-cell receptors. The proposed pharmacophore composes by a hydrogen bond donor and accepting centers and an indole ring, participating in the interaction with T-cell receptors. This model may be used for design of new thymomimetics for medical applications.

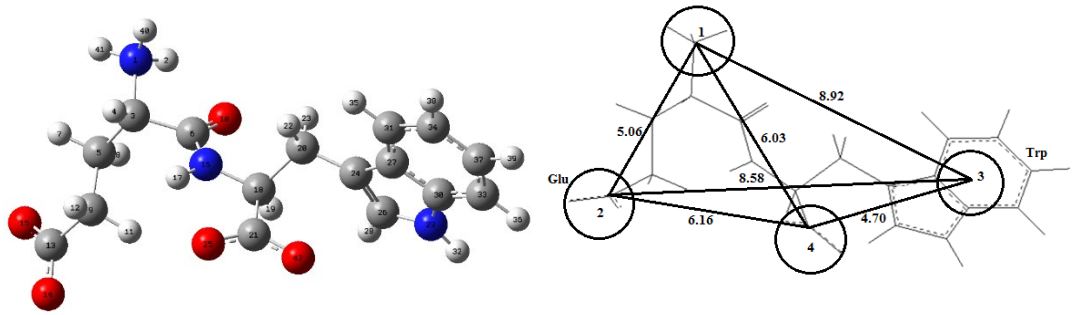

(a) (b)

Fig. 4. The putative bioactive conformation (a) and proposed pharmacophore (b) of thymogen for interaction with T-cell receptors

Thus, the investigations of electronic and conformational properties of investigated biologically active molecules can appear an important basis for additional correlation of the spatial structure and structure-functional interactions of these molecules. The proposed pharmacophore models defines the presence of the similar structural elements participating in the interaction with specific receptors and may be useful for the purposeful synthesis of steady medical products.

References

1. Godjayev N.M., Maksumov I.S. and Ismailova L.I. J.Struct.Chem. 1983, v. 4, p.147 (in Russian).
2. Akverdieva G.A., Godjayev N.M. Journal Modern Technology & Engineering 2017, v. 2 (2), p.140. http://jomardpublishing.com/UploadFiles/Files/journals/JTME/V2N2/HakverdiyevaG.pdf
3. Allinger N.L., Yuh Y., QCPE 395, Quantum chemistry program exchange, Indiana Univ., Indiana, 1982.
4. Frisch M.J., Trucks G.W., Schlegel H.B., Scuseria G.E. and et all, Gaussian 09, Revision D.01, Gaussian, Inc., Wallingford CT, 2013, https://gaussian.com/g09citation/
5. Dennington R., Keith T. A., Millam J.M., GaussView, Version6.0, Semichem Inc., Shawnee Mission, KS, 2016. https://gaussian.com/citation/
6. Trott O. Olson A.J. Journal of Computational Chemistry 2010, v. 31, p. 455. https://doi.org/10.1002/jcc.21334
7. DeLano W.L., The PyMOL molecular graphics system. 2010. https://www.ccp4.ac.uk/newsletters/newsletter40/11_pymol.pdf
8. Akhmedov N.A. and Popov E.M. Molecular Biology 1989, v. 23, p.249 (in Russian).
9. Akhmedov N.A., Akverdiyeva G.A., Godjayev N..M., Popov E.M. Int.J.Peptide and Protein Res. 1986, v. 27, p. 95.
10. Akverdiyeva G.A., Istanbul Üniv. Fen Fak. Astronomi ve Fizik Der. 1996, v. 61, p.61.
11. Akverdieva G.A, Akhmedov N.A., Godjayev N.M. Azerbaijan Journal of Physics 2017, v. 23 (4), p.6. http://physics.gov.az/index1_ru.html.
12. Godjayev N.M., Akyuz S. and Akverdieva G.A. Journal of Molecular Structure, 1997, v. 403, p. 95. DOI: 10.1016/s0022-2860(96)09410-0.
13. Akverdieva G.A., Godjayev N.M. and Akyuz S. Journal of Molecular Structure, 2002, v. 609, p. 115. DOI: 10.1016/s0022-2860(01)00974-7.
14. Akverdieva G.A., Godjayev N.M. and Akyuz S. Journal of Molecular Structure 2009, v. 917, p.21. DOI: 10.1016/j.molstruc.2008.06.028.
15. Akverdieva G.A. Azerbaijan Journal of Physics, 2016, v. 22 (2), p.12. http://physics.gov.az/index1_ru.html

16. Akverdieva G.A., Molecular mechanics study of [D-Arg2] – dermorphin tetrapeptide analogues. Proceedings of 5-th International Conference on Biological Physics (ICBP), Gothenburg, Sweden, 2004, August 23-27, p. 89, B05-158.
17. Akverdieva G.A., Godjayev N.M. and Demukhamedova S.D. Journal of Structural Chemistry 2021, v. 62 (11), p. 1783. DOI 10.26902/JSC_id83831 DOI: 10.26902/jsc_id83831

SMALL–SIZED STRUCTURES DEPOSİTED FROM A SHARP EMITTER ON A NEARBY SURFACE

IS GASANOV, SHO EMINOV, SA ALIYEV, GH MAMMEDOVA, II GURBANOV, EM AKBEROV and FE MAMEDOV

The Institute of Physics of ANAS, Baku, Azerbaijan
E-mail: sabir.eliyev.1950@mail.ru

The processes of applying the nanodroplet phase from a sharp emitter to a nearby moving surface by means of a finely dispersed phase of a liquid metal ion source (LMIS) are considered. In order to deposit narrow strips, the emitting needle was located at a close distance from the moving surface. At a needle-surface distance of the order of 80 μm, massive continuous paths of several microns wide were obtained on the axis of a wide and thin trace of ions (In+, Sn+). The structure of the deposited strips with a length of more than 10 mm is granular. To deposit narrower structures, efficient cooling of the conductive movable substrate is necessary.

Keywords: liquid metal ion source, field emission, nanoparticle, ion beam
PACS: 52.59.Fn, 29.25,Lg, 85.45.Db

To create various surface structures, a very promising method is the deposition of nanodroplets on a conductive surface. For this purpose, liquid metal ion sources with a tip emitter are used. Point emitters have the highest current density, a very small emission zone, and the ability to generate charged droplets of the working substance with nanometer-scale sizes. The possibility of focusing the resulting beams to submicron sizes is used in microtechnology, and the generation of nanoparticles of various compositions is of great interest for the production of thin films and nanotechnology. In liquid metal ion sources, along with field emission of ions, under certain conditions, generation of charged droplets occurs [1]. The sizes of the smallest charged drops are determined from the Rayleigh stability condition [3]

$$E^2/_{8\pi} > 2\sigma/_R$$

where E is the field intensity on the surface of a drop of radius R, σ is the surface tension coefficient of the liquid.

If necessary, the composition of the beam was determined by means of a mass analyzer with crossed electromagnetic fields such as a Wines velocity filter [2,4]. Taking into account the small divergence of the nanoparticle beam, it is possible to obtain narrow paths at horizontal movement of the substrate located at a close distance from the needle. That is, in this case, complex ion optics are not used. As a conductive substrate, polished plates of copper, tungsten, molybdenum, and silicon were used. For precision movement of the substrate in three coordinates, a PZU 2300 brand piezoelectric table controlled by a computer was used, which allowed vertical movement of up to 300 μm with an accuracy of 1 nm and horizontal movement of up to 100 mm. The speed of horizontal movement varied between 0.5 - 2 mm/s.

It is known that at low ion currents the radiation of liquid metal sources is stable. At a certain threshold current (about 40 μA) high-frequency oscillations are excited in the beam, which are accompanied by the generation of nanodroplets of size (2–20) nm and with specific

charge $\frac{q}{m} = 5 \cdot 10^4 \frac{C}{kg}$ (In, Sn) [4]. The oscillations of the beam current are caused by the development of capillary instability on the surface of the Taylor cone which consists of a system of standing waves.

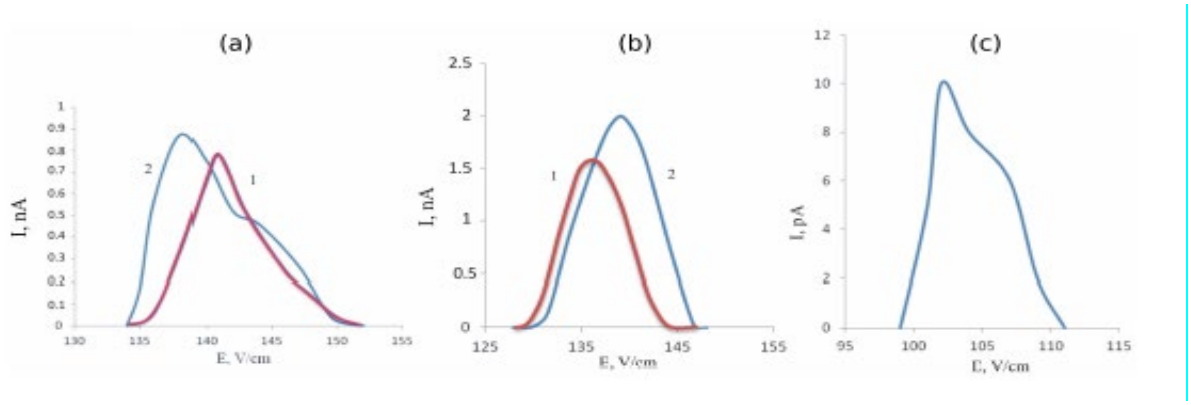

Fig. 1. Ion current through the filter of velocities as function an electric field intensity for In_1^+ (curve 1: I_b = 30 μA, U = 6 kV; curve 2: I_b = 50 μA, U = 6,2 kV) (a) in the beam center, and (b) outside the beam axis. Ion current for In_2^+ I_b = 50 μA, U = 6,2 kV, in the beam center (c).

The ion energy spectra, which were repeatedly reproduced while maintaining the experimental conditions, were recorded in the center of the beam (Fig. 1, a) and outside its axis (Fig. 1, b). The latter were obtained by moving the mass analyzer along the beam axis. The spectra were obtained in two modes: in the absence of nanodroplet generation (curve 1, $I_b = 30\ \mu A, U_b = 6\ kV$) and during their generation (curve 2, $I_b = 50 \mu A,\ \ U_b = 6{,}2 kV$). Ions with an energy of 6 keV correspond to an electric field intensity in the analyzer of about 140.5 V/cm. It should be noted that the input slit of the analyzer was achieved with the calculated value of the potential change between the plates. The position of the analyzer did not change further when registering nanodroplets. The energy spectrum of a diatomic ion $In_2^+$was also recorded in the nanodroplet generation mode (Fig. 1, c).

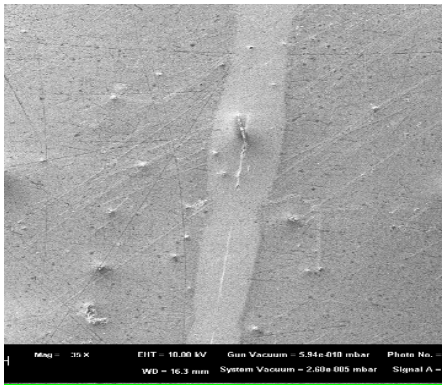

Fig. 2. SEM - image of the indium band on tungsten plate surface.

In the usual extraction of ions by means of an extractor (needle-extractor distance (0.5 - 1 mm)), the emission threshold voltage is (5 ÷ 6) kV. When the extractor was replaced with a flat substrate and the needle approached, the emission voltage decreased markedly. Fig. 2

shows a strip of indium ions and nanoparticles deposited on a tungsten plate. The extraction voltage was 4.5 kV, the needle-plate distance was ~ 200 μm.

The strip has a width of about 200 μm, and it is determined by the diameter of the ion beam. A narrow path is clearly visible in the middle of the strip due to the deposition of nanodroplets. The width of this path is about 20 μm (Fig. 3, a), the central region is significantly elevated compared to neighboring regions, and it has a coarse-grained structure (Fig. 3, b). The characteristic diameter of elongated grains is (50-60) nm, and the length is (100-200) nm. These sizes significantly exceed the sizes of generated nanodroplets [5,6]. Apparently, due to the high density of the ion current, the substrate heats up significantly, the deposited particles do not have time to condense, which leads to their coagulation and the formation of large grains. The calculation shows that at a distance of 10 cm from the needle, the ion current density is about 10 A/cm^2, and the beam power is $3 \cdot 10^4$ W/cm^2. In order for the nanodroplets to condense without adhering to each other, effective dissipation of energy from the substrate is necessary.

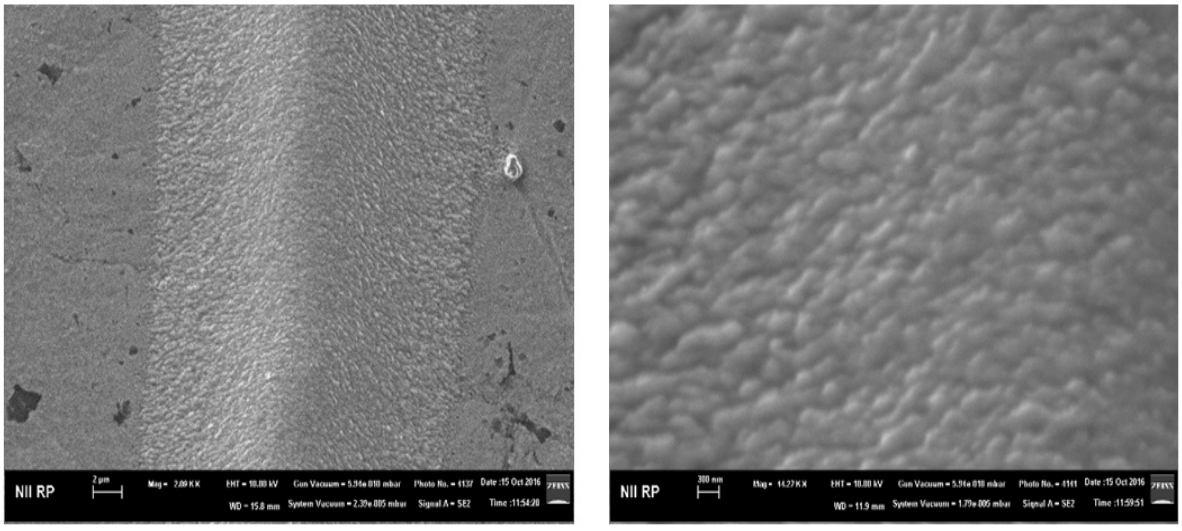

a) b)

Fig. 3. a) SEM image of a trace of deposited nanoparticles, b) trace structure.

To increase the heat removal from the substrate, it was attached to a massive copper radiator.

References

1. Badan V.V., Gasanov I.S. Le Letters to Journal of Theoretical Physics 1989, v. 15 (17), p.49 (in Russian).
2. Gasanov I.S., Gurbanov I.I. JJAP 2008, v. 47 (10), p. 8226.
3. Handbook of Charged Particle Optics. Edited by J. Orloff, CRC Press, London, New York, 2009, p. 665. DOI:10.1080/00107510903220705
4. Badan V.E., Vladimirov V.V., Gorshkov V.P. Letters to Journal of Theoretical Physics 1993, v. 63 (6), p. 47 (in Russian).
5. Gasanov I.S., Gurbanov I.I., and Akbarov E.M. ACTA Physica Polonica A 2018, v. 134 (1), p. 119. DOI: 10.12693/APhysPolA.134.119
6. Akhmadeliyev C., Bischoff L., Mair G.L.R., Aidinis C.J. and Ganetsos Th. Microelectron. Eng. 2006, v. 73-74, p. 120.

PHOTOLUMINESCENCE PROPERTIES OF GERMANIUM SULFIDE LAYERED CRYSTAL DOPED WITH NEODYMIUM

SQ ASADULLAYEVA[1], AO DASHDEMIROV[2], AS ALEKPEROV[2], SH JABAROV[3] and GA QAFAROVA[1]

[1]Institute of Physics, ANAS, Baku, Azerbaijan
[2]Azerbaijan State Pedagogical University, AZ-1000, Baku,Azerbaijan
[3]Azerbaijan State Economic University, AZ1001, Baku, Azerbaijan
E-mail: sasadullayeva@mail.ru

In this work, we report the photoluminescence properties of a GeS: Nd layered crystal at room temperature. The photoluminescence spectrum demonstrates intracentral luminescence transitions with strong Nd^{3+} ion intensities in the 1050-1850nm wavelength range.. The observed maxima are related to the intracentral transitions $^4F_{s/2}$ - $^4I_{11/2}$, $^4F_{s/2}$ - $^4I_{13/2}$, $^4F_{s/2}$-$^4I_{15/2}$, respectively.

Keywords: luminesencse , layered crystal, Intracentral Transitions
PACS: 8.20.hc, 78.40.Fy, 62.58.Pm

Introduction

The rapid development of electronics depends mainly on the provision of its material base with new promising semiconductor materials. From this point of view, layered crystals are considered promising materials for the next generation of technological devices due to their wide application in the manufacture of photodetectors, switches, photovoltaic devices and others. [1-4]. The fact that the electronic properties of this type of material depend on the number of their layers makes them even more interesting from a scientific point of view. Even in its single-layer form, semiconductor 2D materials have demonstrated effective absorption of light, which ensures high sensitivity of photodetectors. Consequently, layered semiconductor 2D materials are good candidates for optoelectronic applications, especially for photodetection [1]. [2] reported a type II van der Waals heterojunction consisting of monolayers of molybdenum disulfide and tungsten diselenide. The junction is electrically tuned, and an atomically thin diode is realized with an appropriate gate bias. black phosphorus showing great potential for thin-film electronics, infrared optoelectronics and new devices in which anisotropic properties are desired [3]. Study [4] examines the electromagnetic regimes of anisotropic 2D material and demonstrates that a wide class of materials can contain highly oriented hyperbolic plasmons. The application of this natural 2D hyperbolic media opens up new possibilities for the dynamic management of hyperbolic plasmons, which is not possible in the 3D version.

GeS compounds with an orthorhombic crystal structure between layered crystals are in the spotlight due to their anisotropic properties. [5-6] If we look at the literature, we see that in the amorphous GeS material although luminescence properties have been studied to some extent, these properties have been little studied in the GeS layered single crystal. [7-11] From this point of view, we have chosen a layered GeS crystal doped with neodymium to study the properties of photoluminescence.

Exsperimental result

Stoichiometric mixtures were weighed electronic scale, then filled into quartz ampoule with diameter 10-15 mm and 10^{-3} torr vaccum were obtained in the ampoule. The synthesis was carried out in two stages: In first stage, the ampoule wea heated up to 300^{o}C with 3-5 deg/min rate and kept at this temperature for 10-12 hours. In the second stage, the temperature of the furnace increased to 1000^{o}C with 2-3 deg/min rate and kept this temperature for 18-20 hours, and then the furnace was cooled together with sample. Activation by neodymium ions is realized using neodymium fluorides doping during synthesis process. The Bridgman method was used to grow Germanium sulfide single crystals.

Photoluminescence measurements were performed using PL/PLE/Raman spectrometer (Tokyo Instruments, Inc.) at room temperature. Photoluminescence from the sample was dispersed through a grating (100 g mm^{-1}) monochromator MS 3401 I (SOL Instruments, Inc) and detected by CCD multiplier DU 491A-1.7 (Tokyo Instruments, Inc.). PL spectra were plotted after correcting the spectral sensitivity of the detection system.

The figure demonstrates the fotoluminescence spectra of GeS:Nd crystals studied at room temperature.

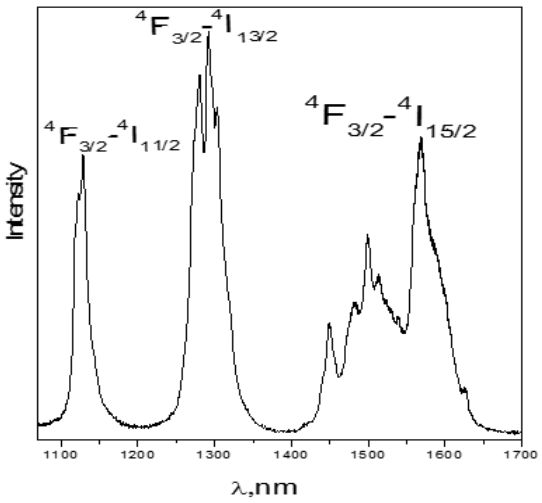

Fig.1. Fotoluminescence spectra of GeS:Nd at room temperature.

The emission of the samples were excited by laser beams 642 nm. The photoluminescence spectrum of GeS:Nd3+ single layered crystals contains intracenteral luminescence peaks of Nd^{3+} ions in wavelength ranges of 1.1–1.175, 1.230–1.3 and 1.4–1.7 μm against a broadband emission background. These lines are due, respectively, to the $^4F_{s/2}$ - $^4I_{11/2}$, $^4F_{s/2}$ - $^4I_{13/2}$, $^4F_{s/2}$-^{4} $I_{15/2}$ intracentral transitions. The intensity of the observed luminescence maxima is very strong

Conclusion

Interband excitation causes intracenteral emission from Nd^{3+} which is associated with transitions from $_4F^{3/2}$ to lower levels. The intensity of the observed luminescence maxima is very strong. According to our results, it will be possible to obtain optical amplification with this crystal.

References

1. Lídia C. Gomes and Carvalho A. Appl. Phys. 2020, v. 128, p. 121101. doi: 10.1063/5.0016003
2. Tikhomirov V.K., Iakoubovskii K., Hertogen P.W., Adriaenssens G.J., Applied Physics Letters 1997, v. 71, p. 2740.
3. Xia F., Wang H., Nat. Commun. 2014, v. 5, p. 4458.
4. Munetoshi Seki, Kan Hachiya , Katsukuni Yoshida. Journal of Non-Crystalline Solids 2003, v. 315, p. 107.
5. Alekperov A.S., Dashdemirov A.O., Ismayilova N.A., Jabarov S.H. Semiconductors 2020, p. 1406.
6. Alakbarov A.S., Dashdemirov A.O., Bayramli R.B., Imanova K.S., Advanced Physical Research 2021, v. 3, p.39.
7. Pan R.K., Haizheng Tao , Zang H.C., ZhaoXiujian. Journal of Non-Crystalline Solids 2003, v. 357, p. 2358.
8. Lan C., Li C., Yin Y., Guo H., Wang. J. Mater. Chem. C 2015, v. 3, p. 8074.
9. Dashdemirov A.O., Asadullayeva S.G., Alekperov A.S., Ismayilova N.A., Jabarov S.H. Journal of Modern Phys B 2021, v. 35, p. 2150305. DOI: 10.1142/S0217979221503057
10. Sukanov M.V., Velmizhov A.P., Kotereva T.V., Skripacov I.V., Churbanov M.F. Optical Materials Express 2019, v. 9, p. 3204.
11. Rajesh Kumar UlaganathanYi-Ying LuChia-Jung KuoChia-Jung Kuo , Yit-Tsong Chen. Nanoscale 2015, v. 8, p. 2015.

ADSORBSION AND PHOTODEGRADATION OF ORANGE G DYE BY COAL LDH /PVA AND COPPER DOPED COAL LDH/PVA NANOCOMPOSITES UNDER VISIBLE LIGHT

GX ABDULLAYEVA, AA AZIZOV, OO BALAYEVA, IA BUNIYATZADE and SJ MAMMADYAROVA

Baku State University, Baku, Azerbaijan
E-mail: abdullayeva1997g@gmail.com

In this work, photocatalytic degradation of Orange G dye was carried out under visible light in the presence of CoAl LDH as a catalyst. The conditions for dye degradation were optimized by pH and contact time. The samples were charactezized by ultraviolet-visible spectroscopy, x-ray powder diffractometer and photoelectric colorimeter. The photodegradation rate reached to maximum at pH2 (92% at 60 minutes) and reached complete equilibrium.

Keywords: layered double hydroxide; photodegradation; visible light
PACS: 07.60.Rd, 62.28.+m

Introduction

Synthetic dyes are necessary substances which are found in the various products ranging from clothes to leather accessories to furniture have negative effects of their widespread use is the fact that up to 12% of these dyes are wasted during the dyeing process, and that approximately 20% of this wastage enters the environment (mostly in water supply) [1]. There are many different methods for removing dye molecules from water: these include adsorption, biodegradation, photodegradation, coagulation, advanced oxidation process (AOP), and membrane processes [1, 2]. Some of the advantages or disadvantages of all these processes are known. Of these methods, AOP is the most effective, as well as a promising area of research. It has been reported to be effective for the removal of soluble organic pollutants from water and soils, as they can provide almost complete degradation [1,3-5]. Orange G (OG) belongs to the class of azo dyes of synthetic origin. It is a form of mono azo and anionic dye, which is soluble in water and stable at any pH [6].

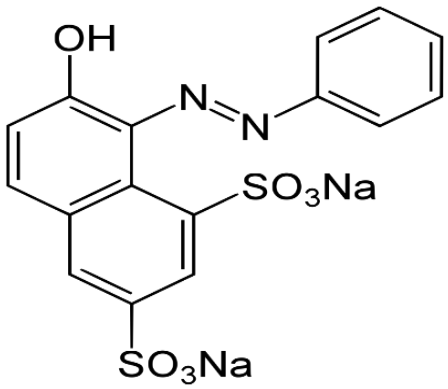

Fig. 1. Chemical formula OG.

Materials and methods

ZnAl LDH/PVA nanocomposite was synthesized using co-precipitation method. A mixed solution of 0.015 mol Co $(NO_3) \cdot 6H_2O$ and 0.005 mol $Al_2 (SO_4)_3 \cdot 18H_2O$ salts was prepared. The mixed solution was titrated with 0.8 M $NaHCO_3$ and 1.6 M NaOH. For the modification of CoAl-LDH/PVA nanocomposite 0.004 g of CuCl2·2H2O was added to 10 ml of glycerin and titrated with 10 ml of ascorbic acid. 1.177mol 10 ml of $N_2H_4 \cdot H_2O$ was used as a reducing agent.

Discussion and conclusions

For calibration curve, 1,3,5,7,9, 10, 20, 30 and 40 ppm OG azo dye solutions were prepared with distilled water. 0.01 g of nanocomposite and 3 ml of orange substances in different concentrations and pH were used in the experiment. The samples were irradiated during 30, 60 and 300 min under visible light (150W). The efficiency of adsorption and photodegradation was estimated using the following equation:

$$R\ (\%) = C_0 - C_e / C_0 \times 100 \qquad (1)$$

where C_0 and Ce are initial and equilibrium concentration of OG, respectively.

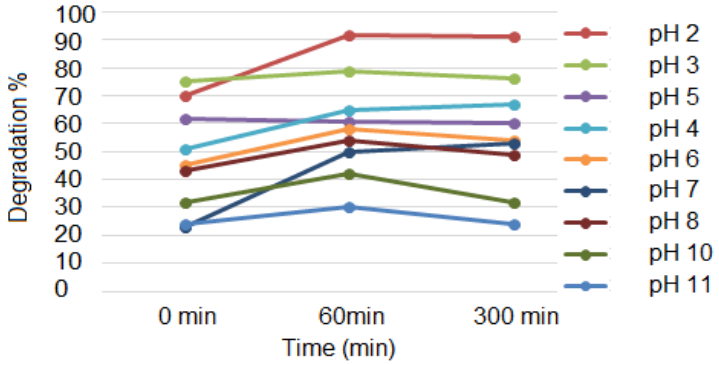

Fig. 2. The adsorption and photodegradation of OG at different pH.

When the sorption efficiency of OG composite at pH3 was 75% the photodegradation reached to 80% at 60 min under visible irradiation (150 watts). The sorption rate at pH2 was lower than at pH3, the photodegradation rate reached maximum at pH2 (92% at 60 minutes).

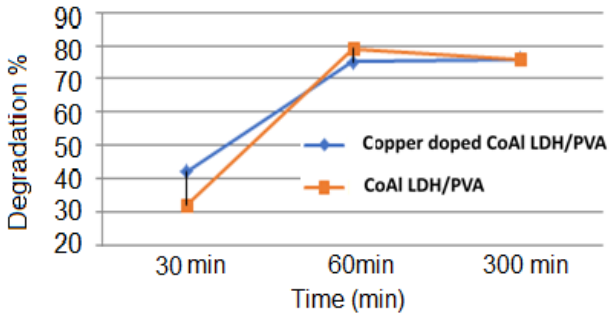

Fig. 3. Visible light photodegradation of OG at pH3 (C_0=10 mg/L).

The sorption rate increased after 30 minutes of exposure to copper doped CoAl LDH / PVA nanocomposite (R% = 32%), Cu + composite (R% = 42%). Copper metal nanoparticles are dispersed in the polymer nanocomposite matrix and form an amorphous structure (Figure 5).

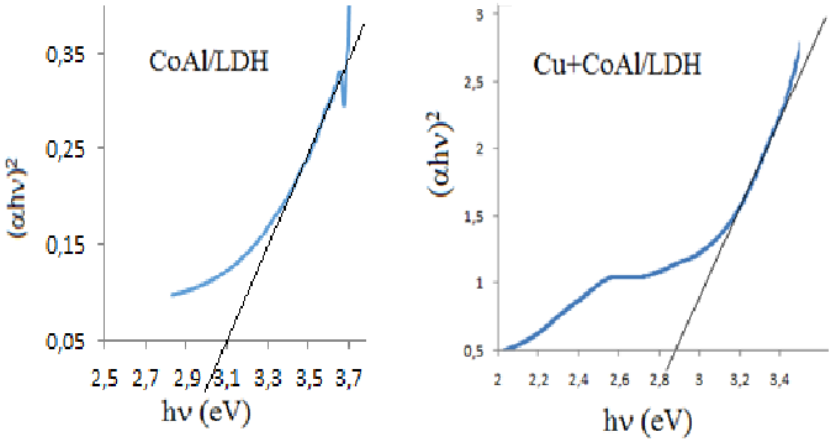

Fig. 4. Optical bandgap of nanocomposites.

Figure 4 shows the optical band gap (Eg) obtained from UV-Vis absorbance spectra of the CoAl-LDH/PVA nanocomposite before the sunlight photodegradation. The purpose of the modification is to reduce the bandgap energy of nanocomposite. The bandgaps of CoAl-LDH / PVA and Cu dopped CoAl-LDH / PVA were 3.1 eV and 2.8 eV, respectively.

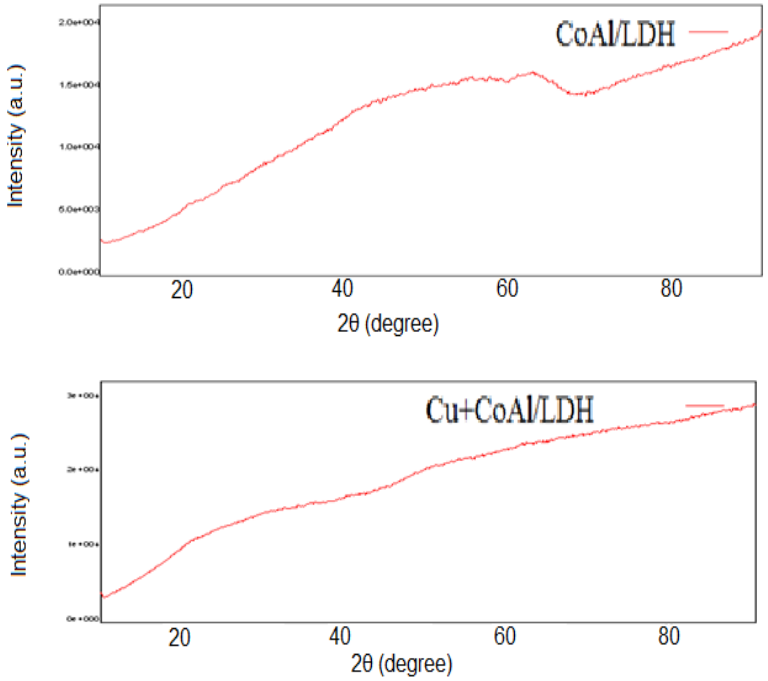

Fig. 5. XRD patterns of nanocomposites.

The XRD patterns are shown in Figure 5. The main diffraction peaks for pure CoAl LDH /PVA were observed at 2θ values of 62.1 corresponding to the lattice plane (110). The intensity of this peak decreased to 62.1 by the modification.

References

1. Rauf M.A., Ashraf S.S. Chemical Engineering Journal 2009, v. 151, p. 10. DOI: 10.1016/j.cej.2009.02.026
2. Martin M.J., Artola A., Balaguer M.D., Rigola M. Chemical Engineering Journal 2003, v. 94, p. 231. DOI.org/10.1016/S1385-8947(03)00054-8
3. Petala M., Tsiridis V., Samaras P., Zouboulis A., Sakellaropoulos G.P., Desalination 2006, v. 195, p. 109. DOI.org/10.1016/j.desal.2005.10.037
4. Chen C. , Zhang X., He W., Lu W., Han H. Science of the Total Environment 2007, v. 382, p. 93. DOI: 10.1016/j.scitotenv.2007.04.012
5. Masarwa A., Calis S.R., Meyerstein N., Meyerstein D., Coordination Chemistry Reviews 2005, v. 249, p. 1937. DOI: 10.1016/j.ccr.2005.01.003
6. https://en.wikipedia.org/wiki/Orange_G

ANALYTICAL SOLUTION OF SCHRÖDINGER EQUATION FOR LINEAR COMBINATION OF THE MANNING-ROSEN AND YUKAWA CLASS POTENTIALS

GA BAYRAMOVA

Department of Solid States Physics, Baku State University, Baku, Azerbaijan
E-mail: gyunel.bayramova.91@mail.ru

In the present work, an analytical solution for bound states of the modified Schrödinger equation is found for the new supposed combined Manning-Rosen potential plus the Yukawa class. To overcome the difficulties arising in case of $l \neq 0$ in the centrifugal part of the Manning-Rosen potential plus the Yukawa class for bound states, we applied the developed approximation. Analytical expressions for the energy eigenvalue and the corresponding radial wave functions for an arbitrary value $l \neq 0$ of the orbital quantum number are obtained. Also eigenfunctions expressed in terms of hypergeometric functions are obtained. It is shown that energy levels and eigenfunctions are very sensitive to the choice of potential parameters.

Keywords: Schrödinger equation, Manning-Rosen potential plus a class of Yukawa potential, Nikiforov-Uvarov method
PACS: 87.15.Kg, 87.16.Gj, 87.50.yg

Introduction

Investigations of the analytical solution of wave equations in potential fields in relativistic and nonrelativistic quantum mechanics have always played and will play an important, perhaps the main, role in research in the field of physics of the nucleus and elementary particles, as well as the physics of atoms and molecules. In potential models, the physical properties of micro-objects are described and interpreted using various wave equations, for example, the Schrödinger equation, the Dirac equation, the Klein – Fock – Gordon equation, and the relativistic finite-difference equation. The exact interaction potentials or phenomenologically introduced ones are used. There are many such potentials. The most famous potentials, widely used in both the relativistic and nonrelativistic regions, are the harmonic oscillator potential and the Coulomb potential, as well as their various combinations. Other types of interaction potentials include, for example, the following potentials: potentials of Kratzer, Morse, Eckart, Manning – Rosen, Pöschl – Teller, Hulthén, Wood – Saxon, Makarov, Hartmann, Ring – Shaped, etc.

The significance of a potential model, first of all, is determined by how well it describes certain properties of the physical system under consideration. Another important aspect of the model is its exact solvability.

In quantum mechanics, exact solutions, analytical and numerical solutions of both relativistic and nonrelativistic wave equations for various potentials are of great interest [1, 2]. Especially, the analytical solutions of the Schrödinger, Klein-Fock-Gordon, and Dirac equations are of great importance in quantum mechanics, because the wave function provides all the important information for a complete description of quantum systems. A small number of potentials can be solved exactly for the Schrödinger equation with any radial and orbital quantum numbers [1, 2]. Traditionally, many quantum systems can be studied only by methods of approximation and numerical solution [3]. Until now, several methods, including supersymmetry, factorization, Laplace transform approach, path integrals, and Nikiforov –

Uvarov (NU) method [4], have been developed and aimed at solving the quantum wave equation.

The NU method is of great practical importance for solving differential equations of the second order, transforming them into equations of hypergeometric type. Moreover, various exponential and hyperbolic potentials are solved analytically using various approximations by the NU method.

In principle, exponential potential models have always attracted considerable attention and are used extensively in various physical systems, including quantum cosmology, nuclear physics, molecular physics, elementary particle physics, and condensed matter physics. Many exponential-type potentials, including the Hulthén potential, Morse potential, Manning – Rosen potential, Woods – Saxon potential, Eckart potential, and Rosen – Morse potential, were previously investigated and some analytical solutions for the bound state were obtained using the approximation for these models in the state $l \neq 0$ [5-25] (and references therein).

The Schrödinger equations were also studied in detail in [26−28].

Some well-known exponential potentials can also be included in the hyperbolic potential model, which makes it possible to understand the natural dynamics of a quantum system [29] (and references therein).

In this paper, the Schrödinger equations for the combined potential, the Manning – Rosen potential plus the Yukawa class for an arbitrary value of the orbital quantum number ($l \neq 0$) are analytically solved using the NU method.

Thus, the main goal of our study is the analytical solution of the modified Schrödinger equation for a linear combination of the Manning – Rosen potential and the Yukawa class in the framework of ordinary quantum mechanics using the Nikiforov – Uvarov method. Applying the developed approximation to overcome the problem arising in the case of $l \neq 0$ in the centrifugal part of the potential, the energy eigenvalues and the corresponding radial wave functions are found for any value of the orbital angular momentum $l \neq 0$.

The article is structured as follows: Section 1 presents a brief description of the Nikiforov – Uvarov method. In Section 2, solutions for bound states of the Schrödinger equation for the Manning – Rosen potential plus the class of the Yukawa potential with an improved approximation scheme obtained using the NU method are given. Particular cases are discussed in Section 3. Further, in Section 4, numerical results for energy levels depending on potential parameters δ and quantum numbers n_r and concluding remarks are presented.

Nikiforov – Uvarov method

The Nikiforov – Uvarov method is successfully used to solve a second-order differential equation, which has the form [4]

$$\chi''(s) + \frac{\tilde{\tau}(s)}{\sigma(s)}\chi'(s) + \frac{\tilde{\sigma}(s)}{\sigma^2(s)}\chi(s) = 0. \quad (1)$$

Here, $\sigma(s)$ and $\tilde{\sigma}(s)$ are the polynomials of not higher than the second degree and $\tilde{\tau}(s)$ is the polynomial of not higher than the first degree. If we take the following factorization for the function $\chi(s)$:

$$\chi(s) = \phi(s)y(s), \tag{2}$$

then, Eq. (1) is reduced to an equation of hypergeometric type

$$\sigma(s)y''(s) + \tau(s)y'(s) + \lambda y(s) = 0, \tag{3}$$

where $\tau(s) = \tilde{\tau}(s) + 2\pi(s)$ and $\tau(s)$ satisfy the condition $\tau(s) < 0$ and the function $\pi(s)$ is defined by the expression

$$\pi(s) = \frac{\sigma'(s) - \tilde{\tau}(s)}{2} \pm \sqrt{\left(\frac{\sigma'(s) - \tilde{\tau}(s)}{2}\right)^2 - \tilde{\sigma}(s) + k\sigma(s)}. \tag{4}$$

Here, k is a parameter. The determination of k is essential in the calculation of $\pi(s)$. This parameter is simply determined from expression (4) by equating the square root discriminant to zero. From here, we can get the general quadratic equation for k. The values of k can be used to calculate the energy eigenvalue using the following formula:

$$\lambda = k + \pi'(s) = -n\tau'(s) - \frac{n(n-1)}{2}\sigma''(s). \tag{5}$$

The polynomial solutions $y(s)$ are given by the Rodrigues relation

$$y_n(s) = \frac{C_n}{\rho(s)}\frac{d^n}{ds^n}[\sigma^n(s)\rho(s)], \tag{6}$$

where C_n is the normalizing constant and $\rho(s)$ is the weight function determined from the equation

$$(\sigma(s)\rho(s))' = \tau(s)\rho(s). \tag{7}$$

At the same time, the function $\phi(s)$ satisfies the condition

$$\frac{\phi'(s)}{\phi(s)} = \frac{\pi(s)}{\sigma(s)}. \tag{8}$$

Solutıon of the Schrödınger equatıon for the sum of the mannıng-rosen potentıal and the yukawa class ın a bound state

The Schrödinger equation for a particle with mass m in a spherical coordinate system has the form [2]

$$-\frac{\hbar^2}{2m}\vec{\nabla}^2\psi(r,\theta,\phi)+V\psi(r,\theta,\phi)=E\psi(r,\theta,\phi). \quad (9)$$

Taking this equation into account, the total wave function in a spherical coordinate system is written as follows:

$$\psi(r,\theta,\varphi)=\frac{\chi(r)}{r}Y_{lm}(\theta,\varphi). \quad (10)$$

The main goal of this study is to find an analytical solution to Eq. (9) for the sum of the Manning – Rosen potential and the Yukawa class in a bound state using the Nikiforov – Uvarov method.

The Manning – Rosen potential is widely used to describe continuous and bound states in an interaction system. This potential is used in various fields, such as atomic and molecular physics, condensed matter and elementary particle physics, and nuclear physics. For a particle, quantum effects can become significant under this potential, especially, when the coupling is strong.

The Manning – Rosen potential is defined as [11, 12]

$$V_{\mathrm{MR}}(r)=\frac{1}{2mb^2}\left[\frac{\eta(\eta-1)e^{-\frac{2r}{b}}}{(1-e^{-\frac{r}{b}})^2}-\frac{Ae^{-r/b}}{1-e^{-\frac{r}{b}}}\right]. \quad (11)$$

Here, the parameter b characterizes the range of potentials and has the dimension of length, A and η are two dimensionless parameters. This potential is also used to describe the vibrations of a diatomic molecule and creates a suitable model for other physical events. Applying the relation $b=1/(2\cdot\delta)$ in Eq. (1), we obtain

$$V_{\mathrm{MR}}(r)=\frac{2\delta^2}{m}\left[\frac{\eta(\eta-1)e^{-4\delta\cdot r}}{(1-e^{-2\delta\cdot r})^2}-\frac{Ae^{-2\delta\cdot r}}{1-e^{-2\delta\cdot r}}\right]=\frac{V_{01}e^{-4\delta\cdot r}}{(1-e^{-2\delta\cdot r})^2}-\frac{V_{02}e^{-2\delta\cdot r}}{1-e^{-2\delta\cdot r}}, \quad (12)$$

where $$V_{01}=\frac{2\delta^2\eta(\eta-1)}{m}, V_{02}=\frac{2\delta^2 A}{m}. \quad (13)$$

Here, δ is the screening parameter.

Our second potential is the Yukawa potential proposed by Yukawa [30] as an effective nonrelativistic potential that well describes strong nucleon interactions.

The potential of the Yukawa class can be represented as

$$V_{\mathrm{YC}}(r)=-\frac{V_0e^{-\delta r}}{r}-\frac{V_0'e^{-2\delta r}}{r^2}. \quad (14)$$

Here, V_0 and $V_0^{'}$ determine the depth of the potential.

For a linear combination of the Manning – Rosen potential with the Yukawa-class potential, we apply new approximations of the Yukawa-class potential in the form [31]

$$\frac{1}{r} \approx \frac{2\delta e^{-\delta r}}{(1-e^{-2\delta r})}, \tag{15}$$

$$\frac{1}{r^2} \approx \frac{4\delta^2 e^{-2\delta r}}{(1-e^{-2\delta r})^2}. \tag{16}$$

Then, the sum of the Manning – Rosen and the Yukawa class potentials can be represented as follows:

$$V(r) = -\frac{V_{014}e^{-4\delta r}}{(1-e^{-2\delta r})^2} - \frac{V_{023}e^{-2\delta r}}{1-e^{-2\delta r}}. \tag{17}$$

Here, $$V_{014} = V_{01} + V_{04}, V_{023} = V_{02} + V_{03}, \tag{18}$$

$$V_{01} = \frac{2\hbar^2\delta^2\eta(\eta-1)}{m},\ V_{02} = \frac{2\hbar^2\delta^2 A}{m}, \tag{19}$$

$$V_{03} = 2\delta V_0,\ \ V_{04} = -4\delta^2 V_0^{'}. \tag{20}$$

A linear combination of these two potentials can be used to study the interactions of a deformed nucleus and spin-orbit coupling pair for a particle in a potential field. Another important property of this potential is its use in describing oscillations inside the hadronic system. Moreover, this potential can serve as a convenient model for other physical events. Considering the Schrödinger equation for a linear combination of the potential, one can obtain a deeper and more accurate estimate of the physical properties of wave functions and energies in bound, discrete, and also continuous states of interacting systems. In this paper, based on research in this direction, we present the solution of the radial Schrödinger equation for a linear combination of the Manning – Rosen and the Yukawa class potentials. Thus, our main goal is to study quantum mechanical systems at large distances. Within the framework of such combined potentials, it is possible to study the considered quantum system at significant distances.

Substituting potentials (17) and function (10) into Eq. (9), we obtain for the radial Schrödinger equation

$$\frac{d^2\chi(r)}{dr^2} + \frac{2m}{\hbar^2}\left[E - \frac{\hbar^2 l(l+1)}{2mr^2} - \frac{V_{014}e^{-4\delta r}}{(1-e^{-2\delta r})^2} + \frac{V_{023}e^{-2\delta r}}{1-e^{-2\delta r}}\right]\chi(r) = 0. \tag{21}$$

Equation (21) shows that for $r \to 0$, the centripetal potential diverges. This equation is exactly solved in case of $l = 0$. When obtaining an analytical solution for the case $l \neq 0$, to overcome difficulties arising in the centrifugal part of the Manning – Rosen potential plus the Yukawa class, we substitute expression (16) into Eq. (21) and obtain

$$\frac{d^2\chi(r)}{dr^2} + \frac{2m}{\hbar^2}\left[E - \frac{2\hbar^2\delta^2 l(l+1)}{m(1-e^{-2\delta r})^2} - \frac{V_{014}e^{-4\delta r}}{(1-e^{-2\delta r})^2} + \frac{V_{023}e^{-2\delta r}}{1-e^{-2\delta r}}\right]\chi(r) = 0. \tag{22}$$

From Eq. (22), we can determine the effective potential for the Manning – Rosen and the Yukawa class sum

$$\widetilde{V}_{eff}(r) = \frac{4\delta^2 l(l+1)e^{-2\delta r}}{(1-e^{-2\delta r})^2} + \frac{2m}{\hbar^2}\frac{V_{014}e^{-4\delta r}}{(1-e^{-2\delta r})^2} - \frac{2m}{\hbar^2}\frac{V_{023}e^{-2\delta r}}{1-e^{-2\delta r}}. \quad (23)$$

To solve Eq. (22) by the NU method, it is necessary to transform it to a certain type of hypergeometric equation, which has the form [4]

$$\chi''(s) + \frac{\tilde{\tau}(s)}{\sigma(s)}\chi'(s) + \frac{\tilde{\sigma}(s)}{\sigma^2(s)}\chi(s) = 0. \quad (24)$$

To reduce Eq. (22) to a hypergeometric equation, which has the form (24), we introduce a new variable $s = e^{-2\delta\cdot r}$:

$$\frac{d}{dr} = \frac{ds}{dr}\frac{d}{ds} = -2\delta e^{-2\cdot\delta\cdot r}\frac{d}{ds} = -2\delta s\frac{d}{ds},$$

$$\frac{d^2}{dr^2} = \left(\frac{ds}{dr}\frac{d}{ds}\right)\left(\frac{ds}{dr}\frac{d}{ds}\right) = -2\delta s\frac{d}{ds}\left(-2\delta s\frac{d}{ds}\right) = 4\delta^2 s\left(\frac{d}{ds} + s\frac{d^2}{ds^2}\right) = 4\delta^2 s\frac{d}{ds} + 4\delta^2 s^2\frac{d^2}{ds^2}. \quad (25)$$

Taking into account substitutions (25) in Eq. (22), we obtain as a result

$$\frac{d^2}{ds^2}\chi(s) + \frac{1}{s}\frac{d}{ds}\chi(s) + \frac{1}{4\delta^2 s^2}\left[\frac{2m}{\hbar^2}E - \frac{4\delta^2 l(l+1)s}{(1-s)^2} - \frac{2m}{\hbar^2}\frac{V_{014}s}{(1-s)^2} + \frac{2m}{\hbar^2}\frac{V_{023}s}{1-s}\right]\chi(s) = 0. \quad (26)$$

We introduce new notation into Eq. (26) in order to rewrite the differential equation in a more compact form:

$$\varepsilon^2 = -\frac{mE}{2\delta\hbar^2},\ \alpha^2 = \frac{mV_{014}}{2\delta^2\hbar^2},\ \beta^2 = \frac{mV_{023}}{2\delta^2\hbar^2}. \quad (27)$$

Taking into account expressions (27) in Eq. (26), we obtain

$$\chi''(s) + \frac{1-s}{(1-s)s}\chi'(s) + \frac{1}{(1-s)^2 s^2}[-\varepsilon^2(1-s)^2 - l(l+1) - \alpha^2 s^2 + \beta^2 s(1-s)]\chi(s) = 0. \quad (28)$$

Now, we can successfully apply the Nikiforov – Uvarov method to solve Eq. (28). Comparing Eq. (28) with Eq. (24), for $\tilde{\tau}(s)$, $\sigma(s)$, and $\tilde{\sigma}(s)$, we obtain

$$\sigma(s) = (1-s)s,\ \tilde{\tau}(s) = 1-s,\ \tilde{\sigma}(s) = -\varepsilon^2(1-s)^2 - l(l+1)s - \alpha^2 s^2 + \beta^2 s(1-s). \quad (29)$$

Using formulas (4) and Eq. (29), we obtain for the function $\pi(s)$

$$\pi(s) = \frac{\sigma'(s)-\tilde{\tau}(s)}{2} \pm \sqrt{\left(\frac{\sigma'(s)-\tilde{\tau}(s)}{2}\right)^2 - \tilde{\sigma}(s) + k\sigma(s)}$$

$$= -\frac{s}{2} \pm \sqrt{\frac{s^2}{4} + \varepsilon^2(1-s)^2 + l(l+1)s + \alpha^2 s^2 - \beta^2 s(1-s) + ks - ks^2}$$

$$= -\frac{s}{2} \pm \sqrt{\frac{s^2}{4} + \varepsilon^2 s^2 + \beta^2 s^2 - k s^2 - 2\varepsilon^2 s + \alpha^2 s^2 - \beta^2 s + l(l+1)s + ks + \varepsilon^2}$$

$$= -\frac{s}{2} \pm \sqrt{(\frac{1}{4} + \varepsilon^2 + \beta^2 + \alpha^2 - k)s^2 - (2\varepsilon^2 + \beta^2 - l(l+1) - k)s + \varepsilon^2}$$

$$= -\frac{s}{2} \pm \sqrt{(a-k)s^2 - (b-k)s + c}. \quad (30)$$

Here,

$$a = \frac{1}{4} + \varepsilon^2 + \alpha^2 + \beta^2, b = 2\varepsilon^2 + \beta^2 - l(l+1), c = \varepsilon^2 . \quad (31)$$

The parameter k can be found from Eq. (30) as follows. From the condition that the discriminant under the square root in Eq. (30) is equal to zero, we obtain

$$(a-k)s^2 - (b-k)s + c = 0,$$

$$D = (b-k)^2 - 4(a-k)c = k^2 + (4c-2b)k + (b^2 - 4ac),$$

$$k^2 + (4c-2b)k + (b^2 - 4ac) = 0, \quad (32)$$

$$k_{1,2} = (b-2c) \pm 2\sqrt{c^2 + c(a-b)}. \quad (33)$$

Substituting Eq. (33) into Eq. (30), we obtain for the function $\pi(s)$

$$\pi(s) = -\frac{s}{2} \pm \begin{cases} (\sqrt{c} - \sqrt{c+a-b})s - \sqrt{c}, \text{for} k = (b-2c) + 2\sqrt{c^2 + c(a-b)}, \\ (\sqrt{c} + \sqrt{c+a-b})s - \sqrt{c}, \text{for } k = (b-2c) - 2\sqrt{c^2 + c(a-b)}. \end{cases} \quad (34)$$

As can be seen from expression (34), the polynomial $\pi(s)$ has four possible values according to the NU method, but we choose the value of $\pi(s)$ for which the function $\tau(s)$ has a negative derivative. Other meanings are not physical. Hence, the corresponding functions $\pi(s)$ and $\tau(s)$ have the following forms:

$$\tau(s) = \tilde{\tau}(s) + 2\pi(s) = (1-s) + 2\pi(s) = 1 - \left[2 + 2(\sqrt{c} + \sqrt{c+a-b})\right]s + 2\sqrt{c},$$

$$\tau'(s) = -\left[2 + 2(\sqrt{c} + \sqrt{c+a-b})\right], \quad (35)$$

$$\pi(s) = \sqrt{c} - s\left[\frac{1}{2} + \sqrt{c} + \sqrt{c+a-b}\right], \quad (36)$$

$$\pi'(s) = -\frac{1}{2} - \left[\sqrt{c} + \sqrt{c+a-b}\right], \quad (37)$$

$$k = (b-2c) - 2\sqrt{c^2 + c(a-b)}\,, \quad (38)$$

$$\lambda = k + \pi'(s). \quad (39)$$

If we substitute expressions (37) and (38) into Eq. (39), we get for λ

$$\lambda = (b-2c) - 2\sqrt{c^2 + c(a-b)} - \frac{1}{2} - (\sqrt{c} + \sqrt{c+a-b}). \quad (40)$$

At the same time, λ_n is defined as follows:

$$\lambda_n = -n\tau'(s) - \frac{n(n-1)}{2}\sigma''(s) = n(2 + 2\sqrt{c} + \sqrt{c+a-b}) + n(n-1). \quad (41)$$

In expressions (40) and (41), the left-hand sides are equal to each other, and therefore, equating the right-hand sides of these expressions, we obtain

$$(b-2c) - 2\sqrt{c^2 + c(a-b)} - \frac{1}{2} - \left[\sqrt{c} + \sqrt{c+a-b}\right] = n(n-1) + 2n(1 + \sqrt{c} + \sqrt{c+a-b}). \quad (42)$$

Solving Eqs. (42) for $\sqrt{c}$, to find the energy eigenvalues, we find the analytical expression

$$\sqrt{c} = \frac{(b-2c) - \frac{1}{2} - (2n+1)\sqrt{c+a-b} - n(n+1)}{1+2n+2\sqrt{c+a-b}}. \quad (43)$$

Here,

$$b - 2c = \beta^2 - l(l+1),$$

$$\sqrt{c+a-b} = \sqrt{\frac{1}{4} + \alpha^2 + l(l+1)}. \quad (44)$$

Substituting expressions (44) into Eq. (43), we obtain

$$\sqrt{c} = \frac{\beta^2 - l(l+1) - \frac{1}{2} - (2n+1)\sqrt{\frac{1}{4} + \alpha^2 + l(l+1)} - n(n+1)}{1+2n+2\sqrt{\frac{1}{4} + \alpha^2 + l(l+1)}}. \quad (45)$$

Taking into account expression (27) in Eq. (45), for the energy spectrum, we obtain an analytical expression in the form

$$E = -\frac{\hbar^2}{2m}\left[\frac{\beta^2 - l(l+1) - \frac{1}{2} - n(n+1) - (2n+1)\sqrt{\frac{1}{4} + \alpha^2 + l(l+1)}}{n + \frac{1}{2} + \sqrt{\frac{1}{4} + \alpha^2 + l(l+1)}}\delta\right]^2. \quad (46)$$

To find the radial function of a particle moving in the Manning – Rosen potential field plus the Yukawa class, we factorize the radial function $\chi(s)$:

$$\chi(s) = \varphi(s)y(s). \quad (47)$$

Applying the NU method, the function $\varphi(s)$ can be found from the condition

$$\frac{\varphi'(s)}{\varphi(s)} = \frac{\pi(s)}{\sigma(s)}. \quad (48)$$

So, solving Eq. (48), we find for the function $\phi(s)$

$$ln\,\phi\,(s) = \int \frac{\pi(s)}{\sigma(s)} ds = \int \frac{(1-s)\sqrt{c} - \left[\frac{1}{2} + \sqrt{c+a-b}\right]s}{(1-s)s} ds$$

$$= \int \frac{\varepsilon}{s} ds - \int \frac{\frac{1}{2} + \sqrt{\frac{1}{4} + \alpha^2 + l(l+1)}}{1-s} ds = ln\, s + \left(\frac{1}{2} + \sqrt{\frac{1}{4} + \alpha^2 + l(l+1)}\right) ln(1-s)$$

$$= ln\, s^{\varepsilon} + ln(1-s)^{\left(\frac{1}{2} + \sqrt{\frac{1}{4} + \alpha^2 + l(l+1)}\right)} = ln\left[s^{\varepsilon}(1-s)^{\left(\frac{1}{2} + \sqrt{\frac{1}{4} + \alpha^2 + l(l+1)}\right)}\right],$$

$$\phi(s) = s^{\varepsilon}(1-s)^{\left(\frac{1}{2} + \sqrt{\frac{1}{4} + l(l+1) + \alpha^2}\right)}. \tag{49}$$

The function $y_n(s)$ is found from the Rodrigues formula in the form

$$y_n(s) = \frac{C_n}{\rho(s)} \frac{d^n}{ds^n}[\sigma^n(s)\rho(s)]. \tag{50}$$

Here, C_n is the normalizing constant, $\rho(s)$ is a weight function found from the solution of the Pearson equation in the form

$$\frac{d}{ds}(\sigma(s)\rho(s)) = \tau(s)\rho(s). \tag{51}$$

Solving Eq. (51) for $\rho(s)$, we get

$$\rho(s) = s^{2\varepsilon}(1-s)^{2\sqrt{\frac{1}{4} + l(l+1) + \alpha^2}}. \tag{52}$$

Substituting the weight function $\rho(s)$ into Eq. (50), we find for the function $y_n(s)$

$$y_n(s) = \frac{C_n}{s^{2\varepsilon}(1-s)^{2\sqrt{\frac{1}{4} + \alpha^2 + l(l+1)}}} \frac{d^n}{ds^n}\left[s^{n+2\varepsilon}(1-s)^{n+2\sqrt{\frac{1}{4} + \alpha^2 + l(l+1)}}\right]. \tag{53}$$

Taking into account that

$$\frac{d^n}{ds^n}\left[s^{n+2\varepsilon}(1-s)^{n+2\sqrt{\frac{1}{4} + \alpha^2 + l(l+1)}}\right] = s^{2\varepsilon}(1-s)^{2\sqrt{\frac{1}{4} + \alpha^2 + l(l+1)}} P_n^{2\varepsilon, 2\sqrt{\frac{1}{4} + \alpha^2 + l(l+1)}}(1-2s), \tag{54}$$

for the function $y_n(s)$, we find

$$y_n(s) = C_n P_n^{2\varepsilon, 2\sqrt{\frac{1}{4} + \alpha^2 + l(l+1)}}(1-2s). \tag{55}$$

Using the obtained expressions (49) and (55) and substituting them into expression (47) for the radial wave function $\chi(s)$, we obtain

$$\chi(s) = \varphi(s)y(s) = C_n \frac{s^{\varepsilon}(1-s)^{\left(\frac{1}{2}+\sqrt{\frac{1}{4}+\alpha^2+l(l+1)}\right)}}{s^{2\varepsilon}(1-s)^{2\sqrt{\frac{1}{4}+\alpha^2+l(l+1)}}} \frac{d}{ds^n}\left[s^{n+2\varepsilon}(1-s)^{n+2\sqrt{\frac{1}{4}+\alpha^2+l(l+1)}}\right]. \quad (56)$$

We can also express the radial wave function $\chi(s)$ with the help of the hypergeometric function using the properties of the Jacobi polynomials. From this, we get

$$P_n^{(p,q)}(2s) = \frac{(-1)^n}{n!2^n(1-s)^p(1+s)^q} \frac{d^n}{ds^n}[(1-s)^{p+n}(1+s)^{q+n}], \quad (57)$$

$$P_n^{(p,q)}(1-2s) = \frac{\Gamma(n+p+1)}{n!\Gamma(p+1)} {}_2F_1(-n, p+q+n+1; p+1; s). \quad (58)$$

In our case,

$$p = 2\varepsilon,\ q = 2Q-1,\ Q = \frac{1}{2}+\sqrt{\frac{1}{4}+\alpha^2+l(l+1)}.$$

Then, for the function $\chi(s)$ we obtain the following expression in compact form:

$$\chi_n(s) = C_n s^{\varepsilon}(1-s)^K \frac{\Gamma(n+2\varepsilon+1)}{n!\Gamma(2\varepsilon+1)} {}_2F_1(-n, 2\varepsilon+2K+n, 1+2\varepsilon; s). \quad (59)$$

Here, C_n is the normalizing constant found from the normalization condition

$$\int_0^{\infty}|R(r)|^2r^2dr = \int_0^{\infty}|\chi(r)|^2dr = 2\delta\int_0^1\frac{1}{s}|\chi(s)|^2ds = 1. \quad (60)$$

Using the integral formulas, we obtain

$$\int_0^1(1-s)^{2(\delta+1)}s^{2\lambda-1}\left\{{}_2F_1(-n, 2(\delta+\lambda+1)+n, 2\lambda+1; s)\right\}^2ds = \frac{(n+\delta+1)n!\Gamma(n+2\delta+2)\Gamma(2\lambda)\Gamma(2\lambda+1)}{(n+\delta+\lambda+1)\Gamma(n+2\lambda+1)\Gamma(2(\delta+\lambda+1)+n)}. \quad (61)$$

In our case, $\lambda = \varepsilon$, $\delta = Q-1$,then,

$$C_n^2\left(\frac{\Gamma(n+2\varepsilon+1)}{n!\Gamma(2\varepsilon+1)}\right)^2\frac{1}{2\delta}\int_0^1 s^{2\varepsilon-1}(1-s)^{2Q}\left[{}_2F_1(-n, 2\varepsilon+2Q+n, 1+2\varepsilon; s)\right]^2ds = 1, \quad (62)$$

$$\int_0^1 s^{2\varepsilon-1}(1-s)^{2Q}\left[{}_2F_1(-n, 2\varepsilon+2Q+n, 1+2\varepsilon; s)\right]^2ds = \frac{(n+Q)n!\Gamma(n+2Q)\Gamma(2\varepsilon)\Gamma(2\varepsilon+1)}{(n+\varepsilon+Q)\Gamma(n+2\varepsilon+1)\Gamma(2\varepsilon+2Q+n)}, \quad (63)$$

$$C_n^2\left(\frac{\Gamma(n+2\varepsilon+1)}{n!\Gamma(2\varepsilon+1)}\right)^2\frac{1}{2\delta}\frac{(n+Q)n!\Gamma(n+2Q)\Gamma(2\varepsilon)\Gamma(2\varepsilon+1)}{(n+\varepsilon+Q)\Gamma(n+2\varepsilon+1)\Gamma(2\varepsilon+2Q+n)} = 1, \quad (64)$$

$$C_n = \sqrt{\frac{2\delta n!(n+Q+\varepsilon)\Gamma(2\varepsilon+2Q+n)\Gamma(2\varepsilon+1)}{(n+Q)\Gamma(n+2Q)\Gamma(2\varepsilon)\Gamma(n+2\varepsilon+1)}}. \quad (65)$$

Discussion of the results and conclusions

In this work, using the Nikiforov – Uvarov method, we solved the modified radial Schrödinger equation for the Manning – Rosen potential plus the Yukawa class for a particle at arbitrary values $l \neq 0$ of the orbital quantum number.

Analytical expressions for the energy eigenvalues and the corresponding eigenfunctions are obtained for an arbitrary value of the orbital quantum number $l \neq 0$ and radial quantum number n. It is shown that the energy eigenvalues and the corresponding eigenfunctions are sensitive to the radial n and orbital l quantum numbers.

In solving the Schrödinger equation for arbitrary values of the orbital momentum, we applied a special approach to the centripetal potential to overcome the problem associated with a component that is proportional to $1/r^2$.

Numerical results for the energy eigenvalues were obtained using the MATHEMATICA package program.

In Table 1, the following parameter values are used: $\eta = 0.75$, $A = 2b$, $V_0 = 1$, and $V_0' = 0.1$. We compare our results with the results calculated for the Manning – Rosen potential

We also compared our results with other results obtained using the traditional method for the Manning – Rosen potential. As can be seen from the comparison of these results, in our case, the particle is also in a deeper stable state.

Using the properties of Jacobi polynomials, the eigenfunctions are expressed in terms of hypergeometric functions. Analytic expressions for the energy spectrum and the corresponding eigenfunctions for the Manning – Rosen potential and the Yukawa class were also obtained.

Table 1. Numerical results for eigenvalues of energy depending on the screening parameter δ for levels 2*p*, 3*p*,3*d*, 4*p*, 4*d*, 4*f*, 5*p*, 5*d*, 5*f*, 5*g*, 6*p*, 6*d*, 6*f*, and 6*g* at the potential parameters: $\eta = 0.75$, $A = 2b$, $V_0 = 1$, and $V_0' = 0.1$

	$1/b$ (δ = 1/2*b*)	Our result	[33]	[34, 35]	[36]	[37]
2*p*	0.025	−0.547719	−0.1205793	−0.1205793	−0.1205271	0.1205273
	0.050	−0.303029	−0.1084228	−0.1084228	−0.1082151	0.1082145
	0.075	−0.237443	−0.0969120	−0.0969120	−0.0964469	0.0964433
	0.100	−0.207645	−0.0860740			
3*p*	0.025	−0.218226	−0.0459296	−0.0459297	−0.0458779	0.0458776
	0.050	−0.118151	−0.0352672	−0.0352672	−0.0350633	0.0350589
	0.075	−0.091562	−0.0260109	−0.0260110	−0.0255654	0.0255422
	0.100	−0.0795369	−0.0181609			
3*d*	0.025	−0.208957	−0.0449299	−0.0449299	−0.0447743	0.0447737
	0.050	−0.112957	−0.0343082	−0.0343082	−0.0336930	0.0336832
	0.075	−0.0874666	−0.0251168	−0.0251168	−0.0237621	0.0237106
4*p*	0.025	−0.109483	−0.0208608	−0.0208608	−0.0208097	0.0208087
	0.050	−0.0573123	−0.0119291	−0.0119292	−0.0117365	0.0117209

	0.075	−0.0436417	−0.0054773	−0.0054773	−0.0050945	0.0050086
4*d*	0.025	−0.105703	−0.0204555	−0.0204555	−0.0203017	0.0202993
	0.050	−0.0552047	−0.0115741	−0.0115742	−0.0109904	0.0109492
	0.075	−0.041985	−0.0052047	−0.0052047	−0.0040331	0.0037985
4*f*	0.025	−0.104216	−0.0202886	−0.0202887	−0.0199797	0.0199762
	0.050	−0.0543757	−0.0114283	−0.0114284	−0.0102393	0.0101784
	0.075	−0.0413335	−0.0050935	−0.0050935	−0.0026443	0.0022810
5*p*	0.025	−0.0610113	−0.0098576	−0.0098576	−0.0098079	0.0098055
	0.050	−0.0303902				
5*d*	0.025	−0.0591336	−0.0096637	−0.0096637	−0.0095141	0.0095074
	0.050	−0.02935546				
5*f*	0.025	−0.0583905	−0.0095837	−0.0095837	−0.0092825	0.0092712
	0.050	−0.0289451				
5*g*	0.025	−0.0579888	−0.0095398	−0.0095398	−0.0090330	0.0090190
	0.050	−0.0287237				
6*p*	0.025	−0.0356142	−0.0044051	−0.0044051	−0.0043583	0.0043531
6*d*	0.025	−0.0345667	−0.0043061	−0.0043061	−0.0041650	0.0041499
6*f*	0.025	−0.0341507	−0.0042652	−0.0042652	−0.0039803	0.0039528
6*g*	0.025	0.0339254	−0.0042428	−0.0042428	−0.0037611	0.0037220

In addition, it was shown that the energy eigenvalues and the corresponding wave eigenfunctions are sensitive to the choice of radial n and orbital l quantum numbers.

Thus, the study of the analytical solution of the modified Schrödinger equation for the Manning – Rosen potential plus the Yukawa class in the framework of quantum mechanics can provide important information on the dynamics in nuclear, atomic, and molecular physics and makes it possible for a deeper study of this problem.

We can conclude that the results obtained will be of interest not only to theoretical physicists, but also to experimental physicists due to precise and more general results.

The author is grateful to A. I. Akhmedov for posing the problem and useful discussions.

References

1. Bagrov V.G., Gitman D.M., Exact solutions of relativistic wave equations, Dordrecht; Boston: Kluwer Academic Publishers, 1990. http://openlibrary.org/books/OL2204930M
2. Landau L. D., Lifshis E.M., Quantum Mechanics. Nonrelativistic theory, Nauka, M., 2006, 757 p.
3. Flugge S., Practical Quantum Mechanics, (Springer, Berlin, 1994).
4. Nikiforov A.F., Uvarov V.B., Special Functions of Mathematical Physics., Birkhäuser, Boston, Springer (1988). https://doi.org/10.1007/978-1-4757-1595-8
5. Ahmadov H.I., Jafarzade Sh.I., Qocayeva M.V., J. Mod. Phys. A 2000, v. 30, p. 1550193. https://doi.org/10.1142/S0217751X15501936
6. Ahmadov H.I., Qocayeva M.V., and Huseynova N.Sh., Journal of Modern Physics E 2017, v. 26 (5), p. 1750028. https://doi.org/10.1142/S0218301317500288
7. Ahmadov A.I., Aslanova S.M., Orujova M.Sh., Badalov S.V., Dong S.H. Physics Letters A 2019, v. 383 (24), p. 3010. https://doi.org/10.1016/j.physleta.2019.06.043
8. Ahmadov A.I., Aslanova S.M., Orujova M.Sh., Badalov S.V. Advances in High Energy Physics 2021, Article ID 8830063, 11 pages, https://doi.org/10.1155/2021/8830063
9. Ahmadov A.I., Nagiyev Sh.M., Qocayeva M.V., Uzun K., Tarverdiyeva V. A. Int. Journal Mod. Phys. A,

2018, v. 33, p. 1850203. https://doi.org/10.1142/S0217751X18502032
10. Morse P.M. Phys. Rev., 1929, v. 34, p. 57. https://doi.org/10.1103/PhysRev.34.57
11. Ahmadov A.I., Demirci M., Aslanova S.M., Mustamin M.F. Physics Letters A, 2020, v. 384 (12), p. 126372. https://doi.org/10.1016/j.physleta.2020.126372
12. Ahmadov A.I., Aydin C., Uzun O. International J. of Modern Physics A, 2014, v. 29 (1), p. 1450002 (12 pages). https://doi.org/10.1142/S0217751X1450002X
13. Nagiyev Sh. M., Ahmadov A. I. and Tarverdiyeva V. A. Adv. High Energy Phys. 2020, Article ID 1356384. DOI: 10.1155/2020/1356384
14. Nagiyev Sh. M., Ahmadov A. I. International Journal of Modern Physics A, 2019, v. 34 (17), p. 1950089 . https://doi.org/10.1142/S0217751X19500891
15. Ahmadov A.I., Naeem M., Qocayeva M.V., Tarverdiyeva V.A. Int. J. Mod. Phys. A, 2018, v. 33, p.1850021.
16. Badalov V. H., Ahmadov H. I., and Ahmadov A. I. J. of Modern Physics E, 2009, v. 18 (3), p. 631. https://doi.org/10.1142/S0218301309012756
17. Dong S.H., García-Ravelo J., Phys. Scr. 2007, v. 75, p. 307. https://iopscience.iop.org/article/10.1088/0031-8949/80/01/017001
18. Lütfüoğlu B. C. Theor.Phys. 2018, v. 69, p. 23. https://ctp.itp.ac.cn/EN/Y2018/V69/I01/23
19. Badalov V.H., Baris B., Uzun K. Modern Physics Letters A, 2019, v. 34 (14), p. 1950107. https://doi.org/10.1142/S0217732319501074
20. Woods R.D., Saxon D.S. Physical Review, 1954, v. 95 (2), p. 577. https://doi.org/10.1103/PhysRev.95.577
21. Eckart C. Phys. Rev. 1930, v. 35, p. 1303. https://doi.org/10.1103/PhysRev.35.1303
22. Rosen N., Morse P.M. Phys. Rev. 1932, v. 42, p. 210-217. https://doi.org/10.1103/PhysRev.42.210
23. Shapovalov V.N., Bagrov, V.G., Meshkov, A.G. Soviet Physics Journal 1972, v. 15, p. 1115. https://doi.org/10.1007/BF00910289
24. Ahmadov, H.I., Dadashov, E.A., Huseynova, N.S., Badalov V. H., The European Physical J. Plus, 2021, v. 136 (2), p. 244. ,https://doi.org/10.1140/epjp/s13360-021-01202-8
25. Yukawa H. Proc. Phys. Math. Soc. Jap. 1935, v. 17, p. 48. https://www.scirp.org/(S(351jmbntvnsjt1aadkposzje)) /reference/ReferencesPapers.aspx?ReferenceID=1734012
26. Qiang W.C, Dong S.H., Phys. Lett. A, 2007, v. 363, p. 169. https://doi.org/10.1016/j.physleta.2006.10.091
27. Ahmadov H.I., Aydin C., Huseynova N.Sh., Uzun O., Int. J. Mod. Phys. E, 2013, v. 22, p. 1350072. https://doi.org/10.1142/S0218301313500729
28. Qiang W.C., Dong Shi-Hai, Physics Letters A, 2007, v. 368 (1-2), p. 13. https://doi.org/10.1016/j.physleta.2007.03.057
29. Ikhdair S.M. and Sever R., Annalen der Physik, 2008, v. 17 (11), p. 879 https://doi.org/10.1002/andp.200810322
30. Lucha W., Schöberl F.F., International Journal of Modern Physics C, 1999, v. 10 (4), p. 619. https://doi.org/10.1142/S0129183199000450
31. Chen Zhao-You, Li Min and Jia Chun-Sheng. Physica Scripta, 2009, v. 79 (5), p. 055002 (7 pages). https://doi.org/10.1088/0031-8949/79/05/055002

ACTIVATION PARAMETERS OF BASIC FLOW IN WATER-ETHANOL-UREA SYSTEMS

EA MASIMOV, BG PASHAYEV, SN HAJIYEVA, LP ALIYEV

Baku State University, Z.Khalilov str., 23, Az1148, Baku, Azerbaijan
E-mail: : p.g.bakhtiyar@gmail.com

The structural features of water-ethanol, water-urea and water-ethanol-urea systems were studied on the basis of experimental estimates of kinematic viscosity at different temperatures and concentrations. For this purpose, the concentration dependences of the Gibbs energy of activation of the viscous flow, the enthalpy of activation of the viscous flow and the entropy of activation of the viscous flow of the studied systems were analyzed. The results show that ethanol has a structuring and then destructive effect on water up to a concentration of 0.15 molar, and urea has a destructive effect on the structure of water, starting from such small concentrations. The addition of urea to the ethanol-water system does not affect the inversion point.

Keywords: water, ethanol, urea, activation parameters of viscous flow.
PACS: 61.20.Ne, 66.20.+d, 82.60.Lf, 31.70.Ks

Introduction

Water is the most abundant substance in nature. This substance, which plays a great role in the geological history of our planet, in the formation of climatic conditions and in the formation of the living world as a source of life, has always attracted the attention of scientists due to its miraculous properties [1-15]. Although water is at first sight a simple substance, the study of its physical and chemical properties shows that it is a very complex substance. Almost all physical and chemical properties of water are anomalous. The unusual properties of water help it to perform a number of functions in a living organism. Water, like the environment, performs very important functions, such as transporting substances through osmosis and diffusion in the body, protecting cells and organs, and protecting the body from cold and heat due to its high heat capacity and evaporating temperature. Changes in the structure or thermodynamics of water for various reasons are reflected in all biochemical processes in living organisms.

Recent studies [5-9] have shown that inversion of concentration-dependent isotherms of some physicochemical parameters found in practice for aqueous solutions of a number of organic substances is observed. For example, in the curves of adiabatic compression in the water-ethanol solution and the partial molar volume of ethanol in the solution, the minimum of the molar fraction of ethanol is observed at values of $x_{inv}^{\beta_s} = 0.06$ [7] and $x_{inv}^{\bar{v}} = 0.07$ [8], respectively, and the first maximum of molecular light intensity at $x_{\max}^{R} = 0.09$ [9]. Researchers claim that quasi-crystalline or clathrate-like (ice-like structures of 100-150 water molecules) structures are formed at inverted concentrations [6]. Since water, ethanol, and urea molecules are present in living organisms, especially in humans, the study of water-ethanol-urea systems is of great interest.

In the presented work kinematic viscosity of systems of 1) water-ethanol in the range of $x_{et.} \in [0\text{-}0.37]$ at temperature of 10-50^{0}C, 2) water-ethanol-urea ($x_{ur.} = 0.02$) at temperature of 20-50^{0}C, in the range of $x_{et.} \in [0\text{-}0.39]$, 3) water-ethanol-urea ($x_{ur.} = 0.12$) at temperature of 20-

50^0C, in the range $x_{et.}$∈[0-0.35], 4) water-urea at temperature of 20-50^0C, in the range $x_{ur.}$∈[0-0.15], 5) water-urea-ethanol ($x_{et.}$ = 0.05) at temperature of 20-50^0C, in the range of $x_{ur.}$∈[0-0.098], was measured. Using the experimental results, the Gibbs energy ($\Delta G_\eta^{\neq}$), the enthalpy of activation of the viscous flow () and the entropy of the activation of the viscous flow ($\Delta H_\eta^{\neq}$) at the considered temperatures and concentrations were calculated and the structural properties of the solution were analyzed based on changes in these parameters.

Experiment

Object of study and methods. Aqueous solutions of different concentrations, consisting of water-ethanol-urea systems, were taken as research objects. Used ethanol (C_2H_5OH) and urea (NH_2CONH_2) are chemically pure substances. Measurements were made at normal atmospheric pressure. The solutions were prepared by gravimetric method. Bidistilled water was used to prepare the solutions. During the preparation of the samples, an analytical scale manufactured by KERN 770 was used and the measurements were taken with an accuracy of 0.0001 g. In the study, the viscosity was measured with a 0.34 mm diameter SMV-2 capillary viscometer. The flow time of the liquid was determined with an accuracy of ± 0.01 sec on the viscometer. All measurements were made three times and their average values were taken as a result of the experiment.

One of the convenient ways to study the structural changes and existing interactions in solutions is the study of the activation parameters ($\Delta G_\eta^{\neq}$, $\Delta H_\eta^{\neq}$, $\Delta S_\eta^{\neq}$) of the viscous flow of solutions [5, 10, 11]. Activation parameters characterizing the process of viscous flow in liquids are determined by the difference between the corresponding thermodynamic functions of 1mol liquid molecules in the active (G_a, H_a, S_a) and bound (G_b, H_b, S_b) states [12]:

$$\Delta G_\eta^{\neq} = G_a - G_b, \quad \Delta H_\eta^{\neq} = H_a - H_b, \quad \Delta S_\eta^{\neq} = S_a - S_b \tag{1}$$

Activation of viscous flow Gibbs energy ($\Delta G_\eta^{\neq}$) according to Eyring's theory [8] has been defined as [12, 13]:

$$\Delta G_\eta^{\neq} = RT\, ln \frac{M\nu}{N_A h} \tag{2}$$

Here ν is the kinematic viscosity of the solution corresponding to the absolute temperature T, R = 8.31 C/(K·mol) - universal gas constant, N_A = $6.02 \cdot 10^{23}$ mol^{-1} - Avogadro's number, h = $6.63 \cdot 10^{-34}$ C · sec - Planck constant, $M = \sum_{i=1}^{N} x_i M_i$ which is the molar mass of the solution. Viscous flow activation enthalpy ($\Delta H_\eta^{\neq}$) has been defined as [10, 11]:

$$\Delta H_\eta^{\neq} = R \frac{\partial\, ln(M\nu/N_A h)}{\partial(1/T)} \tag{3}$$

Viscous flow activation entropy ($\Delta S_\eta^{\neq}$) has been defined as [10-13]:

$$\Delta G_\eta^{\neq} = \Delta H_\eta^{\neq} - T\Delta S_\eta^{\neq} \tag{4}$$

Results and discussion

The dependence of the activation parameters of the viscous flow of water-ethanol, water-urea and water-ethanol-urea systems ($\Delta G_{\eta}^{\neq}$, $\Delta H_{\eta}^{\neq}$, $\Delta S_{\eta}^{\neq}$) on the concentration (x) at a temperature of 20^0C is shown in Figures 1-6. As a result of our research, it was determined that the concentration dependence of all three parameters at other temperatures studied varies with the same regularity at a temperature of 20^0C. Therefore, only graphs of results corresponding to a temperature of 20^0C are given in the study.

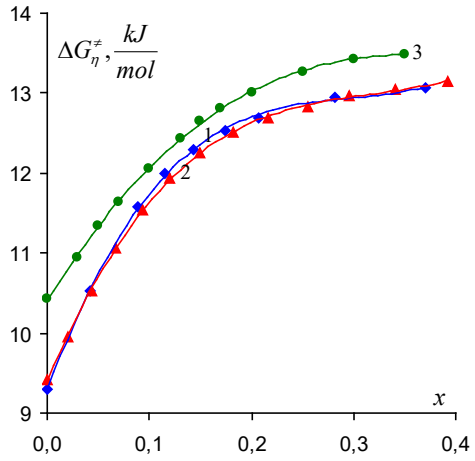

Fig. 1. Dependence of Gibbs energy of activation of viscous flow of water-ethanol-urea systems on molar part of ethanol (T=293.15 K).

1 – $x_{ur.}$=0, **2** – $x_{ur.}$=0.02, **3** - $x_{ur.}$=0.12

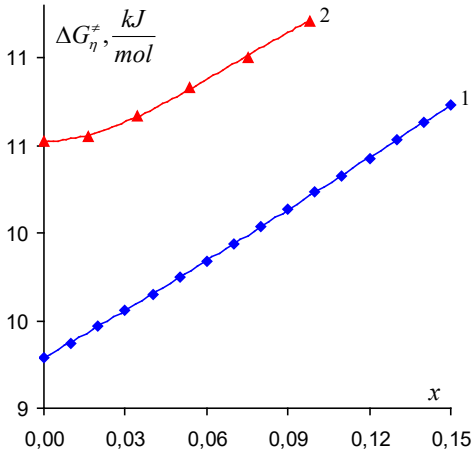

Fig. 2. Dependence of Gibbs energy of activation of viscous flow of water-urea-ethanol systems on the molar fraction of urea (T = 293.15 K).

1 - $x_{et.}$=0, **2** - $x_{et.}$=0.05

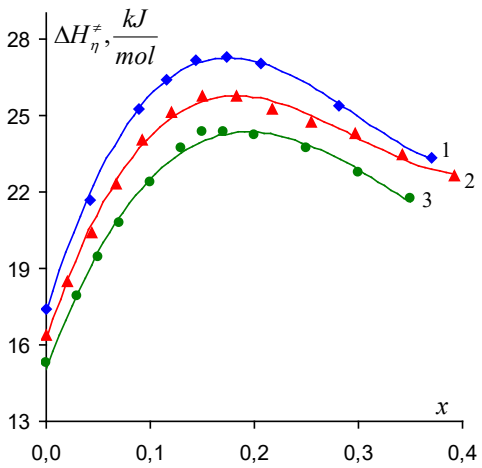

Fig. 3. Dependence of the enthalpy of activation of the viscous flow of water-ethanol-urea systems on the molar part of ethanol (T = 293.15 K).

1 – $x_{ur.}$=0, **2** – $x_{ur.}$=0.02, **3** – $x_{ur.}$=0.12

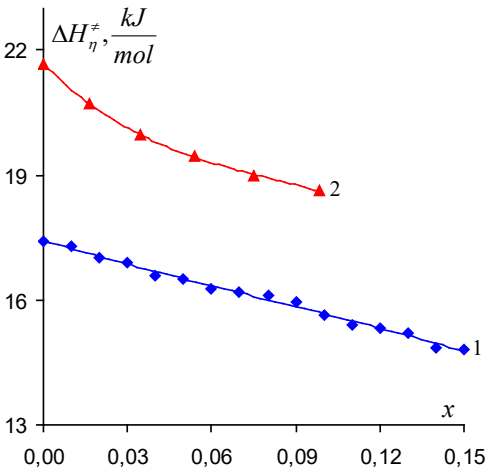

Fig. 4. Dependence of the enthalpy of activation of the viscous flow of water-urea-ethanol systems on the molar part of urea (T = 293.15K).

1 - $x_{et.}$=0, **2** - $x_{et.}$=0.05

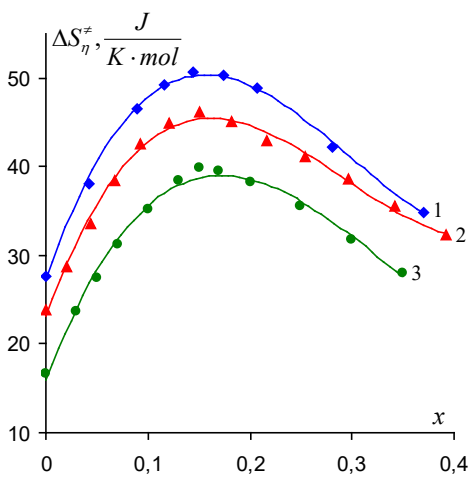

Fig. 5. Dependence of the activation entropy of the viscous flow of water-ethanol-urea systems on the molar part of ethanol (T = 293.15 K).
1 - xkar.=0, 2 - xkar.=0.02, 3 - xkar.=0.12

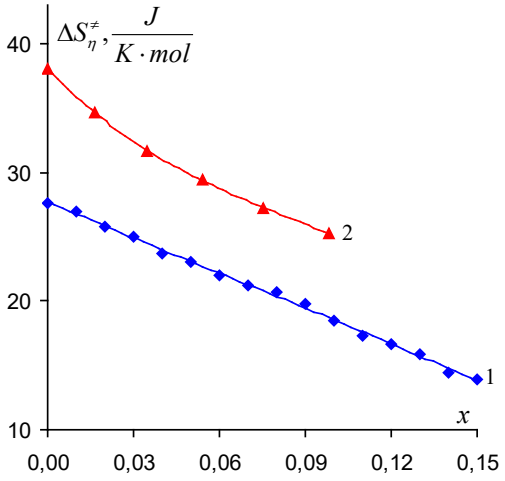

Fig.6. Dependence of activation entropy of viscous flow of water-urea-ethanol systems on the molar part of urea (T = 293.15 K). 1 - xet.=0, 2 - xet.=0.05

As can be seen from Figure 1 and Figure 2, the temperature and concentration in the considered range $\Delta G_\eta^{\neq}$ increase with increasing concentration for the aqueous solutions studied, as well as for a given temperature and concentration $\Delta G_\eta^{\neq}$ (water-ethanol) ≈ $\Delta G_\eta^{\neq}$ (water-ethanol-urea ($x_{ur.}$ = 0.02)) < $\Delta G_\eta^{\neq}$ (water-ethanol-urea ($x_{ur.}$ = 0.12)) and $\Delta G_\eta^{\neq}$ (water-urea) < $\Delta G_\eta^{\neq}$ (water-urea-ethanol ($x_{et.}$ = 0.05))). According to Eyring's theory, $\Delta G_\eta^{\neq}$ 1 mole is the energy expended to cross the potential wall of a molecule [3, 12]. It is clear that in the solutions we studied, along with water molecules, ethanol, urea, or ethanol and urea molecules, respectively, will become active. This will lead to an increase in $\Delta G_\eta^{\neq}$ with the increase in the concentration of both ethanol and urea.

As can be seen from Figure 3, in the water and ethanol and water-ethanol-urea systems in the considered temperature and concentration range, first $\Delta H_\eta^{\neq}$ increases as the ethanol concentration increases, exceeds the maximum and then decreases, as well as for a given temperature and concentration $\Delta H_\eta^{\neq}$ (water-ethanol)> $\Delta H_\eta^{\neq}$ (water -ethanol-urea ($x_{ur.}$ = 0.02))> $\Delta H_\eta^{\neq}$ (water-ethanol-urea ($x_{ur.}$ = 0.12)). Figure 4 shows that in the considered temperature and concentration range, water-urea and water-urea-ethanol systems $\Delta H_\eta^{\neq}$ only decrease with increasing urea concentration, but also $\Delta H_\eta^{\neq}$ (water-urea) < $\Delta H_\eta^{\neq}$ (water-urea-ethanol ($x_{et.}$ = 0.05)). Note that the changes in the solution $\Delta H_\eta^{\neq}$ are characterized in terms of energy. Thus, as the concentration increases, the increase in $\Delta H_\eta^{\neq}$ indicates that the system in question has become relatively more structurally structured, and vice versa [10-13].

Due to the interactions between water molecules and molecules of solute in aqueous solutions, the structure of such solutions differs significantly from the structure of water [5,

6]. Structural changes in the solution are characterized by the parameter $\Delta S_\eta^{\neq}$ [5]. Thus, as the concentration increases, the increase in $\Delta S_\eta^{\neq}$ indicates that the system becomes more structured, and the decrease becomes relatively structured [12, 13]. As can be seen from Figure 5, the temperature and concentration in the considered range $\Delta S_\eta^{\neq}$ first increase with increasing ethanol concentration in water-ethanol and water-ethanol-urea systems, exceeding the maximum at xet.≈0.15 and then decreasing, as well as for a given temperature and concentration $\Delta S_\eta^{\neq}$ (water-. ethanol)> $\Delta S_\eta^{\neq}$ (water-ethanol-urea ($x_{ur.}$ = 0.02))> $\Delta S_\eta^{\neq}$ (water-ethanol-urea ($x_{ur.}$ = 0.12)). Figure 6 shows that in the considered temperature and concentration range, the increase in concentration of urea in water-urea and water-urea-ethanol systems only decreases $\Delta S_\eta^{\neq}$, but also $\Delta S_\eta^{\neq}$ (water-urea) <$\Delta S_\eta^{\neq}$ (water-urea-ethanol ($x_{et.}$ = 0.05)). The increase in $\Delta S_\eta^{\neq}$ with the increase in the concentration of ethanol is primarily due to the structuring effect of ethanol on water at low concentrations, and the decrease in $\Delta S_\eta^{\neq}$ is due to the structural destructive effect of ethanol at high concentrations. xet. $\Delta S_\eta^{\neq}$ is maximum at point $x_{et.}$≈0.15 can be explained by the formation of more stable quasicrystalline structures in solution. At this point, the solution appears to be in its most structured state. The increase in the concentration of urea and the decrease in $\Delta S_\eta^{\neq}$ are due to the destructive effect of urea on the structure of water. The structural destructive effect of urea and the structuring effect of ethanol in small concentrations is also manifested in three-component water-ethanol-urea systems. Thus, the addition of urea to the water-ethanol system ($x_{ur.}$ = 0.02 and $x_{ur.}$ = 0.12) leads to a certain decrease in $\Delta S_\eta^{\neq}$, and the addition of ethanol to the water-urea system at low concentrations ($x_{et.}$ = 0.05) leads to a certain increase in $\Delta S_\eta^{\neq}$.

The interaction of water with alcohol can be explained as follows: at small concentrations of alcohol, its molecules enter the cage without destroying the water cage, and there is a structural effect, mainly by hydrogen bonding with free water molecules. Of course, the entry of alcohol molecules into the cage without destroying the structure of water can only continue to a certain concentration. Most likely, starting from a certain value of this concentration (in this case, it corresponds to the value of $x_{et.}$≈0.15), alcohol molecules gradually form hydrogen bonds with bound water molecules, which form a quasi-crystalline structure, which leads to the collapse of the resulting structure. Urea can be considered as a typical representative of organic substances that have a strong effect on the structure of water. It should be noted that urea increases the solubility of many compounds in water and weakens hydrophobic interactions. Urea also has strong protein denaturing properties. Analysis of the results of ultrasound and thermal measurements shows that urea destroys the structure of water [14, 15]. It seems that urea has a destructive effect on the structure of water, starting from such small concentrations, interacting with the bound water molecules that create the quasicrystalline structure of water.

The figures show that the addition of urea to the water-ethanol system and the addition of ethanol to the water-urea system do not change the nature of the dependencies $\Delta G_\eta^{\neq}$=*f*(*x*), $\Delta H_\eta^{\neq}$=*f*(*x*) və $\Delta S_\eta^{\neq}$=*f*(*x*). In addition, urea do not affect the inversion point observed in $\Delta H_\eta^{\neq}$=*f*(*x*)

və $\Delta S_{\eta}^{\neq}=f(x)$ dependencies. Therefore, the above considerations for the water-ethanol and water-urea system can also be applied to the three-component water-ethanol-urea system.

Conclusion

Analysis of the viscous flow properties of water-ethanol, water-urea and water-ethanol-urea systems shows that ethanol initially has a structuring effect on the structure of water and water-urea systems with increasing concentration, and destructive effect after value $x_{et.}$≈15.15 of concentration. Urea has only a destructive effect on the structure of both water and the water-ethanol system. The addition of urea to the water-ethanol system does not affect the inversion point ($x_{et.}$≈0.15) observed in the dependence $\Delta S_{\eta}^{\neq}=f(x)$.

References

1. Halonen S., Kangas T., Haataja M., Lassi U. Emission Control Science and Technology volume, 2017, 3, pages, p. 161.
2. Capuci A.P.S., de Carvalho N.D., Franco Jr M.R., Malagoni R.A. Revista ION 2016, v. 29, p. 125.
3. Masimov E.A., Hasanov H.Sh., Pashayev B.G. liquid viscosity. Baku, Laman, 2016, 285 p.
4. Massimov E.A., Gasanov G.Sh., Pashaev B.G. Journal of Physical Chemistry 2013, v. 87, p. 969.
5. Dakar G.M., Korableva E.Yu. Journal of Physics. Chemistry 1998, v. 72, p. 662.
6. Dakar G.M. Journal of Physics. Chemistry 2001, v. 75, p. 656.
7. Endo H. Bull. Chem. soc. Jap. 1973, v. 46, p. 1586.
8. Belousov V.P., Panov M.Yu. Thermodynamics of aqueous solutions of non-electrolytes. L.: Chemistry, 1983, 265 p.
9. Woux. M.F. Publishing house of the Leningrad University 1977, p. 131.
10. Massimov E.A., Pashaev B.G., Gasanov G.Sh., Gasanov N.G. Journal of Physical Chemistry 2015, v. 89, p. 1133.
11. Massimov E.A., Pashaev B.G., Gasanov G.Sh. Journal of Physical Chemistry 2017, v. 91, p. 644.
12. Massimov E.A., Pashaev B.G., Radjabov M.R. Journal of Physical Chemistry 2020, v. 94, p. 1909.
13. Massimov E.A., Pashaev B.G., Gasanov G.Sh. Journal of Physical Chemistry, 2019, v. 93, p. 779.
14. Barone G., Rizzo E., Vitagliano V. J Phys. Chem. 1970, v. 74, p. 2230.
15. Kancharla S., Canales E., Alexandridis P. J. Mol. Sc., 2019, v. 20 (22), p. 5761.

Printed: 25.01.2022
Volume 27 p.s.. Amount 100

Baku State University Publising House.
33, Acdemician Z. Khalilov street,
Baku, Azerbaijan
Tel: (+99412) 538 87 39 / 538 50 16
e-mail: bdumetbee@gmail.com
www.bsu.edu.az